New Methods for Data Analysis of Complex Chemical Systems with Practical Applications for Atmospheric Studies

Diogo de Jesus Medeiros

Submitted in accordance with the requirements for the degree of Doctor of Philosophy

The University of Leeds

School of Chemistry

August 2019

The candidate confirms that the work submitted is their own, except where work which has formed part of jointly authored publications has been included. The contribution of the candidate and the other authors to this work has been explicitly indicated below. The candidate confirms that appropriate credit has been given within the thesis where reference has been made to the work of others.

The work in Chapter *3* of the thesis has appeared in publication as follows:

Exploring the features on the OH + SO_2 potential energy surface using theory and testing its accuracy by comparison to experimental data.
Medeiros, D. J.; Blitz, M. *A.; Seakins, P. W.*
Physical Chemistry Chemical Physics
Volume 20, Issue 13. 2018

I was responsible for undertaking the theoretical ab initio calculations and performing the analysis of the experimental data obtained from previous studies. Dr. Mark Blitz provided experimental data from previous studies which were used in the analysis. He also provided important scientific discussions about the SO_2 chemistry which collaborated to the work. Prof. Paul W. Seakins supervised the analysis and provided scientific guidance with respect to understanding of the obtained results.

The work in Chapter *4* of the thesis has appeared in publication as follows:

Kinetics of the reaction of OH with isoprene over a wide range of temperature and pressure including direct observation of equilibrium with the OH Adducts
Medeiros, D. J.;Blitz, M. A.;James, L.;Speak, T. H.;Seakins, P. W.
The Journal of Physical Chemistry A
Volume 122, Issue 37. 2018

I was responsible for performing all the experimental measurements as well as the analysis of the data, including theoretical calculations and fits. I have also written the publication. Leanne James have helped collecting information about the temperature dependence of the CH_4 + OH reaction from the literature during her Masters. This reaction was used to check how well defined our temperature measurements were. Thomas Speak helped with collection of some experimental traces. He also provided insightful verbal discussions on the role of a Hydrogen abstraction in that chemical system. Dr. Mark Blitz and Prof. Paul W. Seakins supervised the analysis and provided scientific guidance with respect to understanding of the obtained results. They have provided critical thinking of the obtained results and proofreading.

ACKNOWLEDGMENTS

The conclusion of this work is an event that brings great happiness to my life. Before any consideration, I can not fail to highlight the direct and definitive contribution of my parents, Izaltina Maria de Jesus Medeiros and Joel Medeiros in my academic formation. I had the pleasure of having parents who showed me from an early age the value of knowledge in the life of the human being. For all the dedication and sacrifice you have undertaken through the education of your two children, I make it a point to eternally register your full names in this work, symbolizing the fact that without your teachings I would never have succeeded.

It is hard to translate into words the value of working with people as bright and yet as simple and fun as Paul and Mark. Thank you immensely for the opportunity to work alongside you and for all the teachings that have been handed down to me during these four years. Time has gone by in the blink of an eye, and it seems like only yesterday that I arrived in Leeds for the first time to find Paul waiting for me at Leeds Bradford Airport. Thank you for having been so supportive and patient during my time in Leeds. I have a deep pride in being able to say that I have had you as my supervisors!

Trev, Lisa, Dwayne, Daniel and Lavinia: Thank you for all the constructive discussions we had during meetings over these four years. Thank you for the opportunity to have worked with each of you.

My fiancee Isabelle: The support you have given me over the PhD is something I will never forget. In that time you proved that the distance between two continents is nothing when love is true. Thank you for all the wonderful moments we have lived through these four years and for making me a better person.

My brother Diego: I always remember the example he set when passing a college entrance exam in the 2000s making me believe that I could too. The

lesson that setting an example can change the world is something I learned from you.

Tom, Freja, and Alex: Thanks for the company at lunchtime for those days when, for some reason, I did not have a Subway. It was a great pleasure to work alongside you and I already miss your company.

I would also like to thank all the other comrades in the Heard and Dainton groups, with whom the coexistence in this period was a very enriching experience.

AGRADECIMENTOS

A conclusão do presente trabalho é um acontecimento que traz grande felicidade à minha vida. Antes de qualquer consideração, não posso deixar de destacar a contribuição direta e definitiva dos meus pais, Izaltina Maria de Jesus Medeiros e Joel Medeiros na minha formação acadêmica. Tive o prazer de ter pais que me mostraram desde cedo o valor do saber na vida do ser humano. Por toda dedicação e safrifício que vocês se submeteram pela educação dos seus dois filhos, eu faço questão de registrar seus nomes por completo nesse trabalho, simbolizando o fato de que sem os seus ensinamentos eu jamais teria conseguido.

É difícil traduzir em palavras o valor de trabalhar com pessoas tão brilhantes e ao mesmo tempo tão simples e divertidas como Paul e Mark. Agradeço imensamente pela oportunidade de trabalhar ao seu lado e por todos os ensinamentos que me foram passados ao longo desses quatro anos. O tempo passou num piscar de olhos, e parece que foi ontem que cheguei em Leeds pela primeira vez para encontrar Paul me esperando no aeroporto. Obrigado por me apoiar e serem tão pacientes durante meu período em Leeds. Eu tenho um orgulho profundo de poder dizer que tive vocês como meus supervisores!

Trev, Lisa, Dwayne, Daniel e Lavinia: obrigado pelas discussões construtivas que tivemos durante reuniões que tivemos ao longo desses quatro anos. Agradeço a oportunidade de ter trabalhado com cada um de vocês.

Minha noiva Isabelle: o apoio que você me dedicou ao longo do doutorado é algo da qual nunca irei me esquecer. Nesse tempo você provou que a distância entre dois continentes não é nada quando o amor é verdadeiro. Obrigado por todos os momentos maravilhosos que vivemos nesses quatro anos e por me fazer uma pessoa melhor.

Meu irmão Diego: eu lembro bem que o seu exemplo ao ser aprovado em um vestibular nos anos 2000 me fez acreditar que eu também seria capaz. A lição de que um exemplo pode mudar o mundo eu aprendi com você.

Tom, Freja e Alex: obrigado pela companhia no almoço nos dias em que eu, por algum motivo, não comi um sanduiche do Subway. For um grande prazer trabalhar ao lado de vocês e eu já sinto falta da sua companhia.

Gostaria de agradecer também a todos os demais companheiros dos grupos Heard e Dainton, com quem a conviviência nesse período foi uma experiência bastante engrandecedora.

ABSTRACT

The hydroxyl radical, OH, is the most important oxidizing agent in the troposphere during daylight periods. This radical, which is predominantly produced from the photolysis of ozone initiates the gas-phase oxidation of the vast majority of volatile organic compounds emitted in the atmosphere.

This thesis is focused on the development and exploitation of useful methods of analysis for the study of atmospherically-relevant processes via direct OH measurements. However, the flexibility of the technique makes it also suitable for the study of high temperature combustion-related chemistry. For example, OH recycling can be an important process for the high temperature oxidation of ethers, a class of oxygenated species often used as fuel additives. Such methods provide the necessary tools for the exploration of complex competing processes, stretching the limits of the conventional bimolecular analysis for measuring rate coefficients. Among them, a new method based on Master Equation calculations via global analysis allows the direct analysis of the temporal evolution of OH radicals undergoing temperature and pressure dependent processes. Such unprecedented analysis can not only provide mechanistic information, but also enables a robust evaluation of the thermochemistry of elementary reactions. The method is very useful in situations where a reaction of interest cannot be isolated from competing processes, as required by conventional analysis techniques. For example, for the high temperature oxidation of alkenes which involve both an OH addition and a hydrogen abstraction mechanism, the global technique is capable of discriminating and quantifying the contribution of each channel.

The reaction of OH radicals with sulphur dioxide (SO_2) was investigated via classical Master Equation analysis. The role of a weakly bound pre-reaction complex formation (~7.2 kJ mol^{-1}) was tested and a comparison of Leeds experimental data with the literature was undertaken. The results indicated that the pre-reaction complex formation is not significant under atmospheric conditions and much of literature data may have been influenced by secondary chemistry associated with SO_2 photolysis. A transition state submerged below

the reagents (-1.0 kJ mol^{-1}) was required to describe the Leeds measurements, which appear to be more consistent than the rest of the literature. The analysis of high temperature equilibration data (OH + SO_2 ⇄ HO-SO_2), allowed the enthalpy of reaction to be determined (110.5 ± 6.6 kJ mol^{-1}). This experimental determination is in excellent agreement with the highest-level theoretical predictions found in the literature (~111.5 kJ mol^{-1}).

The OH + isoprene reaction in the absence of oxygen was explored over a wide range of temperatures (298-794 K) and pressures (~60-1500 Torr). At high enough temperatures (T > 700 K), direct observations of the established isoprene + OH ⇄ isoprene-OH equilibrium were collected. The study also generated unprecedented rate coefficients which were subsequently employed for the study of OH recycling in the presence of O_2. The equilibration data were exploited via a bi-exponential analysis of both experimental and Master Equation-simulated traces and used for the determination of the well-depth for OH addition to carbon C1 (153.5 ± 6.2 kJ mol^{-1}), which is in excellent agreement with our theoretically-derived estimate (154.1 kJ mol^{-1}). This experimental value, however, is dependent on the level of theory at which the vibrational modes of the involved species are treated. The equilibration data also indicated a significant OH loss in the system, incompatible with the reaction of OH with its precursor or diffusion. This process was rationalized as a competing hydrogen abstraction, which interfered in the non-exponential equilibration traces. A global analysis of the data was capable of extracting information about both the OH addition ($k^{\infty}_{addition} = (9.5 \pm 1.2) \times 10^{-11} \left(\frac{T}{298\ K}\right)^{-1.33 \pm 0.32}$ cm^3 $molecule^{-1}$ s^{-1}) and the abstraction channel, ($k^{\infty}_{abstraction} = (1.3 \pm 0.3) \times 10^{-11} \exp\left(\frac{-3.61\ kJ\ mol^{-1}}{RT}\right)$ cm^3 $molecule^{-1}$ s^{-1}). With respect to the OH addition, a comparison with previous investigations suggests that only our measurements at T >700 K were in the fall-off region, contradicting some literature studies.

A new method of analysis via a global multi-temperature, multi-pressure fitting procedure was developed and used for the study of the ethylene + OH

reaction. The method relied on the Master Equation modelling of the OH addition, and a subsequent incorporation of new consumption and formation terms to the rate laws of the involved species. With effect, the simulated traces become comparable to experimental observations and a direct trace analysis is possible. The reaction of OH with ethylene was studied over a range of temperatures (563 – 723 K) and pressures (~60 - 220 Torr), which included pressure dependent data, to test the limits of this global direct trace analysis. Excellent descriptions of OH traces were obtained when the Master Equations were modified to incorporate a hydrogen abstraction and a unimolecular loss of the adduct. A simultaneous fit of 96 traces where direct ethylene + OH ⇄ adduct equilibration was observed enabled the determination of the well-depth of the adduct (111.8 ± 0.20 kJ mol^{-1}). This value is in excellent agreement with our theoretical prediction (111.4 kJ mol^{-1}), calculated at the CCSD(T)/CBS//M06-2X/ aug-cc-pVTZ level of theory. The high pressure limiting rate coefficient for the OH addition extracted from the experimental traces by this technique ($k^{\infty}_{\text{addition}}(T)=(8.13 \pm 0.86)\times10^{-12}\,(\frac{T}{298\text{ K}})^{-0.99 \pm 0.18}$ cm^{-3} molecule^{-1} s^{-1}), is in very good agreement with the IUPAC recommendation for the 100 - 500 K temperature range ($k^{\infty}_{1a}(T)=9\times10^{-12}(\frac{T}{300\text{ K}})^{-0.85}$ cm^{-3} molecule^{-1} s^{-1}). Furthermore, the experimentally derived abstraction rate coefficients $k_{\text{abstraction}}(T) = 3.5 \pm 0.75 \times 10^{-11} \exp\left(\frac{-26.2 \pm 1.3 \text{ kJ mol}^{-1}}{RT}\right)$ cm^{-3} molecule^{-1} s^{-1} are in excellent agreement with previous investigations. The method proved to be robust enough to discriminate and quantify the competing processes influencing the shapes of the experimental OH profiles.

This novel analysis was employed for the study of LIM1, a promising mechanism for the description of OH recycling via isoprene peroxy chemistry. Experiments were undertaken at elevated temperatures (400 <T<600 K) and large concentrations of O_2 were employed ([O_2]~10^{17} molecules cm^{-3}) so as to promote the recycling to the millisecond timescale, compatible with direct experimental techniques for OH detection. Rate coefficients measured in the absence of O_2 were incorporated to help constrain the analysis of the data. The LIM1 mechanism proved to be capable of accurately describing non-

exponential traces collected under such experimental conditions. The OH recycling involves crucial hydrogen shifts, whose barriers were adjusted in unison to provide a good fit to the data. However, very small modifications were necessary for this purpose (~ 2 kJ mol^{-1}). The incorporation of these findings in an atmospheric model enabled the description of approximately 50% of the OH concentration measured in a field campaign performed in a Borneo rainforest, an environment dominated by biogenic volatile organic compounds emissions.

Finally, the thesis concludes in Chapter 7 with a summary of the results of each experimental chapter including suggestions for further areas of study.

TABLE OF CONTENTS

LIST OF FIGURES

LIST OF TABLES

LIST OF ABBREVIATIONS

B3LYP	Becke, Three-Parameter, Lee-Yang-Parr Exchange-Correlation Functional
BR	Branching Ratio
BW	Bartis-Widom Analysis
CBS	Complete Basis Set Limit
CCSD(T)	Coupled Cluster Calculations With Single, Double And Pertubative Triple Excitations
CHEX	Cyclohexane
CI	Configuration Interaction
CORR	Correlation
CPM	Channel Photomultiplier
CSE	Chemically Significant Eigenvalue
DF	Discharge Flow
DFT	Density Functional Theory
di-HPCARP	Dihydroperoxycarbonyl Peroxy
DMC	*trans* 1,4-Dimethylcyclohexane
EGME	Energy Grained Master Equation
EUPHORE	European Photoreactor
FAGE	Fluorescence Assay By Gas Expansion
FTIRS	Fourier Transform Infrared Spectroscopy
GC	Gas Chromatography
HF	Hartree Fock
HIRAC	Highly Instrumented Reactor For Atmospheric Chemistry
HPALD	Hydroperoxycarbonyl Aldehyde
IERE	Internal Energy Relaxation Eigenvalue
ILT	Inverse Laplace Transformation
IUPAC	International Union Of Pure And Applied Chemistry
IVR	Internal Vibrational Energy Redistribution
LFP	Laser Flash Photolysis
LFP-LIF	Laser Flash Photolysis-Laser Induced Fluorescence
LIF	Laser Induced Fluorescence
LIM	Leuven Isoprene Mechanism
LIM1	Leuven Isoprene Mechanism 1

MCM	Master Chemical Mechanism
ME	Master Equation
MESMER	Master Equation Solver For Multi-Energy Well Reactions
MS	Mass Spectrometric Detection
Nd-YAG	Neodymium-Doped Yttrium Aluminium Garnet
ODEs	Ordinary Differential Equations
PLP-CRDS	Pulsed Laser Photolysis-Cavity Ring-Down Spectroscopy
PLP-LIF	Pulsed Laser Photolysis-Laser Induced Fluorescence
PLP-RF	Pulsed Laser Photolysis – Resonance Fluorescence
PMP4(SDTQ)	Møller-Plesset Perturbation Theory With Single, Double, Triple And Quadruple Excitations And Spin Projection
PTR-MS	Proton-Transfer Reaction Mass Spectrometry
PTR-TOF-MS	Proton-Transfer Reaction Time Of Flight Mass Spectrometry
QCISD(T)	Quadratic Configuration Interaction With Single, Double And Pertubative Triple Excitations
RF	Resonance Fluorescence
roQCISD(T)	Restricted Open-Shell Quadratic Configuration Interaction With Single, Double And Pertubative Triple Excitations
RR	Relative Rate
RRKM	Rice–Ramsperger–Kassel–Marcus Theory
TS	Transition State
TST	Transition State Theory
UCPH	Quartz Photochemical Reactor
vdW	van der Waals Pre-Reaction Complex
VOC	Volatile Organic Compound
YAG	Yttrium Aluminium Garnet
ZPE	Zero-Point Energy

Chapter 1. An Introduction to the Atmospheric Chemistry of OH and relevant experimental techniques

Overview of the chapter

The first chapter of this thesis is focused on the chemistry of the most important atmospheric oxidizer during the daylight period: the hydroxyl radical (OH). This molecule which is often referred to as the *detergent* of the atmosphere is responsible to initiate the oxidation of the vast majority of volatile organic compounds (VOCs) in the gas-phase. For this reason, the reactions of VOCs with OH are of great importance for atmospheric studies.

After an introduction regarding the atmospheric chemistry of OH, with considerations about alternative important radicals (NO_3 and Cl atoms), the fundamental differences of direct and indirect kinetic measurements are discussed to provide a familiarization with the nuances of such approaches. A pragmatic description of how direct measurements (vastly used in the experimental work of this thesis) are implemented for monitoring the temporal evolution of OH radicals. The use of simulation chambers to study atmospherically relevant reactions is discussed and demonstrated. Relative-rate experiments are presented in the context of the reactions of cyclohexanes with OH radicals for an elucidative presentation of an indirect measurement of a rate coefficient. Even though all the experimental work undertaken for the current thesis was based on direct radical observations with laser-based techniques, in many occasions the results of previous chamber studies need to be either incorporated into the analysis, or addressed in the discussion section. These needs justify a discussion about the nuances of such apparatus in a more detailed manner, so as to elucidate the limitations and nuances of the technique. Finally, a lifetime calculation based on the bimolecular rate coefficients obtained with both the direct and indirect methods is demonstrated.

1.1 THE ATMOSPHERIC CYCLE OF HOx

The OH radical, often referred to as the *atmospheric detergent*, is the primary oxidizing agent in the atmosphere during daylight periods. The reaction with OH is responsible to initiate the oxidation of the vast majority of volatile organic compounds (VOC) released in the atmosphere.[1] During sunlight periods, its production is dominated by the photolysis of ozone (R1) to produce an excited oxygen atom, denoted as $O(^1D)$; followed by the reaction of this atom with water vapour available in the atmosphere (R2), giving rise to two molecules of OH radicals.

$$O_3 + h\nu \xrightarrow{\lambda < 340\ nm} O_2 + O(^1D) \qquad R1$$

$$O(^1D) + H_2O \rightarrow 2\ OH \qquad R2$$

The main sinks of OH in the troposphere are the reactions with carbon monoxide (CO) and methane (CH_4,) which account for approximately 40% and 15% of the total OH sink flux respectively.[2] As will be discussed later in the chapter, these numbers are very dependent of the environments considered; in remote environments such processes can account to nearly 100% of the OH sink.[3] Furthermore, the reactions with OH are the main removal process for these greenhouse gases from the atmosphere, which denotes that the implications of the OH chemistry into radiative forcing are of primary importance.

In polluted environments, characterized by the presence of large concentrations of nitrogen oxides (NO_x), the reaction of HO_2 radicals with NO (R3) and the photolysis of nitrous acid (HONO) (R4) are also important sources of OH radicals.[4-5] Studies indicate that at early times in the morning, immediately after sunrise, the photolysis of HONO, whose concentration is built up during the night-time period, can become the primary precursor responsible for OH production, despite only accounting for as much as 20% of the OH formation on a 24-hour basis.[4, 6]

$HO_2 + NO \rightarrow OH + NO_2$ R3

$HONO + h\nu \xrightarrow{\lambda < 400\ nm} OH + NO$ R4

Alternative sources of OH radicals include formaldehyde and hydrogen peroxide photolysis[2, 4], alkene ozonolysis via Criegee intermediate formation[7], and the oxidation of atmospherically important VOCs such as isoprene.[8-10] Figure 1.1 shows a generic representation of the HO_x cycle in the atmosphere.

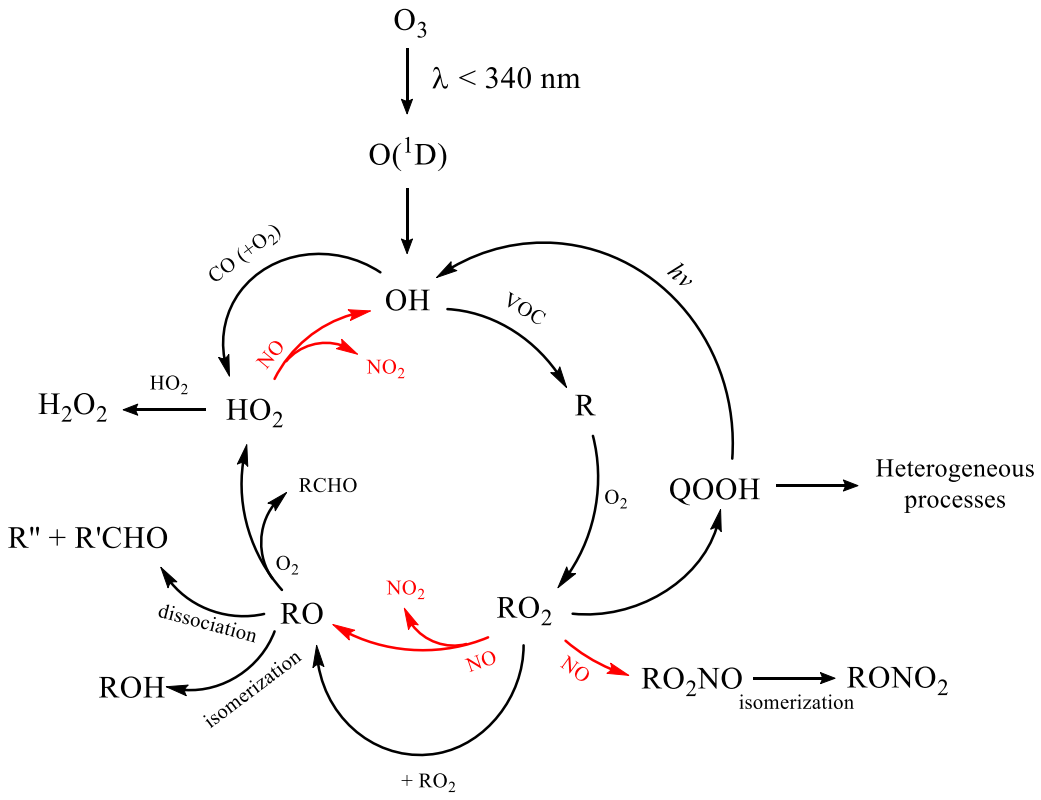

Figure 1.1 – The generic representation of the HOx cycling in the atmosphere. Processes involving NO_x are highlighted in red.

For a good understanding of the OH cycle, an instructive example will be considered. As previously discussed, OH is mostly produced via O_3 photolysis followed by the reaction of the formed $O(^1D)$ atoms with water vapour. The hydroxyl radical is now available to react with an organic pollutant. For the sake of the understanding, a simple alkane will be assumed as an example (VOC= $H_3C\text{-}CH_3$). The reaction of ethane with the OH radical proceeds via a

hydrogen abstraction, leading to the formation of an alkyl radical (R= H_3C-$\dot{C}H_2$) which rapidly reacts with O_2 to form a peroxy radical (RO_2= H_3C-$C(O_2)H_2$). The fate of peroxy radicals is determined by three typical competing paths: (I) reactions with NO (adjacent red arrows in Figure 1.1), (II) isomerization to form a hydroperoxide specie (QOOH) and (III) reaction with another peroxy radical. The relative importance of each channel can vary however, depending on whether a clean or polluted environment is being considered.

In a polluted environment, in the presence of large concentrations of the NO, typically in the order of tens of parts per billion (~10^{11}-10^{12} molecule cm^{-3}), the peroxy radical will predominantly be consumed via its reaction with NO to form an alkoxy radical (RO= H_3C-$C(O)H_2$). To a lesser extent, the RO_2 + NO reactions can lead to the generation of nitrites (RO_2NO), whose prompt isomerization can give rise to a nitrate ($RONO_2$). For example, while the nitrate yield for the *n*-hexyl peroxy + NO reaction was measured to be 0.14 ± 0.02, the yields for the corresponding reactions of NO with *n*-heptyl and *n*-octyl peroxys are 0.18 ± 0.02 and 0.22 ± 0.03, respectively.[11-12]

In pristine environments, however, the fate of peroxy radicals is primarily dictated by two competing processes: (I) a bimolecular reaction with another available RO_2 to form the alkoxy radical (RO= H_3C-$C(O)H_2$); and (II) an internal hydrogen shift to form a hydroperoxide specie, which can potentially photolyze to reform OH radicals. The lack of importance of the NO reactions in this case is justified by the significantly lower concentrations of NO in clean environments. For example, while concentrations of NO as high as 1×10^{12} molecule cm^{-3} have been measured during the summer of 2012 in central London,[13] measurements in the order of 10^9 molecule cm^{-3} of NO were measured in a rainforest of Borneo during the OP3 field campaign.[14] The significant difference of several orders of magnitudes in these numbers and the multiple competing processes presented in Figure 1.1 evidence how the atmospheric chemistry driven in clean and polluted environments can differ substantially from a mechanistic point of view. The isomerization of peroxy

radicals in pristine environments has been the focus of many studies where experimental measurements of OH radicals are critically discussed.[8-10, 14-16]

To date, a considerable number of field measurements of OH were performed in low NOx environments, with nitric oxide concentrations in the order of hundreds of parts per trillion (~ 10^9 molecule cm^{-3}), and largely dominated by biogenic emissions of VOCs. The list of these environments includes from rainforests,[17-19] to Mediterranean pine forests.[20] The large presence of biogenic VOCs in these regions, coupled with a reduced capability of the atmospheric system to recycle OH radicals via the reaction of HO_2 with NO (see Figure 1.1), naturally suggested that low OH concentrations would be measured in such conditions. Surprisingly, systematically high OH concentrations were measured in these environments, up to 0.25 parts per trillion (~ 6×10^6 molecule cm^{-3}) over the rainforest in Suriname for example, surpassing model estimates by a factor of 12.[17] On the other hand, measurements taken in the Cape Grim Baseline Air Pollution Station in northwest Tasmania, Australia, where the results indicate that more than 95% of the OH loss is dominated by methane emissions, the model estimates disagree by only 5-10% of the measurements.[3] These findings suggest a poor understanding of the oxidation of biogenic VOCs, promoting a focus on the study of OH recycling from intermediate peroxy radicals. In this context, isoprene (C_5H_8), the most abundant non-methane biogenic VOC [21] appears as an obvious candidate for a case of study. Chapters 4 and 6 will deal with the chemistry of the isoprene + OH reaction and while Chapter 4 is more focused on this initial reaction, Chapter 6 deals with the chemistry of the isoprene-peroxy radicals.

Returning to the OH cycle (see Figure 1.1), multiple competing channels are also available for the subsequent chemistry of alkoxy radicals (RO = H_3C-$C(O)H_2$ in the ethane example). The first possibility is a reaction with molecular O_2 which abstracts an α-hydrogen atom from the alkoxy radical to form a stable oxidized specie (RCHO= H_3C-C(O)H) and the HO_2 radical. The second possibility is the dissociation via a C-C bond scission. These processes are typically endothermic and their barriers tend not to exceed the exothermicity of the reactions by much more than 13-42 kJ mol^{-1}.[22] Alkoxy

radicals can also isomerize to form a hydroxy-substituted alkyl radical (ROH), in a process which tend to proceed via 1-5-H shifts.[22]

Finally, the produced HO_2 radicals can react with NO to reform OH radicals to close the cycle illustrated in Figure 1.1. For the same reasons discussed for the peroxy radicals, this final reaction is much more dominant for polluted atmospheres. As will be discussed in Chapter 6, however, even at relatively low NOx concentrations the HO_2 + NO reaction cannot be ruled out or ignored, as it can, in percentage terms, be relevant.

Despite the fact that considerably different chemical paths can be undertaken depending on the discussed atmospheric conditions, having an average estimate of the global OH concentration is highly desirable since it can provide means to estimate the lifetimes of pollutants. OH is an extremely reactive specie, and as a consequence, has an atmospheric lifetime of less than a second. In the late 1970s, Singh *et al*. demonstrated that the tropospheric concentration of OH could be estimated from the lifetimes of the now banned industrial solvent methylchloroform (CH_3CCl_3).[23-24] They have used atmospheric measurements of CH_3CCl_3 available along with an industrial inventory of methylchloroform to estimate its lifetime (τ). Aware of the fact that CH_3CCl_3 was predominantly removed via its reaction with OH and assuming a constant CH_3CCl_3 concentration throughout the troposphere, the concentration of OH was estimated (0.41×10^6 molecule cm^{-3}) from the CH_3CCl_3 lifetime and the bimolecular rate coefficient for the mentioned reaction (E1). The literature typically reports tropospheric mean concentrations of OH in the order of $(0.3\text{-}3) \times 10^6$ molecules cm^{-3} for a 24-hour period.[25-26]

$$[OH] = \frac{1}{\tau \times k_{OH + CH_3CCl_3}} \qquad \text{E1}$$

The initial reactions of OH with VOCs can proceed via two main notable mechanisms: (I) by the means of an electrophilic addition to an available π bond or (II) via a hydrogen abstraction process, as exemplified in the case of

ethane. The first channel is naturally important for the oxidation of alkenes and dienes in general, while the abstraction mechanism is important for saturated hydrocarbons. During the night, however, when the OH concentrations are rapidly reduced, so is the importance of the chemistry of this specie. During this time, nitrate (NO_3) chemistry increases in relevance.[1, 27-28] While NO_3 is heavily photolyzed to NO_2 and a ground state oxygen atom $O(^3P)$ during the day, its concentration can rapidly increase after sunset. However, as NO_3 additions to double bonds are typically slower than the OH counterparts,[28] the definition of a dominating process during darkened periods is directly compromised to the relative concentrations of OH and NO_3. At night, NO_3 concentrations can be several orders of magnitude larger than the OH.[27-28]

In the marine boundary layer however, Cl atoms tend to have a key role in the oxidation of VOCs.[29] Reactions between suspended solid particles of NaCl and nitrogenated species such as NO_2 and N_2O_5 can ultimately lead to the formation of ClNO and Cl_2 (R5-R7), species which absorb actinic ultraviolet radiation (λ>290 nm).[29] Photolysis of these species lead to the formation of atomic chlorine, which can in turn, initiate the oxidation process of available VOCs. Reactions of Cl atoms are typically at least an order of magnitude faster than the corresponding OH reactions.[30] Very low ambient Cl concentrations are predicted in the literature ([Cl] < 1×10^5 molecule cm^{-3}),[31] indirectly derived from measurements of Cl precursors and products of its reactions with available hydrocarbons, since no reliable method of direct quantification of this specie is available. [30]

$$2NO_2(s) + NaCl(g) \rightarrow ClNO(g) + NaNO_3(s) \quad \text{R5}$$

$$N_2O_5(g) + NaCl(g) \rightarrow ClNO_2(g) + NaNO_3(s) \quad \text{R6}$$

$$ClNO_2(g) + NaCl(g) \rightarrow Cl_2(g) + NaNO_3(s) \quad \text{R7}$$

1.2 DIRECT AND INDIRECT KINETIC STUDIES

The primary importance of the OH radical for the gas-phase chemistry of the planet explains the interest of the atmospheric community on chemical processes which involve the production and consumption of this specie. The reactions of OH with VOCs have been extensively explored in the last decades via a handful of different experimental approaches and techniques.[32] These include the use of atmospheric simulation chambers[33-39] and pulsed laser photolysis instruments.[40-43] Understanding the nuances of experimental data collected from such instruments is desirable for a good elucidation of the methods of analysis developed in the current thesis.

The investigation of the atmospheric system can be understood as a study of relevant elementary reactions which compose the system, with particular interest on the determination of reaction rate coefficients, their pressure and temperature dependences. The study of these chemical processes for a large number of environmentally important reactions enables the establishment of a scientific knowledge which can be applied in both predictive and deterministic manners. Figure 1.2 shows a schematic representation of how investigations of elementary reactions are tested and incorporated to atmospheric models. The scheme indicates that experimental determinations of rate coefficients can be calculated via direct and indirect approaches; the most important aspects of these variants will be discussed in the next two sections. These experimental measurements can be incorporated into a complex atmospheric model, which can in turn be used to predict, for example, the geographic extent and impacts of the presence of a pollutant in the atmosphere. While atmospheric models are typically employed to elucidate the results of field measurements and atmospheric chambers simulations, the results of such experimental procedures can also be used to feedback and refine the model current description. Section 1.2.2 is dedicated to the presentation of atmospheric simulation chambers, and provides more detailed information about such tools.

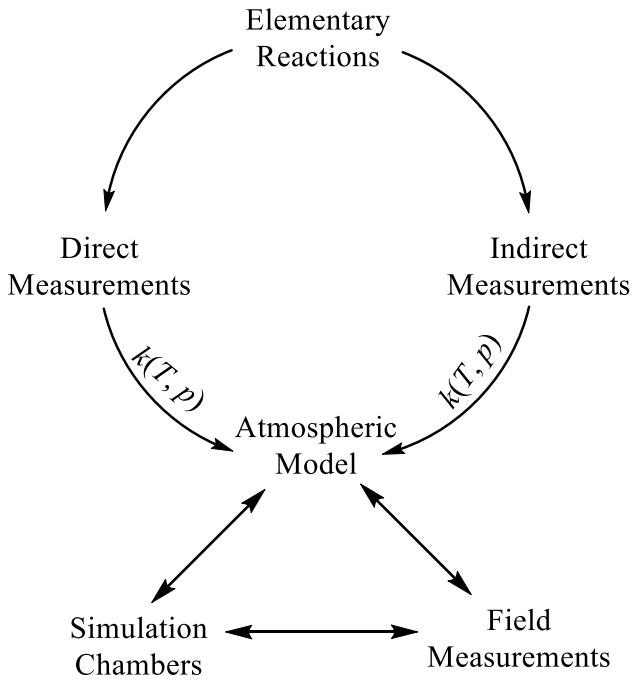

Figure 1.2 – Schematic representation of the tests, incorporation and refinement of atmospheric models.

1.2.1 - Direct Measurements

Experimental measurements of rate coefficients require monitoring the temporal evolution of reactants (or products) involved in a chemical reaction. In some cases, it is possible to isolate the chemistry of interest from competing processes to a very good extent, so that the time evolution of the monitored species are predominantly controlled by the reaction of interest. This is a case where direct measurements of the involved species may be applied. To date, direct measurements of OH reactions are typically undertaken with constant-flow systems which employ radical generation via laser flash photolysis (LFP) coupled with radical detection via laser induced fluorescence (LIF). Details of direct measurements via laser induced fluorescence techniques, significantly implemented for the studies presented in this thesis will be presented in Chapter 2. Here, a more pragmatic description of how the data are collected is considered to enable a familiarization with the most important differences and implications of direct and indirect methods. Experimental instruments and techniques are discussed with a focus on those

employed for the various studies undertaken in this thesis, presented in Chapters 3-6.

As indicated previously, by isolating the chemistry of interest to a good extent, the time-dependent evolution of the involved species will contain information about the desired process. The experimental apparatus used for direct measurements in this thesis typically consisted of a heatable metal tube in which a constant flow of reagents is fed with a carrier gas with the aid of mass-flow controllers. For the generation of OH radicals, the photolysis of a precursor such as hydrogen peroxide is necessary and can be done with the use of ~248 nm radiation. The generated OH radicals can be detected via, as discussed previously, laser induced fluorescence techniques whose basis and principles will be discussed in detail in Chapter 2. The necessary reactant time-profile can be constructed by varying the time delay between the radical generation and its detection, i.e., the time by which OH radicals are consumed by the reaction of interest is the time available between their generation and detection. Figure 1.3 shows an example of a directly measured temporal evolution of OH radicals reacting under pseudo-first order conditions with a large excess of *trans* 1,4-dimethylcyclohexane (DMC). Each point of this graph represents a different delay between the precursor photolysis and OH detection and by the time the subsequent time-point is to be collected, a new fill of gas is fed into the reaction cell, as this is a constant-flow system.

Under pseudo-first-order conditions, [OH]<<[DMC], the deficient reactant decays exponentially, as evidenced in Figure 1.3 where the red line is the fit of a single-exponential decay equation to the data. Also, under such conditions, the observed decay rate is independent of the initial concentration of the specie being monitored. With effect, there is no need to convert the experimental measurements to units of concentration, and arbitrary units can be used for the analysis without compromising its accuracy. The pseudo-first-order rate coefficient ($k'_{DMC+OH} = k_{DMC+OH}$ [DMC]) can be extracted from the fit undertaken with the use of an appropriate mathematical software. The concentration of DMC can now be altered and the measurement repeated to

yield another pseudo-first-order rate coefficient. Finally, the bimolecular rate coefficient of the DMC + OH reaction can be obtained from the slope of a plot of the pseudo-first-order rate coefficients versus the concentration of DMC used for each trace, as demonstrated in Figure 1.4.

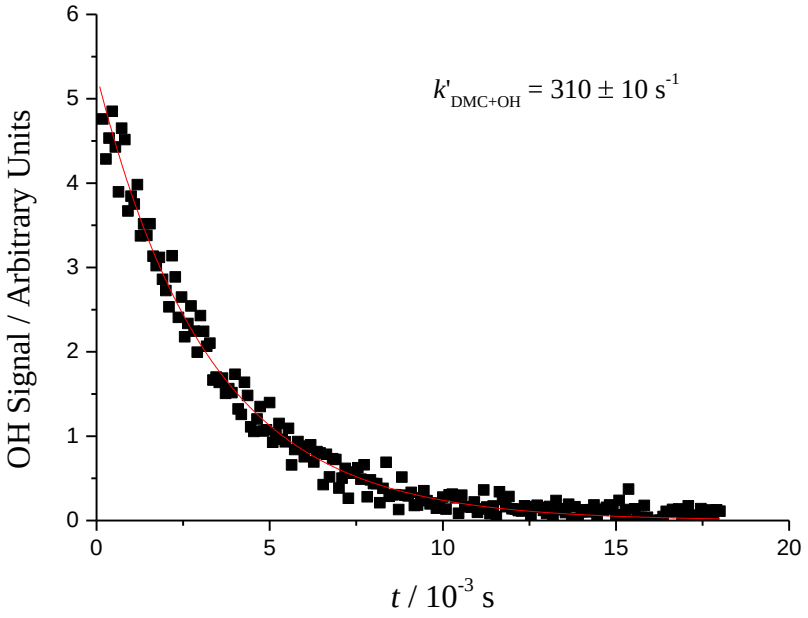

Figure 1.3 - Typical first order decay of OH in the presence of an excess of *trans* 1,4-dimethylcyclohexane (DMC). The red line is a single-exponential fit to the data, which provides a pseudo-first-order rate coefficient for the experimental conditions. T = 298 K and p = 84 Torr, [DMC] = 1.6×10^{13} molecule cm^{-3}.

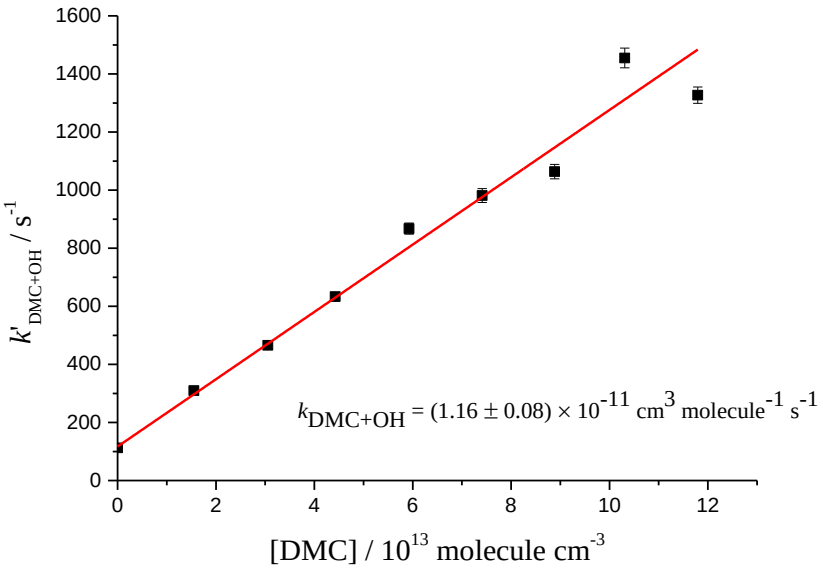

Figure 1.4 – Plot of the pseudo-first-order rate coefficients versus the concentration of the excess reagent (*trans* 1,4 dimethylcyclohexane). T = 298 K, p = 84 Torr. Increased error bars at high DMC concentrations probably caused by a slight shift of the probe wavelength during the experiment.

As indicated by the small uncertainty derived for the bimolecular rate coefficient (k_{DMC+OH} = (1.16 ± 0.08) × 10^{-11} cm^3 $molecule^{-1}$ s^{-1}), direct measurements represent a very good option in terms of precision. With good experimental control, the measurements also tend to have very good accuracies given the fact that the chemistry of interest is observed directly. These aspects make this approach an excellent alternative.

Very unstable species are monitored during the execution of the direct approach, and potential interferences can arise from the presence of stable contaminants, such as other hydrocarbons, which would compete for the OH radicals available. In which case, the chemistry of interest would not be well isolated; the OH time-dependent profiles would contain information about the two competing processes and appropriately accounting for the contribution of the contaminant to the decays is of primary importance.

Despite being very reliable and precise, direct measurements have their most important limitation related to the timescale of the experiments. For example,

the OH recycling from the oxidation of biogenic VOCs such as isoprene, which is a hot topic in terms of atmospheric chemistry discussed in section 1.1, is of the order of hundreds of seconds.[8-9] Therefore, the millisecond window of the direct experiments is not suitable for the study of this process under atmospheric conditions. However, this recycling can be scaled to the millisecond timeframe if high O_2 concentrations are employed to promote the peroxy formation, in combination with high temperatures to enhance the hydrogen shifts of ~90 kJ mol^{-1}, required to regenerate OH according to theoretical predictions.[8] As the experimental apparatus used in this case are typically consisted of simple stainless steel tubes, the instruments tend to be small, facilitating a temperature control which can be accomplished with the use of heating coils. For this thesis, temperatures as high as 790 K were reached with a conventional laser flash photolysis-laser induced fluorescence instrument, when studying the initial reaction of OH with isoprene, as presented in Chapter 4.

As discussed in section 1.1 of the current chapter, at low temperatures the reactions of OH with alkenes and dienes such as isoprene proceed via an addition mechanism to a double bond to form an adduct (VOC-OH). At high enough temperatures, however, a direct equilibration between the OH/VOC and the OH-VOC adducts is observed, as the adducts begin to unimolecularly fall apart back to reagents. As will be demonstrated in detail in Chapters 3, 4 and 5 for the OH + SO_2, isoprene and ethylene reactions respectively, such measurements impose significant constraints to the thermochemistry of the reaction. If this is not the focus of the study however, it can become a significant interference for the OH measurements. Taking the isoprene peroxy study as an example, if the initial isoprene-OH adducts are too short lived, the peroxy formation can be deficient for an investigation of the peroxy-involved recycling. For this reason, even though direct measurements enable a good flexibility in terms of achievable temperatures, the experiments need to be well-planned to make sure the most efficient and useful set of experimental data is generated.

Executing experiments at non-atmospheric conditions means that an appropriate extrapolation of the results to more atmospherically-relevant conditions is a crucially important and challenging task. A global modelling approach to the problem, in which all the experimental data are analysed as a whole can help enhance the amount of information extracted from direct measurements and improve the consistency of the analysis. For example, while the temperature dependence of a chemical process can be *invisible* if only one experimental measurement is to be compared, the analysis of a collection of data representing a considerable range of temperatures can potentially be capable of providing this information. Furthermore, if a consistent Arrhenius formulation is defined for a rate coefficient in the model, in a global analysis, this will have an effect in the modelling of all experimental data which will be tested as its adequacy to adopt this formulation, enhancing therefore the consistency of the obtained results. In Chapter 5, a new and robust global technique to model pressure and temperature-dependent reactions based on Master Equation calculations[44] allows both an evaluation of the thermochemistry of chemical reactions and a mechanistic assessment. The technique will be subsequently applied in Chapter 6 to help elucidate the chemistry of isoprene peroxys, whose data was generated with direct high temperature (T > 400 K), high O_2 (> 1×10^{17} molecule cm^{-3}) detection.

As introduced previously, direct measurements are typically undertaken with constant-flow instruments, a fact which reduces potential issues related to heterogeneous chemistry influencing the experiments. As will be discussed in the next sections, this is a significant drawback for the use of atmospheric simulation chambers, which makes their use for the study of long-lived hydroperoxides in general a difficult task.

1.2.2 – Details about Atmospheric Simulation Chambers

The atmosphere is a complex system directly influenced by countless physical and chemical, natural and anthropogenic processes. Its composition depends not only on physical-chemical processes but also on meteorological and geographic factors, while many other parameters and their effects are still unknown (photochemical sinks, the role of aerosols, etc). As a simple example, the averaged concentration of chlorine atoms in the marine boundary layer of the North Atlantic can increase from 3.3×10^4 Cl cm^{-3} at dawn to 6.5×10^4 Cl cm^{-3} at noontime[45] while the concentrations above the Antarctic Ocean was estimated around 720 Cl cm^{-3}.[46] The atmospheric chemistry driven in these locations is affected by temperature and pressure, which makes the comprehension of field studies a challenging task. In this context, controlled experiments are essential for aiding the elucidation of field measurements, providing valuable insights in both kinetic and mechanistic research. Simulation chambers represent suitable tools for this purpose.

Atmospheric simulation chambers can be made of several distinct materials. Examples of commonly implemented materials include Teflon, as used in the EUPHORE outdoor chamber[47] in Valencia; steel, as used in the Highly instrumented Reactor for Atmospheric Chemistry (HIRAC)[48] housed in Leeds and quartz/glass, as implemented in the UCPH reactor[49], located in Copenhagen.

Large outdoor chambers (~200 m^3) are commonly made of Teflon. In these chambers, the experiments are performed under ambient conditions, and the use of direct solar radiation to initiate the chemistry is implemented, preventing issues inherent to artificial light sources. On the other hand, the progress of the experiments can be interrupted due to meteorological aspects, such as wind, clouds, storms, etc. Teflon is a relatively cheap material when compared to steel and quartz, which represents an important advantage for its use. Since the walls are malleable, the chamber can be built in nearly spherical shape, reducing the surface to volume ratio. Although small Teflon chambers can be encapsulated in a temperature-controlled box, the Teflon bag does not

allow pressure control and heterogeneous chemistry on the surface can be an issue. The HONO formation from reactions between NO_2 and H_2O on the surface is an example of undesirable effect observed in this type of reactor.[50-51]

Metal chambers are the most versatile in terms of instrumentation. Because of their rigid structure, amendments can be made in order to include new ports, flanges and windows. Moreover, additional detection equipment can be fused to its surface improving the detection capabilities. Due to the intrinsic characteristics of metal chambers, pressure and temperature manipulation is possible: the walls not only have relevant thermal conductivity, favouring heat exchange, but they can support pressures as low as a fraction of a millibar. The construction cost of metal chambers is definitely an issue, and for this reason they tend to be small (3-2000 L) when compared to Teflon bags. It is likely that reactions on the walls of metal chambers will occur at a considerable rate, thereby, quantitative assessments of these removal processes are very important for a proper understanding of the experimental results. Hydrogen peroxide is known to significantly decompose on stainless steel surfaces,[52] and this effect is likely to occur for other hydroperoxides.

Custom chambers made of quartz and glass also have the versatility to cover a range of temperatures with the aid of an external shelter for temperature control. Their fragility and cost of construction are limiting, therefore, this type of chamber also tends to be small (0.5-3000 L). Artificial radiation can be emitted through the walls of the chamber, which allows the photolysis lamps to be held outside the reaction cell, enabling a more homogeneous distribution of light. Furthermore, it prevents significant temperature fluctuations inside the reaction cell, an unwanted effect frequently observed in metal chambers, caused by the natural warming of the lamps. The construction project of a chamber presupposes a good knowledge of the experiments that will be conducted with the same. A good choice of the base material is an essential step for the development of a suitable methodology that fits the scientific purposes.

Chamber experiments occur in a timescale of dozens of minutes, and for this reason, the measurements can be susceptible to interference from secondary chemistry. Furthermore, careful checks to ensure the absence of gas leaks are of primary importance, since the presence of contaminants can interfere in the measured kinetics. As demonstrated in Figure 1.1, the presence of NO can have a big influence on the regeneration of OH via the reaction with HO_2 radicals. If pristine environments are to be simulated, a good control over leaks is crucially necessary as to ensure for example, that NO_x species do not leak into the chamber.

1.2.3 – The Indirect Relative-Rate method.

As discussed in the previous sections, the determination of reaction coefficients of elementary reactions represents the heart of chemical kinetics. In environmental terms, the knowledge of these parameters allows, for example, assessments of the impacts caused by the presence of a given pollutant in the atmosphere. The lifetime of a VOC with respect to its removal by an atmospheric process is an important kinetic parameter, which can be used to evaluate the geographic extent of a VOC emission.

Under certain conditions, it is not possible to satisfactorily isolate the chemistry of interest for a time-dependent analysis. In such cases, an indirect determination of the rate coefficient may be an interesting alternative. The most widely used technique for indirectly measuring rate coefficients is the Relative-Rate approach (RR). To introduce the technique, real experimental data obtained from experiments conducted with a simulation chamber, the Highly Instrumented Reactor for Atmospheric Chemistry (HIRAC),[48] will be illustratively presented. In these experiments, the purpose is again the determination of the coefficient for the reaction of OH with *trans* 1,4-dimethylcyclohexane. As will be discussed in Chapters 2, 4, 5 and 6, typical OH precursors, such as hydrogen peroxide (HOOH) photolysis is a good source of OH radicals. In a chamber, the photolysis of HOOH can be induced with the use of germicidal lamps (GE G55T8 / OH 7G UV-C), designed to emit radiation in the ultraviolet range (λ ~254 nm).

The RR technique is based on the intercomparison of the temporal evolution of the molecule of interest and a reference as they compete for a common reactant when well-mixed in the chamber. In this case, the reference will compete with the DMC for OH radicals, generated by HOOH photolysis at ~254 nm (R8-R10).

$$\text{HOOH} + h\nu \xrightarrow{\lambda\sim 254\ \text{nm}} 2\ \text{OH} \qquad \text{R8}$$

$$\text{DMC} + \text{OH} \xrightarrow{k_9} \text{products} \qquad \text{R9}$$

$$\text{reference} + \text{OH} \xrightarrow{k_R} \text{products} \qquad \text{R10}$$

Having reactions R9 and R10 rate coefficients k_9 and k_R respectively, the rate laws for each component in the chamber are given by equations E2 and E3.

$$\frac{d[\text{DMC}]}{dt} = -k_9[\text{OH}][\text{DMC}] \qquad \text{E2}$$

$$\frac{d[\text{reference}]}{dt} = -k_R[\text{OH}][\text{reference}] \qquad \text{E3}$$

Dividing equation E2 by equationE3, followed by an algebraic rearrangement gives:

$$\frac{d[\text{DMC}]}{[\text{DMC}]} = \frac{k_9}{k_R} \times \frac{d[\text{reference}]}{[\text{reference}]} \qquad \text{E4}$$

$$\int_{[\text{DMC}]_0}^{[\text{DMC}]_t} \frac{d[\text{DMC}]}{[\text{DMC}]} = \frac{k_9}{k_R} \times \int_{[\text{reference}]_0}^{[\text{reference}]_0} \frac{d[\text{reference}]}{[\text{reference}]} \qquad \text{E5}$$

$$\ln\left(\frac{[\text{DMC}]_t}{[\text{DMC}]_0}\right) = \frac{k_9}{k_R} \ln\left(\frac{[\text{reference}]_t}{[\text{reference}]_0}\right) \qquad \text{E6}$$

Thus, a plot of $\ln([\text{DMC}]_0/[\text{DMC}]_t)$ versus $\ln([\text{reference}]_0/[\text{reference}]_t)$ (e.g. Figure 1.5) provides a gradient that represents a ratio between the two rate coefficients (see Equation E6). By employing a reference for which the rate

coefficient for its reaction with OH radicals is known, the other one can be easily calculated as the product of the ratio with the reference rate coefficient. In this case, the reference chosen was cyclohexane (CHEX), and the rate coefficient for its reaction with OH was taken from the literature ($k_R = k_{OH+CHEX}$ = (6.97 ± 1.4) × 10^{-12} cm^3 $molecule^{-1}$ s^{-1}).[53] It is worth highlighting that ratios of the concentrations of the species being monitored are implemented in equation E6. Experimental measurements of the monitored species can be undertaken with a range experimental techniques, which include for example gas chromatography (GC), Fourier transform infrared spectroscopy (FTIRS) and Proton-transfer reaction time of flight mass spectrometry (PTR-MS). The measurements with one of such techniques will yield signals which correspond to a concentration of the specie. Even though a calibration procedure would be necessary in order to convert those signals into concentration units, since these signals are proportional to the concentrations, the ratio of the signals at different times is equal to the ratios of the concentrations. For this reason, it is common practice to incorporate direct measured signals, in any units associated with the implemented technique, into equation E6, as demonstrated in equation E7. It is worth also highlighting the fact the OH concentration does not need to be known during the RR measurements, which represents an advantage since the aforementioned experimental methods used to monitor species are well-stablished and commercially available. In economic terms, these methods are advantageous compared to laser-based methods.

$$\ln\left(\frac{S_{DMC,\,t}}{S_{DMC,\,0}}\right) = \frac{k_9}{k_R}\ln\left(\frac{S_{reference,\,t}}{S_{reference,\,0}}\right) \qquad \text{E7}$$

In order to obtain accurate results, k_R must be accurately known and the reference should not be reactive to the specie of interest, in this case, DMC. In contrast to the direct measurements, since this indirect technique relies on the monitoring of stable species, other radicals that can be produced from the subsequent reactions may interfere in the measurements. For example, given the timescale of several minutes for these experiments, if a significant concentration of HO_2 radicals is built in the chamber from secondary reactions,

these radicals can start competing with OH radicals for the VOCs. Furthermore, if $k_{HO2 + VOC} \times [HO_2]$ becomes comparable to $k_{OH+VOC} \times [OH]$, the observed relative rates are now influenced by the relative ratio of $k_{HO2 + VOC} / k_{HO2 + REF}$. For this reason, a good mechanistic knowledge of the system is of primary importance. The amount of HOOH used can be increased for example, providing a greater concentration of OH radicals in the chamber and hopefully diminishing the importance of undesirable side reactions. However, such procedures need to be done with care, as not to consume the VOCs so quickly that not enough measurements can be taken before they are completely removed. The use of multiple references can also help reinforce the reliability of chamber measurements.

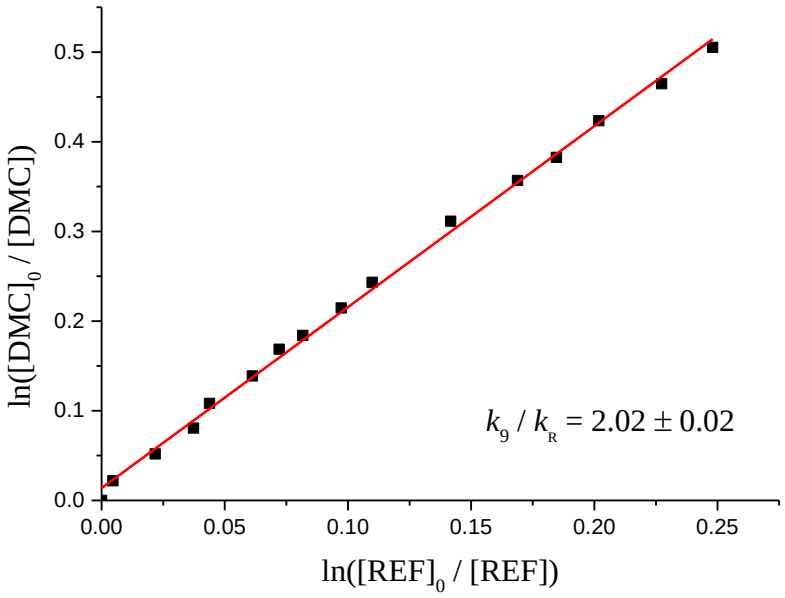

Figure 1.5 – Relative rate plot for the reaction of *trans* 1,4-dimethylcyclohexane with OH competing with the reaction of cyclohexane with OH.

As discussed previously, the ratio between the rate coefficients (k_9/k_R) is the gradient of the corresponding kinetic plot. Using the previously mentioned value of k_R ((6.97 ± 1.4) × 10^{-12} cm^3 $molecule^{-1}$ s^{-1}), k_9 is calculated to be (1.41 ± 0.28) × 10^{-11} cm^3 $molecule^{-1}$ s^{-1}. This value agrees well with that obtained with the direct measurements presented previously ((1.16 ± 0.08) × 10^{-11} cm^3 $molecule^{-1}$ s^{-1}), but includes a much greater uncertainty, due to the

propagation of errors which incorporates the uncertainty of the reference rate coefficient and the slope of the graph. In contrast, direct measurements do not require such procedures.

Finally, using an estimate for the global OH concentration of 1×10^{6} molecules·cm^{-3} as recommended by Prinn *et al.*,[54] a mean rate coefficient based on both, the direct and indirect measurements ($(1.28 \pm 0.15)\times 10^{-11}$ cm^{3} molecule^{-1} s^{-1}), the lifetime of *trans* 1,4 dimethylcyclohexane is estimated to be of approximately 2.2 hours.

In the context of the isoprene + OH reaction, which is the focus of two chapters of the current thesis, the use of chambers as an experimental approach for such investigations would be extremely difficult. The chemistry of isoprene peroxy radicals involves the formation of long lived hydroperoxy species, which are likely to undergo severe heterogeneous chemistry on wall surfaces. Furthermore, the large number of products in this case can make their discrimination and quantification via analytical techniques a very challenging task. Control of leaks would be of primary importance, as very low NO concentrations (< 100 ppt) would need to be employed in the experiments.

Considering the discussed advantages and drawbacks of both direct and indirect measurements, the experimental measurements undertaken for the production of the work presented in the current thesis have made use of the direct approach. This approach is more adequate for an application of the global technique developed in Chapter 4, since the chemistry of interest can be isolated to a better extent when compared to the use of simulation chambers.

1.3 SUMMARY AND CONCLUSIONS

In the current chapter, the importance of radical species for the atmospheric system was discussed in detail. The hydroxyl radical (OH), the most important oxidizing agent in daylight periods in the troposphere, is mostly produced from the photolysis of ozone. The O_3 photolysis forms excited oxygen atoms, $O(^1D)$, whose reaction with water vapour produces the OH radicals. In polluted environments, this radical is greatly reformed from the reaction of another atmospherically important radical, HO_2, with NO. While the chemistry of NO_3 radicals becomes more important during the night, the Cl atoms have a particularly important role in the oxidation of volatile organic compounds in the marine boundary layer.

The differences between direct and indirect techniques for a measuring rate coefficients were highlighted. The direct approach is an excellent option in terms of precision and also accuracy, since the chemistry of interest is directly evaluated and does not depend on a reference rate coefficient, as is the case for the indirect approach. A pragmatic illustration of the forms by which the experimental data is collected was explored, which evidenced a clear difference in the timescale of direct and indirect measurements. The nature of the species being monitored in each approach dictates the types of interfering processes which can take part in the experiments. While direct observations of unstable radicals are susceptible to interferences caused by the presence of stable contaminants, an indirect measurement based on the monitoring of stable species is more susceptible to interfering radicals, which can be generated during the relatively longer experiments in this case.

Atmospheric simulation chambers, useful tools widely used for the investigation of atmospherically relevant gas-phase processes were discussed in detail. They can be built from various materials, which include Teflon, stainless steel, quartz and glass. Choosing a particular material is a decision which compromises the cost of the project and the target chemical systems to be studied with it.

This chapter also demonstrated the importance of accurate measurements of bimolecular rate coefficients and atmospheric estimates of important radicals such as OH, NO_3 and Cl for assessing extension of the impact of a pollutant in the atmosphere. An example of a lifetime calculation based on rate coefficients measured by the means of the relative-rate method was demonstrated.

The next chapter presents the experimental and theoretical techniques by which three atmospherically important OH reactions were studied in the current thesis (OH + SO_2, isoprene (C_5H_8) and ethylene (C_2H_4)). The experimental part of Chapter 2 deals with pulsed laser photolysis instruments, their principles and applications. From this sense, the contents of Chapter 2 are not only a presentation of the techniques by which new experimental data was collected and treated, but represents a continuation of the atmospheric methods, partially introduced in Chapter 1. A good understanding of both chamber techniques and pulsed laser photolysis methods will greatly clarify the reasons behind the particular choice of the laser-based procedure.

1.4 REFERENCES

1. Finlayson-Pitts, B. J.; Pitts, J. N., *Chemistry of the Upper and Lower Atmosphere : Theory, Experiments, and Applications*. Academic Press: San Diego, California, USA. London, UK., 2000.

2. Lelieveld, J.; Gromov, S.; Pozzer, A.; Taraborrelli, D. Global Tropospheric Hydroxyl Distribution, Budget and Reactivity. *Atmospheric Chemistry and Physics* **2016,** *16*, 12477-12493.

3. Sommariva, R. et al. OH and HO_2 Chemistry in Clean Marine Air During SOAPEX-2. *Atmospheric Chemistry and Physics* **2004,** *4*, 839-856.

4. Alicke, B. et al. OH Formation by HONO Photolysis During the Berlioz Experiment. *Journal of Geophysical Research* **2003,** *108*, 8247.

5. Lee, J. D. et al. Detailed Budget Analysis of HONO in Central London Reveals a Missing Daytime Source. *Atmospheric Chemistry and Physics* **2016,** *16*, 2747-2764.

6. Ramazan, K. A.; Syomin, D.; Finlayson-Pitts, B. J. The Photochemical Production of HONO During the Heterogeneous Hydrolysis of NO_2. *Physical Chemistry Chemical Physics* **2004,** *6*, 3836-3843.

7. Stone, D.; Au, K.; Sime, S.; Medeiros, D. J.; Blitz, M.; Seakins, P. W.; Decker, Z.; Sheps, L. Unimolecular Decomposition Kinetics of the Stabilised Criegee Intermediates CH_2OO and CD_2OO. *Physical Chemistry Chemical Physics* **2018,** *20*, 24940-24954.

8. Peeters, J.; Muller, J. F.; Stavrakou, T.; Nguyen, V. S. Hydroxyl Radical Recycling in Isoprene Oxidation Driven by Hydrogen Bonding and Hydrogen Tunneling: The Upgraded LIM1 Mechanism. *Journal of Physical Chemistry A* **2014,** *118*, 8625-8643.

9. Crounse, J. D.; Paulot, F.; Kjaergaard, H. G.; Wennberg, P. O. Peroxy Radical Isomerization in the Oxidation of Isoprene. *Physical Chemistry Chemical Physics* **2011,** *13*, 13607-13613.

10. Fuchs, H. et al. Experimental Evidence for Efficient Hydroxyl Radical Regeneration in Isoprene Oxidation. *Nature Geoscience* **2013,** *6*, 1023.

11. Arey, J.; Aschmann, S. M.; Kwok, E. S. C.; Atkinson, R. Alkyl Nitrate, Hydroxyalkyl Nitrate, and Hydroxycarbonyl Formation from the NOx−Air Photooxidations of C_5−C_8 n-Alkanes. *The Journal of Physical Chemistry A* **2001,** *105*, 1020-1027.

12. Lohr, L. L.; Barker, J. R.; Shroll, R. M. Modeling the Organic Nitrate Yields in the Reaction of Alkyl Peroxy Radicals with Nitric Oxide. 1. Electronic Structure Calculations and Thermochemistry. *The Journal of Physical Chemistry A* **2003,** *107*, 7429-7433.

13. Whalley, L. K. et al. Understanding in Situ Ozone Production in the Summertime through Radical Observations and Modelling Studies During the Clean Air for London Project (Clearflo). *Atmospheric Chemistry and Physics* **2018,** *18*, 2547-2571.

14. Stone, D. et al. Isoprene Oxidation Mechanisms: Measurements and Modelling of OH and HO_2 over a South-East Asian Tropical Rainforest During the OP3 Field Campaign. *Atmospheric Chemistry and Physics* **2011,** *11*, 6749-6771.

15. Paulot, F.; Crounse, J. D.; Kjaergaard, H. G.; Kürten, A.; St. Clair, J. M.; Seinfeld, J. H.; Wennberg, P. O. Unexpected Epoxide Formation in the Gas-Phase Photooxidation of Isoprene. *Science* **2009,** *325*, 730-733.

16. Hansen, R. F.; Lewis, T. R.; Graham, L.; Whalley, L. K.; Seakins, P. W.; Heard, D. E.; Blitz, M. A. OH Production from the Photolysis of Isoprene-Derived Peroxy Radicals: Cross-Sections, Quantum Yields and Atmospheric Implications. *Physical Chemistry Chemical Physics* **2017,** *19*, 2332-2345.

17. Martinez, M. et al. Hydroxyl Radicals in the Tropical Troposphere over the Suriname Rainforest: Airborne Measurements. *Atmospheric Chemistry and Physics* **2010,** *10*, 3759-3773.

18. Whalley, L. K. et al. Quantifying the Magnitude of a Missing Hydroxyl Radical Source in a Tropical Rainforest. *Atmospheric Chemistry and Physics* **2011,** *11*, 7223-7233.

19. Lelieveld, J. et al. Atmospheric Oxidation Capacity Sustained by a Tropical Forest. *Nature* **2008,** *452*, 737-740.

20. Carslaw, N. et al. OH and HO_2 Radical Chemistry in a Forested Region of North-Western Greece. *Atmospheric Environment* **2001,** *35*, 4725-4737.

21. Goldstein, A. H.; Galbally, I. E. Known and Unexplored Organic Constituents in the Earth's Atmosphere. *Environmental Science & Technology* **2007,** *41*, 1514-1521.

22. Orlando, J. J.; Tyndall, G. S.; Wallington, T. J. The Atmospheric Chemistry of Alkoxy Radicals. *Chemical Reviews* **2003,** *103*, 4657-4690.

23. Singh, H. B. Atmospheric Halocarbons: Evidence in Favor of Reduced Average Hydroxyl Radical Concentration in the Troposphere. *Geophysical Research Letters* **1977,** *4*, 101-104.

24. Singh, H. B. Preliminary Estimation of Average Tropospheric HO Concentrations in the Northern and Southern Hemispheres. *Geophysical Research Letters* **1977,** *4*, 453-456.

25. Hewitt, C. N.; Harrison, R. M. Tropospheric Concentrations of the Hydroxyl Radical - a Review. *Atmospheric Environment* **1985,** *19*, 545.

26. Lawrence, M. G.; Jöckel, P.; von Kuhlmann, R. What Does the Global Mean OH Concentration Tell Us? *Atmospheric Chemistry and Physics* **2001,** *1*, 37-49.

27. Russell, A. G.; Cass, G. R.; Seinfeld, J. H. On Some Aspects of Nighttime Atmospheric Chemistry. *Environmental Science & Technology* **1986,** *20*, 1167-1172.

28. Brown, S. S.; Stutz, J. Nighttime Radical Observations and Chemistry. *Chemical Society Reviews* **2012,** *41*, 6405-6447.

29. Finlayson-Pitts, B. J. Chlorine Atoms as a Potential Tropospheric Oxidant in the Marine Boundary Layer. . *Research on Chemical Intermediates* **1993,** *19*.

30. Young, C. J. et al. Chlorine as a Primary Radical: Evaluation of Methods to Understand Its Role in Initiation of Oxidative Cycles. *Atmospheric Chemistry and Physics* **2014,** *14*, 3427-3440.

31. Riedel, T. P. et al. Nitryl Chloride and Molecular Chlorine in the Coastal Marine Boundary Layer. *Environmental Science & Technology* **2012,** *46*, 10463-10470.

32. Pilling, M. J.; Seakins, P. W., *Reaction Kinetics*. Oxford University Press: Oxford, 1995.

33. Bräuer, P. et al. Development of a Protocol for the Auto-Generation of Explicit Aqueous-Phase Oxidation Schemes of Organic Compounds. *Atmospheric Chemistry and Physics Discussions* **2019,** *2019*, 1-52.

34. Di Biagio, C. et al. Complex Refractive Indices and Single Scattering Albedo of Global Dust Aerosols in the Shortwave Spectrum and Relationship to Iron Content and Size. *Atmospheric Chemistry and Physics Discussions* **2019,** *2019*, 1-42.

35. Jiang, X.; Tsona, N. T.; Jia, L.; Liu, S.; Zhang, H.; Xu, Y.; Du, L. Secondary Organic Aerosol Formation from Photooxidation of Furan: Effects of NOx and Humidity. *Atmospheric Chemistry and Physics Discussions* **2019,** *2019*, 1-26.

36. Kaltsonoudis, C.; Jorga, S. D.; Louvaris, E.; Florou, K.; Pandis, S. N. A Portable Dual Smog Chamber System for Atmospheric Aerosol Field Studies. *Atmos. Meas. Tech. Discuss.* **2018,** *2018*, 1-25.

37. Kari, E. et al. Dual Effect of Anthropogenic Emissions on the Formation of Biogenic Soa. *Atmos. Chem. Phys. Discuss.* **2019,** *2019*, 1-35.

38. Massabò, D. et al. ChAMBRe: A New Atmospheric Simulation Chamber for Aerosol Modelling and Bio-Aerosol Research. *Atmos. Meas. Tech.* **2018,** *11*, 5885-5900.

39. Theodoritsi, G. N.; Pandis, S. N. Simulation of the Chemical Evolution of Biomass Burning Organic Aerosol. *Atmos. Chem. Phys. Discuss.* **2018,** *2018*, 1-30.

40. Stone, D.; Blitz, M.; Ingham, T.; Onel, L.; Medeiros, D. J.; Seakins, P. W. An Instrument to Measure Fast Gas Phase Radical Kinetics at High Temperatures and Pressures. *Review of Scientiifc Instruments* **2016,** *87*, 054102.

41. Medeiros, D. J.; Blitz, M. A.; James, L.; Speak, T. H.; Seakins, P. W. Kinetics of the Reaction of OH with Isoprene over a Wide Range of Temperature and Pressure Including Direct Observation of Equilibrium with the OH Adducts. *The Journal of Physical Chemistry A* **2018,** *122*, 7239-7255.

42. Vakhtin, A. B.; Murphy, J. E.; Leone, S. R. Low-Temperature Kinetics of Reactions of OH Radical with Ethene, Propene, and 1-Butene. *The Journal of Physical Chemistry A* **2003,** *107*, 10055-10062.

43. Tully, F. P. Laser Photolysis/Laser-Induced Fluorescence Study of the Reaction of Hydroxyl Radical with Ethylene. *Chemical Physics Letters* **1983,** *96*, 148-153.

44. Glowacki, D. R.; Liang, C. H.; Morley, C.; Pilling, M. J.; Robertson, S. H. MESMER: An Open-Source Master Equation Solver for Multi-Energy Well Reactions. *Journal of Physical Chemistry A* **2012,** *116*, 9545-9560.

45. Wingenter, O. W.; Kubo, M. K.; Blake, N. J.; Smith, T. W.; Blake, D. R.; Rowland, F. S. Hydrocarbon and Halocarbon Measurements as Photochemical and Dynamical Indicators of Atmospheric Hydroxyl, Atomic Chlorine, and Vertical Mixing Obtained During Lagrangian Flights. *Journal of Geophysical Research-Atmospheres* **1996,** *101*, 4331-4340.

46. Wingenter, O. W.; Blake, D. R.; Blake, N. J.; Sive, B. C.; Rowland, F. S.; Atlas, E.; Flocke, F. Tropospheric Hydroxyl and Atomic Chlorine Concentrations, and Mixing Timescales Determined from Hydrocarbon and Halocarbon Measurements Made over the Southern Ocean. *Journal of Geophysical Research-Atmospheres* **1999,** *104*, 21819-21828.

47. Brockmann, K. J.; Kriesche, V.; Etzkorn, T.; Volkamer, R.; Wirtz, K. The European Photoreactor Euphore: A Technical Description. *Proceedings of Eurotrac Symposium '96 - Transport and Transformation of Pollutants in the Troposphere, Vol 2* **1997**, 457-461.

48. Glowacki, D. R. et al. Design of and Initial Results from a Highly Instrumented Reactor for Atmospheric Chemistry (HIRAC). *Atmospheric Chemistry and Physics* **2007,** *7*, 5371-5390.

49. Nilsson, E. J. K.; Eskebjerg, C.; Johnson, M. S. A Photochemical Reactor for Studies of Atmospheric Chemistry. *Atmospheric Environment* **2009,** *43*, 3029-3033.

50. Medeiros, D. J.; Pimentel, A. S. New Insights in the Atmospheric HONO Formation: New Pathways for N_2o_4 Isomerization and NO_2 Dimerization in the Presence of Water. *Journal of Physical Chemistry A* **2011,** *115*, 6357-6365.

51. Schlosser, E. et al. Technical Note: Formal Blind Intercomparison of OH Measurements: Results from the International Campaign Hoxcomp. *Atmospheric Chemistry and Physics* **2009,** *9*, 7923-7948.

52. Lin, C. C.; Smith, F. R.; Ichikawa, N.; Baba, T.; Itow, M. Decomposition of Hydrogen Peroxide in Aqueous Solutions at Elevated Temperatures. *International Journal of Chemical Kinetics* **1991,** *23*, 971-987.

53. Atkinson, R. Kinetics of the Gas-Phase Reactions of OH Radicals with Alkanes and Cycloalkanes. *Atmospheric Chemistry and Physics* **2003,** *3*, 2233-2307.

54. Prinn, R. G.; Weiss, R. F.; Miller, B. R.; Haung, J.; Alyea, F. N.; Cunnold, D. M.; Fraser, P. J.; Hartley, D. E.; Simmonds, P. G. Atmospheric Trends and Lifetime of Ch_3ccl_3 and Global OH Concentrations. *Science* **1995,** *269*, 187-192.

Chapter 2. Experimental Instruments and Theoretical Methods

Overview of the chapter

The relevant experimental and theoretical methods used to investigate atmospherically significant reactions throughout the thesis are presented in this chapter. Methods are split into two distinct groups: section 2.1 presents the experimental techniques used to collect kinetic data for a number of atmospherically important reactions; section 2.2 presents the principles of theoretical methods by which the experimental data were analysed. This chapter will serve as basic introduction, covering the most important methods, the subsequent chapters will also include concise experimental sections, with additional, particular and important experimental or theoretical information.

2.1 EXPERIMENTAL METHODOLOGY

As discussed in Chapter 1, direct radical measurements represent a useful and reliable approach for the study of elementary reactions. In the current work, direct measurements of hydroxyl radicals were undertaken in order to study various atmospherically important processes, such as the reactions of OH with SO_2 (Chapter 3), isoprene (C_5H_8, Chapters 4 and 6) and ethylene (C_2H_4, Chapter 5). While the experimental data were predominantly collected with the use of the conventional low pressure (p < 200 Torr) Laser Flash Photolysis-Laser Induced Fluorescence (LFP-LIF) technique, a recently developed high-temperature (T_{MAX} ~750 K), high pressure (p_{MAX} ~5 atm) instrument was employed in many occasions to expand the experimental horizon. The OH detection in the high pressure instrument is based on a particular laser induced procedure, namely the Fluorescence Assay by Gas Expansion (FAGE).[1] To enable a good understanding of experimental measurements, sections 2.1.1 and 2.1.2 will present the FAGE technique and the basis of laser-induced fluorescence methods. Once the principles are properly introduced, section 2.1.3 presents the LFP-LIF technique in the context of both the low and high pressure instruments.

2.1.1 - Fluorescence Assay by Gas Expansion – FAGE

Fluorescence Assay by Gas Expansion (FAGE) [1] is a widely implemented technique for the detection of radical species. FAGE is a laser-induced fluorescence method (LIF), particularly important for the detection of atmospherically relevant radical species such as OH and HO_2. With a detection limit for the monitoring of OH in the 10^6-10^7 molecule cm^{-3} range,[2] the technique is suitable for field measurements since, as discussed in Chapter 1, the low OH concentrations in pristine environments are often in this range and higher concentrations are generated in polluted atmospheres. The technique is currently being adapted for CH_3O/CH_3O_2 detection, and the recent results obtained from laboratory tests by Onel *et al.* are promising.[3] FAGE is based on specific rovibrational transitions, induced by excitation pulses and the return of

the excited radicals to the ground state via detectable fluorescence emission. In a real experiment however, collisional quenching will compete with fluorescence emission as a mechanism to remove the extra energy. The mitigation of this possibility is of high importance for the method in order to enhance the analytical sensitivity. This technique is typically applied at very low pressures (p ~1 Torr) in order to favour fluorescence emission over collisional quenching.

Two alternative approaches are available for the implementation of the FAGE technique with regards to the OH promotion to an excited state: in the first of them, ground state OH radicals are excited to another rovibrational state at upon 282 nm light absorption and off-resonant fluorescence is detected at ~308 nm. In the alternative approach, resonant fluorescence is detected, i.e., the radicals are both excited and detected at 308 nm. These different approaches have particularities, advantages and drawbacks, and the choice of which one is more appropriate heavily depends on the chemical system being explored and resources available. Detailed schematic diagrams of the two procedures are shown in Figure 2.1.

The LIF technique based on the electronic transition of ground state OH radicals to an upper rovibrational level via ~282 nm light absorption is presented in the left-hand side of Figure 2.1. Radicals are first promoted to the upper state ($A^2\Sigma^+\,(v'=1) \leftarrow X^2\Pi_i\,(v''=0)$) from where a vibrational relaxation to the $A^2\Sigma^+\,(v'=0)$ state proceeds. Subsequently, the radical returns to the ground state by off-resonance fluorescence emission at 308 nm, which can be detected with a photomultiplier. When using this approach, fluorescence can also be detected at 311 nm, corresponding to the $X^2\Pi_i\,(v''=1) \leftarrow A^2\Sigma^+\,(v'=1)$ transition (grey dashed line in Figure 2.1). However, this is a significantly weaker line than the ~308nm one and is merely used as a reference when scanning the wavelength of the probe beam.

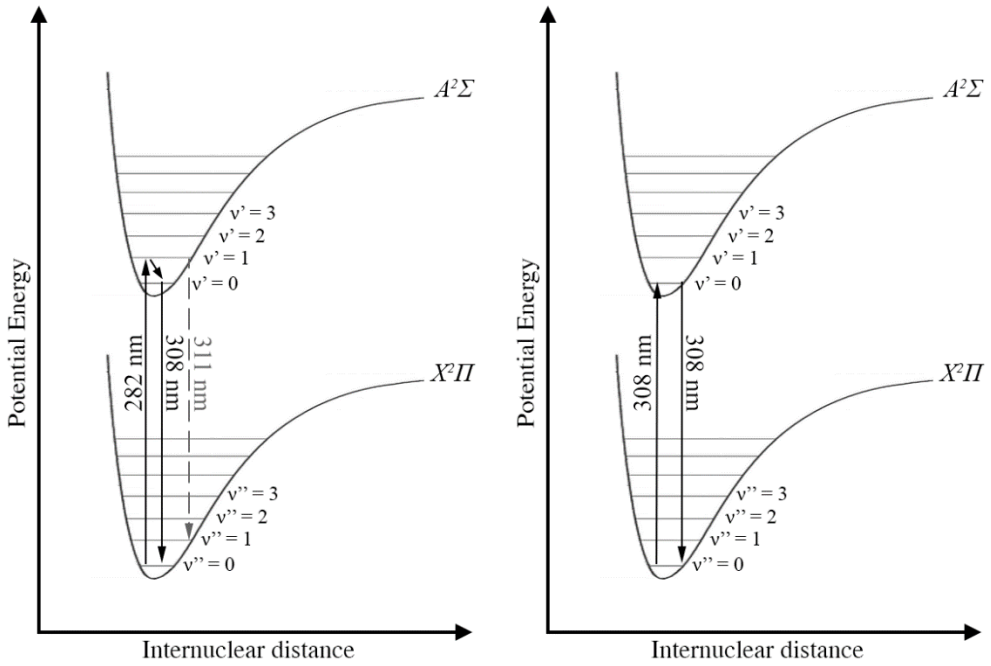

Figure 2.1 – OH electronic transitions. On the left-hand side, the off-resonant approach and the right-hand side shows the resonant fluorescence detection.

The main advantage of the excitation at 282 nm is that in this case, an interference filter can be employed to discriminate fluorescence from scattered laser radiation, simplifying the detection procedure. However, a considerable disadvantage is observed when the technique is implemented for tropospheric investigations: ozone photolysis can become a significant interfering process and lead to the detection of "false OH", that is, OH generated within the FAGE instrument. The photolysis of O_3 produces an excited oxygen atom ($O(^1D)$) that reacts with water vapour to form the interfering OH radicals.[4, 5]

To minimize the O_3 issue, excitation at 308 nm is an interesting alternative[4] since the O_3 absorption cross section is significantly smaller at this wavelength (~25 times smaller)[6] while the OH absorption cross section is ~4 times higher.[7] In this wavelength, the transition occurs between the lowest vibrational levels of both rovibrational states ($A^2\Sigma^+\ (v' = 0) \leftarrow X^2\Pi_i\ (v'' = 0)$). The drawback in this case resides in the discrimination of the fluorescence emitted by excited OH radicals and the probe. The detection therefore requires a more sophisticated operation in which the photomultiplier is only turned on after the probe beam has crossed through the detection cell. This procedure is known as

temporal gating and typically employs a delay generator responsible to turn the detector on with a defined delay in the order of nanoseconds after the probe beam. Turning the detector on too close to the probe represents a risk of increasing the background signal significantly to the point where OH fluorescence becomes negligible. On the other hand, a long delay represents a risk of wasting the majority of the detectable OH fluorescence. For this reason, the definition of the delay to be implemented is a partially empirical process, making sure the compromise between the background signal increase and the improvement of the OH signal is in favour of the latter.

OH radicals are sampled from the system into the detection cell via a pinhole nozzle (~1.0 mm diameter). The detection cell is maintained at very low pressures (~1 Torr) with the aid of a rotary pumps typically coupled to roots blower compressors. The gas expansion in the low pressure chamber not only enhances the fluorescence lifetime of state *A* but minimizes the scattering effects of the laser light.[8]

HO_2 radicals which are also very important for the atmosphere can be indirectly detected via FAGE. This is made by its conversion into OH via titration with NO according to reaction R1:

$$HO_2 + NO \rightarrow OH + NO_2 \qquad \text{R1}$$

The formed OH is then detected as described previously. Figure 2.2 shows an schematic representation of the FAGE instrument taken from the work of Winiberg.[9]

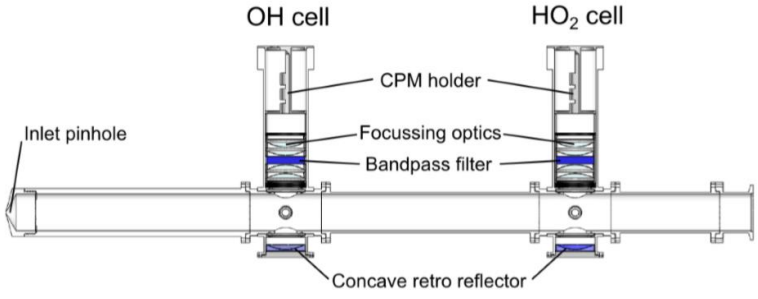

Figure 2.2 - Lateral section of the FAGE instrument attached to HIRAC. Figure reproduced from Winiberg (2014).[9]

2.1.2 - FAGE Calibration

As discussed in Chapter 1, there are situations where the concentration of OH radicals do not need to be determined. For example, under pseudo-first order conditions in which OH is consumed exponentially in time, the concentration of OH radicals do not need to be known for a kinetic evaluation, as demonstrated in Chapter 1. For this reason, in such cases, the LIF signal does not need to be converted into units of concentrations, and arbitrary units of OH can be employed, implying a good level of simplicity to the collection of useful data and its posterior analysis.

In other cases however, the concentrations of OH radicals may need to be known. This is the case, for example, when second order kinetics are being investigated or when the concentration of the radicals are the main subject of study. The technique is typically used in field and chamber investigations[10-13] with the objective of determining the temporal concentration of OH in the days of study, far from the simplicity of the pseudo-first order conditions. In such cases, the FAGE technique requires instrumental calibration. For this reason, a good understanding of the calibration of the technique is desirable for a better understanding of the accuracy of atmospheric OH measurements.

The standard calibration method for OH and HO_2 detection using vacuum ultra-violet (VUV) photolysis of water vapour is presented in the following.[14-17] The method consists in the construction of a calibration curve that relates the FAGE signal normalized to the laser power (S_{OH} / counts s^{-1} mW^{-1}) to known OH radical concentrations produced from water vapour photolysis. Equation E1 presents this relation considering the OH radical.

$$S_{OH} = C_{OH}[OH] \qquad \text{E1}$$

Here, C_{OH} is the sensitivity or calibration factor, with units of counts cm^3 $molecule^{-1}$ s^{-1} mW^{-1}. This factor is affected by several parameters related to the employed equipment and experimental conditions. An extensive discussion of these parameters is presented by Faloona *et al.* [11] and Creasey *et al.*[18, 19]

The water-vapour photolysis generates an OH radical and a hydrogen atom that subsequently reacts with molecular oxygen to yield one molecule of the HO_2 radical. The reactions are:

$$H_2O + h\nu_{(184.9\ nm)} \rightarrow OH + H\cdot \qquad R2$$

$$H\cdot + O_2 \rightarrow HO_2 \qquad R3$$

As observed, the water vapour photolysis produces equal amounts of OH and HO_2. Being the water vapour concentration known via the use of calibrated mass flow controllers, the amount of radicals produced can be obtained from the following expression:

$$[OH] = [HO_2] = [H_2O]_{vap}\, \sigma_{H2O\ 184.9\ nm}\, \Phi_{OH}\, F_{184.9\ nm}\, \Delta t \qquad E2$$

Here, $[H_2O]_{vap}$ is the water vapour concentration, σ_{H2O} is the absorption cross section of water at 184.9 nm, Φ_{OH} is the quantum yield for the photodecomposition of the radical (Φ_{OH}=1), $F_{184.9\ nm}$ is the photon flux of 184.9 nm light and Δt is the exposure time of the air to the radiation.

Two distinct methodologies are available in the literature for the measurement of the $F_{184.9\ nm}\ \Delta t$ product. The first one, described by Stevens *et al.*[8], uses a calibrated phototube for the measurement of $F_{184.9nm}$ while Δt is estimated from the volumetric flow rate and the structural geometry of the flow tube. The second method uses a chemical actinometer to produce O_3 or NO directly from O_2 and N_2O photolysis at 184.9 nm respectively. Then, these products are directly measured with value using commercial gas analysers. Winiberg *et al.* present a complete description of the FAGE instrumentation attached to HIRAC.[9]

2.1.3 - Laser Flash Photolysis Experiments with Detection by Laser Induced Fluorescence (LFP-LIF)

Chemical processes involving free radicals are extremely important for combustion processes[20, 21] and planetary atmospheres.[22, 23] In kinetic investigations, laser flash photolysis is a widely used technique for the generation of radicals, whose consumption can be monitored to allow the determination of reaction coefficients. The combination of this method with the real-time monitoring of radical concentrations by laser induced fluorescence (LIF) spectroscopy has been successfully implemented for the determination of kinetic parameters of several atmospherically relevant reactions and development of new radical detection methods.[24-27] The LIF monitoring procedure is very selective, allowing for example the discrimination between isotope hydroxyl radicals (^{16}OH and ^{18}OH) and its detection limit reaches values below 10^6 molecule cm^{-3}.[15] Despite high levels of selectivity and sensitivity, LIF spectroscopy is generally performed at low pressures (<400 Torr) due to the high collisional quenching of excited states of radicals at high pressures (particularly by O_2). However, in some cases, experimental measurements at elevated pressures are desirable. At elevated temperatures, the high-pressure limit of barrierless reactions can be quite elevated as will be demonstrated in Chapter 4 for the study of the isoprene + OH reaction.

The majority of the kinetic studies presented in Chapters 4 and 5 for the reactions of OH with isoprene and ethylene respectively, were performed with the use of conventional low-pressure (p~100 Torr) laser flash photolysis and detection of OH radicals by laser-induced fluorescence (LFP-LIF).[28, 29] Additionally, high pressure measurements (p > 760 Torr) were undertaken using a recently developed instrument, capable of operating at pressures up to 5 atm and temperatures as high as 750 K. Given the high degree of similarity between a conventional LPF-LIF instrument and the high pressure one being discussed, the latter is presented in detail while its major differences are highlighted in the text. Figure 2.3 presents a schematic representation of this apparatus and Figure 2.4 shows a photograph thereof.

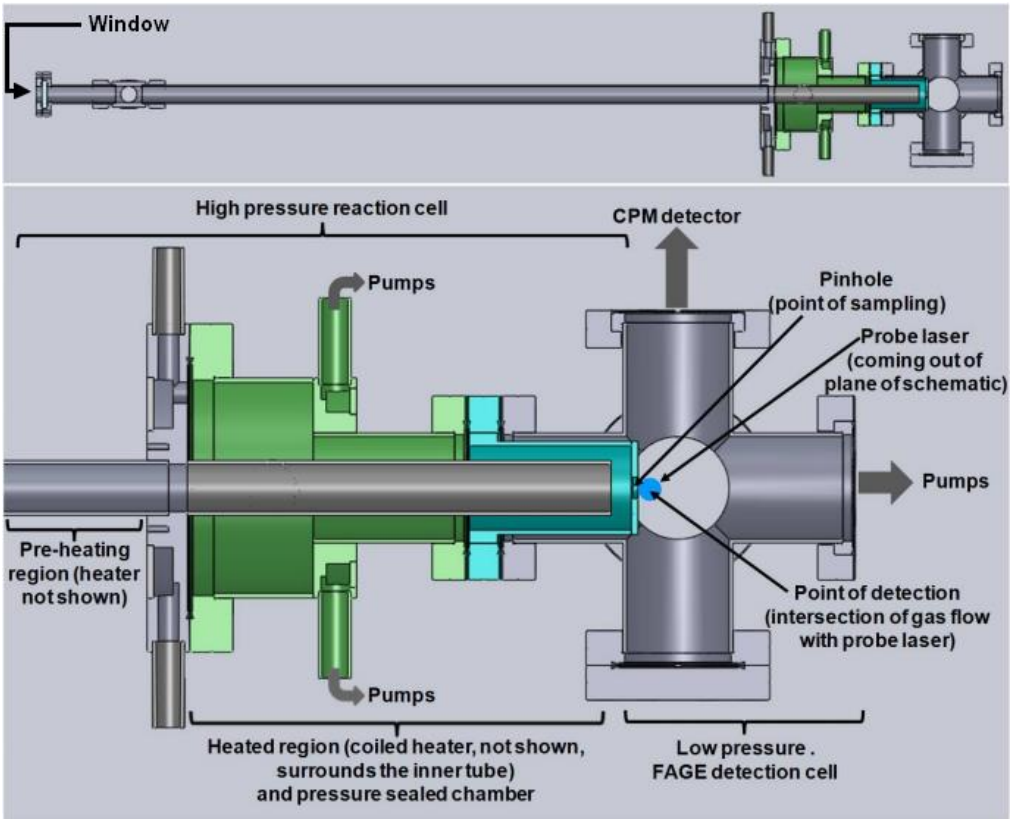

Figure 2.3 - Schematic representation of the high pressure instrument. Upper scheme shows the full apparatus and the lower evidences the interface between the high pressure and detection cells. Figure reproduced from Stone *et al.*[30]

The 6-way cross stainless steel (304L grade) reactor has a high pressure zone, where the reaction occurs, and a low pressure detection cell, where OH radicals are probed. A glass liner of approximately 20 cm long is placed in the reaction cell, in order to reduce the exposure of the chemicals to the metal surface. The high pressure section is 1 m long and 19 mm in internal diameter. OH radicals are generated by pulsed excimer laser photolysis of H_2O_2 (R4) at 248 nm using a Lambda Physik, Compex 200 laser operating on KrF.

$$H_2O_2 + h\nu_{(248\ nm)} \rightarrow 2\ OH \qquad R4$$

Even though the majority of the experiments employed H_2O_2 as the precursor of OH radicals, in the study of isoprene presented in Chapter 4, tert-butyl hydroperoxide ($(CH_3)_3COOH$) photolysis (R5) was implemented in a limited number of experiments to ensure the observable kinetics were independent of the precursor used.

$(CH_3)_3COOH + h\nu_{(248\ nm)} \rightarrow OH + (CH_3)_3CO$ R5

The excimer laser produces a beam with dimensions 24 mm length × 12 mm width which is expanded to occupy the entire volume of the reaction cell and to generate a roughly uniform distribution of radicals in the high pressure zone. The pulses are generated with adjustable frequency (usually between 1 and 10 Hz) and the laser fluence is approximately 15 mJ cm^{-2}, or ~1.87×10^{16} photons cm^{-2}. All experiments presented in the current thesis were performed under low concentrations of OH precursors (typically 1×10^{15} molecule cm^{-3}) so that undesirable effects such as mitigation of the excimer radiation and side reactions are avoided. Considering a ~1×10^{-19} cm^2 $molecule^{-1}$ absorption cross section for H_2O_2 at 248 nm (based on IUPAC recommendation of 7.69×10^{-20} cm^2 $molecule^{-1}$ at 250 nm), the initial OH concentration is estimated to be lower than 3.75×10^{12} molecule cm^{-3}.

The excimer beam enters the high pressure reaction cell through a quartz window, parallel to the gas flow and perpendicular to the probe radiation. The sampling from the high pressure cell to the detection region is made through a pinhole nozzle fixed on a flat plate located inside a pressure-sealed chamber. About 1.2 slm flows into the detection cell while all remaining gas is pumped by an Edwards rotary-pump (model 210 ED660). A valve connected to the discharge pipe allows control of the pressure in the reaction cell, which is measured using a capacitance manometer. In contrast to this instrument, in a conventional LPF-LIF setup, the pinhole does not exist and the reaction is probed within the reaction cell, which is typically kept at lower pressures (p<400 Torr) to avoid collisional quenching of rovibrationally excited radicals, enhancing the collected fluorescence. For this reason, a conventional LPF-LIF instrument requires only one pump that is used to maintain a low pressure throughout the reaction cell, while the high pressure one requires a dedicated pump for the detection cell.

A heating coil (Watlow, WATROD tubular heater) coupled around the reaction cell (located within a pressure-sealed chamber for the high pressure instrument) is used for temperature control by varying the voltage applied to the heater. In our studies, temperatures between 298 K and 794 K have been achieved when considering the reactions of OH with isoprene and ethylene. Three thermocouples (Omega, K-type thermocouples) distributed in the reaction cell are used to monitor the temperature.

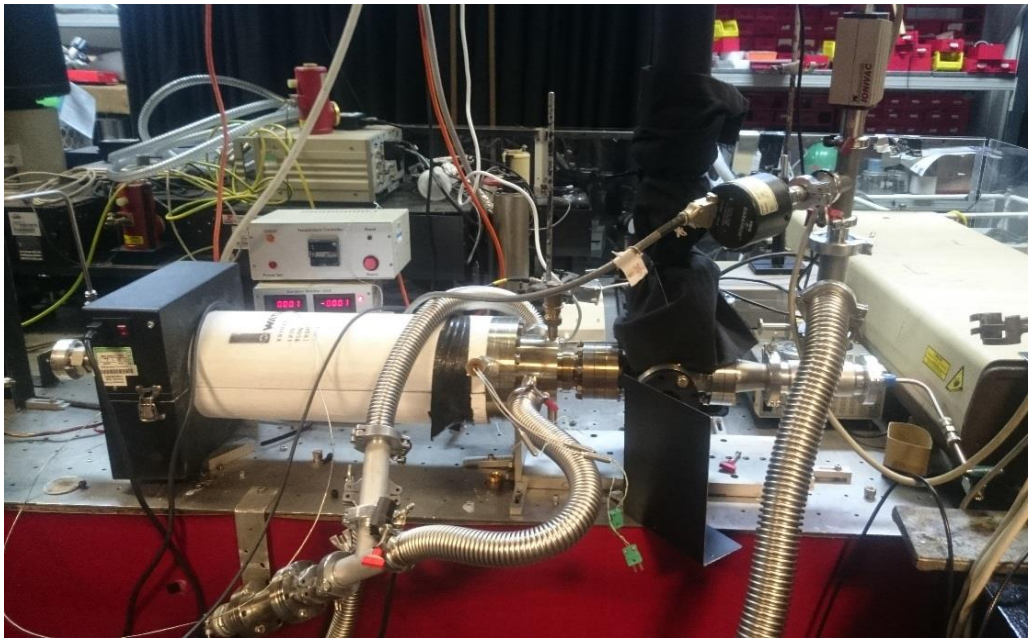

Figure 2.4 - High-pressure LPF-LIF instrument used in our experiments. For more images of the apparatus please refer to Appendix 1.

A rotary pump (Edwards 210 ED660) backed supercharger pump (EUROSERV) is responsible for maintaining the low pressure (~ 1 Torr) in the detection cell. A dye laser (Spectron Laser Systems) operating on Rhodamine-6-G dye is pumped by the 532 nm radiation produced by an Nd:YAG laser (Spectron Laser Systems) to generate the probe radiation at 282 nm. The radicals undergo an electronic transition (OH $A^2\Sigma$ (v = 1) ← $X^2\Pi$ (v = 0)) caused by the probe beam, and these in turn emit fluorescence at ~308 nm when returning to the ground state. A channel photomultiplier (CPM, Perkin-Elmer C1943P), mounted perpendicularly to both probe and excimer beams detects the off-resonant fluorescence at 308 nm after it has passed through an interference filter (Barr Associates, 308 ± 5 nm).

The time delay between the excimer and probe beams is controlled by a delay generator (BNC DG535). A temporal profile of the OH signal is built up by the variation of the delay after the photolysis pulse. Each trace consists of 200 points, which are typically averaged between 5 and 10 times. The fluorescence is also measured at 20 additional points prior to photolysis allowing the measurement of the baseline of the OH signal. As an example Figure 2.5 shows a typical exponential decay, obtained from the isoprene + OH reaction at 298 K and 2 atm.

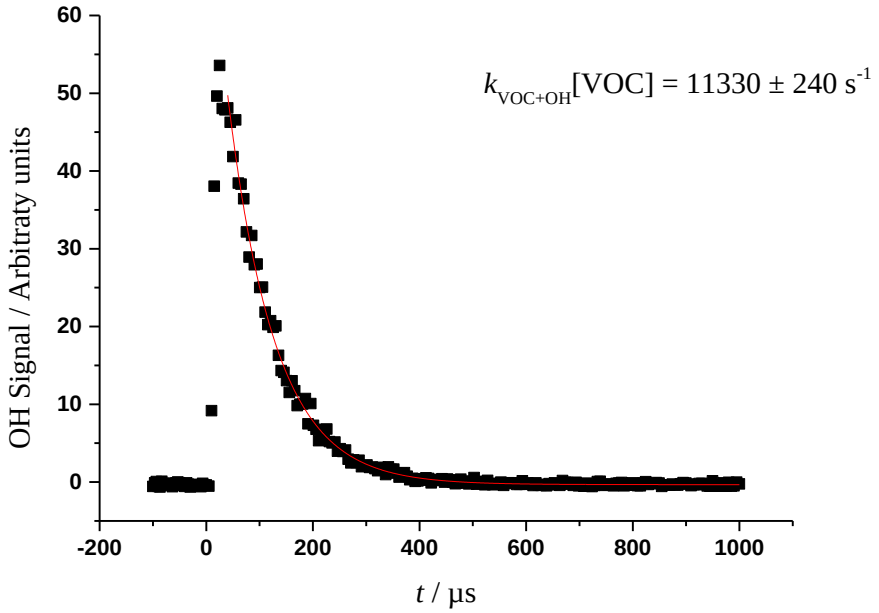

Figure 2.5 - Single exponential decay obtained from the reaction between isoprene (1.00×10^{14} molecules cm^{-3}) and OH radical at 298 K and 2 atm. Low pressure FAGE cell kept at 1 Torr and sampling distance of 5 mm away from the pinhole. Measurements were averaged after 4 scans. Points represented for negative times were probed prior to OH precursor photolysis. The error in the pseudo-first order rate coefficient is quoted at 2σ.

The fluorescence is acquired by the photomultiplier and subsequently stored by a computer. The concentration of the substrate (isoprene or ethylene) is maintained in large excess (determined via measurements from calibrated mass flow controllers and measurement of the total pressure) and hence effectively constant during the scans. Under these pseudo-first order conditions, the observed traces have the form of an exponential decay; hence the pseudo-first

order rate coefficient k'_{VOC+OH} can be extracted from a fit to an exponential decay equation (E3).

$$[OH]=[OH]_0 e^{-k'_{VOC+OH}t} \quad \text{E3}$$

where the pseudo-first order rate coefficient k'_{VOC+OH} is denoted with a prime and is equal product of the bimolecular rate coefficient k_{VOC+OH} (no prime) and the concentration of the VOC (k_{VOC+OH}[VOC]). A bimolecular plot ((k_{VOC+OH}[VOC]) versus [VOC]) allows the estimation of the bimolecular rate coefficient, k_{VOC+OH}, from the gradient of the resulting straight line. An example of a bimolecular plot for the isoprene + OH reaction 298 K and 2 atm is shown in Figure 2.6. The gradient of the blue line represents the rate coefficient of this reaction under the mentioned conditions.

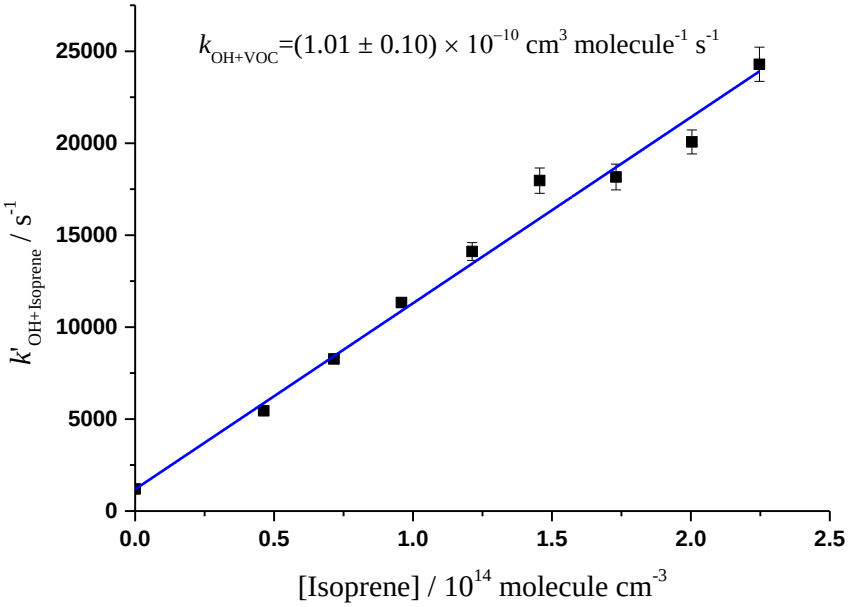

Figure 2.6 - Bimolecular plot for the reaction of isoprene with OH radicals at 298 K and 2 atm. Low pressure FAGE cell kept at 1 Torr and sampling distance of 5 mm. Error bars quoted at 2σ.

The intercept of the bimolecular plot, 1360 ± 680 s^{-1} in the case of Figure 2.6, represents the limit in which OH is lost due to other processes rather than then

the reaction with the VOC. This includes the reaction of OH with precursor and diffusional losses. The combination of these two things can also be measured from an experiment performed in the absence of the VOC. As demonstrated in Figure 2.6, the intercept of the bimolecular plot in this case agrees well with the experimentally determined value ($1200 \pm 40\ s^{-1}$).

The reaction of OH radicals with alkenes and dienes, at least at low temperatures, proceeds via electrophilic addition to an available double bond. Under atmospheric conditions, these processes are typically pressure independent, but at high enough temperatures (more relevant in the context of combustion chemistry, $T > 600$ K), significant competing chemical processes can occur. Not only the OH addition can become pressure dependent, but chemistry such as hydrogen abstractions and decomposition of intermediates can become significant so that they need to be accounted for. This is particularly true for the cases of the OH + isoprene and OH + ethylene, reactions explored in Chapters 4 and 5 respectively. These mechanistic changes can lead to significant deviations from a simple exponential decay of the deficient reagent under pseudo-first order conditions, requiring more complex strategies for analysing the corresponding experimental data. The thesis will present different approaches to deal with relevant chemical processes in terms of gas-phase chemistry. All of these techniques rely, to some extent, on pressure-dependent processes and master equation modelling thereof. For this reason, the principles of these two things are presented in the following, prior to the result chapters.

2.2 THEORETICAL METHODS

2.2.1 - The Lindemann Theory

The Lindemann theory is the simplest mechanism of unimolecular reaction rates and its comprehension will aid the understanding of the OH + SO_2, isoprene and ethylene reactions covered in Chapters 3, 4 and 5 respectively. For this reason, a brief description of the theory is provided here. Initially, the method will be presented with its original formulation, following a unimolecular point of view. Subsequently, a bimolecular perspective of the method is presented, which is more contextualized with the bimolecular reactions investigated in the thesis. Figure 2.7 illustrate the fundamental differences between the two, which will be discussed in the following.

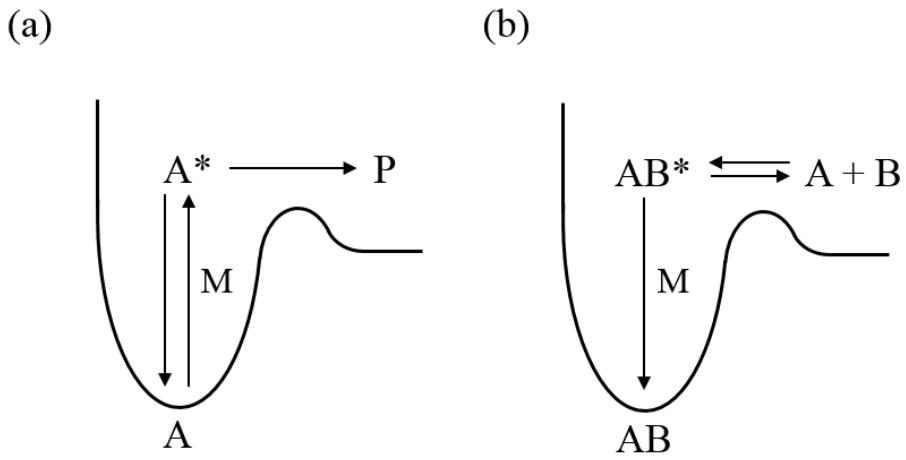

Figure 2.7 - Schematic representation of the Lindemann method for pressure-dependent processes from (a) unimolecular and (b) bimolecular perspectives.

2.2.1.1 The Lindemann Theory From an Unimolecular Perspective

The Lindemann mechanism consists of two elementary steps in the overall unimolecular reaction A→P: an initial reversible bimolecular activation step (R6a and R-6a) via collision with a third body, M, followed by an unimolecular process (isomerization or dissociation) to form products (R). The third body M can be a product, an inert molecule such as the bath gas, or a second molecule of a reactant. By colliding with the third body, a portion of the molecules is energized above a critical quantity, E_0.

$$A + M \xrightarrow{k_{6a}} A^* + M \qquad \text{R6a}$$

$$A^* + M \xrightarrow{k_{-6a}} A + M \qquad \text{R-6a}$$

$$A^* \xrightarrow{k_7} P \qquad \text{R7}$$

In the Lindemann analysis, k_{6a} is considered to be energy independent. If we use the steady-state approximation, the concentration of the activated specie A* is defined as:

$$[A^*]=\frac{k_{6a}[A][M]}{k_{-6a}[M]+k_7} \qquad \text{E4}$$

Therefore, the overall rate of formation is defined by equation E5:

$$\frac{d[P]}{dt}=k_7[A^*]=k_7\frac{k_{6a}[A][M]}{k_{-6a}[M]+k_7} \qquad \text{E5}$$

At high pressures, the rate-limiting step is the activation reaction and $k_{-6a}[M]>>k_7$, thus E5 approximates equation E6 and the rate coefficient k^∞ (equals to $k_7\frac{k_{6a}[A]}{k_{-6a}}$) is independent of pressure (see Figure 2.8).

$$\frac{d[P]}{dt}=k_7\frac{k_{6a}[A]}{k_{-6a}}=k^\infty[A] \qquad \text{E6}$$

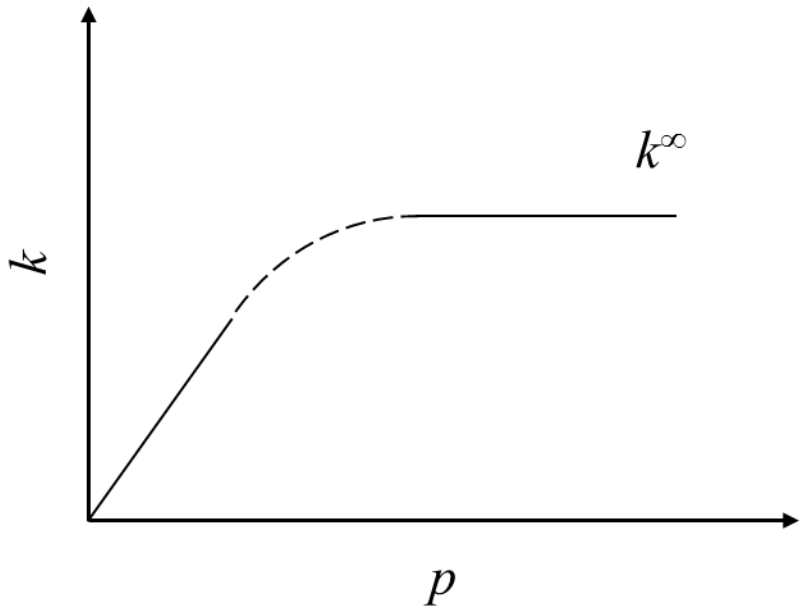

Figure 2.8 - The pressure dependence of a generic rate constant as described by the Lindemann mechanism.

At low pressures, where k_{-6a} [M]<<k_7 equation E6 Ecan be simplified as E7:

$$\frac{\mathrm{d}[\mathrm{P}]}{\mathrm{d}t} = k_{6a}[\mathrm{A}][\mathrm{M}] = k_{\mathrm{bim}}[\mathrm{A}][\mathrm{M}] \qquad \text{E7}$$

In this case, the rate of reaction is the second order rate of activation and the rate is proportional to the pressure (see Figure 2.8). The Lindemann approach also predicts a change in the initial rate of reaction as a function of the concentration at low pressures, in a region defined as the "fall-off" (dotted region of Figure 2.8). For a pseudo-first order process involving the specie A, with rate coefficient k_{uni}, the theory determines a decline of k_{uni} as a function of [M] as indicated by equation E8:

$$k_{\mathrm{uni}} = -\frac{1}{[\mathrm{A}]}\left(\frac{\mathrm{d}[\mathrm{A}]}{\mathrm{d}t}\right) = \frac{k_{6a}[\mathrm{M}]}{1+k_{-6a}[\mathrm{M}]/k_7} \qquad \text{E8}$$

Equation E8 can be simply divided by the limiting high-pressure rate coefficient, k^{∞}, which simplifies the interpretation of the effect of pressure in the unimolecular rate coefficient k_{uni}:

$$k_{uni} / k_{\infty} = \frac{1}{1 + k_7 / k_{-6a}[M]} \qquad \text{E9}$$

From equation E9 it is simple to observe that within the "fall-off" region, the addition of M provokes an increase of k_{uni}. The equation also shows that at the limit where [M]→∞, $k_{uni} / k_{\infty} = 1$.

2.2.1.2 The Lindemann Theory From a Bimolecular Perspective

Even though the Lindemann theory was initially formulated from an unimolecular point of view, a bimolecular perspective of the theory is desirable since the chemical systems explored in the current thesis are all bimolecular association reactions of the OH radical with a substrate. In the bimolecular case, the activation step described in Equation E4 is substituted by the association of the two species to form an energized adduct (R6b) while the reverse reaction is replaced by the unimolecular dissociation of this adduct back to reagents (R-6b). Reactions R6b and R-6b must be linked thorugh the equilibrium constant. The activated adduct AB* is de-energized by colliding with a third body to form the final product AB (R8):

$$A + B \xrightarrow{k_{6b}} AB^* \qquad \text{R6b}$$

$$AB^* \xrightarrow{k_{-6b}} A + B \qquad \text{R-6b}$$

$$AB^* + M \xrightarrow{k_8} AB + M \qquad \text{R8}$$

In this case, the rate law for the intermediate specie AB* is defined in equation E10:

$$\frac{d[AB^*]}{dt} = k_{6b}[A][B] - (k_{-6b} + k_8[M])[AB^*] \qquad \text{E10}$$

Again, applying the steady state approximation, the concentration of [AB*] may be calculated:

$$[AB^*]=\frac{k_{6b}[A][B]}{k_{-6b}+k_8[M]} \qquad E11$$

The rate of formation of the product AB is then formulated in an analogous way to that presented previously for the unimolecular case:

$$\frac{d[AB]}{dt}=k_8[AB^*][M]=k_8\frac{k_{6b}[A][B][M]}{k_{-6b}+k_8[M]} \qquad E12$$

As a consequence, at high enough pressures, the association reaction is rate-limiting step, $k_8[M]>>k_{-6b}$ and therefore:

$$\frac{d[AB]}{dt}=k_{6b}[A][B] \qquad E13$$

Finally, at low pressures, the rate law is now linked via the equilibrium constant of the bimolecular association and the unimolecular decomposition of the adduct back to reagents as defined by equation E14:

$$\frac{d[AB]}{dt}=k_8\frac{k_{6b}[A][B][M]}{k_{-6b}} \qquad E14$$

2.2.2 - Master Equation Calculations with MESMER

The computational package MESMER[31], extensively used in all the analysis presented in this thesis, implements the energy grained master equation (EGME) theoretical approach to describe the macroscopic kinetics of a reaction system; where the behaviour of each isomer is treated at an energy-resolved level. The high number of rovibrational states of these isomers in polyatomic molecules makes their time-revolved treatment computationally impossible. To work around this issue, states of similar energy are grouped into grains as to simplify the problem to a feasible, yet reliable level. This robust method allows the exploration of potential energy surfaces via modelling of the experimental conditions, which may include the use of different bath gases and wide temperature ranges. The technique is also used in a predictive manner, by the extrapolation of experimental measurements to a range of conditions (*T*, *p*) of particular interest. The thermochemistry of particular reactions, such as the OH addition to isoprene (C_5H_8), can be evaluated at high temperatures with relative ease when compared to low temperature measurements and the use of the ME approach in such cases is appropriate. Chapters 4 and 5 will present the use of alternative ME approaches in order to extrapolate high temperature measurements results to room temperature for the isoprene + OH and C_2H_4 + OH reactions respectively. A description of the EGME method is therefore provided in order to simplify the understanding of the multiple analytical strategies implemented throughout the thesis.

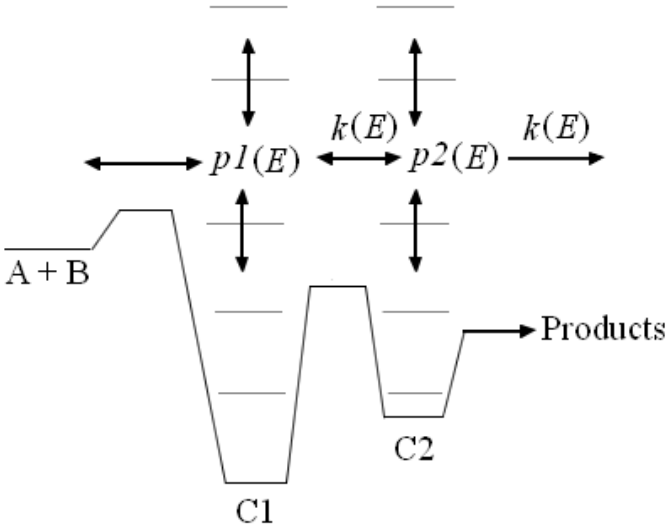

Figure 2.9 - Generic schematic of the processes involved in Master Equation modelling.

As mentioned previously, the EGME approach groups states of similar energy for each species (regents, intermediates and products) into grains ($\Delta E \sim 50$ cm^{-1} within the grain). In general terms, the energy grained master equation can be described as:

$$\frac{d}{dt}x = M\,x \qquad \text{E15}$$

where x is the population density vector and M, the transition matrix, describes the evolution of the population over time, due to reaction and collisional energy transfer (see Figure 2.9). Energy transfer causes population or depopulation of a grain via collision to another grain; MESMER implements an exponential down model, in which the probability of a transition from a grain with energy E, to a grain with energy E' in the downward direction is exponentially reduced according to the energy difference (E-E'):

$$P(E|E') = A(E') \times \exp(-(E-E')/\langle \Delta E \rangle_d) \qquad \text{E16}$$

where $A(E')$ is a normalization factor. The energy transfer parameter $\langle \Delta E \rangle_d$ can assume different values for different bath gases and typically depends on temperature.[32-34] The probability of energy transfer in the upward direction is

obtained via detailed balance from those calculated with equation E16. The temperature dependence of $\langle \Delta E \rangle_d$ is usually defined as:

$$\langle \Delta E \rangle_d(T) = \langle \Delta E \rangle_{d,\,ref}(T/298)^n \qquad \text{E17}$$

The term for population/depopulation of the grains via collisional energy transfer with a bath gas ($CET_i(E,t)$) is incorporated in the Master Equation via the Lennard-Jones collision frequency, as demonstrated in equation E18 for a generic specie *i*:

$$CET_i(E,t) = \omega \int_{E_{i,0}}^{\infty} P\left(E_i|E_i^{'}\right) x_i\left(E_i^{'}, t\right) \mathrm{d}E_i^{'} \; - \omega x_i(E_i,t) \qquad \text{E18}$$

where $P\left(E_i|E_i^{'}\right)$ is the probability that $x_i(E_i,t)$ is populated via collisional energy transfer and ω is the Lennard-Jones collision frequency, calculated via equations E19 and E20.[35] The second term in the right hand side of equation E18 (- $\omega x_i(E_i,t)$) represents the collisional depopulation of $x_i(E_i,t)$.

$$\omega = N_A \pi \sigma_{i,B}^2 \sqrt{8\pi k_B T/\mu_{i,B}}\; \Omega_{i,B}^{(2,2)^*} \qquad \text{E19}$$

$$\Omega_{i,B}^{(2,2)^*} \cong [0.70 + 0.52 \log\left(\frac{k_B T}{\varepsilon_{i,B}}\right)]^{-1} \qquad \text{E20}$$

where *B* represents a collision partner, N_A is the Avogadro constant, $\sigma_{i,B}$ and $\varepsilon_{i,B}$ are the Lennard-Jones collision diameter and interaction energy involving species *i* and *B*, k_B is the Boltzmann constant, *T* is the temperature, $\mu_{i,B}$ is the reduced mass calculated with the molecular weights of *i* and *B*. The reduced collision integral ($\Omega_{i,B}^{(2,2)^*}$) is a quantity that can be approximated by equation E20. The Lennard-Jones parameters ($\sigma_{i,B} = \sigma_i + \sigma_B$; $\varepsilon_{i,B} = \sqrt{\varepsilon_{i,i}\,\varepsilon_{B,B}}$) are typically obtained from tabulated information.[36, 37] They can also be estimated from empirical equations; one example of such formulas involves the molar volume

at melting point (V_m) and the boiling temperature (T_b) of the pure substance (E21-E22).[35]

$$\frac{2}{3} N_A \pi \sigma_i^3 = 2.3\ V_m \qquad \text{E21}$$

$$\varepsilon_i / k_B \cong 1.18\ T_b \qquad \text{E22}$$

Although more accurate energy transfer models such as the double exponential model are available, single-channel unimolecular reaction rates seem to be strongly dependent on the average rate of energy transfer rather than on the exact features of models for collision frequency. [38, 39]

In the case of a chemical process with a well-defined transition state, chemical reaction between grains can be accounted for with microcanonical rate constants ($k(E)$) calculated via RRKM theory.[38] According to this theory, the microcanonical rate coefficients are calculated from the related potential energy surface with the use of equation E23.

$$k(E) = \frac{W(E)}{h\,\rho(E)} \qquad \text{E23}$$

where $W(E)$ is the sum of rovibrational states at the defined transition state structure, h is the Planck constant and $\rho(E)$ is the density of rovibrational states of the intermediate isomer.

For a barrierless process on the other hand, if the high pressure limiting rate constant is known, an Inverse Laplace Transformation (ILT)[39] procedure can be implemented for obtaining the microcanonical rate constants. The ILT algorithm allows their determination from a fit of the available limiting high pressure rate coefficients, which may have been determined experimentally or theoretically. The procedure uses a modified Arrhenius formalism, as described by equation E24.

$$k^{\infty}(T) = A^{\infty} \times \exp(-Ea^{\infty}/RT) \times (T/298)^{n^{\infty}} \qquad \text{E24}$$

where A^{∞} is the pre-exponential factor, Ea^{∞} is the activation energy and n^{∞} is a parameter that allows the adjustment of the curvature of $k^{\infty}(T)$ as a deviation from the classic Arrhenius description. The accuracy of the $k(E)$ obtained from this procedure is highly dependent on how well defined the Arrhenius parameters are, and therefore, reactions with large energetic barriers will naturally require $k^{\infty}(T)$ to be known for a large temperature range. This technique is recommended for association reactions.

Equation E15 represents a set of coupled differential equations relating the grains of the involved species and its solution has the form of equation E25:

$$x = U\, e^{\Lambda t} U^{-1} x(0) \qquad \text{E25}$$

where U is a matrix of eigenvectors obtained by the diagonalization of M, Λ is the vector of corresponding eigenvalues and $x(0)$ contains the initial conditions for each grain. From the solution of the ME with a total of N eigenmodes, the population density of the ith well can be obtained:

$$x_i(E,t) = \sum_{j=0}^{N} c_{ij}(E) e^{\Lambda_j t} \qquad \text{E26}$$

From equation E26, $x_i(E,t)$ is the population density of the ith well, at time t and with energy E. The expansion coefficient c_{ij} is dependent on the jth eigenvector of the transition matrix, the energy E and the initial conditions. Λ_j is the jth eigenvalue of M, with eigenvalues organized in ascending order of absolute values. The integration of $x_i(E,t)$ over E yields the temporal evolution of the species:

$$X_i(t) = \int_{E_{0i}}^{\infty} x_i(E,t) dE = \sum_{j=0}^{N} a_{ij} e^{\Lambda_j t} \qquad \text{E27}$$

where $X_i(t)$ and E_{0i} are the population fraction and the ground-state energy of the specie i, and the amplitudes a_{ij} is defined as in equation E28:

$$a_{ij} = \int_{E_{0i}}^{\infty} c_{ij}(E)dE \qquad \text{E28}$$

Even though this method provides a robust way of modelling complicated processes involving multiple and interconnected wells, its complexity justifies the implementation of alternative and simplified ways of accurately describing the same kinetic problem. For example, the phenomenological rates for an interconnected kinetic system can be described as a set of coupled differential equations such as *M* from equation E15 but heavily simplified via the absence of collisional relaxation kinetics descriptions:

$$\frac{\mathrm{d}}{\mathrm{d}t}X = K\,X \qquad \text{E29}$$

where *K* is the simplified transition matrix and X is the fractional population vector. When solving the full master equation, as discussed previously, it is observed that while the vast majority of the eigenvalues calculated via the diagonalization of *M* are consistent with the timescale of internal energy relaxation of excited intermediates (IERE), a few of them agree with the timescale of a chemical reaction. These very few ones, capable of changing $X_{\mathrm{i}}(t)$, are referred to as chemically significant eigenvalues (CSE).[40] In contrast to them, the IEREs are capable of modifying the individual population densities $x_{\mathrm{i}}(E,t)$ but without changing the species profiles, $X_{\mathrm{i}}(t)$. The determination of the CSEs not only allows the computation of phenomenological rate coefficients, but also enables a considerable simplification of the problem being faced, stretching the possibilities for further developments in terms of data analysis. Chapter 5 presents a newly developed method that deals with such simplifications in order to tackle the occurrence of additional and interfering chemistry on the measured kinetics.

The aforementioned chemically significant eigenvalues can be identified via the procedure described by Bartis and Widom, which takes advantage of the absolute separation between IEREs and CSEs.[41] If *K*(*nxn*) from equation E29 is a matrix that represents the same kinetic system described previously by *M*

(E15), then the diagonalization of K provides a solution to the reduced number of interconnected differential equations being discussed. However, in order to be valid, this solution must be equal (to a numerical precision) to the solution of the full Master Equation. The solution of K yields n eigenvalues and n eigenvectors and by definition, the CSEs obtained from K must be equal to the ones coming from the diagonalization of M. Hence, the elements of the diagonalized form of K can be algebraically determined using the CSEs selected from M and the corresponding $X_i(t)$ which was calculated from the full ME.

The phenomenological rate coefficient $k_{c,i}$ associated with a hypothetical $c \rightarrow i$ reaction can be obtained from equation E29:[42]

$$k_{c,i} = \sum_{j=0}^{N_{CSE}} a_{ij} \Lambda_j a_{jl}^{-1} \qquad \text{E30}$$

where the N_{CSE} is the number of chemically significantly eigenvalues, a_{ij} is the amplitude associated with species i and j calculated with equation E28.

For the separation of IEREs and CSEs, a critical ratio that separates the largest CSE and the lowest IERE is considered. MESMER uses a critical ratio of 0.1, i.e., a reliable separation is considered when CSEs and IEREs are separated by at least an order of magnitude. Finally, the rate coefficients calculated via the Master Equation followed by the Bartis-Widom procedure can be compared to experimental measurements and used to optimize the potential energy surface with the aid of a minimization algorithm, such as the Levenberg-Marquardt procedure.[43-45]

The Master Equation calculations require additional molecular parameters such as vibrational frequencies and rotational constants, which were calculated via theoretical calculations. Details on these calculations will be presented in each chapter, prior to a discussion of the corresponding results.

2.3 REFERENCES

1. Heard, D. E. *Annual Review of Physical Chemistry* **2006,** *57* (1), 191-216.
2. Heard, D. E.; Pilling, M. J. *Chemical Reviews* **2003,** *103* (12), 5163-5198.
3. Onel, L.; Brennan, A.; Seakins, P. W.; Whalley, L.; Heard, D. E. *Atmos. Meas. Tech.* **2017,** *10* (10), 3985-4000.
4. Stone, D.; Whalley, L. K.; Heard, D. E. *Chemical Society Reviews* **2012,** *41* (19), 6348-6404.
5. Smith, G. P.; Crosley, D. R. *Journal of Geophysical Research: Atmospheres* **1990,** *95* (D10), 16427-16442.
6. Sander, S. P.; Friedl, R. R.; DeMore, W. B.; Golden, D. M.; Kurylo, M. J.; Hampson, R. F.; Huie, R. E.; Moortgat, C. K.; Ravishankara, A. R.; Kolb, C. E.; Molina, M. J. *Chemical Kinetics and Photochemical Data for Use in Atmospheric modelling*; Pasadena, California, 2000.
7. McGee, T. J.; McIlrath, T. J. *Journal of Quantitative Spectroscopy & Radiative Transfer* **1984,** *32* (2), 179-184.
8. Stevens, P. S.; Mather, J. H.; Brune, W. H. *J. Geophys. Res.-Atmos.* **1994,** *99* (D2), 3543-3557.
9. Winiberg, F. A. F. Characterisation of FAGE apparatus for HOx detection and application in an environmental chamber. University of Leeds, Leeds, 2014.
10. Crounse, J. D.; Paulot, F.; Kjaergaard, H. G.; Wennberg, P. O. *Physical Chemistry Chemical Physics* **2011,** *13* (30), 13607-13613.
11. Martinez, M.; Harder, H.; Kubistin, D.; Rudolf, M.; Bozem, H.; Eerdekens, G.; Fischer, H.; Klüpfel, T.; Gurk, C.; Königstedt, R.; Parchatka, U.; Schiller, C. L.; Stickler, A.; Williams, J.; Lelieveld, J. *Atmospheric Chemistry and Physics* **2010,** *10* (8), 3759-3773.
12. Stone, D.; Evans, M. J.; Edwards, P. M.; Commane, R.; Ingham, T.; Rickard, A. R.; Brookes, D. M.; Hopkins, J.; Leigh, R. J.; Lewis, A. C.; Monks, P. S.; Oram, D.; Reeves, C. E.; Stewart, D.; Heard, D. E. *Atmospheric Chemistry and Physics* **2011,** *11* (13), 6749-6771.
13. Whalley, L. K.; Stone, D.; Dunmore, R.; Hamilton, J.; Hopkins, J. R.; Lee, J. D.; Lewis, A. C.; Williams, P.; Kleffmann, J.; Laufs, S.; Woodward-Massey, R.; Heard, D. E. *Atmospheric Chemistry and Physics* **2018,** *18* (4), 2547-2571.
14. Aschmutat, U.; Hessling, M.; Holland, F.; Hofzumahaus, A., A tunable source of Hydroxyl (OH) and Hydroperoxy (HO_2) radicals: in the range between 10^6 and 10^9 cm^{-3}. In *Physico-Chemical Behaviour of Atmospheric Pollutants*, Restelli, G. A. a. G., Ed. European Comission, Brussels: 1994; pp 811-816.
15. Heard, D. E.; Pilling, M. J. *Chemical Reviews* **2003,** *103*, 5163-5198.
16. Schultz, M.; Heitlinger, M.; Mihelcic, D.; Volzthomas, A. *J. Geophys. Res.-Atmos.* **1995,** *100* (D9), 18811-18816.
17. Winiberg, F. A. F.; Smith, S. C.; Bejan, I.; Brumby, C. A.; Ingham, T.; Malkin, T. L.; Orr, S. C.; Heard, D. E.; Seakins, P. W. *Atmospheric Measurement Techniques* **2015,** *8*, 523-540.
18. Creasey, D. J.; Halford-Maw, P. A.; Heard, D. E.; Pilling, M. J.; Whitaker, B. J. *J. Chem. Soc.-Faraday Trans.* **1997,** *93* (16), 2907-2913.
19. Faloona, I. C.; Tan, D.; Lesher, R. L.; Hazen, N. L.; Frame, C. L.; Simpas, J. B.; Harder, H.; Martinez, M.; Di Carlo, P.; Ren, X. R.; Brune, W. H. *J. Atmos. Chem.* **2004,** *47* (2), 139-167.
20. Dooley, S.; Curran, H. J.; Simmie, J. M. *Combust. Flame* **2008,** *153* (1-2), 2-32.
21. Zador, J.; Taatjes, C. A.; Fernandes, R. X. *Prog. Energy Combust. Sci.* **2011,** *37* (4), 371-421.
22. Cody, R. J.; Romani, P. N.; Nesbitt, F. L.; Iannone, M. A.; Tardy, D. C.; Stief, L. J. *J. Geophys. Res.-Planets* **2003,** *108* (E11), 16.
23. Moses, J. I., *Photochemistry in giant-planet atmospheres*. Astronomical Soc Pacific: San Francisco, 2000; Vol. 212, p 196-206.
24. Miyazaki, K.; Nakashima, Y.; Schoemaecker, C.; Fittschen, C.; Kajii, Y. *Review of Scientific Instruments* **2013,** *84* (7).
25. Michael, J. V.; Keil, D. G.; Klemm, R. B. *Journal of Chemical Physics* **1985,** *83*, 1630-1636.
26. Campuzano-Jost, P.; Williams, M. B.; D'Ottone, L.; Hynes, A. J. *J. Phys. Chem. A* **2004,** *108* (9), 1537-1551.

27. Blitz, M. A.; Hughes, K. J.; Pilling, M. J. *J. Phys. Chem. A* **2003,** *107* (12), 1971-1978.
28. Onel, L.; L., T.; Blitz, M.; Seakins, P. W.; Bunkan, A. J. C.; Solimannejad, M.; Nielsen, C. J. *The Journal of Physical Chemistry A* **2013,** *117* (41), 10736-10745.
29. Onel, L.; Blitz, M. A.; Seakins, P. W. *J. Phys. Chem. Lett.* **2012,** *3* (7), 853-856.
30. Stone, D. B., M; Ingham, T.; Onel, L.; Medeiros, D. J.; Onel, L.; Seakins, P. W. *Review of Scientific Instruments* **2016,** *87* (5), 054102.
31. Glowacki, D. R.; Liang, C. H.; Morley, C.; Pilling, M. J.; Robertson, S. H. *Journal of Physical Chemistry A* **2012,** *116* (38), 9545-9560.
32. Blitz, M. A.; Green, N. J. B.; Shannon, R. J.; Pilling, M. J.; Seakins, P. W.; Western, C. M.; Robertson, S. H. *The Journal of Physical Chemistry A* **2015,** *119* (28), 7668-7682.
33. Miller, J. A.; Klippenstein, S. J. *J. Phys. Chem. A* **2003,** *107*, 2680-2692.
34. Greenwald, E. E.; North, S. W.; Georgievskii, Y.; Klippenstein, S. J. *J. Phys. Chem. A* **2005,** *109* (27), 6031-6044.
35. Gardiner, J. W. C., *Combustion Chemistry*. Springer-Verlag: New York, Berlin, Heidelberg, Tokyo, 1984.
36. Bird, J. O. H. C. F. C. a. R. B., *Molecular Theory of Gases and Liquids*. Wiley: London, 1963.
37. Reid R. C. ; Sherwood, T. K., *The properties od Gases and Liquids*. 2 ed.; McGraw-Hill: New York, 1966.
38. Baer, T.; Hase, W. L., *Unimolecular Reaction Dynamics: Theory and Experiments*. Oxford University Press: 1996.
39. Davies, J. W.; Green, N. J. B.; Pilling, M. J. *Chemical Physics Letters* **1986,** *126*, 373.
40. Miller, J. A.; Klippenstein, S. J. *The Journal of Physical Chemistry A* **2006,** *110* (36), 10528-10544.
41. Bartis, J. T.; Widom, B. *Journal of Chemical Physics* **1974,** *60* (9), 3474-3482.
42. Miller, J. A.; Klippenstein, S. J. *Physical Chemistry Chemical Physics* **2013,** *15* (13), 4744-4753.
43. Levenberg, K. *Quarterly Journal of Applied Mathmatics* **1944,** *II* (2), 164-168.
44. Marquardt, D. *SIAM Journal on Applied Mathematics* **1963,** *11* (2), 431-441.
45. Moré, J., The Levenberg-Marquardt algorithm: Implementation and theory. In *Numerical Analysis*, Watson, G. A., Ed. Springer Berlin Heidelberg: 1978; Vol. 630, pp 105-116.

Chapter 3. The Role of the Pre-reaction Complex in the OH + SO_2 Reaction

Overview of the chapter

As discussed in the previous Chapter, the Master Equation (ME) method is a powerful and versatile approach used to deal with kinetic systems of interconnected wells. It allows the exploration of these kinetic systems at an energy-resolved level, and is widely employed for the majority of studies of pressure dependent processes in this thesis. The technique also allows the extrapolation of experimental results, often obtained under experimental conditions that do not necessarily reflect their final practical application. In this chapter, the results of Master Equation modelling undertaken to better understand the chemistry of the OH + SO_2 reaction, a process of primary importance for the atmosphere, are presented. The relevance of a pre-reaction complex to understand experimental measurements of $k_1(T,p)$ available in the literature, for a wide range of temperature (260 – 580 K), pressure (13-695 Torr) and bath gases (He,N_2,Ar,SF_6) is investigated. The theoretical calculations indicate that the pre-reaction complex is weakly bound (~7.2 kJ mol^{-1}) and all the ME fits point to a lack of importance for the complex formation. The reaction appears to be predominantly controlled by the inner transition state, which according to our best ME model, is submerged under the starting reactants (~-1.0 kJ mol^{-1}), supporting a slight negative temperature dependence of $k_1^{\infty}(T)$. Only a portion of the measurements explored could be reconciled, and a brief discussion of possible interferences affecting these measurements is provided. The enthalpy of the reaction ($\Delta_{R1}H_{0K}$ = 110.5 kJ mol^{-1}), obtained with the ME fits, is in excellent agreement with theoretical predictions available in the literature. This chapter presents a classic example of ME modelling where experimental rate coefficients are used to enable a critical assessment of the related potential energy surface diagram and its understanding will serve as a basis for the next chapters where more complex fitting strategies are employed.

3.1 LITERATURE BACKGROUND OF THE OH + SO_2 REACTION

The reaction of sulphur dioxide, SO_2, with OH radicals (R1) is of primary importance in the atmosphere. It leads to the formation of a key intermediate, the hydroxysulfonyl radical ($HOSO_2$), which can further react with O_2 and H_2O (R2-R3)[1-2] to give sulfuric acid (H_2SO_4). Sulfuric acid can readily promote nucleation and represents an important precursor for aerosols in the atmosphere.[1] It is also directly related to the occurrence of acid rain, which implicates health, environmental and economic consequences.[3]

$OH + SO_2 + M \rightarrow HOSO_2 + M$	R1
$HOSO_2 + O_2 \rightarrow SO_3 + HO_2$	R2
$SO_3 + H_2O \rightarrow H_2SO_4$	R3

Alternatively, SO_2 from the gas phase can dissolve into water droplets, particles, clouds and fogs in the atmosphere and be oxidized within the aqueous phase by species such as O_3, O_2 and H_2O_2.[4] Strongly acidic fogs can be formed due to evaporation of water from the droplets (pH~1.7)[5] and because of their sufficiently small size (< 1 μm),[6] they represent a considerable health concern. They can be efficiently inhaled, cause irritation of the respiratory tract and be particularly harmful to those suffering from respiratory diseases such as asthma.[4, 7] It is estimated that around 50,000 people die every year in the United Kingdom as a result of respiratory diseases caused by air pollution, such as particulate matter, ozone and NO_2;[8] this number denotes the importance of understanding chemical reactions involved in particulate formation.

Reaction R1 has been explored recently in experimental investigations with particular interest on determining both the high pressure limit ($k_1^{\infty}(T)$)[9-10], and pressure dependent ($k_1(T, p)$) rate coefficients for a wide range of conditions.[11-12] These studies indicate difficulties in the determination of reliable kinetic parameters of this reaction. The existence of a van der Waals pre-reaction complex has been postulated[10] in order to rationalize the small high pressure limiting rate coefficients k_1^{∞} that were measured by Blitz *et al.*,[10] since much

faster coefficients would be expected for a simple barrierless reaction to form $HOSO_2$. With the complex, reaction R1 is now split into two processes, a barrierless formation of the complex (R1,vdW) and the subsequent product ($HOSO_2$) formation via a transition state (R1,TS).

$$OH + SO_2 \xrightarrow{k_{1,vdW}} HO—OSO \qquad \text{R1,vdW}$$

$$HO—OSO \xrightarrow{k_{1,TS}} HOSO_2 \qquad \text{R1,TS}$$

where $k_{1,vdW}$ is the rate coefficient for the pre-reaction complex formation and $k_{1,TS}$ is the rate coefficient for product formation. Figure 3.1 shows a schematic representation of the related potential energy surface against the reaction coordinate.

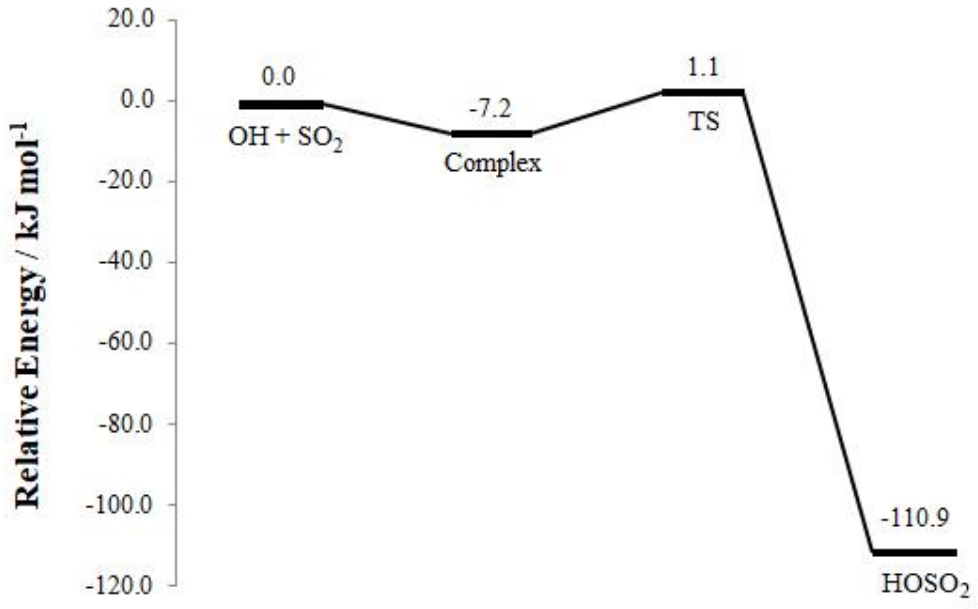

Figure 3.1 - Potential energy diagram for the OH + SO_2 reaction. Relative energies were calculated at the CCSD(T)/CBS//M06-2X level of theory. A more detailed description of the calculations is provided later in the chapter.

After these previous studies were published, [9-13] the postulated pre-reaction complex has been identified via theoretical calculations by Miriyala *et al.*[14] The theoretical level at which the electronic energies were calculated by Miriyala *et al.* is relatively low (MP2(full)/aug-cc-pVTZ) when compared to the beyond-CCSDT correlation energy calculations reported by Donald G.

Truhlar's group[13] for the rest of the potential energy surface (excluding the pre-reaction complex). From the work of Long *et al*.,[13] the authors predict k_1^{∞} to be 1.25×10^{-12} cm^3 molecule^{-1} s^{-1} at 298 K, significantly higher compared to the experimental value of $(7.2 \pm 3.3)\times10^{-13}$ cm^3 molecule^{-1} s^{-1} reported by Blitz *et al*.[11] However, the main difference between these two studies is related to the temperature dependence of k_1^{∞}; while the work by Long *et al*. reports a barrier of 1.1 kJ mol^{-1} for R1[13], the experimental results do not indicate an increase of k_1^{∞} with increasing temperature, and a negative activation energy has been assigned.[11]

The study of Blitz *et al.*[11] has also indicated that only a combination of their data with a portion of those reported by Wine *et al*.[12] could be reconciled, suggesting that SO_2 photolysis may have interfered significantly in the measurements of many flash photolysis studies found in the literature.[15-18]

In this chapter, the reconciled data from Blitz *et al.*[11] was coupled with high temperature dissociation measurements ($k_{-1}(T,p)$),[9] where OH was observed to be in equilibrium with SO_2. An attempt to describe the total dataset, which also includes measurements by Wine *et al.*[12], via Master Equation (ME) modelling and mathematical fitting is performed. A list of all the data used in this analysis is presented in Table 1 of Appendix 2. The recently identified pre-reaction complex is incorporated in the analysis and an attempt to further refine the related potential energy surface is presented. Since the phenomenological rate coefficients can be directly calculated via the ME, this case represents the simplest fitting strategy implemented throughout the thesis, where adjustable parameters are optimised to provide a good match between experimental values of $k_1(T,p)$ and the phenomenological rate coefficients calculated via ME. Alternative, and more complex, strategies will be required to analyse other systems in the following chapters, such as the reaction of isoprene with OH radicals at elevated temperatures. A good understanding of the procedure used for the OH + SO_2 case will help introduce the analysis of the subsequent chapters. Although simplistic compared to the subsequent

chapters, this study incorporates experimental data generated with a variety of bath gases (*M* = He, N_2, SF_6, Ar) for a wide pressure range (~10 - ~700 Torr).

3.2 *AB INITIO* AND MASTER EQUATION CALCULATIONS

Additional *ab initio* calculations were undertaken in order to further refine the analysis of the experimental data, with particular interest on the recently identified pre-reaction complex. Stationary points of the involved species were calculated with the DFT functional M06-2X [19] and the aug-cc-pVQZ basis set.[20-24] Molecular structures were optimized with the aid of the Gaussian 09 D.01 software[25] using analytic gradients and the Berny algorithm[26] in redundant internal coordinates. Single point energies (SPE) of the M06-2X/aug-cc-pVQZ optimized geometries were computed via coupled cluster calculations with single, double and triple excitations, the triples being described perturbatively (CCSD(T)).[27] SPE results were extrapolated to the complete basis set limit (CBS) using the extrapolation scheme presented by Peterson *et al.*[23] and Dunning's correlation consistent basis sets (aug-cc-pV*X*Z, X=D, T, Q). Harmonic vibrational frequencies, rotational constants, force-constant matrices and zero-point energies (ZPE) were calculated at the M06-2X/ aug-cc-pVQZ level. The hindered rotor approach was used to describe the internal rotation around the O_2S-OH bond. The potential was mapped out via a relaxed scan of the dihedral angle with respect to this rotation, with 24 steps of 15°. A restricted structure optimization of the molecule at the M06-2X/ aug-cc-pVQZ level of theory was performed for each step of the scan. Using this description of a hindered rotor, MESMER uses the procedure presented by Sharma *et al.*[28] to project out the respective vibrational modes. Figure 3.2 shows a diagram of the potential energy for the OH + SO_2 reaction.

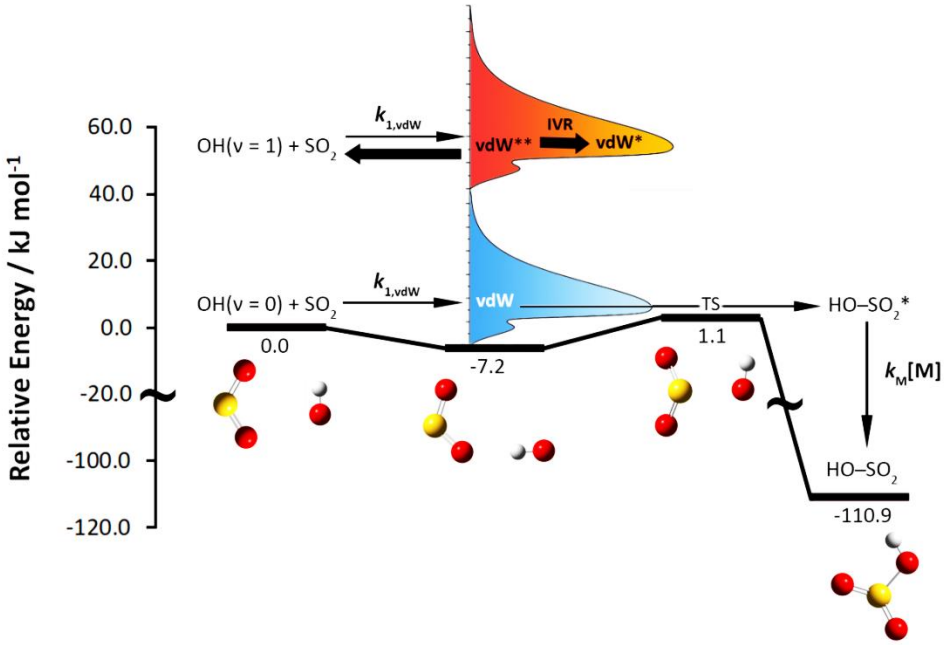

Figure 3.2 - Potential energy diagram for the OH + SO_2 reaction, where a van der Waals complex, vdW, is formed before proceeding over the transition-state, TS, to form the hydroxysulfonyl radical, $HOSO_2$. The energies of the stationary states are those calculated in this work, with zero point energies added. Also included is OH(v=1) + SO_2 reaction, which initially forms a "hot" vdW(**) that either re-dissociates back to reagents or undergoes intramolecular energy redistribution (IVR) to vdW(*), which does not significantly re-dissociate to OH(v=1) + SO_2; the two thick arrows indicate that these processes are in competition. The Boltzmann energy distribution of the vdW is illustrated; it resides mostly above the binding energy of this complex.

All the ME modelling was performed with the aid of the computational package MESMER.[29] The inverse Laplace transformation (ILT) method was implemented to describe the complex formation (R1,vdW) and RRKM rate theory[30] was used for the subsequent reaction over the transition state (R1,TS). For the first step, even though there are no measurements available for this rate coefficient, this reaction is expected to be close to the gas kinetic collision frequency. Barrierless reactions typically present a negative temperature dependence, which can be reasonably described in the form of equation E1 :

$$k_{1,\mathrm{vdW}} = A \times \left(\frac{T}{298\ \mathrm{K}}\right)^{n} \qquad \text{E1}$$

where *A* and *n* are adjustable parameters, modified to provide a good fit to the data. In some cases, these parameters were fixed in order to briefly assess the sensitivity of the model to them. Additionally, the relative energy of the transition state is also defined as an adjustable parameter. The coupled reactions R1,vdW and R1,TS were solved by MESMER to compute $k_1(p, T)$ and a least-squares fit was used to minimize the sum of squared residuals calculated by subtracting the calculated rate coefficients from the experimental measurements. Additionally, energy transfer parameters for helium and argon ($<\Delta E_{d,He}>$ and $<\Delta E_{d,Ar}>$ respectively) and their temperature dependencies ($<\Delta E_{down}> = <\Delta E_{d,M}> \times (T/298)^m$), were also allowed to float.

3.3 RESULTS AND DISCUSSION

Stationary points that represent reagents, the pre-reaction complex, the transition state and the product ($OH\text{-}SO_2$) had their energies calculated as described previously. The results of the calculations are presented in Table 3.1, which includes zero-point energy corrections. The pre-reaction complex was identified to be 7.2 kJ mol^{-1} below the reagents. The calculations from this work are in good agreement with those reported by Long *et al.* [13] and Klopper *et al.*[1] with respect to $\Delta_R H_{0K}(HOSO_2)$. When extrapolated to 298 K, about 5 kJ mol^{-1} is added to the binding energy. A very small barrier has been calculated for the overall process (~1 kJ mol^{-1}) in the present work, while the investigation of Miriyala *et al.*[14] reports a significant barrier of 22.2 kJ mol^{-1}. As will be discussed later, a transition state slightly submerged below the entrance channel is necessary for a good fit to the experimental data. The highest-level calculations currently available in the literature are the beyond-CCSD(T) computations by Long *et al.*[13], which also indicates a small barrier (TS ~1 kJ mol^{-1} compared to reagents). Given the great discrepancy with the barrier calculated by Long *et al.*, the results of Miriyala *et al.* are therefore considered in a qualitative manner.

Table 3.1 – Comparison of theoretical calculations for the OH + SO_2 reaction. All the energies include zero-point corrections and are relative to OH + SO_2. The table also includes an experimental measurement by Blitz *et al.*[9]

	vdW / kJ mol^{-1}	TS / kJ mol^{-1}	$\Delta_R H_{0K}(HOSO_2)$ / kJ mol^{-1}	$\Delta_R H_{298K}(HOSO_2)$ / kJ mol^{-1}
Miriyala *et al.* 2017 [14]	-17.6	22.2	-109.2	
This study 2019	-7.2	1.2	-110.9	
Klopper *et al.* 2008 [1]			-109.4	-114.7 ± 3
Long *et al.* 2017 [13]		1.1	-111.5	
Somnitz (2004) [31]			-103.6	
Blitz *et al.* (2003)[9] (Experimental)				-113 ± 6

In a previous study of Blitz *et al.*,[10] rate coefficients for the removal of vibrationally excited hydroxyl radicals (OH(ν > 0)) in the presence of SO_2 (R1(ν)) have been measured, which allowed the determination of k_1^{∞}.

$$OH(\nu>0) + SO_2 \rightarrow HOSO_2^{**} \qquad R1(\nu)$$

In reaction R1(ν) , the nascent product $HOSO_2$**(vdW**) is indicated with two stars to denote additional internal energy from the vibrationally excited OH. While $HOSO_2$** can react in different ways, and since it is unlikely that the formation of OH(ν=0) from it is significant, the measured removal rate coefficient represents k_1^{∞}. This is known as the proxy method for determining the high pressure limiting rate coefficient, first introduced by Smith.[32] The importance of the van der Waals complex is that it can potentially influence the energy transfer between the reagents.

In the study of Blitz *et al.*,[10] the measured $k_1(v>0)$ were faster than k_1^{∞} for the same experimental conditions. In order to enable significant energy redistribution within the vdW complex, its lifetime would need to be considerably long (~1-100 picoseconds). A sufficiently long lifetime would provide a proxy for the high pressure limit rate coefficient for the formation of the pre-reaction complex, which should be close to the gas kinetic collision frequency (~10^{-10} cm^{-3} $molecules^{-1}$ s^{-1}) (see Table 3.2 for estimates of the rate coefficients for vdW formation, calculated via ME modelling). However, not only does the analysis of Blitz *et al*. indicate much smaller $k_1(v>0)$ than the gas kinetic collision frequency, but the rate coefficients also increase with the level of excitation, being higher for more the elevated vibration levels. This implies a short lifetime for the complex, which suggests that the re-distribution of the additional energy of vdW** by its vibrational modes would occur partially throughout the complex (see Figure 3.2 for $OH(v=1) + SO_2$). Internal vibrational energy redistribution (IVR) usually occurs on a femto-picosecond timescale[33] and our ME calculations indicates that the lifetime of the vdW complex above T=250 K is of approximately a picosecond. As illustrated in Figure 3.2, the Boltzmann distribution of the vdW, formed from the reaction of $OH(v=0)$ with SO_2 is mostly above the transition state to products. Even though the $k_1(v>0)$ rate coefficients measured by Blitz et *al.* are qualitatively consistent with the potential energy surface depicted in Figure 3.2 and deserve good attention in the future, this chapter will focus on the data related to $OH(v=0) + SO_2$. The investigation the $k_1(v>0)$ provides, however, estimates for $k_1^{\infty}(T)(v=0)$ which will be used later on in the chapter for a comparison with the obtained results.

As reaction R1 consists of two steps, it is safer to assume that the measured kinetic data are related to the total OH loss rather than OH reacting with SO_2 to give $HOSO_2$. For this reason, in the MESMER fitting, the literature data have been assigned as the total removal of OH. For the equilibrium measurements of Blitz *et al.*[9], the calculated total loss of $HOSO_2$ was regressed to best fit $k_{-1}(T,p)$. The phenomenological rate coefficients, which are measured experimentally,[34] correspond to eigenvalues of the transition matrix *M*

described in Chapter 2, if the model implemented is correct. For a simple reaction, an eigenvalue may represent a single rate coefficient, however, for a case like reaction R1, it will be a mix between $k_{1,vdW}$ and $k_{1,TS}$, (reactions R1,vdW and R1,TS respectively, see section 3.1) and will represent the phenomenological loss of OH. This was observed in the literature, for example, in the reaction of methanol (CH_3OH) with OH radicals.[35] Even though these reactions seems to be a one-step process, the rate coefficients measured at low temperatures increase drastically, which indicated that in this case, it is mostly controlled by a pre-reaction complex formation.

The first attempt to fit the full dataset (presented in Appendix 2) is presented in Figure 3.3. The best-fit ME calculated rate coefficients (y axis) are plotted against the experimental measurements (x axis) along with the y=x red line (Fitted $k(T,p)$ = Experimental $k(T,p)$). The fitted rate coefficients used in this type of plot are those calculated from the ME calculations utilizing only the best-fit adjusted parameters. In this type of graph, a good fit is indicated by the proximity of the points to they=x line, i.e., best-fit rate coefficients (y axis) are close to the experimental measurements (x axis). It is very clear from Figure 3.3 that, as previously indicated by Blitz *et al.*[11] on their previous study using a simplistic approach (absence of the pre-reaction complex), their measurements cannot be reconciled with all the measurements of Wine *et al*.[12]

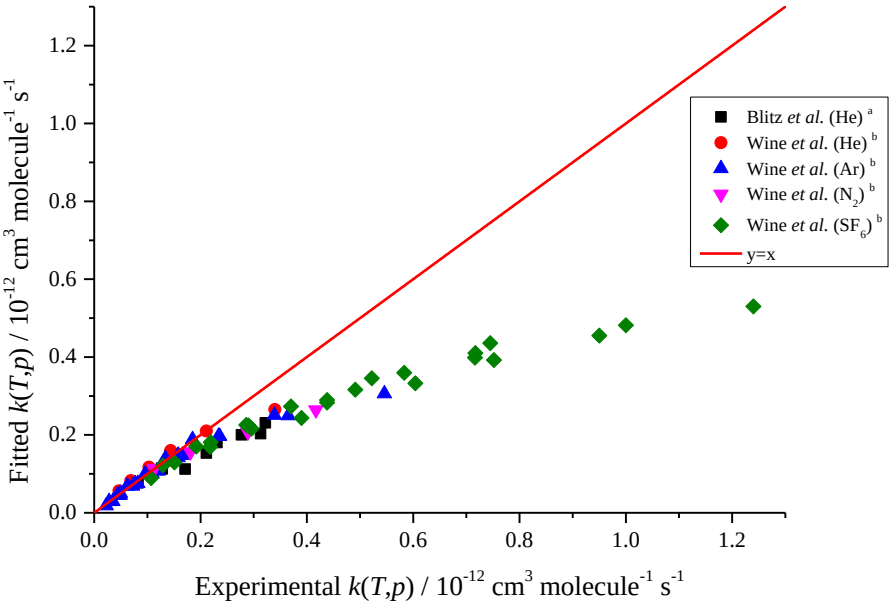

Figure 3.3 - The result of the ME fit to the full dataset. a - Blitz *et al.*[9, 11] b – Wine *et al.*[12]. The y=x line is presented in red. High temperature reverse coefficients by Blitz *et al.*[9] were suppressed from the figure for illustrative purposes.

The systematic deviation of a good portion of data from the y=x line as observed in Figure 3.3 suggests a fundamental problem with some data. A careful inspection of the results show that while the experimental data reported by Wine *et al*. indicates a $\Delta_{R1}H_{0K}$ value of ~ -102 mol^{-1}, the data by Blitz *et al*. [9, 11] incorporated in the fit suggest a much deeper value, of approximately -111 kJ mol^{-1}. Both the data sets were further analysed individually and will be discussed in the following, but it is worth highlighting that such differences have a significant impact on the predicted pressure-dependent rate coefficients. For example, Wine *et al*. have measured a rate coefficient of 1×10^{-12} cm^3 molecule^{-1} s^{-1} at 300 K and 500 Torr of SF_6. However, in order to agree to the measurements of Blitz *et al*., a rate coefficient of about 6×10^{-13} cm^3 molecule^{-1} s^{-1} would be necessary. As the measurements by Blitz *et al*. indicate a deeper $\Delta_{R1}H_{0K}$ of -111 kJ mol^{-1}, this would imply faster rate coefficients, but an opposite effect is observed. For this reason, it is postulated that the measurements by Wine *et al*. were affected by fast interfering processes, which significantly competed with the OH + SO_2 reaction.

The work of Blitz *et al.*[11] indicated a significant interference of SO_2 photolysis in the measured kinetics, which has been accounted for in their study. To do this, the authors have monitored OH formation as a function of laser fluence when SO_2 is flashed at 248 nm in the presence of a high excess of H_2 in the absence of any OH precursor. The observed quadratic dependence of $[OH]_0$ (the OH concentration initially formed), on laser fluence suggests that a 2-photon absorption process is taking place (R4), which corroborates the mechanism proposed by Effenhauser *et al.*[36] According to the latter, the photolysis process is consisted of an initial promotion of the ground state SO_2 to an excited B-state with a long lifetime (~10-100 μs); followed by a second photon absorption that promotes the B-state SO_2 into a dissociative state that is rapidly converted to products. Even though the generation of excited $O(^1D)$ atoms is among the possibilities reported by Effenhauser *et al.*, the authors were unable to quantify the yield of this channel.

In the presence of high excess of H_2 as controlled by Blitz *et al.*,[11] $O(^1D)$ will react with H_2 to give OH(ν=0 - 4) and a hydrogen atom (R5). The arising vibrationally excited OH (ν=1-4) rapidly cascades down to the ground-state and can be detected via laser-induced fluorescence. Blitz *et al*. estimate the cross section for the second photon absorption to be $\sigma_2 = (5.5 \pm 2.0) \times 10^{-18}$ cm^2 $molecule^{-1}$.

$$SO_2 + 2h\nu \rightarrow O(^1D) + SO \qquad \text{R4}$$

$$O(^1D) + H_2 \rightarrow OH(\nu=1\text{-}4) + H \qquad \text{R5}$$

The majority of the points in Figure 3.3 are located below the y=x line, i.e., experimental measurements are significantly larger than the fitted rate coefficients. The potential SO_2 photolysis, which have not been taken into account in the work of Wine *et al.*[12], goes in some way to explain the observed disagreement, since SO, a product of the photolysis, can react very rapidly with OH radicals ($k^{\infty}_{OH+SO} = (8.17 \pm 0.36)\times10^{-11}\times(T/298\ K)^{-1.35\pm0.11}$ cm^3 $molecule^{-1}$ s^{-1} for T=295 – 703 K).[37] The consistency of the measurements by

Wine *et al*. were submitted to another test, by removing all the data points corresponding to the measurements of Blitz *et al*.[9, 11] and re-attempting the fit; the result of this new attempt is presented in Figure 3.4. The poor fit is an indication that the rate coefficients reported by Wine *et al*. are internally inconsistent

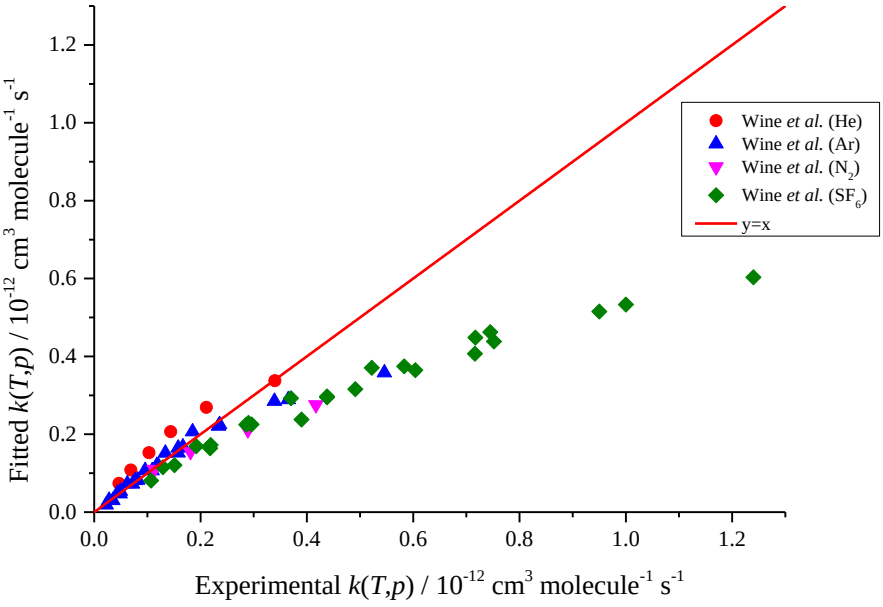

Figure 3.4 - The result of the Master Equation fit to the experimental measurements of Wine *et al.* [12]. The y=x line is presented in red.

Even though this result raises questions regarding the validity of these experimental measurements, further attempts to reconcile at least a portion of their measurements with those of Blitz *et al*. were undertaken. By doing so, a good agreement could only be obtained when their data where Ar is the bath gas is combined with the measurements by Blitz *et al*. The result of this combination is a much better fit (R^2=0.93), as depicted in Figure 3.5.

.

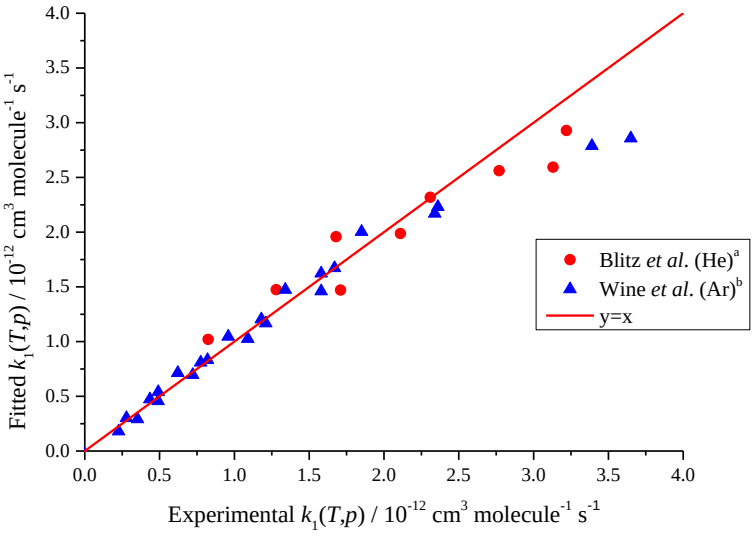

Figure 3.5 - The result of the ME fit to the experimental measurements of Blitz *et al.*[9, 11] and those of Wine *et al.* [12] in argon. The y=x line is presented in red. High temperature reverse coefficients by Blitz *et al.*[9] were suppressed from the figure for illustrative purposes.

From this point, this dataset (presented in Figure 3.5) is considered to be the basis for exploring the potential energy diagram related to the OH+SO_2 reaction. A number of parameters were floated during the fitting exercises, and in some occasions, some of these parameters were kept fixed to test the sensitivity of the experimental data to these parameters. The list of floated parameters are presented in Table 3.2 and they include: the enthalpy of reaction $\Delta_{R1}H_{0K}$, the energy transfer parameters for helium and argon and their temperature dependence, $<\Delta E_{d,He}>$, $<\Delta E_{d,Ar}>$ and *m* respectively (see Table 3.2), the pre-exponential factor and the temperature dependence of the van der Waals complex (R1,vdW) and finally, the energy of the transition state relative to the reagents.

Table 3.2 - Master Equation fits to the experimental data, where $<\Delta E_{down}> = <\Delta E_{d,M}> \times (T/298)^{m}$.

	$\Delta_{R1}H_{0K}$ / kJ mol^{-1}	$<\Delta E_{d,He}> \times (T/298)^{m}$ /cm^{-1}		$<\Delta E_{d,Ar}> \times (T/298)^{0.5}$ /cm^{-1}	ILT$^{(a)}$= A $\times (T/298)^{n}$	TS/kJ mol^{-1}	χ^2/pts$^{(b)}$
Vibration **Model A**	-114.4 ± 0.8	208 ± 28	1.0 fixed	185 ± 15	$(1.4 \pm 3.1) \times 10^{-10}$ -0.87 ± 3.05	-0.99 ± 0.23	1.54
Vibration **Model B**	-114.4± 0.8	208 ± 29	1.0 fixed	185 ± 16	1.4×10^{-10} fixed -0.87 fixed	-1.00 ± 0.23	1.54
Hindered **Model C**	-110.5 ± 0.8	145 ± 17	1.0 fixed	127 ± 9	$(1.4 \pm 3.5) \times 10^{-10}$ -0.87 ± 2.01	-0.99 ± 0.20	1.31
Hindered **Model D**	-110.5 ± 0.8	145 ± 17	1.0 fixed	127 ± 9	1.4×10^{-10} fixed -0.87 fixed	-0.99 ± 0.20	1.31
Hindered **Model E**	-110.5 ± 6.6	145 ± 37	1.00 ± 1.94	127 ± 32	1.4×10^{-10} fixed -0.87 fixed	-0.99 ± 0.21	1.31
Model F	-114.3 ± 0.8	1343 ± 422	1.0 fixed	274 ± 14	1.4×10^{-10} fixed -0.87 fixed	1.1 fixed	4.98
Model G	-111.5 fixed	697 ± 109	1.0 fixed	312 ± 14	1.4×10^{-10} fixed -0.87 fixed	1.1 fixed	5.86
ILT(TS) **Model H**	-109.1 ± 6.6	120 ± 30	0.76 ± 1.83	116 ± 30	$5.76 \pm 0.77 \times 10^{-13}$ -0.84 ± 0.27		1.15

(a)Units are cm^3 molecule^{-1} s^{-1}. (b) Weighted by uncertainties in the rate coefficients. Number of points equals 36.

Table 3.2 presents the results of the fits of the different variants of the model depicted in Figure 3.2 to the experimental data along with the goodness of fit (χ^2/pts). A total of eight variants were constructed, and their details are now discussed. In variant A, all the vibrational modes of all the species are described as harmonic oscillators. From the fit, the rate coefficient for the formation of the van der Waals complex is very fast but ill-defined ($k_{1,vdW} = (1.4 \pm 3.1) \times 10^{-10}$ cm^3 molecule^{-1} s^{-1}). On the other hand, the energy of the transition state (relative to OH + SO_2) is submerged below the reactants (-0.38 ±0.16 kJ mol^{-1}) and well-defined, diverging from the *ab initio* estimates (see table 3.1) which indicates a slightly positive barrier. From these results and according to model A, reaction R1 is predominantly controlled by the inner (submerged) transition state. Model B is very similar to A, but maintains the pre-exponential factor of the pre-reaction complex formation fixed. The two models indicate a slightly negative energy of the transition state, which contrasts with *ab initio* predictions, however, the absolute difference is small (~ 2 kJ mol^{-1}). This submerged TS implies that the overall rate coefficient will present a negative temperature dependence, in contrast to the positive dependence reported in the work of Long *et al*. No significant variation is observed in the returned parameters when model B is compared to model A and the impact of fixing the mentioned parameter on the uncertainties of them is negligible. This is an evidence that the vdW complex formation and its parameters are not strongly correlated to the other ones. Both the models return -114.4 kJ mol^{-1} for $\Delta_{R1}H_{0K}$.

The use of rigid harmonic rotors, as implemented in models A and B can lead to inaccurate calculations of the density of states of the species involved in the model. This effect can have a severe impact on the entropy of the reaction, $\Delta_R S$, something that propagates to significant changes in the returned $\Delta_{R1}H_{0K}$. As will be evidenced in the following chapter where the chemistry of isoprene is explored, much better agreement between experimental measurements and theoretical predictions of the thermochemistry of that reaction is obtained when the hindered rotor approach is used to describe low frequency vibrations with considerable degrees of anharmonicity ($\nu \leq 350$ cm^{-1}) of the involved

species, when compared to an analogous vibration-only model. The relevant degrees of anharmonicity of some of these low vibrational modes (typically bends and torsional vibrations) can be better described via the implementation of the hindered rotor approach. A low vibrational mode can be visually inspected and when this mode corresponds to a clear rotational torsion, the implementation of a hindered rotor description is considered. Although the anharmonicity of bends and coupled modes are admittedly important, the results obtained in chapters 3 and 4 of this thesis indicate a very good agreement between thermochemical parameters obtained from *ab initio* calculations and experimental determinations when rotational torsions are treated with the hindered rotor approach and the remaining modes are described as harmonic vibrations.

The subsequent model variants (C-H) will implement this approach to describe a small torsional vibration (ν=309 cm^{-1}) around the OH─SO_2 bond of the product. Thus, model C is analogous to model A, but includes the mentioned hindered rotor description. As expected based on the result of model A, $k_{1,vdW}$ remains ill-defined ($k_{1,vdW}$ = (1.4 ± 3.5) × 10^{-10} cm^3 $molecule^{-1}$ s^{-1}) and when this parameter is fixed (model D), no relevant change is observed in the returned parameters or their uncertainties. This leads to the same conclusion reported when models A and B were compared: the pre-reaction complex does not play an important role in the kinetics. However, the inclusion of a hindered rotor provoked a significant change in the returned $\Delta_{R1}H_{0K}$ (-110.5 ± 0.8 kJ mol^{-1}) when D is compared to the analogous vibration-only model B (-114.4± 0.8 kJ mol^{-1}). This variation of 3.9 kJ mol^{-1} arises mainly because the entropy of reaction calculated with model D ($\Delta S_{R1,298\ K}$ = -142.8 J k^{-1} mol^{-1}) is lower than that when model B is the one of choice ($\Delta S_{R1,298\ K}$ = -150.4 J K^{-1} mol^{-1}). The value obtained from model D represents the best experimental measurement of $\Delta_{R1}H_{0K}$ obtained in this work, which is in excellent agreement with the theoretical predictions by Klopper *et al.*[1] Long *et al.*[13] and the calculations undertaken in this investigation (see Table 3.1).

Despite the good agreement, the returned $\Delta_{R1}H_{0K}$ values are dependent on the energy transfer parameters of helium. The equilibrium measurements of Blitz *et al.*[9], performed in helium, impose strong constrains on the thermochemistry of the reaction, justifying the dependence of $\Delta_{R1}H_{0K}$ for the energy transfer parameters of that bath gas. While in the previously discussed models, the temperature dependence of $<\Delta E_{d,He}>$, *m*, has been set to 1.0, which is consistent with measurements for different systems[38], model E has that temperature dependence as an additional adjustable parameter. This attempt returns unity as a result, however, according to its uncertainty the parameter is ill-defined. With effect, having *m* adjusted has caused the uncertainties of the other parameters to increase significantly. The uncertainties obtained with model E probably represents a more realistic estimate of the current accuracy of $\Delta_{R1}H_{0K}$. The correlation between *m* and $\Delta_{R1}H_{0K}$ was found to be close to unity, where the enthalpy of reaction increases with *m*. For this reason, additional experimental measurements of $k_1(T,p)$, preferably at elevated temperatures (T > 300 K) to promote pressure dependence are desirable in order to indicate a preferable theoretical investigation with confidence.

From Table 3.2 it is noticed that even for model, E, where uncertainties are greater than in the other cases, the transition state is submerged even when the uncertainties are considered (-0.99 ± 0.21 kJ mol^{-1}), indicating that the accuracy of the *ab initio* calculations currently available are not superior to 1 kJ mol^{-1}. Although the agreement observed is a considerable achievement, the small discrepancy significantly influences the prediction of rate coefficients at room temperature. Also, significant correlation coefficients between the energy transfer parameters $<\Delta E_{d,He,Ar}>$ and $\Delta_{R1}H_{0K}$ (ρ_{corr}>0.8) are observed. However, the ab initio estimations of $\Delta_{R1}H_{0K}$ presented in table 3.1 give some support to the obtained $\Delta_{R1}H_{0K}$. The values for the energy transfer parameter $<\Delta E_{d,He}>$ obtained from the ME fits (~150 cm^{-1}) are similar to those estimated in chapters 4 and 5 for the reactions of OH with isoprene and ethylene respectively, and also agree with the values previously reported in the work of Blitz *et al.*[11]

The derived uncertainties of the adjustable parameters indicate the level of precision in which these parameters are known based on the experimental data. Usually, the process by which a rate coefficient is extracted from the experimental data involves the use of a fit of an analytical equation suitable to describe the system. This is the case of the exponential decay equation employed for the analysis of first order processes, as presented in Chapter 2. Nonetheless, when the complexity of the problems is enhanced, more variables tend to be introduced as a response and more steps tend to be undertaken before the solutions can be obtained. This effect can eventually become a compromise to the precision of derived solutions, given that errors need to be propagated and a certain degree of interdependence between the various variables can be developed. For this reason, reducing the number of necessary transformations of the data is an interesting strategy from the point of view of data analysis. The reaction currently being studied is a great example to show how a very small error, in the order of 1 kJ mol^{-1} is the threshold between a good and a bad agreement to theoretical predictions. The development and exploitation of more accurate techniques can potentially also calibrate the accuracy of theoretical calculations, which for binding energies, is typically believed to be of the order of a few kcal mol^{-1}.

Attempts to fit the data by fixing the TS relative energy and $\Delta_{R1}H_{0K}$ to the theoretical values calculated by Long *et al*. were made in models F and G. While in model F the TS energy is fixed to 1.1 kJ mol^{-1} and $\Delta_{R1}H_{0K}$ is an adjustable parameter, in model G $\Delta_{R1}H_{0K}$ is fixed to -111.5 kJ mol^{-1}. Model F shows that by fixing the barrier to 1.1 kJ mol^{-1} it is not possible to obtain a good fit to the data as evidenced by the fact that the goodness of fit is increased by a factor of ~3.8 when compared to the previous models (C-E). Model G provides a similarly poor fit: when $\Delta_{R1}H_{0K}$ is also fixed to the aforementioned theoretical value the goodness of fit is increased by a factor of ~4.5 when compared to previous models (C-E). These results reinforce the understanding that above 250 K, the OH + SO_2 reaction is mainly controlled by the inner transition state (TS in Figure 3.2), diminishing the importance of the pre-reaction complex. All the modelling presented so far assumes the transition

state structure is unchanged as the temperature varies. This is a reasonable approximation over large barriers, and even though this is not the case for the current work, where the barrier from the vdW complex to the TS is 8.2 kJ mol^{-1}, the fact that the pre-reaction complex is unimportant for the chemistry eliminates any burden for the use of this approximation. For barrierless processes or processes with small barriers ($E_a \leq 4$ kJ mol^{-1}) the transition state can change with temperature and generally becomes more similar to the adduct structure as temperature is increased.[39]

Finally, the reaction has been treated using a one-transition state approach via an inverse Laplace transformation $k_1^{\infty} \times (T/298)^n$ to calculate the microcanonical rate coefficients (model H). The parameter n allows flexibility to account for a possible change of the inner TS with temperature and the result of this fit is presented on the last row of Table 3.2. The negative temperature dependence obtained (n=-0.83) is aligned with the results of the previous method where the TS was found to be submerged under the starting reactants. Figure 3.6 shows a comparison between the high pressure limiting rate coefficients calculated with model H and the predictions of $k_1^{\infty}(T)$ by Long *et al.*[13] and Blitz *et al.*[11]

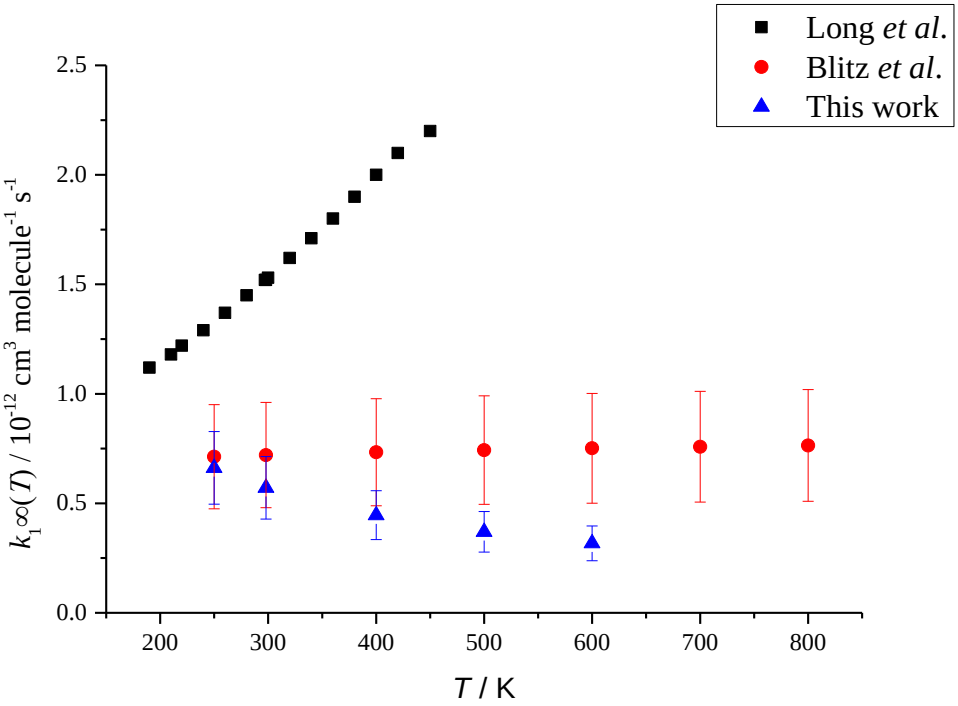

Figure 3.6 – A comparison of the estimates of the high pressure limiting rate coefficients obtained with the use of model H with the previous predictions by Long *et al.* [13] and Blitz *et al.*[11]

3.4 SUMMARY AND CONCLUSIONS

The current chapter presented an example of a classic Master Equation analysis in which experimental measurements of the OH + SO_2 reaction were used to enable an assessment of the potential energy surface related to this chemical process. The investigation made use of experimental data covering a wide range of temperatures (260 – 580 K), pressures (13 -695 Torr) and carrier gasses (He, N_2, Ar, SF_6) highlighting the versatility of the ME method. A weakly bound (~7.2 kJ mol^{-1}) pre-reaction complex formation was identified, but this was found to be unimportant as the chemistry appears to be controlled by an inner transition state. The results of ME fits to the experimental data show that the transition state is slightly submerged (~ -1.0 kJ mol^{-1}) below the starting reagents (OH + SO_2), causing a slightly negative temperature dependence, as observed for barrierless processes in general. Furthermore, the enthalpy of reaction derived from the ME analysis (~110.5 ± 6.6 kJ mol^{-1}) is in excellent agreement with theoretical estimates available in the literature.

Since the chapter provided that a real application of the ME method, its contents will serve the basis of the more complex analysis strategies required to analyse the chemistry of isoprene and ethylene, covered in Chapters 4 and 5 respectively. While the analysis of the current chapter purely based on fits involving experimentally derived rate coefficients, the analysis implemented in the next chapter (4) also involves the exploration of species profiles calculated via the Master Equation.

3.5 REFERENCES

1. Klopper, W.; Tew, D. P.; Gonzalez-Garcia, N.; Olzmann, M. Heat of Formation of the $HOSO_2$ Radical from Accurate Quantum Chemical Calculations. *J Chem Phys* **2008,** *129*, 114308.

2. Mai, T. V. T.; Duong, M. V.; Nguyen, H. T.; Huynh, L. K. Ab Initio Kinetics of the $HOSO_2 + {}^3O_2 \rightarrow SO_3 + HO_2$ Reaction. *Physical Chemistry Chemical Physics* **2018,** *20*, 6677-6687.

3. Singh, A.; Agrawal, M. Acid Rain and Its Ecological Consequences. *J Environ Biol* **2008,** *29*, 15-24.

4. Finlayson-Pitts, B. J.; Pitts, J. N., Jr., *Chemistry of the Upper and Lower Atmosphere: Theory, Experiments and Applications*. Academic Press: San Diego, CA, 2000.

5. Jacob, D. J.; Hoffmann, M. R. A Dynamic Model for the Production of H^+ NO_3^-, and SO_4^{2-} in Urban Fog. *Journal of Geophysical Research: Oceans* **1983,** *88*, 6611-6621.

6. Ganor, E.; Levin, Z.; Pardess, D. Determining the Acidity and Chemical Composition of Fog, Haze and Cloud Droplets in Israel. *Atmospheric Environment. Part A. General Topics* **1993,** *27*, 1821-1832.

7. Goldstein, I. F.; Weinstein, A. L. Air Pollution and Asthma: Effects of Exposures to Short-Term Sulfur Dioxide Peaks. *Environmental Research* **1986,** *40*, 332-345.

8. Neslen, A. Europe Escalates Action against Uk for Breaching Air Pollution Limits 06/02/2017. https://www.theguardian.com/environment/2017/feb/06/european-commission-escalates-action-uk-breaching-air-pollution-limits (accessed 23/02/2017).

9. Blitz, M. A.; Hughes, K. J.; Pilling, M. J. Determination of the High-Pressure Limiting Rate Coefficient and the Enthalpy of Reaction for $OH + SO_2$. *The Journal of Physical Chemistry A* **2003,** *107*, 1971-1978.

10. Blitz, M. A.; Salter, R. J.; Heard, D. E.; Seakins, P. W. An Experimental Study of the Kinetics of OH/OD(v = 1,2,3) + SO_2: The Limiting High-Pressure Rate Coefficients as a Function of Temperature. *The Journal of Physical Chemistry A* **2017,** *121*, 3175-3183.

11. Blitz, M. A.; Salter, R. J.; Heard, D. E.; Seakins, P. W. An Experimental and Master Equation Study of the Kinetics of OH/OD + SO_2: The Limiting High-Pressure Rate Coefficients. *The Journal of Physical Chemistry A* **2017,** *121*, 3184-3191.

12. Wine, P. H.; Thompson, R. J.; Ravishankara, A. R.; Semmes, D. H.; Gump, C. A.; Torabi, A.; Nicovich, J. M. Kinetics of the Reaction $OH + SO_2 + M \rightarrow HOSO_2 + M$. Temperature and Pressure Dependence in the Fall-Off Region. *The Journal of Physical Chemistry* **1984,** *88*, 2095-2104.

13. Long, B.; Bao, J. L.; Truhlar, D. G. Reaction of SO_2 with OH in the Atmosphere. *Physical Chemistry Chemical Physics* **2017,** *19*, 8091-8100.

14. Miriyala, V. M.; Bhasi, P.; Nhlabatsi, Z. P.; Sitha, S. Formation of a Pre-Reaction Hydrogen-Bonded Complex and Its Significance in the Potential Energy Surface of the $OH + SO_2 \rightarrow HOSO_2$ Reaction: A Computational Study. *Journal of Theoretical and Computational Chemistry* **2017,** *16*, 1750046.

15. Lee, Y. Y.; Kao, W. C.; Lee, Y. P. Kinetics of the Reaction $OH + SO_2$ in He, N_2, and O_2 at Low Pressure. *The Journal of Physical Chemistry* **1990,** *94*, 4535-4540.

16. Leu, M. T. Rate Constants for the Reaction of Hydroxyl with Sulfur Dioxide at Low Pressure. *The Journal of Physical Chemistry* **1982,** *86*, 4558-4562.

17. Martin, D.; Jourdain, J. L.; Le Bras, G. Discharge Flow Measurements of the Rate Constants for the Reaction $OH + SO_2 + He$ and $HOSO_2 + O_2$ in Relation with the Atmospheric Oxidation of Sulfur Dioxide. *The Journal of Physical Chemistry* **1986,** *90*, 4143-4147.

18. Paraskevopoulos, G.; Singleton, D. L.; Irwin, R. S. Rates of OH Radical Reactions. The Reaction $OH + SO_2 + N_2$. *Chemical Physics Letters* **1983,** *100*, 83-87.

19. Zhao, Y.; Truhlar, D. G. The M06 Suite of Density Functionals for Main Group Thermochemistry, Thermochemical Kinetics, Noncovalent Interactions, Excited States, and Transition Elements: Two New Functionals and Systematic Testing of Four M06-Class Functionals and 12 Other Functionals. *Theoretical Chemistry Accounts* **2008,** *120*, 215-241.

20. Dunning, T. H. Gaussian-Basis Sets for Use in Correlated Molecular Calculations .1. The Atoms Boron through Neon and Hydrogen. *Journal of Chemical Physics* **1989,** *90*, 1007-1023.

21. Kendall, R. A.; Dunning, T. H.; Harrison, R. J. Electron-Affinities of the 1st-Row Atoms Revisited - Systematic Basis-Sets and Wave-Functions. *Journal of Chemical Physics* **1992,** *96*, 6796-6806.

22. Woon, D. E.; Jr., T. H. D. Gaussian Basis Sets for Use in Correlated Molecular Calculations. III. The Atoms Aluminum through Argon. *J Chem Phys* **1993,** *98*, 1358-1371.

23. Peterson, K. A.; Woon, D. E.; Dunning, T. H. Benchmark Calculations with Correlated Molecular Wave Functions. IV. The Classical Barrier Height of the $H+H_2 \rightarrow H_2+H$ Reaction. *J Chem Phys* **1994,** *100*, 7410-7415.

24. Wilson, A. K.; van Mourik, T.; Dunning, T. H. Gaussian Basis Sets for Use in Correlated Molecular Calculations. Vi. Sextuple Zeta Correlation Consistent Basis Sets for Boron through Neon. *Journal of Molecular Structure: THEOCHEM* **1996,** *388*, 339-349.

25. Frisch, M. J. et al., Gaussian 09, Revision D.01. Wallingford CT, 2009.

26. Li, X. S.; Frisch, M. J. Energy-Represented Direct Inversion in the Iterative Subspace within a Hybrid Geometry Optimization Method. *Journal of Chemical Theory and Computation* **2006,** *2*, 835-839.

27. Raghavachari, K.; Trucks, G. W.; Pople, J. A.; Headgordon, M. A 5th-Order Perturbation Comparison of Electron Correlation Theories. *Chemical Physics Letters* **1989,** *157*, 479-483.

28. Sharma, S.; Raman, S.; Green, W. H. Intramolecular Hydrogen Migration in Alkylperoxy and Hydroperoxyalkylperoxy Radicals: Accurate Treatment of Hindered Rotors. *Journal of Physical Chemistry A* **2010,** *114*, 5689-5701.

29. Glowacki, D. R.; Liang, C. H.; Morley, C.; Pilling, M. J.; Robertson, S. H. MESMER: An Open-Source Master Equation Solver for Multi-Energy Well Reactions. *Journal of Physical Chemistry A* **2012,** *116*, 9545-9560.

30. Baer, T.; Hase, W. L., *Unimolecular Reaction Dynamics: Theory and Experiments*. Oxford University Press: 1996.

31. Somnitz, H. Quantum Chemical and Dynamical Characterization of the Reaction OH + SO_2 → $HOSO_2$ over an Extended Range of Temperature and Pressure. *Physical Chemistry Chemical Physics* **2004,** *6*, 3844-3851.

32. Smith, I. W. M. The Collision Dynamics of Vibrationally Excited Molecules. *Chemical Society Reviews* **1985,** *14*, 141-160.

33. Glowacki, D. R.; Reed, S. K.; Pilling, M. J.; Shalashilin, D. V.; Martinez-Nunez, E. Classical, Quantum and Statistical Simulations of Vibrationally Excited $HOSO_2$: IVR, Dissociation, and Implications for OH + SO_2 Kinetics at High Pressures. *Physical Chemistry Chemical Physics* **2009,** *11*, 963-974.

34. Blitz, M. A.; Hughes, K. J.; Pilling, M. J.; Robertson, S. H. Combined Experimental and Master Equation Investigation of the Multiwell Reaction $H+SO_2$. *Journal of Physical Chemistry A* **2006,** *110*, 2996-3009.

35. Shannon, R. J.; Blitz, M. A.; Goddard, A.; Heard, D. E. Accelerated Chemistry in the Reaction between the Hydroxyl Radical and Methanol at Interstellar Temperatures Facilitated by Tunnelling. *Nature Chemistry* **2013,** *5*, 745.

36. Effenhauser, C. S.; Felder, P.; Huber, J. R. Two-Photon Dissociation of Sulfur Dioxide at 248 and 308 nm. *Chemical Physics* **1990,** *142*, 311-320.

37. Blitz, M. A.; McKee, K. W.; Pilling, M. J. Temperature Dependence of the Reaction of OH with SO. *Proceedings of the Combustion Institute* **2000,** *28*, 2491-2497.

38. Blitz, M. A.; Green, N. J. B.; Shannon, R. J.; Pilling, M. J.; Seakins, P. W.; Western, C. M.; Robertson, S. H. Reanalysis of Rate Data for the Reaction $CH_3 + CH_3 \rightarrow C_2H_6$ Using Revised Cross Sections and a Linearized Second-Order Master Equation. *Journal of Physical Chemistry A* **2015,** *119*, 7668-7682.

39. Greenwald, E. E.; North, S. W.; Georgievskii, Y.; Klippenstein, S. J. A Two Transition State Model for Radical-Molecule Reactions: A Case Study of the Addition of OH to C_2H_4. *Journal of Physical Chemistry A* **2005,** *109*, 6031-6044.

Chapter 4. Kinetics of the Reaction of OH with Isoprene over a Wide Range of Temperatures and Pressures

Overview of the chapter

This chapter focuses on exploring the addition reaction of the hydroxyl radical to isoprene, C_5H_8, via laser flash photolysis (LFP). The OH radicals were monitored via laser induced fluorescence (LIF) over a wide range of temperature (298 - 794 K) and pressures of nitrogen ranging from 50 to 1670 Torr. Above 700 K, regeneration of OH from decomposition of the HOC_5H_8 adducts has been observed: the OH decays were no longer single exponentials and a more robust approach is required for a proper elucidation of the problem. Also, an abstraction mechanism is tentatively identified and its contribution to the measured kinetics is assessed.

A versatile and simple approach is applied to explore an important phenomenon in the atmospheric chemistry of alkenes: radical recycling from multiple intermediate species. This strategy relies on master equation calculations of the corresponding potential energy diagram, which were supported by *ab initio* calculations. The solution of the master equation (ME) calculations consisted of OH profiles which can be compared to experimental traces via their respective fits to an appropriate analytical equation. In the current study, a bi-exponential equation was used since is capable of incorporating not only the recycling rate coefficients but also competing irreversible losses of OH.

The literature data for the isoprene + OH reaction have been significantly extended with the results of the kinetic measurements presented in this chapter, which were also incorporated in a scientific paper published in 2018. Measurements undertaken using the new high pressure system described in Chapter 2 are used to complement the investigation.

4.1 INTRODUCTION

Biogenic sources are responsible for the great majority of the atmospheric emissions of volatile organic compounds (~1150 Tg C/yr), accounting for more than 90% of the total emissions.[1] Isoprene, C_5H_8, is the most abundant biogenic hydrocarbon emission.[2-3] It reacts rapidly with the OH radical (R1, $k_{298\ K} = 1.0 \times 10^{-10}$ cm^3 $molecule^{-1}$ s^{-1})[4] and can lead to significant local air quality issues in the presence of nitrogen oxides (NOx), via ozone formation.[5]

$$OH + C_5H_8 \rightarrow \text{Products} \qquad \text{R1}$$

In low NOx/high isoprene environments such as forests, it was expected that ambient [OH] would be low since there is a rapid loss route for OH with isoprene, but no obvious route for OH recycling. However, field campaigns in a variety of such environments which includes boreal forests[6], Mediterranean pine forests,[7] and rain forests[8-9] have measured surprisingly high concentrations of the hydroxyl radical, with discrepancies observed for the measured:modelled [OH] being up to 10:1.[8] These measurements suggest the existence of an efficient mechanism for OH regeneration; the implications of a higher concentration of ambient OH on the lifetime of methane, and therefore on radiative forcing, are important.[10]

Multiple mechanisms[11] describing OH production from $RO_2 + HO_2$ reactions[12] and epoxide formation from OH + isoprene-OH adducts[13] have been recently explored as attempts to explain the observed [OH] discrepancy. Even though these processes provide some enhancement of OH levels, they are incapable of significantly reducing the gap between measurement and model. At present, the most promising mechanism for OH regeneration is the Leuven Isoprene Mechanism, proposed by Peeters and co-workers.[14-15] Under low NOx conditions the OH-isoprene-O_2 radical formed in reactions R1-R2, can undergo radical-radical reactions, radical uptake or photolysis[16] combined as R3. Alternatively the peroxy radical can isomerize to form a hydroperoxycarbonyl (HPALD) species (R4) which can in turn photolyse to give OH (R5).

Alternatively the peroxy radical can react with O_2 directly to give a dihydroperoxycarbonyl (di-HPCARP) species (R6) that will subsequently decompose to form OH (R7).

$OH + C_5H_8 \rightarrow HOC_5H_8$ R1a

$HOC_5H_8 + O_2 \rightarrow HOC_5H_8O_2$ R2

$HOC_5H_8O_2 \rightarrow$ products R3

$HOC_5H_8O_2 \rightarrow HPALD + HO_2$, $HPALD + hv \rightarrow OH +$ products (R4,R5)

$HOC_5H_8O_2 + O_2 \rightarrow$ di-HPCARP $\rightarrow OH +$ products (R6,R7)

The original Leuven Isoprene Mechanism (LIM0)[14] appeared to fulfil the gap between field observations and models, but chamber studies[17] suggested that HPALD formation was being overestimated. Even though the revised LIM1 mechanism[15] is in better agreement with chamber measurements, the modelled HPALD photolysis does not provide enough OH to match model and experiment. However, the LIM1 mechanism does highlight another potential route to OH generation via the formation of dihydroperoxy carbonyl peroxy species (di-HPCARP). The LIM mechanisms have been compared with some chamber mechanisms,[17,18] but at present agreement is semi-qualitative at best. Part of the issue emerges from the unpredictability, potential competing processes and timescales of the chamber tests in general. Reactions generally occur on long timescales (minute/hour) at room temperature and it is difficult to rule out undesirable secondary or heterogeneous chemistry. Additionally, a NOx contribution to the observed chemistry cannot be eliminated in certain chambers.[19] The resulting product spectra can be complex and the discrimination of the components emerging from low NOx chemistry can be a difficult task. However, quantitative validation of the role of the LIM1 mechanism remains desirable given the significance of evaluating the HOx consumption in tropical zones. Chapter 6 of the thesis is focused on shedding light on the isoprene peroxy chemistry via numerical and Master Equation

modelling of LFP-LIF data and provides a critical assessment of the LIM1 mechanism.

An alternative experimental approach to chamber studies is to monitor OH recovery on millisecond timescales at higher temperatures utilizing direct methods.[20] Under these approaches, heterogeneous processes are diminished while NOx contributions can be rigorously eliminated. However, in order to favour the isomerization so that it is observable on the millisecond timescale, high temperatures are necessary. As a consequence, the use of elevated temperatures demands high oxygen concentrations to guarantee a significant $HOC_5H_8O_2$ concentration as reaction R2 reaches equilibrium. Quenching of the fluorescence signal at the resulting high pressures and concentrations of O_2 make conventional OH monitoring via laser induced fluorescence (LIF)[21] difficult. However, with the use of the recently developed high pressure instrument based on the FAGE technique, described in Chapter 2, such measurements are possible. OH temporal profiles become multi-exponential under the mentioned experimental conditions, with rapid preliminary OH loss via reaction R1 followed by OH recycling. The recycling manifests in the experimental traces as a visible change in the decay rate. Recycling parameters can be extracted from such profiles more accurately if the initial OH decay can be constrained to previously measured rate coefficient values for reaction R1, but little high temperature literature data were available prior to the current study, with no data above 420 K. The rate coefficient, k_1, falls monotonically over the range 250 – 420 K with increasing temperature, which is consistent with an addition process. The highest reported measurements are at 410 - 420 K.[22-24]

The bimolecular view of the Lindemann mechanism for pressure dependent processes presented in Chapter 2 is very useful for the understanding of the chemistry of the OH + isoprene reaction. At low temperatures, reaction R1 occurs by means of a pressure dependent addition mechanism to the terminal carbons (C_1 and C_4) due to a competition between the stabilization by collisions with the bath gas, M, and the dissociation of the chemically activated

HOC_5H_8 adduct ($HOC_5H_8^*$) back to reactants (R-1a). This predominant route is favoured by the formation of stabilized allylic radicals. At elevated temperatures (T > 700 K), a hydrogen abstraction from the methyl (R1b) which also forms an allylically stabilized radical, may contribute significantly.[25] Even though no previous studies of the abstraction channel of the isoprene + OH reaction are available, this mechanism has been explored for similar species.[25-26] For example, the reaction of 2-methylpropene, an alkene that contains both allylic and vinylic hydrogens, with OH radicals was investigated in the theoretical work by Sun and Law.[25] Their canonical variational transition-state theory calculations[27] suggest abstraction rate coefficients as fast as ~3.0×10^{-12} cm^3 $molecule^{-1}$ s^{-1} at 750 K.

$$OH + C_5H_8 \xleftrightarrow{M} HOC_5H_8 \qquad \text{(R1a,R–1a)}$$

$$OH + C_5H_8 \xrightarrow{k_{1b}} C_5H_7 + H_2O \qquad \text{(R1b)}$$

At high pressures, the rate limiting step is isoprene + OH association (R1a) and the high pressure limiting rate coefficient, k_1^∞, is equal to k_{1a}. For such a large system with a strongly bound adduct, the high pressure limit is reached at low absolute pressures. However, at elevated temperatures the dissociation back to reagents becomes competitive with collisional stabilization and the reaction can exhibit a pressure dependence. The equilibrium constant characterized by the competition between the adduct formation and unimolecular decomposition can be linked in terms of the thermodynamics of the system, as indicated in Equation E1.

$$\frac{k_{1a}}{k_{-1a}} = K = e^{-\frac{\Delta G^0}{RT}} \qquad \text{E1}$$

The previous work on the kinetics of the OH + isoprene reaction indicates excellent agreement. The IUPAC recommendation for the room temperature rate coefficient of 1.0×10^{-10} cm^3 $molecule^{-1}$ s^{-1} is reported with errors of ~15%.[4] The available measurements were undertaken via direct LFP methods

and also via the relative rate approach using different reference reactions. Even though the high pressure limit of reaction R1 appears to be reached at 50 – 100 Torr at room temperature, some controversy regarding the onset of the pressure independent region still remains. While Singh and Li[28] (1 – 3 Torr He), Chuong and Stevens[24] (2-6 Torr He) and Dillon *et al*.[29] (5 – 200 Torr N_2 and air) do not report a pressure dependence at such low pressures, two measurements from the same research group, McGivern *et al*.[30] (0.5 – 20 Torr Ar) and Park *et al*. (2 – 8 Torr Ar) tested positive for this dependence. No evidence of any role for the abstraction reaction at room temperature has been reported in these studies.

The work of Hynes and co-workers[31-32] appears as an exception to the general consensus on k_1^{∞}. They have carried out two studies on the isoprene + OH reaction, which included *in situ* measurements of isoprene concentrations, but the measured room temperature rate coefficient is approximately 20% lower than the IUPAC recommendation. The reason for the disagreement between the work of Hynes and co-workers and the other studies (a selection of which are presented in Table 1) is not fully elucidated, however, recent measurements of the isoprene absorption cross section by Dillon *et al*.[29] shed some light on the observed discrepancies.

The objectives of the work presented in this chapter are: (I) to further characterise the high pressure apparatus by comparison with the room temperature rate coefficient for the OH + isoprene reaction, (II) to generate new data on reaction R1 at the higher temperatures required to observe OH recycling on a millisecond timescale (450 - 794 K), (III) to experimentally define a value for the well depth of the HOC_5H_8 adduct via an innovative analytical approach based on ME calculations, (IV) to investigate whether there is evidence for OH abstraction from isoprene and finally (V) to use the MESMER programme[33] to compare previous measurements of reaction R1 obtained from the literature.[34]

4.2 METHODOLOGY

4.2.1 - Laser flash photolysis experiments with detection by laser induced Fluorescence (LFP-LIF)

Isolated kinetic studies for the reactions of isoprene with OH were performed with the use of laser flash photolysis and detection of OH radicals by laser-induced fluorescence (LFP-LIF)[35-36] using both a conventional low pressure pressures (p = 50 – 150 Torr) LFP-LIF instrument and a recently developed instrument, capable of operating at high pressures (~5 atm maximum pressure) and temperatures (~ 750K maximum temperature). Additional details on the operation of these apparatus can be found in the literature.[37] Experiments were carried out under conditions where OH was lost by a simple pseudo-first-order process and also at sufficiently high temperatures such that direct equilibration between OH/VOC and the OH-VOC adducts was observed. Such experiments provide strong constraints on the thermochemistry of the reactions.[38]

A mixture of OH precursor, H_2O_2 (50% (w/w) Sigma Aldrich), isoprene (Sigma Aldrich, >99%) and nitrogen bath gas were flowed through the reaction cell. OH radicals were generated along the flow tube by pulsed excimer laser (Lambda Physik, Compex 200) photolysis at 248 nm. Alternatively, a limited number of experiments implemented a YAG laser (Quantel, Q-smart laser) at 266 nm to generate OH radicals from H_2O_2 photolysis. These 266 nm experiments represent a good check to ensure the independence of the measured kinetics to the potential photolysis of isoprene.

In the high-pressure setup, isoprene/N_2 mixtures were manometrically made up in stainless steel high-pressure cylinders of 10 litres and left to mix 48 hours before use. In the low-pressure instrument, isoprene was prepared as a diluted mixture (~10%) in N_2 stored in 5 litre darkened bulbs. The concentration of isoprene in the reactor was determined by the composition of the isoprene/N_2 mixture, the flow rates measured with calibrated mass flow controllers, and the total pressure in the corresponding reactor.

As described in Chapter 2, while the high pressure instrument employs a low-pressure detection cell, in the conventional LFP-LIF instrument the flowing gas is probed within the reaction cell. In both cases, OH is interrogated by a pulsed beam from a Spectron dye laser operating on the dye rhodamine, pumped by a YAG laser. Experiments were typically performed with a repetition rate of 5 Hz, although checks were undertaken to ensure the observed kinetics were independent of this rate. As another instrumental check, tertiary-butyl hydroperoxide was used as the OH precursor in a limited number of measurements at 298 K to verify whether the measured coefficients are independent of the implemented precursor.

Proton-transfer reaction time of flight mass spectrometry (Kore Technology, Series I PTR-TOF-MS), was implemented for a tentative detection of the product of the allylic hydrogen abstraction during a few experiments. For this purpose, the exhaust gas from the high pressure apparatus was vented to atmospheric pressure and subsequently sampled into the PTR-TOF-MS spectrometer.

As indicated previously, all the analysis presented in this thesis relies to some degree on Master Equation modelling. These calculations require information about the species involved, including vibrational frequencies, rotational constants and relative potential energies. This information was obtained via theoretical computations, and the main details of the calculations are presented below, prior to a discussion of the measured rate coefficients.

4.2.2 - Computational Methods: *Ab initio* Calculations and Master Equation (ME) Modelling

Structures of reactants and products were computed with the modern DFT functional M06-2X[39] and a large basis set (6-311++G(3df,2p)).[40] Structure optimizations were carried out using the Gaussian 09 D.01 programme suite[41], with the use of analytical gradients and the Berny algorithm[42-43] in redundant internal coordinates. High performance coupled cluster calculations with single, double and triple excitations, the latter treated perturbatively (CCSD(T)),[44] were implemented to calculate single point energies of M06-2X/6-311++G(3df,2p) optimized geometries. For a more accurate evaluation of the potential energy surface (PES), the single point energies were extrapolated to the complete basis set limit (CBS) using the extrapolation scheme presented by Helgaker *et al.*[45] and Truhlar's calendar basis sets (Jun-cc-pV*X*Z, X=D,T,Q).[46-47] These basis set variations are constructed by removing diffuse functions from the analogue fully augmented basis set (aug-cc-pV*X*Z). More specifically, the Jun-cc-pV*X*Z basis sets remove the diffuse functions from H and He atoms and also remove the highest angular momentum diffuse functions from all the other atoms. A slight deviation from the original formulation of the calendar basis sets is considered by Gaussian 09 since by default, s and p diffuse functions are always introduced. In the extrapolation scheme presented by Helgaker *et al.*, the Hartree-Fock (HF) and the correlation energies are extrapolated separately, according to equations E2 and E3. The employed Hartree-Fock extrapolation scheme was originally presented by Feller *et al.*[48]

$$HF(X)=HF_{CBS} + b\times\exp(-cX) \qquad \text{E2}$$

$$E_{CORR}(X)=E_{CORR(CBS)} + \alpha X^{-3} \qquad \text{E3}$$

where $HF(X)$ is the Hartree-Fock energy calculated with the jun-cc-pV*X*Z basis set. X is the cardinal number for the corresponding basis set (2=D, 3=T, 4=Q). The CBS limit extrapolated Hartree-Fock energy (HF_{CBS}), b and c are parameters obtained from solving the 3×3 system of HF equations. $E_{CORR}(X)$ is the correlation energy calculated at the CCSD(T)/Jun-cc-pV*X*Z level of theory.

$E_{CORR(CBS)}$ corresponds to the CBS limit correlation energy and α is a floated parameter.

Zero-point energies, force-constant matrices, vibrational frequencies and rotational constants, required inputs for the ME calculations were computed at the M06-2X/6-311++G(3df,2p) level as expensive CCSD(T) calculations would be computationally prohibitive.[49] However, the use of the M06-2X functional coupled with an extensive basis set has been considered appropriate for the study of the isoprene + OH reaction in the presence of O_2[15], and the photolysis of important products of this reaction, such as HPALDs.[50] Harmonic vibrational frequencies were corrected with a scaling factor of 0.983, following the recommendation for a similar methodology (M06-2X/6-311++G(d,p)).[51] The calculated enthalpies of reaction with respect to the OH additions to carbons C_1 and C_4, presented in section 4.4.1, were used for a comparison with experimental determinations presented in section 4.4.5.

The approximation of the harmonic oscillator was used for the majority of the vibrational frequencies in the calculation of the densities of states. However, due to the structures of the stabilized allylic radicals, a few vibrational frequencies of isoprene, and the resulting adducts, are better represented by the hindered rotor approximation. For example, the $>C_1=C_2<$ double bond in the isoprene structure has a single-bond analogue in the product structure, which provides an augmented torsional degree of freedom to the molecule, with respect to this bond. Figure 4.1 shows all the torsions that were described with the hindered rotor approximation for both isoprene and the two most stable isoprene-OH adducts considered in the analysis. The descriptions of these hindered rotors were obtained through 360° relaxed scans of the dihedral angle respective to the specific rotation, with steps of 15°. Restricted optimizations at the M06-2X/6-311++G(3df,2p) level were applied at each step. In order to avoid inconsistencies in the number of degrees of freedom of species in the ME calculations, the description of a hindered rotor requires the removal of a corresponding vibrational frequency. MESMER uses the projection method proposed by Sharma *et al*.[52] to define the mode related to the internal rotation.

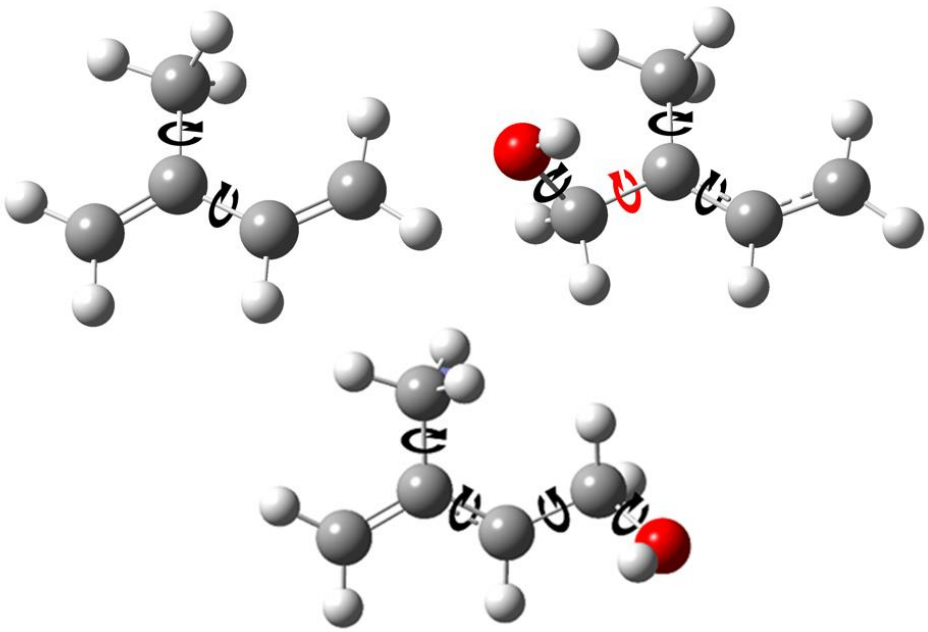

Figure 4.1 - The rotational torsions described with the hindered rotor approximation (curved arrows) for isoprene (top left), the isoprene-OH adduct 1 (top right) and the adduct rising from OH addition to carbon 4 (bottom). Grey, red and white spheres represent carbon, oxygen and hydrogen atoms respectively. The structure of the higher energy adducts formed following OH addition at carbons 2 and 3 are presented as Cartesian coordinates in Appendix 3. The hindered rotor potential for the rotational torsion of adduct 1 depicted with a red curved arrow is presented in Figure 4.2.

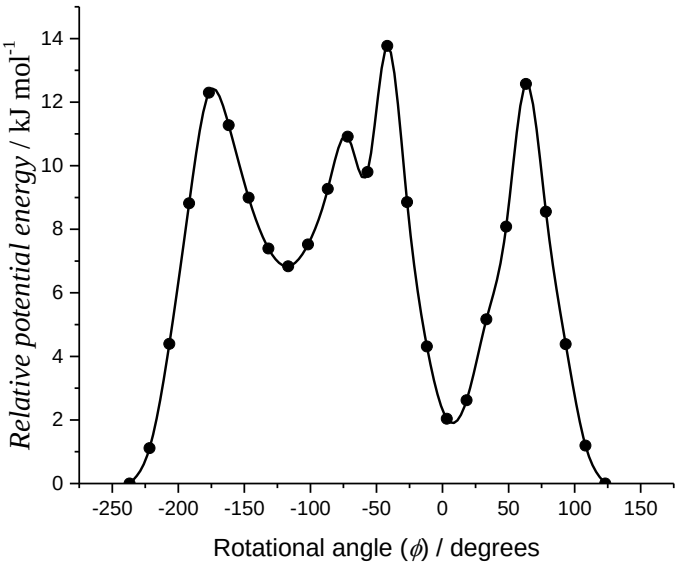

Figure 4.2 – The hindered rotor potential for the rotational torsion indicated by a red curved arrow in Figure 4.1. The energies are relative to that of the lowest energy conformer (ϕ = 123.2°), whose image is presented in Figure 4.1 and Cartesian coordinates are available in Appendix 3.

4.3 DATA ANALYSIS

4.3.1 - Single Exponential Traces

At temperatures below 650 K, OH reacted under pseudo-first-order conditions via a simple removal process; in this regime, the concentration of OH as a function of time is given by:

$$[OH]_t = [OH]_0 e^{-k_1' t} \qquad \text{E4}$$

where k_1' is the pseudo-first-order rate coefficient given by:

$$k_1' = k_1[C_5H_8] + k_{1st} \qquad \text{E5}$$

Here k_1 is the bimolecular rate coefficient for reaction R1 and k_{1st} represents the rate coefficient for the loss processes due to diffusion and reaction of OH with the constant concentration of precursor, k_p. As the OH LIF signal is proportional to [OH], the [OH] in E4 can be replaced by the OH LIF signal and the resulting exponential fit (inset to Figure 4.3) to the LIF data, returns k_1'. Under these conditions, a plot of k_1' *vs* $[C_5H_8]$ should give a straight line, as shown in Figure 4.3, where the gradient is k_1 and the intercept is the sum of the first order loss processes. The resulting k_1 rate coefficients are summarised in Table 4.1, where N_2 was implemented as the bath gas for all measurements.

Table 4.1 - Experimental Determinations of k_1 from Single Exponential Decays

T / K	p / Torr	$k_1 \times 10^{11}$ / cm^3 molecule^{-1} s^{-1} [a]	T / K	p / Torr	$k_1 \times 10^{11}$ / cm^3 molecule^{-1} s^{-1} [a]
298	1290	9.90 ± 0.14	473	99	4.98 ± 0.36
298	1365	10.01 ± 0.12	475	1394	5.61 ± 0.50
298	96[b]	10.60 ± 0.36	477	128	5.3 ± 1.0
298	56	10.40 ± 0.32	478	114	6.12 ± 0.36
337	57	8.28 ± 0.22	508	1673	5.7 ± 1.2
406	1367	6.68 ± 0.54	533	132	4.91 ± 0.24
417	1497	7.2 ± 1.6	540	141	5.27 ± 0.36
418	1418	6.24 ± 0.34	564	1350	4.74 ± 0.44
426	103	5.56 ± 0.26	573	51	4.4 ± 1.1
433	1546	6.0 ± 1.5	618	1536	3.99 ± 0.46
472	99	5.81 ± 0.86	630	1373	4.71 ± 0.56

a – Errors are 2σ. b – Data where p<150 Torr were recorded on the low pressure, conventional LFP/LIF apparatus. Other data were from the high pressure apparatus.

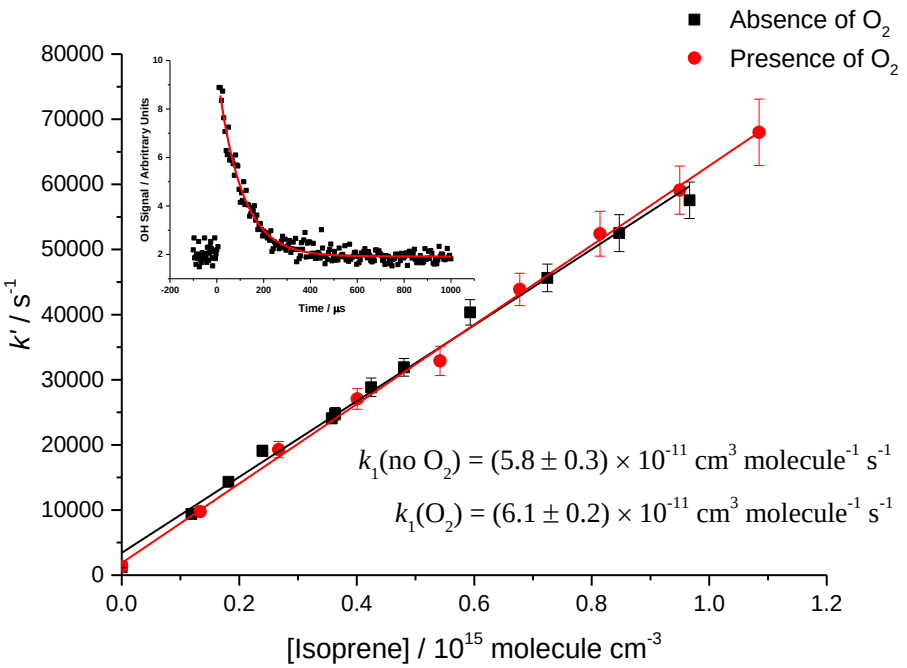

Figure 4.3 - Bimolecular plot for Reaction 1 at T = 406 K and p = 2 atm of N_2. The inset shows a typical single exponential decay, generated with $[C_5H_8]$ = 1.00 × 10^{14} molecule cm^{-3} and $[O_2]$ = 7.70 × 10^{18} molecule cm^{-3}. The points presented in the inset were averaged after 4 scans. Error bars and uncertainties in the bimolecular plot are at the 2σ level. Red circles represent data acquired in the presence of oxygen and black squares represent data in absence of O_2.

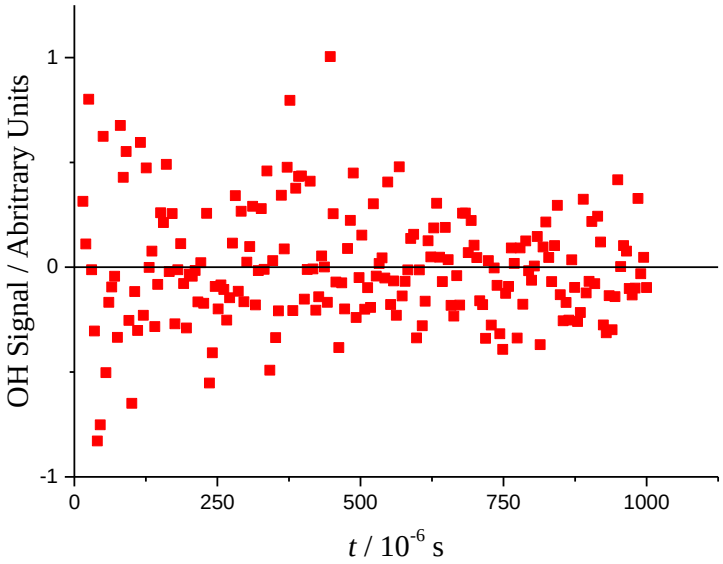

Figure 4.4 – Residual plot for the single exponential fit of trace presented in Figure 4.3 at T = 406 K and p = 2 atm of N_2, $[C_5H_8]$ = 1.00 × 10^{14} molecule cm^{-3} and $[O_2]$ = 7.70 × 10^{18} molecule cm^{-3}.

The bimolecular rate coefficients included in Figure 4.3 show that, considering the uncertainties, no significant difference is observed with the addition of O_2 to the system. Furthermore, the small errors evidence the good quality of experimental data collected for this work.

4.3.2 - High Temperature Equilibrium Traces

At high enough temperatures (T >700 K), the rates of decomposition of the OH-C_5H_8 adducts (R-1a) become comparable with that of the forward addition of OH to isoprene and the OH decays become multi-exponential in nature (see Figure 4.5 for an example). The obtained equilibrium traces were analysed by fitting to the chemical scheme S4.1:

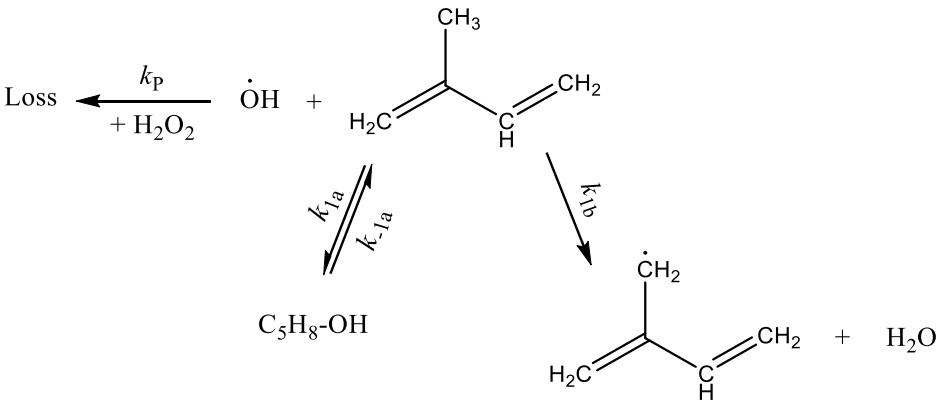

S4.1

where C_5H_8-OH represents the OH-isoprene adducts. As will be reported in section 4.4.4, additions to the C_2 and C_3 carbons are negligible and can be ignored. A kinetic scheme incorporating two adducts would be a tri-exponential decay, but if the properties of the adducts are similar, then the decays can be well approximated by a biexponential decay. As expected, the experimental data were not better fitted with a tri-exponential equation, so our data were analysed based on models derived from Scheme S1; the role of both adducts 1 and 4 is assessed via MESMER modelling in Section 4.4.

The analytical solution of the temporal evolution of the OH concentration in scheme S4.1 is described by the bi-exponential equation E6:

$$OH(t)=OH_0\left(\frac{-k'_{OH}-\lambda_-}{\lambda_+-\lambda_-}\left(\exp(\lambda_+ t)-\exp(\lambda_- t)\right)+\exp(\lambda_- t)\right)+b \qquad \text{E6}$$

where $\lambda_{-,+}=\frac{-(k'_{OH}+k_3)\pm\sqrt{(k'_{OH}+k_3)^2-4(k'_{OH}k_3-k'_{1a}\times k_{-1a})}}{2}$, $k'_{OH}=k'_{1a}+k'_D$, and $k_3=k_{-1a}$. k'_{1a} is the pseudo-first order rate coefficient for the addition channel of reaction R1, k'_D is the sum of the pseudo-first order OH losses besides addition, $k_D = k_{1st} + k_{1b}'$, where k_{1st} is the sum of the OH reaction with the precursor ($k_p[H_2O_2]$) and diffusion, (which is small compared to $k_p[H_2O_2]$). k'_{1b} is the rate coefficient of the hydrogen abstraction channel of reaction R1 and is equal to $k_{1b}[C_5H_8]$. b is equal to the signal when no OH is present. For each temperature and pressure, k_{1st} was measured prior to the OH-trace acquisition with added isoprene; k_{1st} was fixed to its measured value in the data fitting procedure. b was determined for each trace by recording points before time zero.

Over the temperature range 729 – 794 K, a total of 28 traces were recorded that exhibited equilibrium behaviour. Figure 4.5 clearly demonstrates non-single exponential behaviour at 729 K and 130 Torr of N_2. The red line is a fit using equation E6 to the data, and as can be seen, it provides an excellent description of OH temporal behaviour. From equation E6, λ_+ is the numerically larger reciprocal time constant and is approximately equal to k'_1 and the smaller reciprocal time constant, λ_-, is approximately equal to $k_D + k'_{1b}$. In Figure 4.5, the green line is the significantly poorer fit when the abstraction channel, k'_{1b}, is set to zero. It is evident that abstraction, or some other loss process, is required in order to describe the chemistry of the system; this abstraction channel is discussed in Sections 4.4.3 and 4.4.4. Therefore, the parameters k_{1a}, k_{-1a} and k_{1b} along with the initial OH signal are required to provide a good fit to the data

In order to reliably determine the parameters, all the equilibrium traces were simultaneously analysed via a global non-linear multi-temperature least-squares fit procedure, using the OriginPro 2016 software.[53] For the global

fitting, the addition rate coefficient as a function of temperature was assigned the flexible function:

$$k_{1a}(T) = A_{1a}\,(T/298)^{n} \qquad \text{E7}$$

where k_{1a} was fixed to the room temperature value, 1.0×10^{-10} cm^3 molecule^{-1} s^{-1}. Both the adduct dissociation and the abstraction rate coefficients can be parameterized by Arrhenius expressions:

$$k_{-1a}(T) = A_{-1a} \times \exp(-E_{-1a} / RT) \qquad \text{E8}$$

$$k_{1b}(T) = A_{1b} \times \exp(-E_{1b} / RT) \qquad \text{E9}$$

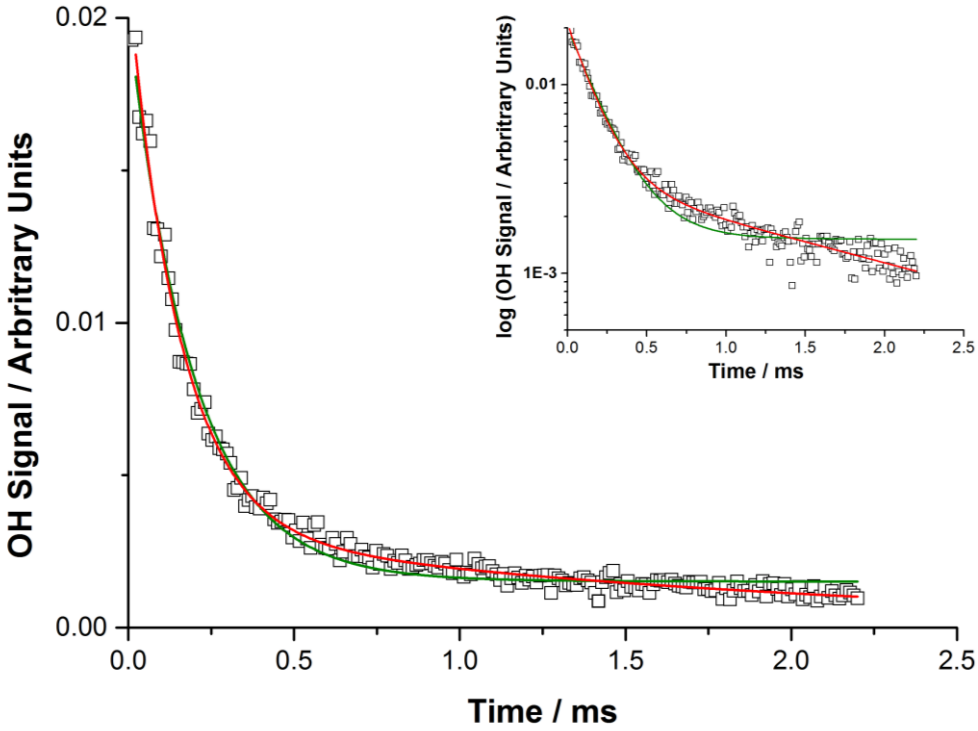

Figure 4.5 - Example of a non-exponential trace acquired at T = 729 K, p = 130 Torr N_2 and [isoprene] = 2.3×10^{14} molecule cm^{-3}. The inset shows the same decay trace with a logarithmic scale for the OH signal. The long-time decay of OH shows that there is a significant process by which OH is lost from the system (modelled as k_{1b}). The green lines shows fits of equation E7 to the data where the abstraction was suppressed and the red lines represent fits where the abstraction was considered.

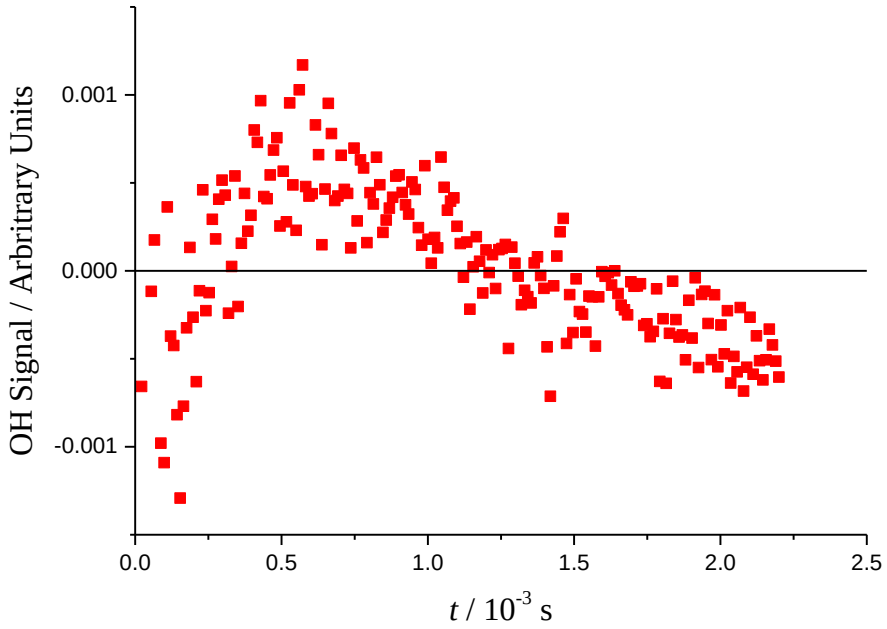

Figure 4.6 - Residual plot of the green fit presented in Figure 4.5, where the contribution of the competing hydrogen abstraction is supressed from the model.

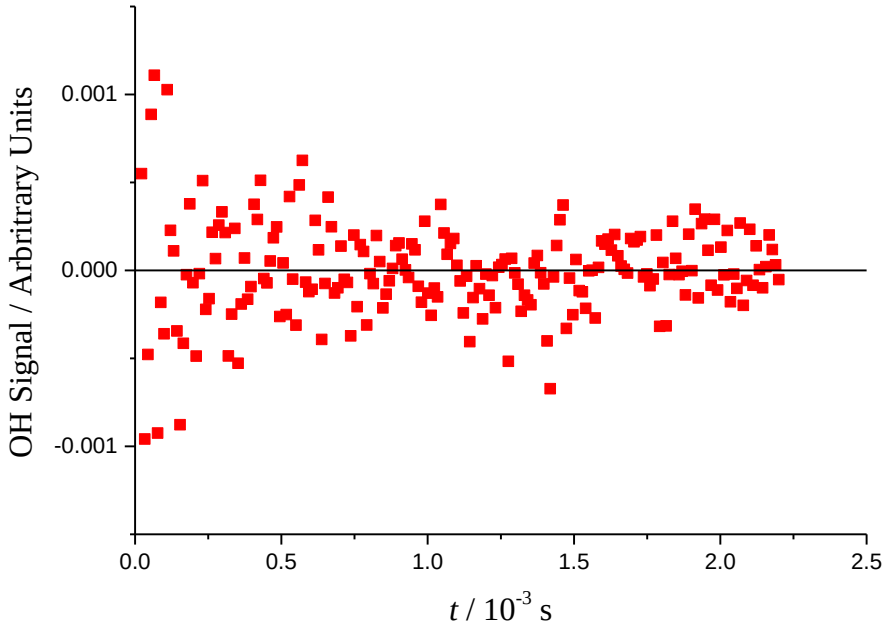

Figure 4.7 – Residual plot of the red fit presented in Figure 4.5, where the contribution of the competing hydrogen abstraction is included in the model.

However, the temperature range is too small for both Arrhenius parameters to be uniquely defined. Therefore, A_{-1a} was fixed to 10^{13} s^{-1} and E_{1b} was fixed to 3.6 kJ mol^{-1}, the theoretical value calculated in this study, see Section 4.4.1.

Other fixed Arrhenius values could have been chosen but they would all generate, within error, the same values for $k_{-1a}(T)$ and $k_{1b}(T)$ over the experimental temperature range. Therefore, only three rate coefficient parameters, plus the initial OH signal were adjusted in this global analysis. The results are summarized in Table 4.2. Examples of global analysis fits to the data are shown in Figure 4.8. The Arrhenius parameterization allows global fits over a range of temperatures, but primarily generates values of $k_{-1a}(T)$ to input into the MESMER analysis (section 4.4.4). It is these rate coefficients, not the Arrhenius parameters, which are used to define the well depth in Section 4.4.4.

Table 4.2 - Experimental conditions, number of OH + C_5H_8 ⇌ HOC_5H_8 equilibrium traces and obtained rate coefficients

T / K	p / Torr	[isoprene] / 10^{14} molecule cm^{-3}	OH Loss /s^{-1}	Number of traces	$k_{1a} \times 10^{11}$ / cm^3 molecule^{-1} s^{-1}	k_{-1a} / s^{-1}	$k_{1b} \times 10^{12}$ / cm^3 molecule^{-1} s^{-1}
729	100	1.3-5.0	100	6	1.77 ± 0.74	990 ± 870	6.94 ± 2.77
729	130	1.6-6.0	220	6	1.77 ± 0.74	990 ± 870	6.94 ± 2.77
766	120	0.5-3.9	80	9	1.61 ± 0.68	3000 ± 2600	7.14 ± 2.78
794	100	1.2-5.0	110	7	1.50 ± 0.63	6500 ± 5500	7.29 ± 2.79

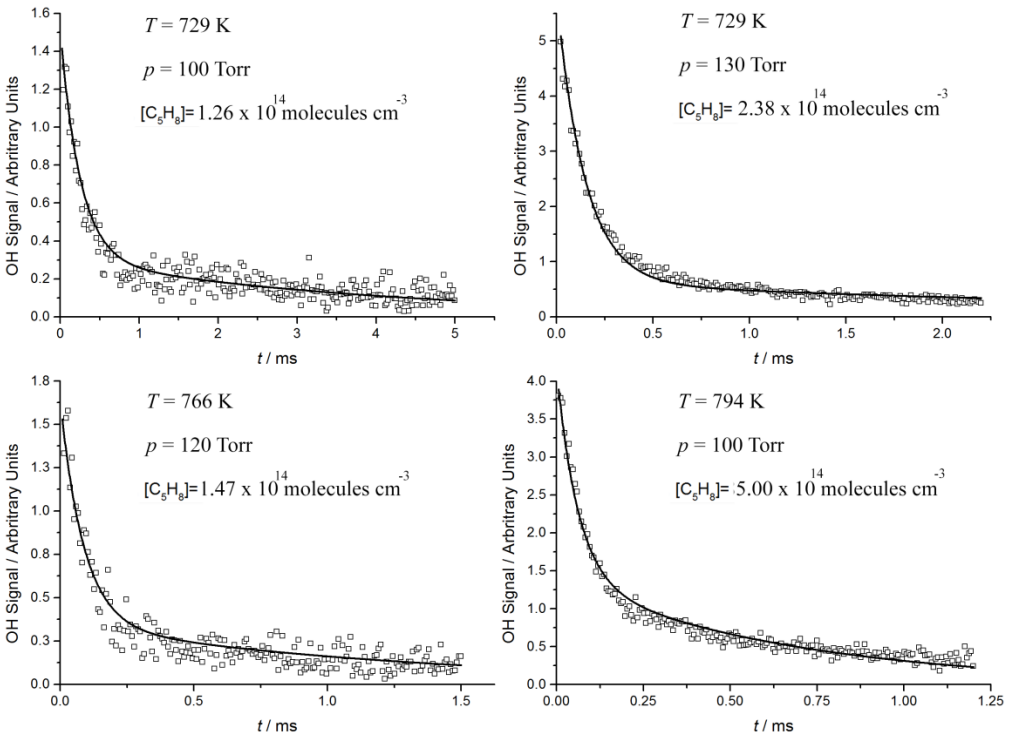

Figure 4.8 - Examples of fits of non-exponential traces acquired at T >725 K and p ~ 100 Torr.

4.4 RESULTS AND DISCUSSION

4.4.1 - *Ab initio* calculations

Figure 4.9 shows the potential energy surface for OH addition and H-abstraction from isoprene at the CCSD(T)/CBS//M06-2X/6-311++G(3df,2p) level of theory. OH addition to C_2 or C_3 carbons produces adducts with significantly higher energies as there is no allylic stabilization of the resulting radicals. The energy difference between the C_1 and C_4 adducts is approximately 10 kJ mol^{-1} (in good agreement with previous literature, see Table 4.3) and small compared to the total well depth. Whilst Table 3 shows that there is some variation in the absolute well-depths from various *ab initio* calculations, the energy difference between the two lowest energy adducts is very consistent at (10.1 ± 0.4) kJ mol^{-1}. In the subsequent MESMER analysis assessing the role of both adducts, the energy difference is fixed to our calculated value (10.1 kJ mol^{-1}), but the absolute well depth of the C_1 adduct is allowed to float. The barrier for the abstraction reaction is calculated to be 3.6 kJ mol^{-1}.

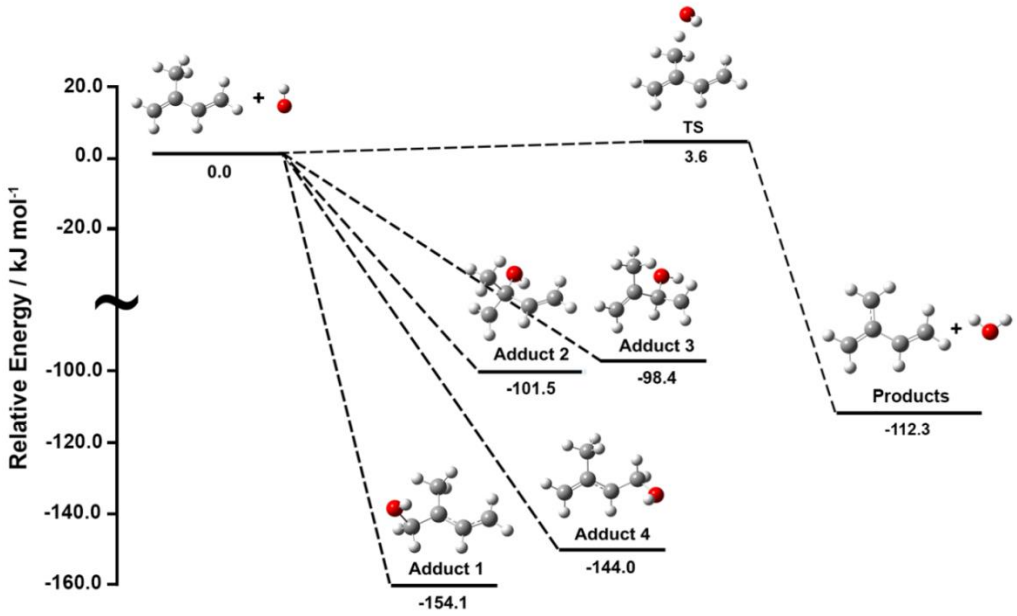

Figure 4.9 - The potential energy diagram for the OH addition to isoprene. Relative energies were calculated at the CCSD(T)/CBS//M06-2X/6-311++G(3df,2p) level and include zero-point energy corrections.

Table 4.3 - Theoretically calculated well-depths for the isoprene + OH reaction with respect to the additions at carbons 1 and 4. All well-depths are corrected for zero-point energies

Methodology	Reference	Well-depth adduct C_1 / kJ mol^{-1}	Well-depth adduct C_4 / kJ mol^{-1}	Energy Difference between adducts/ kJ mol^{-1}
CCSD(T)/CBS//M06-2X/6-311++G(3df,2p)	This work	154.1	144.0	10.1
CCSD(T)/6-311G**// B3LYP/6-31G	Lei *et al.*[54]	145.6	135.1	10.5
roQCISD(T)/6-31++G**// B3LYP/6-311++G**	Greenwald *et al.*[55]	156.1 [a]	146.4	9.7
PMP4-(SDTQ)/6-311G**// MP2/6-311G**+ΔZPE/ B3LYP/6-31G**	Stevens *et al.*[56]	158.6	148.1	10.5
CBS-APNO	Peeters *et al.*[14]	163.2	153.6	9.6

a –including basis set correction at the roMP2 level of theory

The CCSD(T) method implemented in this work is known for accurately computing molecular properties and energies[44, 49, 57] and is often referred to as "Gold Standard" of computational chemistry.[58] Our calculated well-depth differs from that obtained by Lei *et al.*[54] by 8.5 kJ mol^{-1}, who have implemented a similar methodology. The use of smaller basis sets for the calculations of single point energies and structural optimizations as a computational constraint (6-311G** [59-66] and 6-31G[64, 67-75] respectively) contributes to the observed well-depth discrepancy. London dispersion forces which are accounted for at the M06-2X level, and neglected by the B3LYP [76-79] functional also contribute to the discrepancy.

Greenwald *et al.*[55], have applied the restricted open-shell quadratic configuration interaction (CI) technique, with perturbative triple excitations[44, 80] to study the isomeric branching of the isoprene + OH reaction. In this correlated method, quadratic terms are included in the configuration coefficients to correct for size consistency. The authors have done a very

careful study when obtaining the stationary structures of the four possible isoprene-OH adducts. They have located 58 different local minima for the adducts at the B3LYP/6-311++G** level, and implemented the lowest energy conformations in subsequent roQCISD(T) computations. The roQCISD(T)/6-31++G**// B3LYP/6-311++G** methodology was validated against previous calculations on the ethylene-OH case, where the well-depth was calculated to within ~3.35 kJ mol^{-1}.[55, 81] They also report that the relative well-depths obtained at the PMP4(SDTQ)/6-311G**// B3LYP/6-311++G** level of theory are qualitatively aligned with those computed at the superior roQCISD(T)/6-31++G**//B3LYP/6-311++G** level.

Stevens *et al.*[56] have used the less computationally demanding fourth-order Møller-Plesset perturbation theory with single, double, triple and quadruple excitations and spin projection (PMP4(SDTQ)) to investigate the OH addition to isoprene. In the Møller-Plesset perturbation theory, the Hartree-Fock wavefunction is corrected for electron correlation by a combination with configurational functions, originated from single, double, triple, etc. excitations.[82-83] In their study, PMP4(SDTQ)/6-311G** single point energies computed for MP2/6-311G** optimized structures were subsequently corrected with zero-point energies calculated at the B3LYP/6-31G** level. Their calculations show a well-depth only 2.51 kJ mol^{-1} deeper than that reported by Greenwald *et al.*

Peeters *et al*. have employed the Complete Basis Set method CBS-APNO[84] to compute electronic energies while investigating the regeneration of HO_x in the oxidation of isoprene.[14] The authors have verified that the CBS-APNO method systematically overestimated the well-depth of the CH_2=CH–$\dot{C}H_2$ + O_2 and for this reason, a correction of 4.18 kJ mol^{-1} has been applied. This fact suggests that the reported isoprene + OH well-depth might also be slightly overestimated by the CBS-APNO method.

4.4.2 - Rate Coefficients for the OH + Isoprene Reaction, R1

Figure 4.3 shows an example of a typical experimental decay (inset) and bimolecular plot obtained at 406 K and 2 atm of nitrogen bath gas. Checks were carried out to ensure that the rate coefficients were invariant (within experimental error) of laser energy density (15 – 50 mJ cm^{-2}) or repetition rate (1 – 10 Hz). Below 400 K, the addition of oxygen had no effect on the measured rate coefficient for reaction R1 as can be seen from Figure 4.3. Experiments in the presence of oxygen at temperatures > 450 K, where OH recycling was observed, will be presented in a subsequent chapter focused on the validation of the LIM1 mechanism.

A major issue when sampling the monitored species prior to detection, is whether the transit time from the sampling pinhole to detection influences the kinetic measurements.[21, 85-87] In this study room temperature pseudo-first-order rate coefficients of up to 70,000 s^{-1} are in excellent agreement with the literature data. At higher first order rate coefficients, the influence of transport can be observed, but can potentially be accounted for with a biexponential analysis.[85] None of the measurements reported in this study required such corrections, i.e. transport is effectively instantaneous on the timescales of the chemical reaction. The analysis of the exponential decays is inset a few points to allow for the ~20 μs transport time.

Figure 4.10 illustrates the observed temperature dependence of k_1 from 298 – 794 K. In addition to varying the temperature, the pressure was also varied to ensure that measurements were always being made at the high pressure limit, i.e. that the observed bimolecular rate coefficients correspond to k_1^{∞}. No evidence for any pressure dependence was observed from 50 – 1670 Torr for the 298 – 650 K temperature range and these observations were consistent with the modelling discussed in the subsequent sections. Measurements performed at $T \geq 725$ K and p ~100 Torr are located in the fall-off region. For example, at 794 K, with $k_{1a,\,794K} = (1.50 \pm 0.63) \times 10^{-11}$ cm^3 $molecule^{-1}$ s^{-1}, our measurements are ~40% lower than our best estimate for k_{1a}^{∞} at that temperature (2.49×10^{-11} cm^3 $molecule^{-1}$ s^{-1}). Excellent agreement is observed

between the measurements performed with the high and low-pressure instruments, as evidenced by the proximity of the black and blue triangles in Figure 4.10.

A least-squares fit to the combined experimental data from both apparatus of the form $k_1^{\infty} = \mathrm{A}\,(\frac{T}{298\ \mathrm{K}})^{-n}$ gives:

$$k_1^{\infty} = (10.4 \pm 0.4) \times 10^{-11} \left(\frac{T}{298\ \mathrm{K}}\right)^{-1.34 \pm 0.12} \ \mathrm{cm^3\ molecule^{-1}\ s^{-1}} \qquad \text{E10}$$

where errors are at the 2σ level. The negative temperature dependence is consistent with previous literature and is dominated by the addition reaction; however, this work considerably extends the range of temperatures studied. A full discussion on the values of k_1 is presented in Section 4.5.

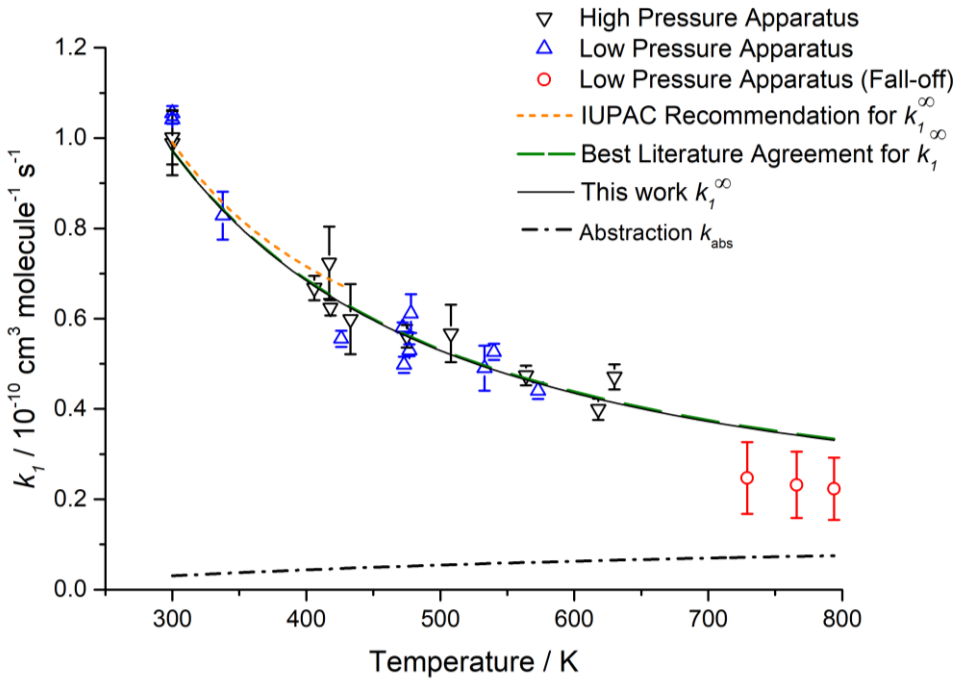

Figure 4.10 - Comparison of experimental measurements using the high pressure instrument (black squares), measurements at the high pressure limit with a conventional low-pressure instrument (blue triangles) and at the fall-off region (red circles). The dotted line shows the IUPAC recommendation for the temperature dependence of the isoprene + OH reaction, the dashed line shows our best estimate for the high-pressure limit k_1^{∞}, which was obtained from a ME from this work and selected data as will be discussed in section 4.4.5. The continuous line represents k_1^{∞} as obtained based purely on our measurements. Errors are statistical at the 2σ level.

As can be seen from Table 4.4, the room temperature rate coefficients for reaction R1 are in excellent agreement with the IUPAC recommendation and the bulk of the experimental literature providing evidence that the new apparatus works well and can generate reliable rate coefficients.

Table 4.4 - Comparison of Experimental Determinations of k_1

Author/date	Technique	Conditions	$10^{10}k_1$/cm^3 molecule^{-1} s^{-1} at 298 K	$k_1(T)$/ cm^3 molecule^{-1} s^{-1}
This work	LFP[a] – high pressure OH detection	T = 298–630 K p = 1290–1670 Torr	0.99 ± 0.09	$(9.4 \pm 0.2) \times 10^{-11} \left(\frac{T}{298\ K}\right)^{-1.28 \pm 0.71} + (1.3 \pm 0.6) \times 10^{-11} \exp\left(\frac{-3.61\ kJ\ mol^{-1}}{RT}\right)$ b $(9.7 \pm 0.8) \times 10^{-11} \left(\frac{T}{298\ K}\right)^{-1.10 \pm 0.20}$ c $(2.0 \pm 0.2) \times 10^{-11} \exp\left(\frac{480 \pm 58}{T}\right)$ c
This work	LFP/LIF	T = 298–794 K p = 50–140 Torr	1.06 ± 0.02 (t-butOOH) 1.04 ± 0.02 (H_2O_2)	$(9.6 \pm 0.2) \times 10^{-11} \left(\frac{T}{298\ K}\right)^{-1.39 \pm 0.56} + (1.3 \pm 0.6) \times 10^{-11} \exp\left(\frac{-3.61\ kJ\ mol^{-1}}{RT}\right)$ b $(10.5 \pm 0.4) \times 10^{-11} \left(\frac{T}{298\ K}\right)^{-1.38 \pm 0.12}$ c* $(1.8 \pm 0.1) \times 10^{-11} \exp\left(\frac{527 \pm 20}{T}\right)$ c*
This work	LFP/LIF[d] Combined data	T = 298–794 K p = 50–1670 Torr	n/a	$(9.5 \pm 1.2) \times 10^{-11} \left(\frac{T}{298\ K}\right)^{-1.33 \pm 0.32} + (1.3 \pm 0.6) \times 10^{-11} \exp\left(\frac{-3.61\ kJ\ mol^{-1}}{RT}\right)$ b $(10.4 \pm 0.4) \times 10^{-11} \left(\frac{T}{298\ K}\right)^{-1.34 \pm 0.12}$ c* $(1.8 \pm 0.2) \times 10^{-11} \exp\left(\frac{522 \pm 28}{T}\right)$ c*
IUPAC[4] (2013)	Review	n/a	1.00 ± 0.15	$2.7\times10^{-11} \exp(390\pm100/T)$
Atkinson and Aschmann[88] (1984)	RR[e]	T = 295 K p = 760 Torr air	1.02 ± 0.04	
Atkinson *et al.*[89] (1982)	RR	T = 299 K p = 735 Torr air	1.00 ± 0.05	
Campuzano-Jost *et al.* [31] (2000)	LFP/LIF	T = 251–342 K p = 60–600 Torr	0.856 ± 0.026	$2.7\times10^{-11} \exp((336\pm74)/T)$
Campuzano-Jost *et al.* [32] (2004)	LFP/LIF	T = 251–342 K p = 60–600 Torr	0.847 ± 0.059	$2.68\times10^{-11} \exp((348\pm136)/T)$
Chuong and Stevens[24] (2000)	DF[f]/LIF	T = 300–423 K p = 2–6 Torr He	1.10 ± 0.04	n/a

Chuong and Stevens (2002)[90]	DF/LIF	T = 300 K p = 100-150 Torr Ar	1.08 ± 0.05	
Dillon *et al.*[91] (2017)	LFP/LIF	T = 241–356 K p = 5–200 Torr (N_2 or air)	0.93 ± 0.04	$(1.93\pm0.08)\times10^{-11}\exp((446\pm12)/T)$
Edney *et al.*[92] (1986)	RR	T = 297 K p = 1 atm air	1.01 ± 0.02	
Gill and Hites[93] (2002)	RR	T = 298–363 K p = 1 atm He	1.01 ± 0.19	$2.54\times10^{-11}\exp((409\pm42)/T)$
Hites and Turner[23] (2009)	RR/MS[g]	T = 323–413 K p = 1 atm	n/a	$4.0\times10^{-11}\exp((249\pm20)/T)$
Iida *et al.*[94] (2002)	RR	T = 298 K p = 760 Torr air	1.04 ± 0.04	
Karl *et al.*[95] (2004)	GC / LIF[h]	T = 294 K p = 760 Torr air	1.00 ± 0.12	
Kleindienst *et al.*[22] (1982)	FP/RF	T = 297– 23 K p = 50–200 Torr Ar	0.93 ± 0.15	$2.36\times10^{-11}\exp((409\pm28)/T)$
McGivern *et al.*[30] (2000)	LFP/LIF	T = 295 K p = 0.5–20 Torr Ar	0.99 ± 0.05	
McQuaid *et al.*[96] (2002)	RR	T = 298 K p = 760 Torr air	1.11 ± 0.23	
Ohta [97] (1983)	RR	T = 297 K p = 760 Torr air	0.990 ± 0.027	
Park *et al.*[98] (2004)	LFP/LIF	T = 279 – 336 K p = 1-8 Torr	1.08 ± 0.19	$(3.49\pm0.46)\times10^{-11}\exp((366\pm40)/T)$
Poppe *et al.*[99] (2007)	LIF / MS / GC[h]	T = 295 K p = 760 Torr	1.02 ± 0.09	
Singh and Li[28] (2007)	RR/DF/ MS	T = 240 – 340 p = 1-3 Torr He	1.04 ± 0.19	$2.3\times10^{-11}\exp((444\pm27)/T)$

Vimal *et al.*[100] (2008)	DF / RF / LIF	T = 300 – 363 K p = 2 –5 Torr He	1.02 ± 0.06	
Zhang *et al.*[101] (2001)	DF / MS	T = 298 K p = 1.9 Torr He	9.1	
Zhang *et al.*[102] (2000)	DF / MS	T = 298 K p = 70–120 Torr N_2	1.01 ± 0.08	

* – Measurements in the fall-off region (729 -794 K) were previously corrected to the high-pressure limit via Master Equation modelling. a – LFP = laser flash photolysis, b – Obtained from a Master Equation fit using the Trust region reflective algorithm[103], c – Obtained from a simple non-linear least squares fit, d – LIF = laser induced fluorescence, e – RR = relative rate methodology RF = Resonance fluorescence, f – DF = discharge flow, g – MS = mass spectrometric detection, h – Chamber study where rate coefficients were fitted with experimental modelling. Uncertainties reported at 2σ for our data.

4.4.3 - The Abstraction Channel R1b

From Figure 4.5, the fact that the green line fit (no abstraction) to the data is a much worse fit than the red line fit (with abstraction) is a strong evidence that there is another loss process for OH in reaction R1. Abstraction is invoked to explain this behaviour as it is has been observed in many other OH + alkene reactions and our calculations predict an abstraction barrier consistent with both our observations and those of other studies, see below. A good example is the reaction between OH and C_2H_4, where the abstraction becomes measurably significant above 650 K, and is characterized with a (24.9 ± 1.2) kJ mol^{-1} barrier to abstraction.[104-105] This reaction will be used as a test case in Chapter 5, where a new analysis method based on modifications to the ME transition matrix is presented. When compared to the ethylene case, the barrier to H-abstraction at the CH_3 group in the present system is expected to be much lower as the electron delocalization of the resulting allylic radical, C_5H_7, leads to resonant stabilization, absent in the ethylene case.

The energy barrier of the allylic H abstraction from isoprene was theoretically explored with the aid of the Gaussian 09 D.01 software at the CCSD(T)/CBS//M06-2X/6-311++G(3df,2p) level of theory (see Figure 4.9). The calculated energetic barrier is equal to 3.6 kJ mol^{-1}, consistent with an allylic abstraction having a lower barrier than a vinylic abstraction. As evidenced from the red line fit to the data in Figure 4.5, incorporation of abstraction, k_{1b}, produces good fits to the experimental kinetic traces (also see global analysis traces, Figure 4.8). Abstraction reactions with barriers can be described using an Arrhenius description, and in the analysis of the equilibrium kinetic data - see Section 4.3.2 - the abstraction rate coefficient, k_{1b}, was modelled with equation E11. It was noted that over the temperature range of the experiments k_{1b} and E_{1b} were not uniquely pinpointed; many sets of Arrhenius parameters could reproduce k_{1b}. Therefore, in this data analysis E_{1b} was fixed to our theoretical value, 3.6 kJ mol^{-1}, and returned:

$$k_{1b} = (1.3 \pm 0.6) \times 10^{-11} \exp\left(\frac{-(3.6 \pm 3.5)\ \text{kJ mol}^{-1}}{RT}\right) \text{cm}^3\ \text{molecule}^{-1}\ \text{s}^{-1}. \qquad \text{E11}$$

This fixed value of E_{1b} provided the best fit to the data, but it is acknowledged other combinations of Arrhenius parameters can also provide an equal fit to the data. As an exercise, E_{1b} was floated, but bounded very close to our calculated value, so that essentially, the value is unchanged. The returned uncertainty of 3.5 kJ mol^{-1} (2σ) provides an estimate of how well E_{1b} is known. Using E11, k_1 can be divided up into k_{1a} and k_{1b} for all the temperatures carried out in this study. Summaries of k_{1a} and k_{1b} are given in the Appendix 3, in Tables A3.2 and A3.3.

While it is acknowledged that there are significant errors in extrapolating E11 to room temperature, the results suggest that ~3 ± 2% of the R1 occurs via abstraction at 298 K, $k_{1b}(298\ \text{K}) = 3.1 \times 10^{-12}$ cm^3 molecule^{-1} s^{-1}. Atkinson *et al*. have predicted negligible hydrogen abstraction from the OH + isoprene reaction at room temperature, with an estimate for the upper limit of the branching ratio of 1%.[106] However, the ability of previous experiments to observe abstraction were probably not any better than 5%, so the present estimate of ~3 ± 2% does not contradict previous studies. It is noted that OH abstraction from 3-methyl-1-butene has been verified in a chamber study[107] and product analysis reveals that the allylic H abstraction accounts for 5-10% of the overall OH reaction. Also, while no previous study has observed abstraction via R1, studies on the isoprene + Cl reaction indicate significant abstraction at room temperature (~15%).[108] The stable product of Cl abstraction at the CH_3 site, 2-methylene-3-butenal, was tentatively identified via atmospheric pressure ionization mass spectrometry.[108]

In our high pressure apparatus, the total pressure is considerably greater than 1 atmosphere. This means that it is straightforward to exhaust the reaction gas mixture from our time-resolved experiments into the proton-transfer mass spectrometer, where the stable products can be analysed; the transfer time is a few seconds. The peak related to the mass of 2-methylene-3-butenal (m/z = 83) was monitored in the 298-473 K temperature range, in the presence of [O_2] (>

1×10^{18} molecule cm^{-3}) to promote the oxidation of the potential allylic radical formed upon H abstraction. Figure 4.11 shows the variation of the *m/z* = 83 peak at room temperature, before and after the excimer laser is fired (5 Hz). Both the spectra were collected in the presence of H_2O_2, which means that when the laser is fired, the isoprene + OH chemistry is initiated. The observed promotion of peak *m/z* = 83 when the laser is fired corroborates the occurrence of abstraction via the allylic hydrogen. The promotion was also verified to be independent of isoprene concentration, which indicates that photolysis of isoprene is unlikely to be causing the observed effect.

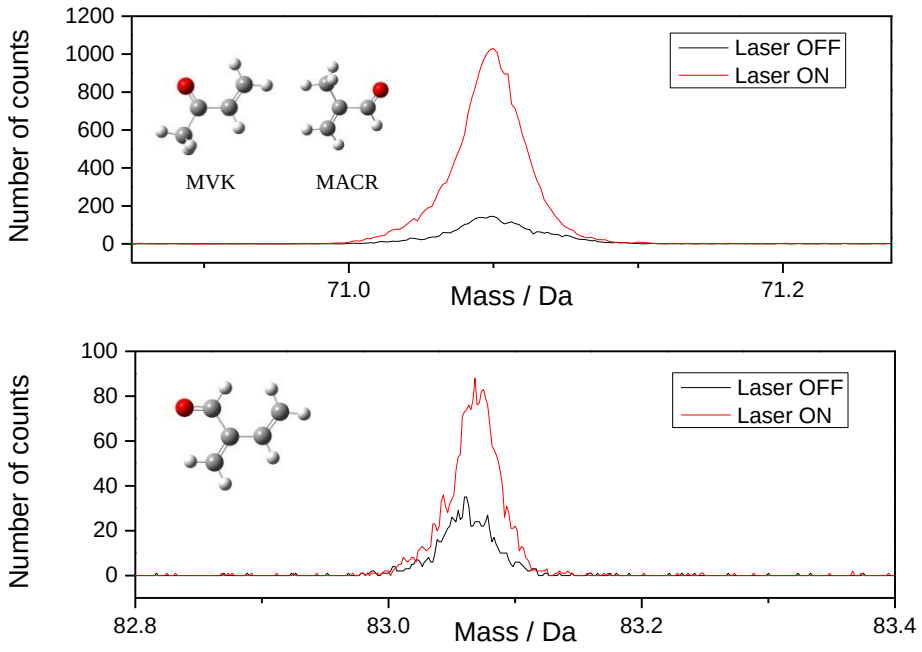

Figure 4.11 - The change in the *m/z* = 71 and *m/z* = 83 Da peaks at room temperature when the excimer laser is OFF (black line, no OH radicals generated) and ON (red line). $[C_5H_8]$ = 5.3 × 10^{13} molecule cm^{-3}, $[O_2]$ = 1.2 × 10^{19} molecule cm^{-3}, T = 298 K, p = 1200 Torr. The mass m/z = 71 Da peak corresponds to methyl vinyl ketone (MVK) and methacrolein (MACR, 2-methylprop-2-enal) and the peak m/z = 83 corresponds to 2-methylene-3-butenal.

The stable products of the addition channel, R1a, in the presence of O_2 are expected to be methyl vinyl ketone and methacrolein, formed via $HOC_5H_8O_2$ self-reaction.[109] These products have identical mass and were observed with the proton-transfer mass spectrometer (m/z = 71) in much larger amounts compared to 2-methylene-3-butenal, see Figure 4.11. This result is evidence of

direct abstraction, R1b, that is small, but not negligible at room temperature. The ratio of the peak areas ($a_{m/z}$ = 83 / $a_{m/z}$ = 71) ~ 0.07, is consistent with the reduced abstraction branching ratio if one assumes the molecules to have similar PTR-TOF-MS sensitivities. The fact that the laser on:off ratios are different for the different masses is justified by the fact that while the $a_{m/z}$ = 83 signal is, in absolute terms, about an order of magnitude smaller than the $a_{m/z}$ = 71 one. Therefore, the background signal represents a larger portion of the area under the red line for the $a_{m/z}$ = 83 signal.

4.4.4 - Interpretation of OH + Isoprene ⇄ Adducts Equilibria

The isoprene molecule has four potential sites of OH addition as illustrated in Figure 4.9, however, a two-adduct model was adopted in the ME calculations. Additions to the terminal carbons are believed to be dominant since they lead to the formation of stabilized allylic radicals.[110] Additions at C_1 and C_4, which account together for more than 90% of the total additions[98, 110] were therefore selected for implementation in our analysis. A ME calculation including the four possible additions reveals that the equilibrium fractions of the radicals generated from additions to carbons 2 and 3, together, account for less than 0.1% at 729 K. The significant equilibrium fractions of adducts 1 and 4 (~65% and ~35% respectively) justifies why in the analysis only these two adducts are considered.

In the analysis of the experimental data, see Section 4.3.2, only one well was considered when determining the adduct dissociation rate coefficient, ($k_{-1a,expt}$). However, the current ME model considers two adducts (1 and 4) leading to the calculation of two individual recycling coefficients, corresponding to the decomposition of each intermediate being modelled. This creates a problem: how to compare these two modelled recycling coefficients with an experimental one obtained via a bi-exponential fit? Formally speaking, the two adduct model leads to tri-exponential theoretical OH decays, but is was verified that to a very good approximation these decays can be modelled by a biexponential equation, and when fitted with equation E6 yields $k_{-1a,calc}$. In the analysis, the parameters of the ME are adjusted in order that $k_{-1a,calc}$ best fits k_{-}

$_{1a,expt}$. This analysis means that both adducts are considered but tests reveal that if the ME analysis had only considered adduct 1, the returned HOC_5H_8 binding energy would not increase much, being approximately 2 kJ mol^{-1} greater.

The unimolecular coefficients $k_{-1a,expt}$ (see Table 4.2) were used to characterize the well-depths of the isoprene + OH reaction with the aid of the computational ME solver package MESMER[33] and the numerical computing suite MATLAB R2016a [111] via the Trust Region Reflective Algorithm[103]. The logic is as follows: the ME was solved at the temperature and pressure of the experiments and generated an OH vs time profile, OH(t). This OH(t) was then passed to MATLAB where it is fitted to using equation E6, thus determining the calculated overall coefficient $k_{-1a,calc}$. The parameters of the ME - binding energy, energy transfer for each bath gas M ($A_{<\Delta E>d,M}$) and $k_1^{\infty}(T)$ were then adjusted by MATLAB in order to best fit $k_{-1a,calc}$ to $k_{-1a,expt}$, by minimizing the least-squares difference (χ^2). The results are given in Table 4.5. In this analysis the well-depths for adducts 1 and 4 were adjusted in unison, maintaining their constant 10.1 kJ mol^{-1} difference, see Table 4.3. In the following discussion of the binding energy only adduct 1 is reported, as the energy of adduct 4 is simply 10.1 kJ mol^{-1} higher.

Parameters obtained from a ME fit are dependent on the description of the molecular parameters (rotors, bends and vibrations) of the species involved in the reaction scheme. For example, the returned parameters are sensitive to the density of states of the reagents and adducts. This effect is evident when a vibration-only model is compared to a system where ten small harmonic vibrational frequencies of the reactants and products ($\leq$ 350 cm^{-1}) are replaced by the hindered rotor approximation (see Figure 4.1). The returned well-depth for addition at carbon 1 when the hindered rotors are used, (153.5 ± 6.2) kJ mol^{-1}, is in excellent agreement with the theoretically calculated value at the CCSD(T)/CBS//M06-2X/6-311++G(3df,2p) level (154.1 kJ mol^{-1}). However, the well-depth obtained with a less realistic vibration-only description of the system is significantly deeper, (166.5 ± 7.0) kJ mol^{-1}. Differences between our experimentally determined well-depth and

theoretical values obtained at the different levels of theory presented range from 0.6 to 9.7 kJ mol^{-1}. Our best estimate of the binding energy, based purely on the measurements of this work is (153.5 ± 6.2) kJ mol^{-1} and is given in Table 4.5.

Table 4.5 - Comparison of Experimental and calculated $k_{-1a.}$ Uncertainty at 1σ.

T / K	$k_{-1a,expt}$ / s^{-1}	$k_{-1a,calc}$ / s^{-1}	Adduct 1 Well-depth / kJ mol^{-1}
729	990 ± 870	1180	153.5 ± 6.2
766	3000 ± 2600	3160	
794	6500 ± 5500	6000	

The importance of the allylic hydrogen abstraction in the returned well-depths has also been explored in this investigation. If direct abstraction is neglected, then a unimolecular loss from the generic adduct presented in scheme S1 needs to be invoked (R8) to account for the slope observed at longer times of the equilibrium traces:

$$C_5H_8\text{-}OH \xrightarrow{k_R} \text{Loss} \qquad \text{(R8)}$$

From Scheme S4.1, the solution is now given by $k_3 = k_{-1a} + k_R$, where the slope of the slow decay of the equilibrium traces, λ_-, is approximately equal to k_R. If the abstraction route is supressed, i.e. $k_{1b} = 0$, k_R can provide an equally good fit to the data, but this reaction scheme skews k_{-1a}, which is the crucial parameter required to assign the binding energy of the adduct, C_5H_8-OH. For instance, at the highest temperature, 794 K, the value of k_{-1a} from Table 4.5 is 6500 ± 5500 s^{-1}. However, if the highest temperature data are analysed with k_R, the returned value for k_{-1a} is 4810 ± 4200 s^{-1}. This lower values of k_{-1a} increases the binding energy of the adduct by 3.8 kJ mol^{-1}. Even though it is acknowledged that the experimental observations can be equally described using k_R, there is no evidence for R8. Our theoretical calculations have identified the direct abstraction channel, R1b, see Figure 4.9. In addition, R8 predicts negligible abstraction at room temperature but R1b predicts 3%; our proton transfer mass spectrometer observes the abstraction product at room temperature, see Figure 4.11 and Section 4.4.3. Therefore, the direct abstraction channel, R1b, is the favoured explanation of the slow decay, λ_-.

Potential interference from radical-radical reactions ($R+O_2$ does not happen to any extent at these high temperatures) could also contribute to OH loss from the equilibrium system, but is considered unlikely using the following reasoning. The typical precursor concentration employed in the more sensitive equilibrium experiments (~1×10^{14} molecule cm^{-3}, calculated from OH removal in the absence of isoprene), the laser energy density (~15 mJ cm^{-2} or ~2×10^{16} photons cm^{-2}), the precursor cross-section (~1×10^{-19} cm^2 $molecule^{-1}$ for H_2O_2) and the quantum yield, (2 for OH production from H_2O_2) is ~ 4×10^{11} molecule cm^{-3}. If R + R is equal to 10^{-10} cm^3 $molecule^{-1}$ s^{-1} (upper limit) then this implies a k_{1b} ~40 s^{-1}, which is much lower than experimentally observed k_{1b}. In some experiments with varying [OH] but similar [C_5H_8] and temperature, no significant change in the kinetic parameters were observed. Additionally, at T = 766 K the photolysis wavelength was changed to 266 nm (fourth harmonic from Quantel, Q-smart laser, ~ 10 mJ / pulse). Any minor photolysis of isoprene at 248 nm that could contribute to the radical pool and hence secondary chemistry, will be significantly reduced with this longer wavelength photolysis. The 266 nm data are wholly consistent with the other data, which is further evidence that little additional chemistry is occurring, other than that given by scheme S1.

4.4.5 - Master Equation Modelling and Comparison with Literature

In this section the master equation modelling package MESMER, described previously, has been used to compare various experimental values of k_1 with a particular emphasis in determining the onset of pressure dependence. The complete data set of temperature and pressure dependent rate coefficients (187 values) from the references in Table 4.4 were fitted with the aid of MATLAB R2016a via the Trust Region Reflective Algorithm, in an analogous procedure to that described in the previous section. The only difference in the analysis that now MESMER also returns the forward isoprene + OH rate coefficients (k_{1a}) to MATLAB. A 10% uncertainty was assigned for all the rate coefficients considered in this analysis. The fitting parameters were: the adduct well depth, $A_{<\Delta E>d,M}$ for the relevant bath gases used, and the high pressure limiting values of $A_{1a,\,C1}$, $A_{1a,\,C4}$ and n in the same format as equation E7. The pre-exponential

factors for additions to carbons 1 and 4 were linked to maintain their constant ratio ($A_{1a,\ C1}$ / $A_{1a,\ C4}$ ~ 1.5).[30] The vibrational and rotational constants of isoprene and the OH-C_5H_8 adducts were calculated at the M06-2X/6-311++G(3df,2p) level of theory. Lennard Jones parameters were obtained from the work of Dibble *et al*.[112] and Lei *et al*.[54] A comparison of the complete experimental and fitted data is shown in Figure 4.12 and the resulting parameters are presented in Table 4.6.

The proximity of most data points to the y = x line is expected from the IUPAC evaluation, where most studies are in excellent agreement. Three studies clearly stand out from the trend from this quantitative analysis; the low pressure measurements of Chuong and Stevens using discharge flow with OH detection by LIF, McGivern *et al*. using laser flash photolysis and LIF detection and the higher pressure LFP/LIF studies of Campuzano-Jost *et al*. Both of the low pressure measurements have been superseded by further, higher pressure measurements from the same research groups[90, 98, 101] which are in good agreement with the IUPAC evaluation and the y = x line of this comparison. However, other low pressure, discharge flow/LIF studies from Stevens' group, Vimal *et al*.[100], at 363 K point to some potentially interesting properties of the OH/isoprene system in comparison to OH/butadiene at low pressures. Over the pressure range of 1-6 Torr of helium at 363 K, the OH + isoprene reaction is reported to show some pressure dependence (as does the study of Singh and Li under similar conditions), however, under identical conditions, the reactions of OH with the smaller butadiene and 1-butene molecules (which would be expected to demonstrate greater fall-off behaviour), show no pressure dependence. Vimal *et al*.[100] used molecular dynamics simulations to investigate whether differences in the mechanism of internal energy distribution in isoprene and 1,3-butadiene could explain the lack of pressure dependence in 1,3 butadiene. Although their calculations suggested differences in the mechanisms of IVR between the two compounds, they reported that further studies were required to identify whether such differences in IVR mechanisms could account for the varying pressure

dependence. Our ME simulations suggest that at 363 K, the high-pressure limit should be reached at 0.4 Torr of He.

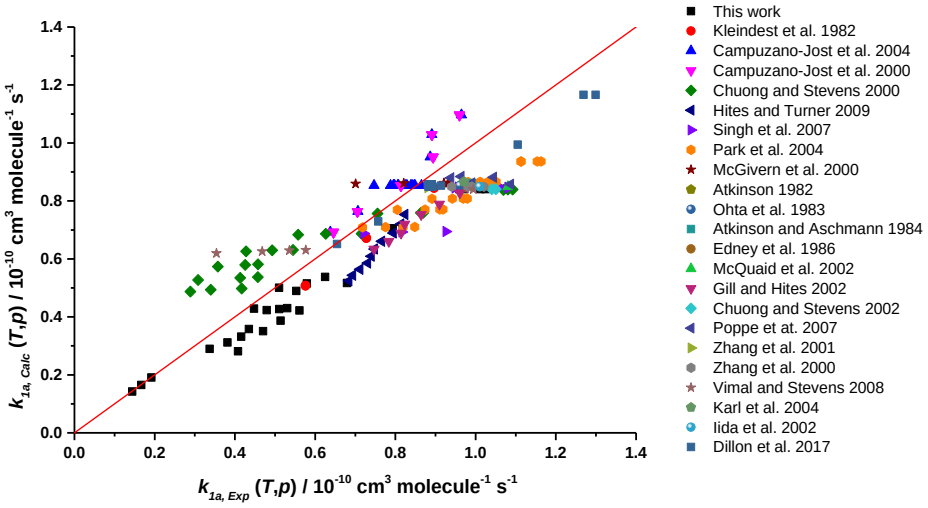

Figure 4.12 - Correlation plot for experimental data points from all the data in Table 3 and the calculated rate coefficients generated by MESMER by allowing the well-depth, $A_{<\Delta E>d,M}$, A and n to be floated. The resulting parameters are shown in the second column of Table 4.6.

The work of Singh and Li [28] reports a pressure dependence of k_1 at 340 K over the 1 – 3 Torr pressure range of He. Their equivalent measurements of k_{1a}^{∞} at 1 and 2 Torr ((7.21 ± 0.65) × 10^{-11} and 8.16 × 10^{-11} cm^3 molecule^{-1} s^{-1} respectively, corrected for abstraction with equation E11) are in good agreement with the set of selected studies presented previously, with ME predicted values of 7.92 × 10^{-11} and 7.98 × 10^{-11} cm^3 molecule^{-1} s^{-1} respectively. However, the rate coefficient measured at 3 Torr (9.26 × 10^{-11} cm^3 molecule^{-1} s^{-1}) is ~16% higher than the current calculations predict (8.00 × 10^{-11} cm^3 molecule^{-1} s^{-1}). The simulations suggest that, in helium at 340 K, the high-pressure limit should be reached at 0.2 Torr.

It is not easy to explain the discrepancy between the Campuzano-Jost *et al.*[31-32] values and the remaining studies; Campuzano-Jost *et al.* recognised, but were

unable to rationalize, the difference in their value of k_1 and other literature data. A number of checks were carried out by Campuzano-Jost *et al*. but they were unable to identify the origin of the discrepancy. Given the high value of the rate coefficient k_1, it is very unlikely that radical-radical processes could influence the OH decays and the invariance of the rate coefficients with photolysis laser power suggests such secondary chemistry plays no role in OH decays. Rate coefficients lower than the expected value can be an indication of recycling reactions,[113-114] but the invariance of our measured rate coefficients at low temperatures with large concentrations of oxygen at least rules out oxygen leaks as a possible route to OH recycling in the Campuzano-Jost *et al*. experiments. Given the good agreement in the temperature dependence of k_1 with other measurements, the simplest explanation is some systematic error in determining isoprene concentrations in the reaction cell. That explanation is supported by the recent studies of Dillon *et al*.[91] who determined UV absorption cross sections for isoprene which are approximately 10% greater than those of Campuzano-Jost *et al*. and in good agreement with another determination by Martins *et al*.[115] Dillon *et al*. re-evaluated the Campuzano-Jost data using their new cross sections, generally bringing the Campuzano-Jost *et al*. data in closer agreement to the IUPAC evaluation.

Removing the data sets from Campuzano-Jost *et al*., Chuong and Stevens, Vimal *et al*. and McGivern *et al*. produces a much better fit (as shown in Figure 4.13 and Table 4.6) with χ^2 being reduced from 601.34 (~3.22 per point) for the complete data set to 56.53 for the selected data set of 115 data points (~0.49 per point). χ^2 =0.49 implies that the data is on average within 6% of the fitted value. The resulting best fit parameters in the form of E8 are $A_{1a} = 9.52 \times 10^{-11}$ cm^3 molecule^{-1} s^{-1} and $n_{1a}^{\infty} = -1.39$. Studies represented in Figure 4.13 are the preferred ones (including this work), and are referred to as 'Selected Data'.

The returned parameters from the fittings where uncertainties were assigned as 10% of the measured coefficients are summarised in Table 4.6. It contains the returned parameters from considering the complete dataset and the selected

data. While the k_{1a} data at high temperatures, where equilibria is observed, has much larger than 10% error, it is consistent with the selected data, under this 10% error criteria.

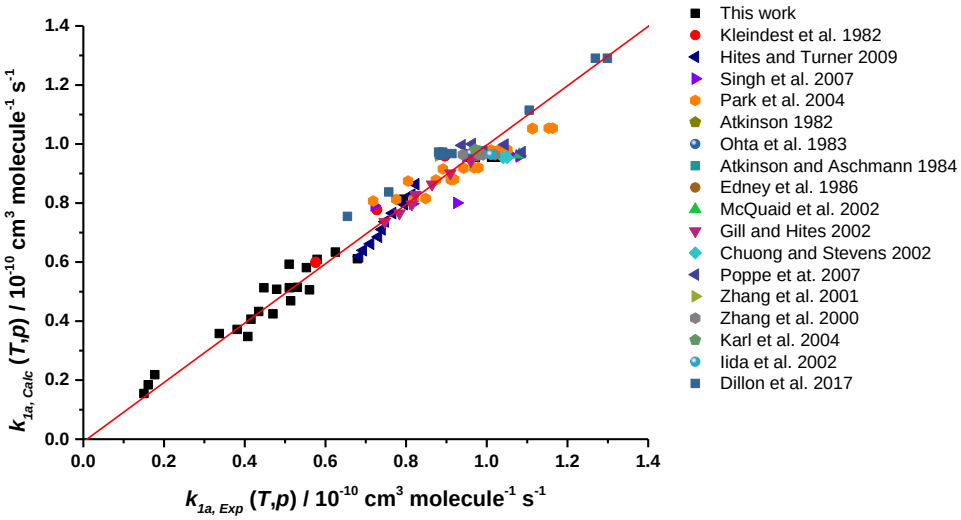

Figure 4.13 - Correlation plot for experimental data points from selected data in Table 4 (see text) and the calculated rate coefficients generated by MESMER by allowing the well-depth, $A_{<\Delta E>d,M}$, A and n to be floated. The resulting parameters are shown in the 'selected data' column of Table 4.6.

The returned well-depth is virtually unaffected by which data are used as the well depth is almost exclusively determined by the high temperature data in this study. The other parameters associated with the fit: $A_{<\Delta E>d,M}$, A_{1a} and n_{1a} are more dependent on the data set used. For each dataset used, fitted parameters are reported with either all possibilities of $A_{<\Delta E>d,M}$ floated or with some fixed. Varying the degree of flexibility in fitting $A_{<\Delta E>d,M}$ makes little difference to the returned values of A and n^{∞}; these parameters are mainly dependent on the datasets considered in the analysis.

Table 4.6 - Returned parameters from MESMER fits to this work and the literature data using a two-adduct model and accounting for H abstraction with all data given an equal uncertainty of 10%. $\langle \Delta E \rangle_{d,M} = A_{\langle \Delta E \rangle d,M} \times (T/298)^{mc}$

	All Data			Selected Data		
Well depth, E/kJ mol^{-1}	153.1	153.1	152.9	154.0	153.6	153.6
$A_{\langle \Delta E \rangle d}$ / cm^{-1} He(m=1.00)	150 (Fixed)	150 (Fixed)	100	150 (Fixed)	150 (Fixed)	100
Ar (m=0.50)	250 (Fixed)	250 (Fixed)	250	250 (Fixed)	250 (Fixed)	100
N_2 (m=0.25)	200 (Fixed)	200	190	200 (Fixed)	150	150
$A \times 10^{11}$ / cm^3 molecule^{-1} s^{-1}	8.32	8.33	8.34	9.55	9.52	9.52
n^{∞}	-1.45	-1.45	-1.45	-1.44	-1.39	-1.39
χ^2 per point	3.31	3.31	3.22	0.56	0.49	0.49

Table 4.7 - Returned parameters from MESMER fits to this work and the literature data and accounting for H abstraction with our higher temperature data given the uncertainties reported in Table 2. $\langle \Delta E \rangle_{d,M} = A_{\langle \Delta E \rangle d,M} \times (T/298)^{m}$

	This work Two adduct model		This work One adduct model (C_1)		Selected Data		
Well depth, E/kJ mol^{-1}	153.7 ± 5.9	153.5 ± 6.2	156.0 ± 3.9	156.0 ± 4.2	153.6 ± 4.9	153.4 ± 5.1	153.2 ± 5.0
$A_{\langle \Delta E \rangle d}$ / cm^{-1} He(m=1.00)	n/a	n/a	n/a	n/a	150 (Fixed)	150 (Fixed)	100 ± 350
Ar (m=0.50)	n/a	n/a	n/a	n/a	250 (Fixed)	250 (Fixed)	100 ± 340
N_2 (m=0.25)	200 (Fixed)	150 ± 110	200 (Fixed)	150 ± 70	200 (Fixed)	150 ± 90	150 ± 90
$A \times 10^{11}$ / cm^3 molecule^{-1} s^{-1}	9.53 ± 0.64	9.47 ± 0.65	9.46 ± 0.41	9.46 ± 0.42	9.46 ± 0.14	9.46 ± 0.14	9.47 ± 0.16
n^{∞}	-1.35 ± 0.15	-1.33 ± 0.16	-1.33 ± 0.10	-1.32 ± 0.10	-1.34 ± 0.07	-1.33 ± 0.07	-1.33 ± 0.07
χ^2 per point	0.50	0.48	0.49	0.48	0.42	0.41	0.41

The analysis was also performed with the use of a single-adduct model; the results for this case are also included in Table 4.7. Little variation is observed in the returned parameters, with the well-depths varying by 2.5 kJ mol^{-1}. This small change is justified by the reduced equilibrium fraction of adduct 4 (~35%) compared to adduct 1 (~65%) and the small energetic difference to adduct 1 (~10 kJ mol^{-1}). Finally, the last three columns of Table 7 shows results, including uncertainties, obtained from fits where the selected data was incorporated, and the uncertainties of our high temperature measurements (T > 720 K) were appropriately set as those of Table 4.2.

4.4.6 - Analytical Representation of Pressure and Temperature for k_{1a}, $k_{-1a,C1}$, and $k_{-1a,C4}$

In order to provide analytical representations for the present master equation calculations, the output from our MESMER equations have been fitted using a Troe formalism:

$$k_{1a}(T,[\mathrm{M}]) = \frac{k_{1a,0}(T)[M]}{1+\frac{k_{1a,0}(T)[M]}{k_{1a}^{\infty}(T)}}F(x) \qquad \text{E12}$$

$$k_{-1a,\,C1}(T,[M]) = k_{1a}(T,[\mathrm{M}]) \times (\mathrm{R}T)^{-1} \times \exp(\Delta H_{C1}^{\ominus}/\mathrm{R}T) \times \exp(-\Delta S_{C1}^{\ominus}/\mathrm{R}) \qquad \text{E13}$$

$$k_{-1a,\,C4}(T,[M]) = k_{1a}(T,[\mathrm{M}]) \times (\mathrm{R}T)^{-1} \times \exp(\Delta H_{C4}^{\ominus}/\mathrm{R}T) \times \exp(-\Delta S_{C4}^{\ominus}/\mathrm{R})] \qquad \text{E14}$$

where [M] is the concentration of the buffer gas, $k_{1a,0}(T)$ is the low-pressure termolecular rate coefficient, $k_{1a}^{\infty}(T)$ is the high-pressure limit rate coefficient, and $F(x)$ is the collision broadening factor. The collision broadening factor - *F(x)* - is calculated according to the formulation of Troe and Ushakov[116], see Appendix 3. It is worth mentioning that if the standard broadening factor for atmospheric studies of 0.6is used,[30,54] without a temperature dependence, a poor fit is produced. $k_{-1a,\,C1}$ and $k_{-1a,\,C4}$ are the decomposition rate coefficients for adducts 1 and 4, respectively, and are related to k_{1a} via E13 and E14 using their thermodynamic parameters: ΔH_{C1}, ΔS_{C1} and ΔH_{C4} ΔS_{C4}

A global non-linear least-squares fit to the MESMER data using the Troe formalism was carried out, where $k_0(T)$ and $k_{1a}^{\infty}(T)$ were defined according to equations E7a and E7b respectively.

$$k_0(T) = A_0 \times (T/298)^n \text{ cm}^6 \text{ molecule}^{-2} \text{ s}^{-1} \quad \text{E7a}$$
$$k_{1a}^{\infty}(T) = A_{1a} \times (T/298)^m \text{ cm}^3 \text{ molecule}^{-1} \text{ s}^{-1} \quad \text{E7b}$$

A_0, A_{1a}, n and m, *and F(x)(* F_{cent}A, F_{cent}B, x_0 and b), $\Delta H_{C1,C4}$ $\Delta S_{C1,C4}$ were adjusted to provide a good fit to the simulated pressure dependent coefficients $k_{1a}(T,[M])$. The results are given in Table 4.8, and these fits to the MESMER data are shown in Figure 4.14, where N_2 was defined as the bath gas. Additional Troe fits where helium and argon were simulated as the buffer gases are also given in Table 4.8.

Table 4.8 - Troe fit parameters to MESMER-simulated rate coefficients, for different buffer gases.

	N_2	He	Ar
A_{1a} / 10^{-11} cm^3 molecule^{-1} s^{-1}	9.5	9.6	9.5
n	-1.26	-1.30	-1.30
A_0 / 10^{-21} cm^6 molecule^{-2} s^{-1}	1.68	1.10	1.43
m	-14.08	-12.50	-13.27
b	0.08	0.08	0.08
x_0	0.90	0.88	0.90
FcentA	0.10	0.11	0.13
FcentB	-0.0012	-0.0012	-0.0009
$\Delta H_{C1}^{\ominus}$ / J mol^{-1}	154043	154308	154512
$\Delta S_{C1}^{\ominus}$ / J mol^{-1} K^{-1}	108.9	109.3	109.6
$\Delta H_{C4}^{\ominus}$ / J mol^{-1}	147251	147495	147696
$\Delta S_{C4}^{\ominus}$ / J mol^{-1} K^{-1}	102.8	103.1	103.5

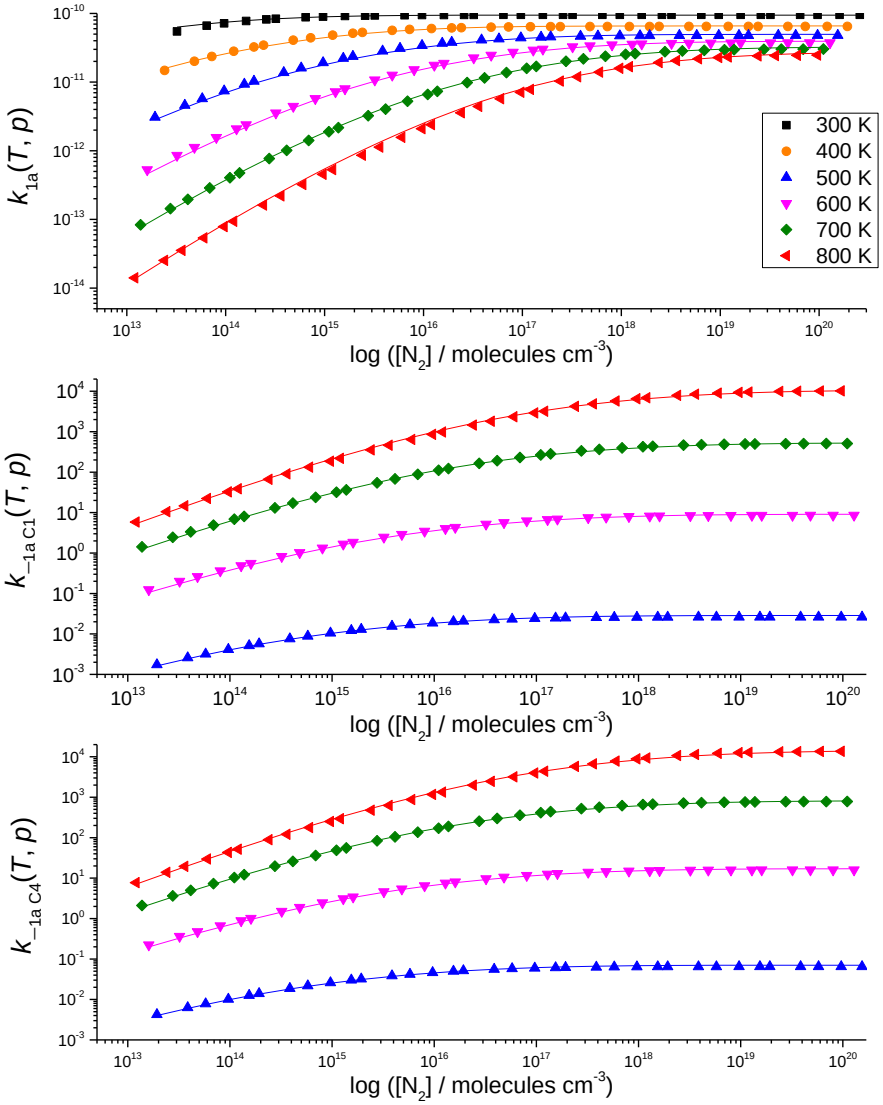

Figure 4.14 - Fits of the Troe formalism to MESMER-simulated rate coefficients where N_2 was implemented as the buffer gas at various temperatures. Markers represent MESMER-simulated rate coefficients and the lines of the same colour are the Troe fits to the data.

4.5 SUMMARY AND CONCLUSIONS

Measurements of the rate coefficient for the reaction of OH with isoprene, k_1, made around room temperature using a new apparatus for high pressure studies are in good agreement with the extensive literature data, hence validating this new apparatus.

Above 700 K the OH temporal profiles exhibit biexponential behaviour, consistent with the establishment of the OH + C_5H_8 ⇌ adduct equilibrium. The experimental adduct dissociation data, k_{-1a}, were fitted to using a master equation model where the adduct binding energy was adjusted. This analysis determined a well depth of (153.5 ± 6.2) kJ mol^{-1} for adduct 1, C1, and (143.4 ± 6.2) kJ mol^{-1} for adduct 4, C4. This value is in agreement with the present *ab initio* calculations (well depth for C1 adduct = 154.1 kJ mol^{-1}) on the R1 potential energy surface. However, it is noted that the well depth determined from the experimental data is dependent on how the internal modes of reagents and adducts are treated, and only when the low vibrations are treated as hindered rotor does experiment and theory show agreement. The approach based on the species profiles used to explore multiple recycling proved to be useful in this study and may be used in analogous situations.

The analysis of the > 700 K equilibrium data required an additional minor, but significant abstraction channel, R1b. Our *ab initio* calculations have identified this direct abstraction channel and the proton transfer mass spectrometer provides evidence that this channel is operating even at room temperature: $k_{1b} = (1.3 \pm 0.3) \times 10^{-11} \exp\left(\frac{-3.61 \text{ kJ mol}^{-1}}{RT}\right)$ cm^3 molecule^{-1} s^{-1}.

Our experimental data on reaction k_1, together with the extensive literature data on this reaction, have been assessed using master equation analysis with the MESMER programme. This analysis indicates that there is no pressure dependence in the pressure range of the literature data, contradicting some previous studies. A selected dataset was then used to provide our recommended value for $k_{1a}(T,[M])$. A Troe parametrization of $k_{1a}(T,[M])$

provides an analytical form of our MESMER analysis. The temperature range for OH + isoprene studies has been significantly extended to ~800 K with a high pressure limit recommendation of:

$$k_1^{\infty} = (9.5 \pm 0.2) \times 10^{-11} \left(\frac{T}{298\ \mathrm{K}}\right)^{-1.33 \pm 0.07} + (1.3 \pm 0.3) \times 10^{-11} \exp\left(\frac{-3.61\ \mathrm{kJ\ mol^{-1}}}{RT}\right).$$

Chapter 4 introduced an extra layer of complexity when compared to Chapter 3, by the need of the computation of overall OH recycling coefficients, derived from contributions of multiple OH recycling species. This was accomplished by analysing the Master Equation-simulated OH profiles, whose shape is influenced by all the modelled C_5H_8-OH adducts. In contrast, in the classic ME analysis exemplified in Chapter 3, adjustable parameters were floated to provide a good fit to experimentally determined rate coefficients, which corresponded to an eigenvalue of the ME.

In Chapter 5, a new method of analysis which expands the horizons of ME calculations will developed. The reaction of ethylene with OH radicals will be used as a test case due to its simplicity, atmospheric relevance and wide previous literature coverage. The method incorporates additional pieces of chemistry in the ME in order to enable a direct comparison of Master Equation-simulated traces and raw experimental profiles. This adds another layer of complexity to the problem as the experimental traces contain pressure and temperature dependent information about multiple competing process in which OH is involved. Nonetheless, as will be discussed, a direct raw-trace fitting not only allows an accurate evaluation of the thermochemistry of a chemical process, but also represents a critical mechanistic assessment.

4.6 REFERENCES

1. Goldstein, A. H.; Galbally, I. E. Known and Unexplored Organic Constituents in the Earth's Atmosphere. *Environmental Science & Technology* **2007,** *41*, 1514-1521.

2. Hantson, S.; Knorr, W.; Schurgers, G.; Pugh, T. A. M.; Arneth, A. Global Isoprene and Monoterpene Emissions under Changing Climate, Vegetation, CO_2 and Land Use. *Atmospheric Environment* **2017,** *155*, 35-45.

3. Guenther, A.; Karl, T.; Harley, P.; Wiedinmyer, C.; Palmer, P. I.; Geron, C. Estimates of Global Terrestrial Isoprene Emissions Using Megan (Model of Emissions of Gases and Aerosols from Nature). *Atmospheric Chemistry and Physics* **2006,** *6*, 3181-3210.

4. IUPAC Evaluated Kinetic Data. http://iupac.pole-ether.fr/index.html (accessed February).

5. Utembe, S. R.; Jenkin, M. E.; Derwent, R. G.; Lewis, A. C.; Hopkins, J. R.; Hamilton, J. F. Modelling the Ambient Distribution of Organic Compounds During the August 2003 Ozone Episode in the Southern Uk. *Faraday Discussions* **2005,** *130*, 311-326.

6. Tan, D. et al. HOx Budgets in a Deciduous Forest: Results from the Prophet Summer 1998 Campaign. *Journal of Geophysical Research-Atmospheres* **2001,** *106*, 24407-24427.

7. Carslaw, N. et al. OH and HO_2 Radical Chemistry in a Forested Region of North-Western Greece. *Atmospheric Environment* **2001,** *35*, 4725-4737.

8. Whalley, L. K. et al. Quantifying the Magnitude of a Missing Hydroxyl Radical Source in a Tropical Rainforest. *Atmospheric Chemistry and Physics* **2011,** *11*, 7223-7233.

9. Lelieveld, J. et al. Atmospheric Oxidation Capacity Sustained by a Tropical Forest. *Nature* **2008,** *452*, 737-740.

10. Saunois, M. et al. The Global Methane Budget 2000-2012. *Earth System Science Data* **2016,** *8*, 697-751.

11. Seakins, P. W.; Blitz, M. A., Developments in Laboratory Studies of Gas-Phase Reactions for Atmospheric Chemistry with Applications to Isoprene Oxidation and Carbonyl Chemistry. In *Annual Review of Physical Chemistry, Vol 62*, Leone, S. R.; Cremer, P. S.; Groves, J. T.; Johnson, M. A., Eds. Annual Reviews: Palo Alto, 2011; Vol. 62, pp 351-373.

12. Winiberg, F. A. F. et al. Direct Measurements of OH and Other Product Yields from the HO_2 + $CH_3C(O)O_2$ Reaction. *Atmospheric Chemistry and Physics* **2016,** *16*, 4023-4042.

13. Paulot, R.; Crounse, J. D.; Kjaergaard, H. G.; Kurten, A.; St. Clair, J. M.; Seinfeld, J. H.; Wennberg, P. O. Unexpected Epoxide Formation in the Gas-Phase Photooxidation of Isoprene. *Science (Washington, D. C., 1883-)* **2009,** *325*, 730 - 733.

14. Peeters, J.; Nguyen, T. L.; Vereecken, L. HOx Radical Regeneration in the Oxidation of Isoprene. *Physical Chemistry Chemical Physics* **2009,** *11*, 5935-5939.

15. Peeters, J.; Muller, J. F.; Stavrakou, T.; Nguyen, V. S. Hydroxyl Radical Recycling in Isoprene Oxidation Driven by Hydrogen Bonding and Hydrogen Tunneling: The Upgraded LIM1 Mechanism. *Journal of Physical Chemistry A* **2014,** *118*, 8625-8643.

16. Hansen, R. F.; Lewis, T. R.; Graham, L.; Whalley, L. K.; Seakins, P. W.; Heard, D. E.; Blitz, M. A. OH Production from the Photolysis of Isoprene-Derived Peroxy Radicals: Cross-Sections, Quantum Yields and Atmospheric Implications. *Physical Chemistry Chemical Physics* **2017,** *19*, 2341-2354.

17. Crounse, J. D.; Paulot, F.; Kjaergaard, H. G.; Wennberg, P. O. Peroxy Radical Isomerization in the Oxidation of Isoprene. *Physical Chemistry Chemical Physics* **2011,** *13*, 13607-13613.

18. Fuchs, H. et al. Experimental Evidence for Efficient Hydroxyl Radical Regeneration in Isoprene Oxidation. *Nature Geoscience* **2013,** *6*, 1023-1026.

19. Seakins, P. W. A Brief Review of the Use of Environmental Chambers for Gas Phase Studies of Kinetics, Chemical Mechanisms and Characterisation of Field Instruments. *The European Physical Journal, Web of Conferences* **2010,** *9*, 143-163.

20. Eskola, A. J.; Carr, S. A.; Shannon, R. J.; Wang, B.; Blitz, M. A.; Pilling, M. J.; Seakins, P. W.; Robertson, S. H. Analysis of the Kinetics and Yields of OH Radical Production from the $CH_3OCH_2 + O_2$ Reaction in the Temperature Range 195-650 K: An Experimental and Computational Study. *Journal of Physical Chemistry A* **2014,** *118*, 6773-6788.

21. Stone, D.; Blitz, M.; Ingham, T.; Onel, L.; Medeiros, D. J.; Seakins, P. W. An Instrument to Measure Fast Gas Phase Radical Kinetics at High Temperatures and Pressures. *Review of Scientific Instruments* **2016,** *87*, 054102.

22. Kleindienst, T. E.; Harris, G. W.; Pitts, J. N. Rates and Temperature Dependences of the Reaction of OH with Isoprene, Its Oxidation-Products, and Selected Terpenes. *Environmental Science & Technology* **1982,** *16*, 844-846.

23. Hites, R. A.; Turner, A. M. Rate Constants for the Gas-Phase Beta-Myrcene Plus OH and Isoprene Plus OH Reactions as a Function of Temperature. *International Journal of Chemical Kinetics* **2009,** *41*, 407-413.

24. Chuong, B.; Stevens, P. S. Kinetic Study of the OH Plus Isoprene and OH Plus Ethylene Reactions between 2 and 6 Torr and over the Temperature Range 300-423 K. *Journal of Physical Chemistry A* **2000,** *104*, 5230-5237.

25. Sun, H.; Law, C. K. Kinetics of Hydrogen Abstraction Reactions of Butene Isomers by OH Radical. *The Journal of Physical Chemistry A* **2010,** *114*, 12088-12098.

26. Smith, G. P. Laser Pyrolysis Studies of OH Reaction Rates with Several Butenes at 1200 K. *International Journal of Chemical Kinetics* **1987,** *19*, 269-276.

27. D G Truhlar, a.; Garrett, B. C. Variational Transition State Theory. *Annual Review of Physical Chemistry* **1984,** *35*, 159-189.

28. Singh, S.; Li, Z. Kinetics Investigation of OH Reaction with Isoprene at 240-340 K and 1-3 Torr Using the Relative Rate/Discharge Flow/Mass Spectrometry Technique. *Journal of Physical Chemistry A* **2007,** *111*, 11843-11851.

29. Dillon, T. J.; Dulitz, K.; Gross, C. B. M.; Crowley, J. N. Temperature Dependent Rate Coefficients for the Reactions of the Hydroxyl Radical with the Atmospheric Biogenics Isoprene, alpha-pinene and delta-3-carene. *Atmospheric Chemistry and Physics Discussions* **2017,** *17*, 15137-15150.

30. McGivern, W. S.; Suh, I.; Clinkenbeard, A. D.; Zhang, R. Y.; North, S. W. Experimental and Computational Study of the OH-Isoprene Reaction: Isomeric Branching and Low-Pressure Behavior. *Journal of Physical Chemistry A* **2000,** *104*, 6609-6616.

31. Campuzano-Jost, P.; Williams, M. B.; D'Ottone, L.; Hynes, A. J. Kinetics of the OH-Initiated Oxidation of Isoprene. *Geophysical Research Letters* **2000,** *27*, 693-696.

32. Campuzano-Jost, P.; Williams, M. B.; D'Ottone, L.; Hynes, A. J. Kinetics and Mechanism of the Reaction of the Hydroxyl Radical with h_8-isoprene and d_8-isoprene: Isoprene Absorption Cross Sections, Rate Coefficients, and the Mechanism of Hydroperoxyl Radical Production. *Journal of Physical Chemistry A* **2004,** *108*, 1537-1551.

33. Glowacki, D. R.; Liang, C. H.; Morley, C.; Pilling, M. J.; Robertson, S. H. MESMER: An Open-Source Master Equation Solver for Multi-Energy Well Reactions. *Journal of Physical Chemistry A* **2012,** *116*, 9545-9560.

34. Blitz, M. A.; Green, N. J. B.; Shannon, R. J.; Pilling, M. J.; Seakins, P. W.; Western, C. M.; Robertson, S. H. Reanalysis of Rate Data for the Reaction $CH_3 + CH_3 \rightarrow C_2H_6$ Using Revised Cross Sections and a Linearized Second-Order Master Equation. *Journal of Physical Chemistry A* **2015,** *119*, 7668-7682.

35. Onel, L.; Blitz, M.; Seakins, P. W.; Bunkan, A. J. C.; Solimannejad, M.; Nielsen, C. J. Gas Phase Reactions of OH with Methyl Amines in the Presence or Absence of Molecular

Oxygen. An Experimental and Theoretical Study. *Environmental Science and Technology* **2013,** *Submitted*.

36. Onel, L.; Blitz, M. A.; Seakins, P. W. Direct Determination of the Rate Coefficient for the Reaction of OH Radicals with Monoethanol Amine (MEA) from 296 to 510 K. *Journal of Physical Chemistry Letters* **2012,** *3*, 853-856.

37. Onel, L.; Blitz, M. A.; Breen, J.; Rickardcd, A. R.; Seakins, P. W. Branching Ratios for the Reactions of OH with Ethanol Amines Used in Carbon Capture and the Potential Impact on Carcinogen Formation in the Emission Plume from a Carbon Capture Plant. *Physical Chemistry Chemical Physics* **2015,** *17*, 25342-25353.

38. Seakins, P. W.; Pilling, M. J.; Niiranen, J. T.; Gutman, D.; Krasnoperov, L. N. Kinetics and Thermochemistry of R+HBr ↔ RH+Br Reactions - Determinations of the Heat of Formation of C_2H_5, i-C_3H_7, sec-C_4H_9, and t-C_4H_9. *Journal of Physical Chemistry* **1992,** *96*, 9847-9855.

39. Zhao, Y.; Truhlar, D. G. The M06 Suite of Density Functionals for Main Group Thermochemistry, Thermochemical Kinetics, Noncovalent Interactions, Excited States, and Transition Elements: Two New Functionals and Systematic Testing of Four M06-Class Functionals and 12 Other Functionals. *Theoretical Chemistry Accounts* **2008,** *120*, 215-241.

40. Frisch, M. J.; Pople, J. A.; Binkley, J. S. Self-Consistent Molecular-Orbital Methods .25. Supplementary Functions for Gaussian-Basis Sets. *Journal of Chemical Physics* **1984,** *80*, 3265-3269.

41. Frisch, M. J. et al., Gaussian 09, Revision D.01. Wallingford CT, 2009.

42. Peng, C. Y.; Ayala, P. Y.; Schlegel, H. B.; Frisch, M. J. Using Redundant Internal Coordinates to Optimize Equilibrium Geometries and Transition States. *Journal of Computational Chemistry* **1996,** *17*, 49-56.

43. Li, X. S.; Frisch, M. J. Energy-Represented Direct Inversion in the Iterative Subspace within a Hybrid Geometry Optimization Method. *Journal of Chemical Theory and Computation* **2006,** *2*, 835-839.

44. Raghavachari, K.; Trucks, G. W.; Pople, J. A.; Headgordon, M. A 5th-Order Perturbation Comparison of Electron Correlation Theories. *Chemical Physics Letters* **1989,** *157*, 479-483.

45. Helgaker, T.; Klopper, W.; Koch, H.; Noga, J. Basis-Set Convergence of Correlated Calculations on Water. *Journal of Chemical Physics* **1997,** *106*, 9639-9646.

46. Papajak, E.; Zheng, J.; Xu, X.; Leverentz, H. R.; Truhlar, D. G. Perspectives on Basis Sets Beautiful: Seasonal Plantings of Diffuse Basis Functions. *Journal of Chemical Theory and Computation* **2011,** *7*, 3027-3034.

47. Kendall, R. A.; Dunning, T. H.; Harrison, R. J. Electron-Affinities of the 1st-Row Atoms Revisited - Systematic Basis-Sets and Wave-Functions. *Journal of Chemical Physics* **1992,** *96*, 6796-6806.

48. Feller, D. The Use of Systematic Sequences of Wave-Functions for Estimating the Complete Basis Set, Full Configuration-Interaction Limit in Water. *Journal of Chemical Physics* **1993,** *98*, 7059-7071.

49. Ramabhadran, R. O.; Raghavachari, K. Extrapolation to the Gold-Standard in Quantum Chemistry: Computationally Efficient and Accurate CCSD(T) Energies for Large Molecules Using an Automated Thermochemical Hierarchy. *Journal of Chemical Theory and Computation* **2013,** *9*, 3986-3994.

50. Liu, Z.; Nguyen, V. S.; Harvey, J.; Muller, J. F.; Peeters, J. Theoretically Derived Mechanisms of HPALD Photolysis in Isoprene Oxidation. *Physical Chemistry Chemical Physics* **2017,** *19*, 9096-9106.

51. Alecu, I. M.; Zheng, J.; Zhao, Y.; Truhlar, D. G. Computational Thermochemistry: Scale Factor Databases and Scale Factors for Vibrational Frequencies Obtained from Electronic Model Chemistries. *Journal of Chemical Theory and Computation* **2010,** *6*, 2872-2887.

52. Sharma, S.; Raman, S.; Green, W. H. Intramolecular Hydrogen Migration in Alkylperoxy and Hydroperoxyalkylperoxy Radicals: Accurate Treatment of Hindered Rotors. *Journal of Physical Chemistry A* **2010,** *114*, 5689-5701.

53. OriginLab *Originpro*, Northampton, MA.

54. Lei, W. F.; Zhang, R. Y.; McGivern, W. S.; Derecskei-Kovacs, A.; North, S. W. Theoretical Study of Isomeric Branching in the Isoprene-OH Reaction: Implications to Final Product Yields in Isoprene Oxidation. *Chemical Physics Letters* **2000,** *326*, 109-114.

55. Greenwald, E. E.; North, S. W.; Georgievskii, Y.; Klippenstein, S. J. A Two Transition State Model for Radical−Molecule Reactions: Applications to Isomeric Branching in the OH−Isoprene Reaction. *The Journal of Physical Chemistry A* **2007,** *111*, 5582-5592.

56. Stevens, P. S.; Seymour, E.; Li, Z. J. Theoretical and Experimental Studies of the Reaction of OH with Isoprene. *Journal of Physical Chemistry A* **2000,** *104*, 5989-5997.

57. Řezáč, J.; Šimová, L.; Hobza, P. CCSD[T] Describes Noncovalent Interactions Better Than the CCSD(T), CCSD(TQ), and CCSDT Methods. *Journal of Chemical Theory and Computation* **2013,** *9*, 364-369.

58. Řezáč, J.; Hobza, P. Describing Noncovalent Interactions Beyond the Common Approximations: How Accurate Is the "Gold Standard," CCSD(T) at the Complete Basis Set Limit? *Journal of Chemical Theory and Computation* **2013,** *9*, 2151-2155.

59. Wachters, A. J. H. Gaussian Basis Set for Molecular Wavefunctions Containing Third-Row Atoms. *The Journal of Chemical Physics* **1970,** *52*, 1033-1036.

60. Hay, P. J. Gaussian Basis Sets for Molecular Calculations. The Representation of 3d Orbitals in Transition-Metal Atoms. *The Journal of Chemical Physics* **1977,** *66*, 4377-4384.

61. Krishnan, R.; Binkley, J. S.; Seeger, R.; Pople, J. A. Self-Consistent Molecular Orbital Methods. XX. A Basis Set for Correlated Wave Functions. *The Journal of Chemical Physics* **1980,** *72*, 650-654.

62. McLean, A. D.; Chandler, G. S. Contracted Gaussian Basis Sets for Molecular Calculations. I. Second Row Atoms, Z=11–18. *The Journal of Chemical Physics* **1980,** *72*, 5639-5648.

63. Raghavachari, K.; Trucks, G. W. Highly Correlated Systems. Excitation Energies of First Row Transition Metals Sc–Cu. *The Journal of Chemical Physics* **1989,** *91*, 1062-1065.

64. Binning, R. C.; Curtiss, L. A. Compact Contracted Basis Sets for Third-Row Atoms: Ga–Kr. *Journal of Computational Chemistry* **1990,** *11*, 1206-1216.

65. McGrath, M. P.; Radom, L. Extension of Gaussian-1 (G1) Theory to Bromine-Containing Molecules. *The Journal of Chemical Physics* **1991,** *94*, 511-516.

66. Curtiss, L. A.; McGrath, M. P.; Blaudeau, J. P.; Davis, N. E.; Jr., R. C. B.; Radom, L. Extension of Gaussian-2 Theory to Molecules Containing Third-Row Atoms Ga–Kr. *The Journal of Chemical Physics* **1995,** *103*, 6104-6113.

67. Rassolov, V. A.; Ratner, M. A.; Pople, J. A.; Redfern, P. C.; Curtiss, L. A. 6-31g* Basis Set for Third-Row Atoms. *Journal of Computational Chemistry* **2001,** *22*, 976-984.

68. Rassolov, V. A.; Pople, J. A.; Ratner, M. A.; Windus, T. L. 6-31g* Basis Set for Atoms K through Zn. *The Journal of Chemical Physics* **1998,** *109*, 1223-1229.

69. Blaudeau, J.-P.; McGrath, M. P.; Curtiss, L. A.; Radom, L. Extension of Gaussian-2 (G2) Theory to Molecules Containing Third-Row Atoms K and Ca. *The Journal of Chemical Physics* **1997,** *107*, 5016-5021.

70. Francl, M. M.; Pietro, W. J.; Hehre, W. J.; Binkley, J. S.; Gordon, M. S.; DeFrees, D. J.; Pople, J. A. Self-Consistent Molecular Orbital Methods. XXIII. A Polarization-Type Basis Set for Second-Row Elements. *The Journal of Chemical Physics* **1982,** *77*, 3654-3665.

71. Gordon, M. S. The Isomers of Silacyclopropane. *Chemical Physics Letters* **1980,** *76*, 163-168.

72. Hariharan, P. C.; Pople, J. A. Accuracy of AH_n Equilibrium Geometries by Single Determinant Molecular Orbital Theory. *Molecular Physics* **1974,** *27*, 209-214.

73. Hariharan, P. C.; Pople, J. A. The Influence of Polarization Functions on Molecular Orbital Hydrogenation Energies. *Theoretica chimica acta* **1973,** *28*, 213-222.

74. Hehre, W. J.; Ditchfield, R.; Pople, J. A. Self—Consistent Molecular Orbital Methods. XII. Further Extensions of Gaussian—Type Basis Sets for Use in Molecular Orbital Studies of Organic Molecules. *The Journal of Chemical Physics* **1972,** *56*, 2257-2261.

75. Ditchfield, R.; Hehre, W. J.; Pople, J. A. Self-Consistent Molecular-Orbital Methods. IX. An Extended Gaussian-Type Basis for Molecular-Orbital Studies of Organic Molecules. *The Journal of Chemical Physics* **1971,** *54*, 724-728.

76. Becke, A. D. Density-Functional Thermochemistry. III. The Role of Exact Exchange. *The Journal of Chemical Physics* **1993,** *98*, 5648-5652.

77. Lee, C.; Yang, W.; Parr, R. G. Development of the Colle-Salvetti Correlation-Energy Formula into a Functional of the Electron Density. *Physical Review B* **1988,** *37*, 785-789.

78. Vosko, S. H.; Wilk, L.; Nusair, M. Accurate Spin-Dependent Electron Liquid Correlation Energies for Local Spin Density Calculations: A Critical Analysis. *Canadian Journal of Physics* **1980,** *58*, 1200-1211.

79. Stephens, P. J.; Devlin, F. J.; Chabalowski, C. F.; Frisch, M. J. Ab Initio Calculation of Vibrational Absorption and Circular Dichroism Spectra Using Density Functional Force Fields. *The Journal of Physical Chemistry* **1994,** *98*, 11623-11627.

80. Pople, J. A.; Head-Gordon, M.; Raghavachari, K. Quadratic Configuration-Interaction - a General Technique for Determining Electron Correlation Energies. *Journal of Chemical Physics* **1987,** *87*, 5968-5975.

81. Greenwald, E. E.; North, S. W.; Georgievskii, Y.; Klippenstein, S. J. A Two Transition State Model for Radical-Molecule Reactions: A Case Study of the Addition of OH to C_2H_4. *Journal of Physical Chemistry A* **2005,** *109*, 6031-6044.

82. Cremer, D. Møller–Plesset Perturbation Theory: From Small Molecule Methods to Methods for Thousands of Atoms. *Wiley Interdisciplinary Reviews: Computational Molecular Science* **2011,** *1*, 509-530.

83. Pople, J. A.; Head-Gordon, M.; Raghavachari, K. Corrections to Correlations Energies Beyond Fourth Order Moller-Plesset (MP4) Perturbation Theory. Contributions of Single, Double, and Triple Substitutions. *International Journal of Quantum Chemistry* **1988,** *34*, 377-382.

84. Ochterski, J. W.; Petersson, G. A.; Jr., J. A. M. A Complete Basis Set Model Chemistry. V. Extensions to Six or More Heavy Atoms. *The Journal of Chemical Physics* **1996,** *104*, 2598-2619.

85. Baeza-Romero, M. T.; Blitz, M. A.; Goddard, A.; Seakins, P. W. Time-of-Flight Mass Spectrometry for Time-Resolved Measurements: Some Developments and Applications. *International Journal of Chemical Kinetics* **2012,** *44*, 532-545.

86. Taatjes, C. A. How Does the Molecular Velocity Distribution Affect Kinetics Measurements by Time-Resolved Mass Spectrometry? *International Journal of Chemical Kinetics* **2007,** *39*, 565-570.

87. Moore, S. B.; Carr, R. W. Molecular Velocity Distribution Effects in Kinetic Studies by Time-Resolved Mass-Spectrometry. *International Journal of Mass Spectrometry and Ion Processes* **1977,** *24*, 161-171.

88. Atkinson, R.; Aschmann, S. M. Rate Constants for the Reaction of OH Radicals with a Series of Alkenes and Dialkenes at 295 K. *International Journal of Chemical Kinetics* **1984,** *16*, 1175-1186.

89. Atkinson, R.; Aschmann, S. M.; Winer, A. M.; Pitts, J. N. Rate Constants for the Reaction of OH Radicals with a Series of Alkanes and Alkenes at 299 ± 2 K. *International Journal of Chemical Kinetics* **1982,** *14*, 507-516.

90. Chuong, B.; Stevens, P. S. Measurements of the Kinetics of the OH-Initiated Oxidation of Isoprene. *Journal of Geophysical Research-Atmospheres* **2002,** *107*, 4162.

91. Dillon, T. J.; Dulitz, K.; Gross, C. B. M.; Crowley, J. N. Temperature Dependent Rate Coefficients for the Reactions of the Hydroxyl Radical with the Atmospheric Biogenics Isoprene, alpha-pinene and delta-3-carene. *Atmospheric Chemistry and Physics* **2017,** *17*, 15137-15150

92. Edney, E. O.; Kleindienst, T. E.; Corse, E. W. Room-Temperature Rate Constants for the Reaction of OH with Selected Chlorinated and Oxygenated Hydrocarbons. *International Journal of Chemical Kinetics* **1986,** *18*, 1355-1371.

93. Gill, K. J.; Hites, R. A. Rate Constants for the Gas-Phase Reactions of the Hydroxyl Radical with Isoprene, alpha- and beta-pinene, and Limonene as a Function of Temperature. *Journal of Physical Chemistry A* **2002,** *106*, 2538-2544.

94. Iida, Y.; Obi, K.; Imamura, T. Rate Constant for the Reaction of OH Radicals with Isoprene at 298 ± 2 K. *Chemistry Letters* **2002,** *31*, 792-793.

95. Karl, M. et al. Kinetic Study of the OH-Isoprene and O_3-Isoprene Reaction in the Atmosphere Simulation Chamber, Saphir. *Geophysical Research Letters* **2004,** *31*, 4.

96. McQuaid, J. B.; Stocker, D. W.; Pilling, M. J. Kinetics of the Reactions of OH with 3-methyl-2-cyclohexen-1-one and 3,5,5-trimethyl-2-cyclohexen-1-one under Simulated Atmospheric Conditions. *International Journal of Chemical Kinetics* **2002,** *34*, 7-11.

97. Ohta, T. Rate Constants for the Reactions of Diolefins with OH Radicals in the Gas-Phase - Estimate of the Rate Constants from Those for Monoolefins. *Journal of Physical Chemistry* **1983,** *87*, 1209-1213.

98. Park, J.; Jongsma, C. G.; Zhang, R. Y.; North, S. W. OH/OD Initiated Oxidation of Isoprene in the Presence of O_2 and NO. *Journal of Physical Chemistry A* **2004,** *108*, 10688-10697.

99. Poppe, D.; Brauers, T.; Dorn, H. P.; Karl, M.; Mentel, T.; Schlosser, E.; Tillmann, R.; Wegener, R.; Wahner, A. OH-Initiated Degradation of Several Hydrocarbons in the Atmosphere Simulation Chamber Saphir. *J. Atmos. Chem.* **2007,** *57*, 203-214.

100. Vimal, D.; Pacheco, A. B.; Iyengar, S. S.; Stevens, P. S. Experimental and Ab Initio Dynamical Investigations of the Kinetics and Intramolecular Energy Transfer Mechanisms for the OH+1,3-butadiene Reaction between 263 and 423 K at Low Pressure. *Journal of Physical Chemistry A* **2008,** *112*, 7227-7237.

101. Zhang, D.; Zhang, R. Y.; Church, C.; North, S. W. Experimental Study of Hydroxyalkyl Peroxy Radicals from OH-Initiated Reactions of Isoprene. *Chemical Physics Letters* **2001,** *343*, 49-54.

102. Zhang, R. Y.; Suh, I.; Lei, W.; Clinkenbeard, A. D.; North, S. W. Kinetic Studies of OH-Initiated Reactions of Isoprene. *J. Geophys. Res. Atmos.* **2000,** *105*, 24627-24635.

103. Moré, J. J.; Sorensen, D. C. Computing a Trust Region Step. *SIAM Journal on Scientific and Statistical Computing* **1983,** *4*, 553-572.

104. Baulch, D. L. et al. Evaluated Kinetic Data for Combustion Modelling. *Journal of Physical and Chemical Reference Data* **1992,** *21*, 411-734.

105. Tully, F. P. Hydrogen-Atom Abstraction from Alkenes by OH, Ethene and 1-butene. *Chemical Physics Letters* **1988,** *143*, 510-514.

106. Atkinson, R.; Aschmann, S. M.; Tuazon, E. C.; Arey, J.; Zielinska, B. Formation of 3-Methylfuran from the Gas-Phase Reaction of OH Radicals with Isoprene and the Rate Constant for Its Reaction with the OH Radical. *International Journal of Chemical Kinetics* **1989,** *21*, 593-604.

107. Atkinson, R.; Tuazon, E. C.; Aschmann, S. M. Products of the Gas-Phase Reaction of the OH Radical with 3-methyl-1-butene in the Presence of NO. *International Journal of Chemical Kinetics* **1998,** *30*, 577-587.

108. Nordmeyer, T.; Wang, W.; Ragains, M. L.; Finlayson-Pitts, B. J.; Spicer, C. W.; Plastridge, R. A. Unique Products of the Reaction of Isoprene with Atomic Chlorine: Potential Markers of Chlorine Atom Chemistry. *Geophysical Research Letters* **1997,** *24*, 1615-1618.

109. Jenkin, M. E.; Young, J. C.; Rickard, A. R. The MCM V3.3.1 Degradation Scheme for Isoprene. *Atmospheric Chemistry and Physics* **2015,** *15*, 11433-11459.

110. Peeters, J.; Boullart, W.; Pultau, V.; Vandenberk, S.; Vereecken, L. Structure-Activity Relationship for the Addition of OH to (Poly)Alkenes: Site-Specific and Total Rate Constants. *Journal of Physical Chemistry A* **2007,** *111*, 1618-1631.

111. *MATLAB and Optimization Toolbox Release R2016a*. Natwick : Math Works Inc.: 2016.

112. Dibble, T. S. Isomerization of OH-Isoprene Adducts and Hydroxyalkoxy Isoprene Radicals. *Journal of Physical Chemistry A* **2002,** *106*, 6643-6650.

113. Papadimitriou, V. C.; Karafas, E. S.; Gierczak, T.; Burkholder, J. B. $CH_3CO + O_2 + M$ ($M = He, N_2$) Reaction Rate Coefficient Measurements and Implications for the OH Radical Product Yield. *Journal of Physical Chemistry A* **2015,** *119*, 7481-7497.

114. Baeza-Romero, M. T.; Glowacki, D. R.; Blitz, M. A.; Heard, D. E.; Pilling, M. J.; Rickard, A. R.; Seakins, P. W. A Combined Experimental and Theoretical Study of the Reaction between Methylglyoxal and OH/OD Radical: OH Regeneration. *Physical Chemistry Chemical Physics* **2007,** *9*, 4114-4128.

115. Martins, G. et al. Valence Shell Electronic Spectroscopy of Isoprene Studied by Theoretical Calculations and by Electron Scattering, Photoelectron, and Absolute Photoabsorption Measurements. *Physical Chemistry Chemical Physics* **2009,** *11*, 11219-11231.

116. Troe, J.; Ushakov Vladimir, G. Representation of "Broad" Falloff Curves for Dissociation and Recombination Reactions. *Zeitschrift für Physikalische Chemie* **2014,** *228*, 1-10.

Chapter 5. Kinetics of the reaction of ethylene with OH radicals: developing a global Master Equation-based, raw-trace fitting technique

Overview of the chapter

The current chapter focuses on the development of a novel strategy to explore experimental traces via a global multi-temperature, multi-pressure fitting procedure which relies on Master Equation (ME) calculations from the corresponding potential energy surface. A new transition matrix is constructed as a modification of the original ME, via the inclusion of intrinsic formation and consumption terms such as diffusional losses, reactions with radical precursors, unimolecular losses of intermediate species and side reactions. The method is presented in the context of the ethylene + OH reaction due to its simplicity and wide previous literature coverage. This technique reduces the number of mathematical transformations necessary when conventionally converting experimental traces into rate coefficients with propagated errors and subsequent implementation in ME fits (see Chapter 2 for an example of a classic ME fit). A global raw-trace fit, with a large number of experimental profiles covering a wide range of temperature and pressures, not only allows a good assessment of the thermochemistry of the reactions involved, but also represents a test of the mechanism implemented. Systematic inconsistencies observed in the fits can provide insightful information regarding potentially missing pieces of chemistry. The OH abstraction from ethylene at elevated temperatures is used to exemplify the last assertion.

5.1 INTRODUCTION

Ethylene, also known as ethene (C_2H_4), is the simplest possible alkene. It is extensively used in the manufacture of polymers of wide applicability, such as polyethylene (PE)[1], polyvinyl chloride (PVC) and polyethylene terephthalate (PET). It is also a precursor of ethylene glycol, an industrially important compound, largely used in the production of detergents and surfactants.[2-3] Ethylene is employed in agriculture as a fruit ripening hormone[4]; and also plays additional important roles in the development of plants, influencing not only their growth, but also seed germination, flowering, root stretching and sex determination.[5]

The traditional understanding suggests that global emissions of ethylene to the atmosphere are dominated by biogenic sources, accounting for approximately 75% of the total emissions.[6-7] In one year, 8-25 Tg of ethylene were estimated in the past to be emitted into the troposphere from natural sources.[5] Plant emissions are believed to account for the majority of natural emissions, with small contributions from soil (~3 Tg) and ocean (~1 Tg).[5, 8] Emissions of ethylene by vegetation can be significantly enhanced via the "ethylene stress" phenomenon (~10-400 times), which can be provoked by agents of different nature, including (i) physical (high temperature, freezing, mechanical damage, etc), (ii) chemical (ozone, sulfur dioxide) or (iii) biotic (insect wounding, pathological infection) factors.[8]

The most significant anthropogenic sources of ethylene include industry, biomass burning and traffic. More recent estimates[9] attempt to discriminate the ethylene emissions from biomass burning as these can have both a human and natural causes. According to these evaluations, in one year, 2.7 Tg of ethylene are emitted into the troposphere from natural sources.[6, 9], while 1.05 Tg/yr and 5.35 Tg/yr of ethylene are believed to be emitted from anthropogenic sources and biomass burning respectively.[6, 9] However, these estimates, are based on a compilation of data from 1997 and do not reflect a decline of industrial and traffic emissions observed since 1994.[10]

When released in the atmosphere, the gas-phase oxidation, predominantly initiated by the reaction with hydroxyl radicals (R1) is the major removal process for ethylene.[11] Ethylene has a relatively short lifetime with respect to the removal by OH radicals ($\tau \sim 6 - 30$ h) and represents a significant atmospheric OH sink.[11-12] The C_2H_4 + OH reaction is also relevant for combustion chemistry.[11, 13]

$$OH + C_2H_4 \xrightarrow{k_1} \text{Products} \qquad \text{R1}$$

At low temperatures ($T \leq 500$ K) the ethylene + OH reaction proceeds mostly via a pressure-dependent OH addition to the π-bond. Under such temperatures, the collisional stabilization of the chemically activated C_2H_4-OH* adduct (R2) competes with the unimolecular decomposition of the C_2H_4-OH* adduct (R-1a):

$$OH + C_2H_4 \xleftrightarrow{k_{1a},\ k_{-1a}} HOC_2H_4^* \qquad \text{(R1a, R-1a)}$$

$$HOC_2H_4^* + M \xrightarrow{k_2} HOC_2H_4 + M \qquad \text{(R2)}$$

At elevated temperatures ($T > 600$ K), however, the abstraction of a hydrogen atom becomes significant and eventually turns into the major channel of this reaction[14-16]:

$$C_2H_4 + OH \xrightarrow{k_{1b}} H_2O + C_2H_3 \qquad \text{(R1b)}$$

Previous studies of the ethylene + OH reaction were carried out via diverse techniques, among them direct measurements using Pulsed Laser Photolysis – Laser Induced Fluorescence (PLP-LIF)[17-18], Pulsed Laser Photolysis – Resonance Fluorescence (PLP-RF)[19-20]; Pulsed Laser Photolysis-Cavity Ring-Down Spectroscopy (PLP-CRDS)[11] and indirect measurements using the relative rate method (RR).[21-22] IUPAC recommends $k_1^{\infty}=(9.0\times10^{-12})\times(\frac{T}{300\text{ K}})^{-0.85}$ for the high pressure limit rate coefficients in the 100-500 K temperature

range. This recommendation is based on the work of Vakhtin *et al.*[17], which is in good agreement with the measurements by Fulle *et al.*[23] Nielsen *et al.*[24] and Lloyd *et al.*[25]

The temperature and pressure dependencies of the ethylene + OH reaction have been extensively explored in previous investigations. Even though the bulk of the experimental literature is focused on temperatures above 298 K, the studies of Vakhtin *et al.*,[17] and Cleary *et al.*[11] have covered lower temperatures. Vakhtin *et al.* [17] have studied the reaction in the 96 – 296 K temperature range and 0.2 – 100 Torr of N_2 via PLP-LIF using a pulsed Laval nozzle apparatus. Using the Troe formalism[26], they have extrapolated their pressure dependent measurements to the high pressure limit, giving a temperature dependence in the form of $k_{1a}^{\infty}=(8.7 \pm 0.7)\times10^{-12}\times(\frac{T}{300\ \mathrm{K}})^{-0.85 \pm 0.11}$ cm^3 molecule^{-1} s^{-1}. These results were later questioned by the theoretical study of Greenwald *et al.*[18] and the experimental investigation by Cleary *et al.*[11] Greenwald was unable to obtain a good agreement between the high pressure rate coefficients reported by Vakhtin and the bulk of the previous literature investigations. However, a good agreement is observed when the pressure dependent rate coefficients measured by Vakhtin *et al.* are compared to estimates for the same experimental conditions, computed via Master Equation (ME) modelling.[27-28] The authors conclude that the disagreement observed for the high pressure coefficients could be caused by an inappropriate extrapolation of $k_{1a}(T,p)$, since Vakhtin's measurements were performed at very low pressures, far from the onset of the high pressure limit.

Cleary *et al.*, on the other hand, have investigated the C_2H_4 + OH reaction via PLP-LIF, exploring the 200 – 400 K temperature range, in pressures ranging from 5 to 600 Torr of He and N_2. They also performed additional measurements via PLP-CRDS at 100-760 Torr of SF_6. They utilized the MESMER package[27] to optimize the energy transfer parameter ($\langle\Delta E\rangle_{d,M}$), the pre-exponential factor and the temperature dependence of R1a, in the form of equation E1, using a large set of $k_{1a}(T, p)$.

$$k_{1a}^{\infty}=A\times\left(\frac{T}{298\ \mathrm{K}}\right)^{n} \qquad \text{E1}$$

The best-fit parameters were then used to calculate the pressure dependent coefficients at the experimental conditions of Vakhtin *et al*. Their procedure significantly underestimated the values reported by Vakhtin and the authors suggest that a more dramatic negative temperature dependence of k_{1a}^{∞} could reduce the discrepancy. They also acknowledged that the theoretical level at which the system was described in their own study may be inappropriate. They have treated the problem as a single well system, and in contrast, a two transition state model was employed in the work of Greenwald *et al*, who as described previously, managed to reconcile the literature measurements.

The kinetic isotope effect of this reaction has been explored by Liu *et al*.[15] in the 343 – 1173 K temperature range and has provided insightful mechanistic information. In their work OH radicals were generated via electron beam pulse radiolysis of water and detected via resonance absorption. This temperature range covers a regime where OH addition dominates, but also those where the dissociation back to reagents competes with the addition, as well as conditions at which the H-abstraction is likely the most important process. Between 343 K and 563 K, no difference was observed between OH + C_2H_4 and OH + C_2D_4 ($k_{OH+C2H4} = k_{OH+C2D4} = 1.65 \times 10^{-12}$ exp(480/T) cm^3 $molecule^{-1}$ s^{-1}) reactions as well as between reactions OD + C_2H_4 and OD + C_2D_4 ($k_{OD+C2H4} = k_{OD+C2D4} = 1.35 \times 10^{-12}$ exp(480/T) cm^3 $molecule^{-1}$ s^{-1}). However, as the rate coefficients indicate, the OH pairs are 22% faster than the OD ones, suggesting a secondary isotope effect, consistent with an OH/OD addition mechanism where no O-H or C-H bonds are formed or broken.[29] In the fall-off regime, statistical-weight effects for the hot adducts ($OH\text{-}C_2H_4^*$ or $OH\text{-}C_2D_4^*$) back to reagents would justify a reverse isotope effect. In the high pressure limit however, R2 should dominate and the ratio between $k_{OH+C2H4}$ and $k_{OH+C2D4}$ gets close to the unity. The experiments by Liu *et al*. were performed at 1 atm of argon and given the lack of isotope effect between $k_{OH+C2H4}$ and $k_{OH+C2D4}$ (and $k_{OD+C2H4}$ and $k_{OD+C2D4}$), the high pressure limit assumption was made in this temperature range. These results have also been compared to estimates via conventional

transition state theory (TST), showing a very good agreement. Internal isotope scrambling is considered unimportant under their experimental conditions since it would not only mean a primary isotope effect, which as discussed previously has not been detected, but because no relevant OH signal has been detected in OD + C_2H_4 experiments. Above 720 K, the authors have determined a positive activation energy of approximately 5 kcal mol^{-1}. In this case, while a primary isotope effect is observed between OH + C_2H_4 and OH + C_2D_4, a secondary effect is detected between the OH + C_2H_4 and OD + C_2H_4 reactions. These results are consistent with an abstraction mechanism and were also verified and confirmed via a classic TST calculation. They observed small systematic under prediction of the experimental rate coefficients which was partially justified by the lack of quantum mechanical tunnelling effects in the theoretical calculations. While the primary isotope effect is caused by the difference in activation energies (H or D abstraction), the secondary one is due to statistical-weight effects.

At elevated temperatures, where the abstraction chemistry should start to dominate, two conflicting studies covering relatively wide temperature ranges are found in the literature: measurements via electron beam pulse radiolysis of water coupled with resonance absorption detection of OH by Liu *et al.*(1987)[30] (T = 343 - 1173 K) and the PLP-LIF measurements by Tully (1988)[16] (T = 650 – 901 K). A literature review published by Baulch *et al.*[31] a few years later, in 1992, recommends the measurements reported Tully. The rate coefficients reported by Liu *et al.* are systematically greater than those presented by Tully, and is suggested by the last that this was partially caused by the large C_2H_4 concentrations employed by Liu *et al.* in their study. According to Tully, this caused the time span of experimental traces to be too short in order to clearly discriminate the abstraction channel from the OH addition. Tully has investigated the fact that non-exponential OH traces were collected at the temperatures of his work, and making the assumption that the chemistry is dominated by the H abstraction, accounted for the deviations from exponential behaviour as diffusional losses. According to his work, the abstraction is the dominating channel above the temperature of 650 K.

Liu *et al*. [30] on the other hand have fitted simple exponential equations to their measurements to extract pseudo-first order rate coefficients and calculate the second order rate coefficients $k_1(T, p)$ from bimolecular plots, although their experimental data clearly shows non-exponential behaviour at 603 K. From the measured rate coefficients and using a steady state approximation of the excited C_2H_4-OH*, the temperature dependence of the abstraction coefficients were obtained as well as those related to the addition ones. According to their results, the abstraction only dominates the chemistry above 748 K. However, a direct comparison to the measurements by Tully can be misleading given that the experiments were done at different pressures and buffer gases: while Tully covered the 100-350 Torr pressure range using He for ~90% of their measurements, Liu *et al*. employed argon as the buffer gas and a unique pressure of 760 Torr. It is important to note that the definition of a region where the abstraction dominates depends on the pressure dependence of the addition reaction.

The chemistry of C_2H_4 at elevated temperatures (T>900 K) is of particular interest for combustion chemistry.[32-33] The simplicity of this alkene is attractive for the prediction of the chemistry of larger hydrocarbons. A satisfactory understanding of the high temperature chemistry of C_2H_4 could potentially translate into improvements of the current combustion models. The vinyl radical formed from the hydrogen abstraction from ethylene is also interesting for the combustion of hydrocarbons in general.[33] Moreover, ethylene is a common intermediate specie in the combustion of large hydrocarbons reinforcing the importance of the sub-mechanism of the ethylene oxidation.[32] Due to this evident applicability to combustion systems, measurements of the H-abstraction rate coefficients above 900 K were in general obtained from mechanistic fits of complex reactive systems like flames. This was the case for the work of Westbrook *et al*.[32] and Bhargava and Westmoreland.[33] Such complex models naturally introduce heavily significant errors in the estimates, and for this reason, these studies will covered in a less detailed manner.

The work of Westbrook *et al.*[32] was performed in a jet-stirred reactor between 1003-1253 K. Measurements of H_2, C_2H_4, CH_4 and CO_2 were collected as a function of the reactor temperature and, using a numerical combustion model, the authors estimated rate coefficients which agree with the previously discussed measurements of Tully. However, this agreement is based on a very poor fit of their model to their measurements. Even though the authors do not quote errors for their estimates, it is important to note that they will be very significant. Nonetheless, their recommendation for the abstraction rate coefficient is $k_{1b} = 3.32\times10^{-11}\exp(\frac{-2897\ \mathrm{K}}{T})$ cm^3 molecule^{-1} s^{-1}.

Similarly, estimates by Bhargava and Westmoreland[33] were based on mechanistic fits of laminar flame data. Molecular beam mass spectrometry was undertaken to monitor the composition of a flame enriched with C_2H_4/O_2 in the 1400-1800 K temperature range. A total of 42 individual species were mapped and the model fits have provided a modified Arrhenius temperature dependence for $k_{1b} = 9.182\times10^{-19}T^{2.31}\exp(\frac{-1459\ \mathrm{K}}{T})$ cm^3 molecule^{-1} s^{-1}.

Srinivasan *et al.*[34] have investigated the reaction in the 1463-1931 K temperature range using shock tube experiments and direct OH detection via multi-pass absorption spectrometry. The authors recommend a temperature dependence in the form of $k_{1b} = (10.2 \pm 5.8)\times10^{-10}\exp(\frac{-(7411 \pm 871)\ \mathrm{K}}{T})$ cm^3 molecule^{-1} s^{-1}. They also acknowledge that the work of Bhargava and Westmoreland[33], based on complex mechanistic fit to laminar flame data surprisingly agrees to their measurements, despite the complexity with laminar flame data.

A study by Vasu *et al.*[35] in which shock tube experiments were undertaken in order to study the abstraction in the ~970-1440 K temperature range was published in 2010. Experiments were performed in pressures between 1520 and 7600 Torr of argon. Their OH traces collected via absorption spectroscopy were fitted with a natural gas combustion mechanism from where k_{1b} was obtained. The authors provide a comparison with the previous literature, and

their measurements agree well with the shock tube study by Srinivasan *et al.*[34], the jet-stirred reactor measurements of Wetstbrook *et al.*[32] and the results of Bhargava and Westmoreland[33] based on molecular-beam mass spectrometry. Their recommended Arrhenius formulation for the abstraction is $k_{1b} = 3.4\times10^{-18} T^{2.745} \exp(\frac{-1115\ \mathrm{K}}{T})$ cm^3 molecule^{-1} s^{-1}. A summary of the high temperature data on R1 is presented in Figure 5.1.

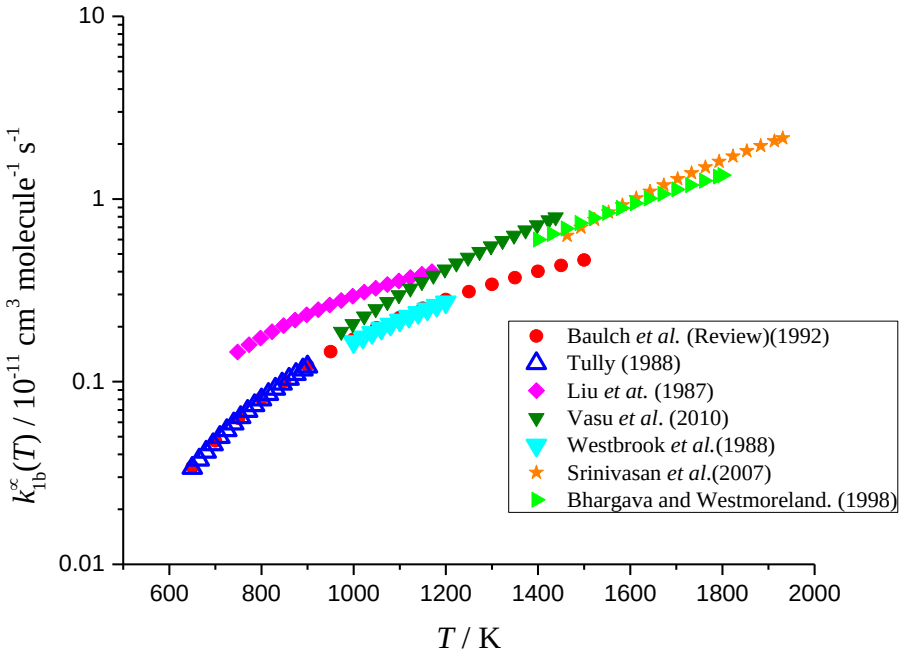

Figure 5.1 - Comparison of experimental recommendations for the ethylene + OH from different investigations. Red circles represent the recommendation from the review by Baulch *et al.*[31], blue open triangles refer to the work of Tully[16], pink diamonds refer to the work of Liu *et al.*[30], olive triangles correspond to the report of Vasu *et al.*[35], cyan triangles refer to the work of Westbrook *et al.*[32], orange stars correspond to the study of Srinivasan *et al.*[34], light green triangles refer the work of Bhargava and Westmoreland.[33]

The structural and chemical simplicity of the ethylene case makes the study of this reaction a benchmark for testing and validating analytical methods and theoretical calculations.[14, 36-37] For example, in the case of relatively simple dienes such as isoprene and 1,3-butadiene, multiple OH addition sites are available. The description of concurrent unimolecular decompositions of the

various possible adducts, with different enthalpies of formation and molecular properties make the analysis of such molecules more complicated when compared to the ethylene example.

Equilibrium traces, observed due to the competition between reactions R1a and R-1a, or analogue reactions for similar systems, can be used for a characterization of the equilibrium constant via analytical equations.[38] Under pseudo-first order conditions, the temporal profile of the OH radical can be described by a simple exponential equation, however, when the decomposition of the rising adduct becomes significant, the OH traces become multi-exponential in nature. For this reason, a more robust and versatile equation, capable of accurately describing the OH recycling is required. One must however, be aware of the implications of the use of a more versatile equation, with additional fitting parameters when describing temporal profiles. For example, the flexibility of the bi-exponential equation, which is commonly employed to describe radical recycling in chemical systems,[39-40] allows the description of non-exponential features with some ease. However, an inadvertent single trace analysis using this equation can easily suppress the existence of other relevant chemical processes, given the capability of this formulation to provide a good fit even when the chemistry of the system is not fully accounted for. This is the case because the large number of extra parameters can compensate the lack of the description of a real process in the model. For example, in the case of ethylene, the negligence of the hydrogen abstraction in competition with the addition of OH to describe experimental traces generated at elevated temperatures (T > 600 K) may lead to an overestimation of the addition reaction. Despite this fact and given the versatility of the fitting equation, it is possible that a "good" fit is obtained, with a low least-squares difference (χ^2), so that conclusions based only on the goodness of the fit are questionable.

A global fit of a big collection of experimental data is a reliable and computationally feasible way of testing the ability of a candidate model to describe the experimental observations. In this form of fitting, a few key

parameters of the system are defined as functions of local variables, which relate to and are valid only for one unit of analysis, in this work, an experimental trace. For example, in a global analysis, the pseudo-first order rate coefficient of the reaction of ethylene with OH is obtained through the product of the bimolecular reaction coefficient (*global variable*) with the concentration of the excess reagent (*local variable*, exclusive of a single trace). Alternatively, if multiple temperatures are to be analysed, the bimolecular rate coefficients can be defined in the form of a simple Arrhenius parametrization, where both the pre-exponential factor and the activation energy are defined as *global parameters*. *Global parameters* are shared by all the units of analysis, and in this example, used to calculate bimolecular rate coefficients at a given temperature. The establishment of these relationships imposes links that help constrain the analysis, so that experimental traces generated under the same experimental conditions are "forced" to have a pseudo-first order rate coefficient proportionally-related to the corresponding ethylene concentrations.

In a global analysis, the inability to describe a group of experimental traces may indicate an incomplete understanding of the chemistry involved, and can provide valuable insights for a satisfactory elucidation of the problem. In the ethylene example, the non-inclusion of the hydrogen abstraction in the model would probably result in a contrast between good fits for traces where OH addition dominates the chemistry, and poor fits where the abstraction becomes important. A systematic characteristic of traces where a poor fit is obtained may also provide new insights about the missing piece of the chemistry. An example will be explored later on in this chapter when analysing non-exponential traces obtained at elevated temperatures for the ethylene + OH reaction.

Despite being robust and versatile, global analysis requires extra care in data processing, and the complexity of the chemical system is rapidly translated into more complicated computational programming. The definition of multiple reaction constants as a function of other variables such as the temperature, the appropriate input of the experimental conditions of each trace and the adequate

linking of adjustable parameters are examples of tasks that make a global analysis a difficult procedure. The non-triviality of the computation of pressure-dependent rate coefficients makes the global analysis of traces generated under various pressures of different bath gases even more challenging.

In this study a new procedure to analyse the kinetics of pressure and temperature dependent reactions, through a direct global fit of a chemical model to the raw experimental traces is presented. The method represents a step forward in the ability to analyse relatively complex kinetic problems, and allows not only the determination of thermochemical and kinetic parameters, but also a mechanistic evaluation of the system. The unprecedented analysis of the ethylene + OH reaction yields a remarkable agreement with theoretical calculations, where a discrepancy between predictions and measurements are in the order of 1 kJ mol^{-1}, thus providing an excellent testbed of this method of data fitting.

5.2 METHODOLOGY

5.2.1 - Experimental details

Experiments were carried out using a conventional laser flash photolysis instrument where OH radicals were monitored *in situ* by laser induced fluorescence.[40-41] Detailed descriptions of the operation of such type of apparatus are provided in Chapter 2 and therefore only a succinct description is presented here. Ethylene (Air Products, 99.6%), the OH precursor (H_2O_2, 50% (w/w) Sigma Aldrich) and the carrier gas (N_2, BOC oxygen free) were flowed into the LPF-LIF instrument. Typical experimental pressures ranged from 50 to 250 Torr of N_2. Hydrogen peroxide was delivered through a temperature stabilized glass bubbler, and its concentration in the reaction cell was estimated based on its vapour pressure and the controlled flow rates. The initial OH concentration was estimated to be ~ 4×10^{12} molecule cm^{-3}, for the typical H_2O_2 concentration (~ 1×10^{15} molecule cm^{-3}), laser fluence (~15 mJ cm^{-2} or ~2×10^{16} photons cm^{-2}), crossection of the precursor at 248 nm (~1×10^{-19} cm^2

molecule^{-1} for H_2O_2)[42] and quantum yield, (2 for OH production from H_2O_2). Ethylene was prepared as a diluted mixture in nitrogen and stored in a 2 L glass bulb. Its concentration in the reaction cell (~1×10^{15} – ~1×10^{16} molecule cm^{-3}) was determined manometrically.

Under first-order conditions near room temperature, as discussed on many occasions in the previous chapters, the OH profiles have the form of an exponential decay, described by equation E2.

$$[OH]_t = [OH]_0 e^{-k't} \qquad \text{E2}$$

k' represents the pseudo-first-order rate constant, defined as:

$$k' = k_1[C_2H_4] + k_{loss} \qquad \text{E3}$$

Here k_1 is the bimolecular rate constant for reaction R1 and k_{loss} represents the rate coefficient for the losses due to diffusion and reaction of OH with its precursor. In this work, however, experiments were conducted at sufficiently high temperatures ($T \geq 560$ K) such that the equilibrium between OH/ethylene and the OH-C_2H_4 adduct was established. Previous studies show that the thermochemistry of the reaction is significantly sensitive to such measurements.[38, 43] Non-exponential experimental traces obtained at such conditions were treated using a new analytical approach, which involves the description of pressure-dependent reactions via Master Equation modelling. For this reason, and to guarantee a good understanding of the method, the next section (5.2.1) is dedicated to details of the *ab initio* calculations that gave support for the ME modelling of the OH addition to ethylene. Once the ME method is properly introduced, the analysis method is presented in more detail in the following sections (5.2.2-5.2.7).

5.2.2 - Supporting Ab Initio Calculations

Molecular structures and properties of the relevant species were computed with the M06-2X density functional theory method and the aug-cc-pVTZ version of Dunning's correlation consistent basis sets. Redundant internal coordinates were optimized using the Berny algorithm with the aid of the Gaussian 09 D.01 computational suite. Force-constant matrices, rotational constants, harmonic vibrational frequencies and zero-point energies required for ME calculations were all calculated with the M06-2X/aug-cc-pVTZ methodology. High performance coupled cluster calculations with single, double and triple excitations, the triples described iteratively (CCSD(T)), were undertaken for a more accurate estimate of the single point energies of the M06-2X/aug-cc-pVTZ stationary points. The single point energies were extrapolated to the complete basis set limit (CBS) using the aug-cc-pV*X*Z basis sets (*X*=2,3,4) and a mixed Gaussian/exponential extrapolation scheme as proposed by Peterson *et al.*[44]:

$$E(X) = E_{cbs} + Ae^{-(X-1)} + Be^{-(X-1)^2} \qquad \text{E4}$$

where $E(X)$ is the total energy calculated with the respective aug-cc-pVXZ basis set, E_{cbs} is the complete basis set extrapolation of the total energy, *A* and *B* are proportionality constants. A set of three equations containing three variables (E_{cbs}, *A* and *B*) is obtained from the use of three basis-sets, as presented in the following:

$$E(2) = E_{cbs} + Ae^{-(2-1)} + Be^{-(2-1)^2} \qquad \text{E5}$$

$$E(3) = E_{cbs} + Ae^{-(3-1)} + Be^{-(3-1)^2} \qquad \text{E6}$$

$$E(4) = E_{cbs} + Ae^{-(4-1)} + Be^{-(4-1)^2} \qquad \text{E7}$$

The unique mathematical solution of this set of equations yields the complete basis set extrapolation of the electronic energy (E_{cbs}), and the constants *A* and

B. The enthalpy of formation of the adduct, $\Delta_R H_{0K}(C_2H_4\text{-}OH)$, was calculated with this methodology and its value of 111.4 kJ mol^{-1} will later on be used for a comparison against an experimental determination. This will provide some insight on the accuracy of the novel analytical method being used.

As detailed in the context of the isoprene + OH reaction in Chapter 4, the hindered rotor approximation was also implemented here for the description of two internal rotations of the C_2H_4-OH adduct, related to small harmonic vibrational frequencies (< 350 cm^{-1}). Figure 5.2 shows the rotations described with the hindered rotor approach. The potential was constructed through a relaxed scan of the dihedral angle respective to the rotation, with steps of 15°. A partial structure optimization was performed at the end of every step, until a 360° coverage was obtained. In possession of the force constant matrix and the hindered rotor potentials, MESMER applies the procedure described by Sharma *et al.*[45] to project out the modes related to the internal rotations. If easily identifiable, the modes can be directly indicated to MESMER along with a list of harmonic vibrational frequencies.

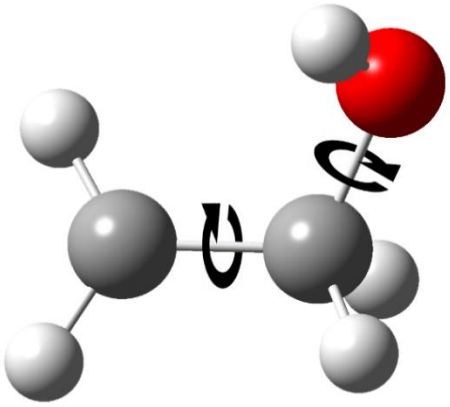

Figure 5.2 - Internal rotations described with the hindered rotor approach for the C_2H_4-OH adduct.

5.2.3 - Modifying the full Master Equation transition matrix

As discussed previously, the direct analysis of experimental traces in a global fashion represents a robust alternative not only for obtaining kinetic parameters, but also, testing a candidate chemical mechanism. The analysis will be presented in the context of the ethylene + OH reaction, but its use can be easily extended for the study of other gas-phase reactions. The global method is based on the coupling of four main steps which will be described below. For illustrative and simplicity purposes, examples of fits to single traces will be displayed, even though a global procedure is being applied. Unless stated otherwise, the bimolecular rate constants used in the model were defined as a function of temperature. After a more generic description of the method, a more programmatic view with a focus on the implementation thereof is provided.

The first step of the method (I) consisted of a Master Equation modelling of the pressure-dependent reactions involved, with the definition of the conventional ME transition matrix as covered in Chapter 2. In our context, this is the case of the OH addition, while the abstraction is taken to be pressure-independent. The solution of the ME problem ultimately leads to the computation of modelled traces which one could, in theory, consider for a direct comparison to experimental ones. However, the comparison using a simulated trace at the current stage will neglect unavoidable competing processes such as OH losses due to various other channels. To clarify this assertion, Figure 5.3 shows a comparison between an experimental trace obtained for the OH + C_2H_4 reaction at ~610 K and ~110 Torr of N_2, and the corresponding ME simulation. It is important to notice that this simulation considers only the equilibrium established between the OH addition and the unimolecular decomposition of the C_2H_4-OH adduct. The figure also includes an attempt to fit the trace using a single exponential equation (E2), represented by the black line.

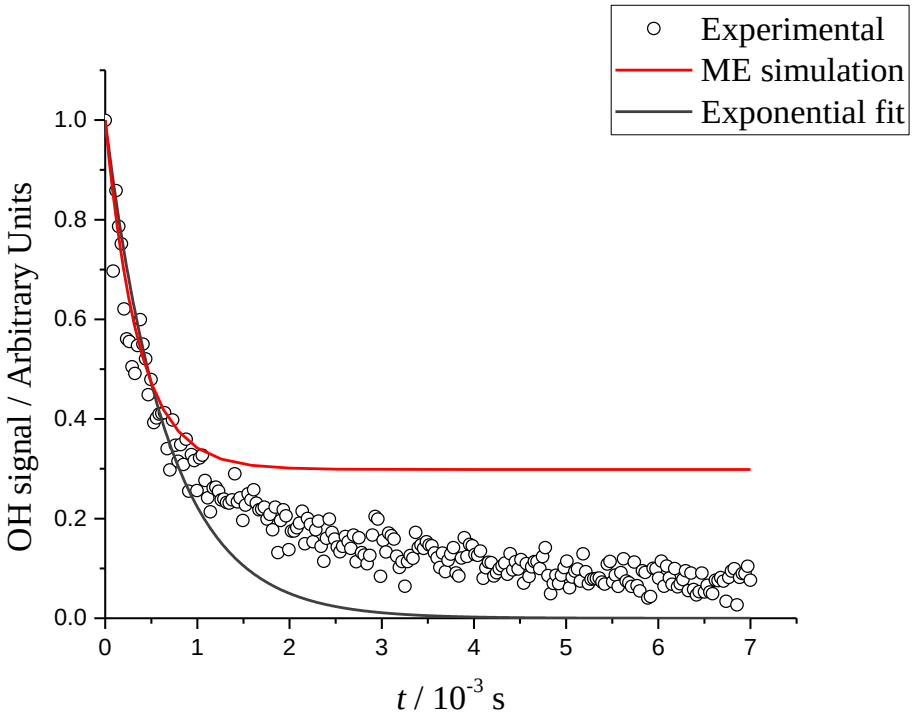

Figure 5.3 - Example of an OH trace recorded at ~610 K and ~110 Torr of N_2 using a conventional LFP-LIF instrument (open circles). $[C_2H_4] = 9.5 \times 10^{14}$ molecule cm^{-3}. The red line shows a Master Equation simulation under the same experimental conditions and the black line depicts a single exponential fit to the data.

The poor single-exponential fit evidences the establishment of the aforementioned equilibrium given that this trace was collected under pseudo-first order conditions. The ME simulation represents an idealized model, where OH can be consumed exclusively via its reaction with C_2H_4 or be reformed via unimolecular decomposition of C_2H_4-OH. However, as indicated previously, a real experiment incorporates intrinsic competing processes involving the OH radical. It is clear from this point that these processes need to be incorporated in the ME simulated traces in order to allow a direct comparison to the experimental ones. This need is addressed in the following step of the analysis technique. Competing processes will be incorporated as additional consumption or formation terms in the rate laws of the involved species.

The second part of the analysis procedure (II) consisted of the augmentation of the set of ordinary differential equations (ODEs), represented by the transition

matrix constructed in step 1, to incorporate new formation or consumption terms related to additional processes. These additional processes, such as the measurable OH loss due to its reaction with the precursor and due to diffusion, are not going to be treated as a function of internal energy. It is common practice of PLF-LIF experiments to measure k_{loss} (see equation E3) prior to the execution of an experiment involving the chemistry of interest. Due to its simplicity, this loss will be used as a first example of a process to be incorporated to the current transition matrix. The value of k_{loss} of the OH trace presented in Figure 5.3 was measured to be ~100 s^{-1}. This means that an additional consumption term is added as a constant loss to all the OH grains modelled via the ME, which will perturb the shape of the ME simulation presented in that figure. It is important to emphasize that this loss, which was experimentally measured in the absence of C_2H_4, is not being treated as a function of energy, but is simply spanned throughout all the grains of OH to impose an overall loss of that specie. Since the reaction of OH with its precursor does not influence the chemistry of interest (C_2H_4 + OH) beyond representing an alternative loss of OH, a ME model that incorporates explicitly the OH + H_2O_2 reaction would not present any feasible advantage, and would merely increase the computational costs. This fact justifies the incorporation of a simple constant loss term in the transition matrix to account for k_{loss}.

Once the transition matrix has been altered as described in step II, the third step can be undertaken (III) which consists of solving the new set of ODEs using the same procedure as discussed in detail in Chapter 2. Figure 5.4 depicts the fits presented previously along with the last one which incorporates k_{loss}.

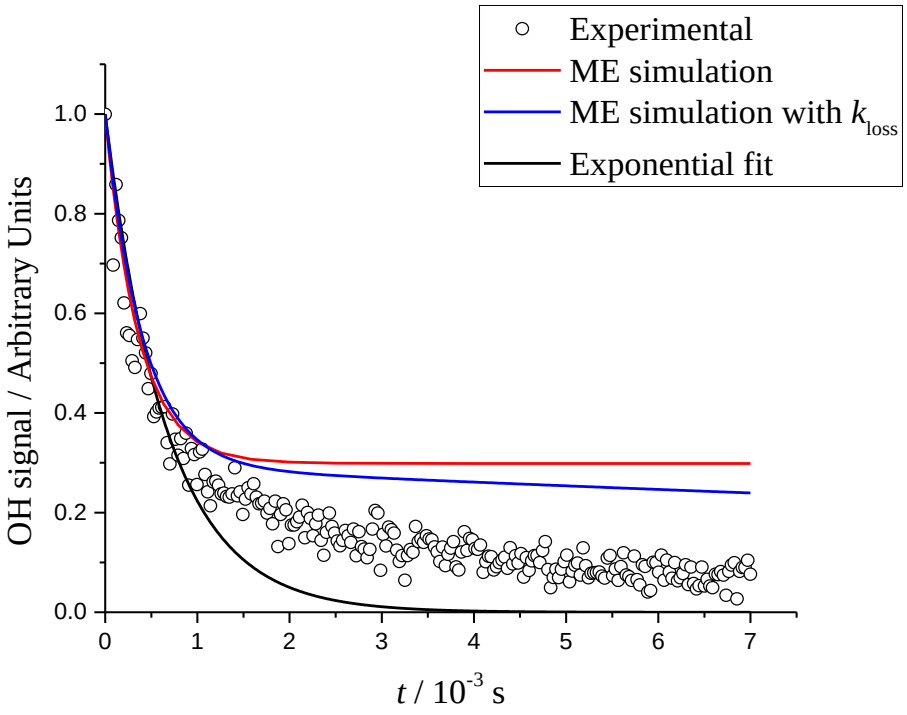

Figure 5.4 - Example of an OH trace recorded at ~610 K and ~110 Torr of N_2 using a conventional LFP-LIF instrument (open circles). $[C_2H_4]$ = 9.5 × 10^{14} molecule cm^{-3}. The red line shows a Master Equation simulation under the same experimental conditions and the black line depicts a single exponential fit to the data. The blue line represents a ME fit in which the transition matrix was altered to incorporate k_{loss} the sum of the pseudo-first order loss due to reaction of OH with its precursor and diffusion.

At the current stage it is clear that even though the inclusion of k_{loss} has moved the simulation in the correct direction, i.e., it has introduced a visible slope to the simulated trace (note the difference between the red and blue lines); it is evident that this was not sufficient to provide a good comparison to the experimental measurements. As indicated previously, this figure is a representative example from a total of 96 traces being fitted simultaneously. A careful inspection of all the traces indicates a systematic overestimation of the recycling by the model, as denoted by the blue line being on top of the black open markers. From this point, it seems logical to postulate that one or more significant processes are competing for and removing OH radicals from the system, given this systematic overestimation.

Two main candidates stand out as potential interferences: the first is a hydrogen abstraction, which as discussed in the introductory section, is known to be of significant importance for the chemistry of this reaction at elevated temperatures. The second is a possible loss of the C_2H_4-OH adduct, via for example, its reaction with O_2. Even though oxygen was not added intentionally in any of these experiments, H_2O_2 can potentially decompose to give O_2 and it is difficult to rule out the presence of small amounts of this gas in the system. This will be discussed further later on in this chapter, but an important thing can be noticed with regards to these two potential interfering channels: the H abstraction is a bimolecular process that involves ethylene. Therefore, its effect must scale appropriately with changes in the concentration of ethylene. On the other hand, the concentration of the adduct is limited by the deficient reactant, OH, and for this reason should be independent of the C_2H_4 concentration. This is where a global analysis stands out as being superior and more robust when compared to a single-trace analysis: these systematic aspects can be simply assessed in a global fashion by imposing a relationship between model parameters, such as bimolecular rate constants and their temperature dependencies. From this point, one can pick a piece of chemistry of preference, alter the transition matrix as explained previously in step II, solve the system again and proceed with another comparison.

If one assumes, for example, the loss of the adduct to be the missing piece of chemistry to be tested, and if this loss is known or easily measurable, then the problem is analogous to the case of the incorporation of k_{loss}. On the other hand, if this loss is not known, then this aspect leads to the fourth step of this analysis procedure, which is (IV) the definition of adjustable parameters followed by a mathematical minimization in order to obtain a good agreement between the solution of the ODEs and the experimental observations.

Typical adjustable parameters include: temperature dependencies of rate coefficients, energy transfer parameters for pressure-dependent steps and enthalpies of formation. This technique is being incorporated into the

computational package MESMER[27], which in the near future will be fully capable of dealing with such problems.

Our results indicate the occurrence of both the hydrogen abstraction and a removal of the adduct and these results will be discussed after the presentation of a slight modification in the method just described which, when valid, not only simplifies the treatment of the problem but also allows a more detailed presentation of the method. In reality, this slight simplification was used for all the calculations presented in section 5.3, dedicated to results and discussion. Section 5.2.4 presents the simplification while section 5.2.5 shows a practical application of it.

5.2.4 - Augmentation of the Bartis-Widom scheme

As discussed in Chapter 2, the Bartis-Widom (BW) analysis is a useful technique that allows a heavy simplification of the ME modelling via the suppression of the collisional relaxation kinetics. The ME calculations of the OH addition to C_2H_4 will basically yield two phenomenological rate coefficients, the first related to the addition itself and the second corresponding to the unimolecular decomposition of the adduct back to reagents. If one assumes the chemical model to be consisted of these two processes, where OH is taken to be the deficient reactant and ethylene is the excess reagent, then the rate laws of the involved species are those described by equations E8-E10.

$$\frac{\mathrm{d[OH]}}{\mathrm{d}t} = -k_{1a,BW}[\mathrm{OH}][\mathrm{C_2H_4}] + k_{-1a,BW}[\mathrm{HOC_2H_4}] \qquad \text{E8}$$

$$\frac{\mathrm{d[C_2H_4]}}{\mathrm{d}t} = 0 \qquad \text{E9}$$

$$\frac{\mathrm{d[HOC_2H_4]}}{\mathrm{d}t} = k_{1a,BW}[\mathrm{OH}][\mathrm{C_2H_4}] - k_{1a,BW}[\mathrm{HOC_2H_4}] \qquad \text{E10}$$

where $k_{1a,BW}$, and $k_{1b,BW}$ are the phenomenological rate coefficients that describe the interconversion between the involved species. Equations E8-E10 represent the set of coupled ODEs used to obtain the species profiles. The problem may be defined in a matrix formulation, as presented in Figure 5.5.

$$\begin{array}{|c|} \hline \dfrac{\mathrm{d}X}{\mathrm{d}t} \\ \hline X_1' \\ \hline X_3' \\ \hline \end{array} = \begin{array}{|cc|} \multicolumn{2}{c}{K} \\ \hline -k'_{1a,BW} & k_{-1a,BW} \\ \hline k'_{1a,BW} & -k_{-1a,BW} \\ \hline \end{array} \times \begin{array}{|c|} \hline X \\ \hline X_1 \\ \hline X_3 \\ \hline \end{array}$$

Figure 5.5 - Matrix formulation of the OH + Ethylene addition reaction as simplified via the Bartis-Widom approach.

where X_i' represents the rate of specie *i*, indexes 1 and 3 refers to OH and the C_2H_4-OH adduct respectively. As the concentration of C_2H_4 (i = 2) is taken to be constant, it was incorporated into $k'_{1a,BW}$ which is equal to the product $k_{1a,BW} \times [C_2H_4]$ and its rate law was therefore not included in the matrix scheme. The simplified transition matrix *K* as presented in Figure 5.5 can also be modified to account for k_{loss} or any other competing processes in analogy to the case presented for the full ME. The modified BW-transition matrix accounting for k_{loss} is presented in Figure 5.6.

$$\begin{array}{|c|} \hline \dfrac{\mathrm{d}X}{\mathrm{d}t} \\ \hline X_1' \\ \hline X_3' \\ \hline \end{array} = \begin{array}{|ccc|} \multicolumn{3}{c}{K} \\ \hline -k'_{1a,BW} & k_{-1a,BW} & -k_{loss} \\ \hline k'_{1a,BW} & -k_{-1a,BW} & 0 \\ \hline \end{array} \times \begin{array}{|c|} \hline X \\ \hline X_1 \\ \hline X_3 \\ \hline 1 \\ \hline \end{array}$$

Figure 5.6 - Matrix formulation of the OH + Ethylene addition reaction as simplified via the Bartis-Widom approach, modified to incorporate kloss.

The boundary conditions for these ODEs are the initial concentrations of the species: as $X_1(0) = 1$, $X_3(0) = 0$. From this point the problem may either be solved algebraically or via a numerical integration procedure. The main advantage of the use of the BW transition matrix relies on its simplicity, which allows its transportation to alternative software such as MATLAB[46], enabling a wide range of mathematical treatment to the data. This versatility is also translated into more freedom, for example, to link adjustable parameters. The main disadvantage of this approach is that, unlike the direct modification of the full ME, it relies on the numerical separation of the chemically significant eigenvalues (CSE) from those related to internal energy relaxation (IERE).

Therefore, in the case where the CSEs are not clearly separated, the BW transition matrix may not be accurate enough to be used and the species profiles are not reliable enough. It is important to clarify that in the present study this has not been observed, i.e., a separation of more than one order of magnitude was observed for all the experimental conditions explored in the current thesis. This aspect will be discussed in the Results and Discussion section (5.3).

Due to its validity and simplicity, the experimental data have been in reality explored via the use of the BW transition matrix. To improve the quality of the fits, as exemplified in Figure 5.4, the transition matrix was modified to incorporate a competing H-abstraction and unimolecular losses of the C_2H_4-OH adduct. Even though this adduct loss might be occurring via a bimolecular channel (via O_2 reaction for example), the use of a unimolecular parameter provides an estimate of how fast this process occurs compared to the recycling of OH. Furthermore, if one assumes an educated guess for the bimolecular rate coefficient of the C_2H_4-OH + O_2 reaction, an estimate the concentration of O_2 getting into the reaction cell can be obtained.

5.2.5 - Accounting for hydrogen abstraction and C_2H_4-OH loss in the BW scheme

At low temperatures, the chemistry of the OH addition represents the bulk of the mechanism that defines the experimental observations. However, in a real high temperature experiment (T>500 K), as discussed previously, competing loss processes of the involved species also play a significant roles that will interfere in experimental measurements. For a typical laser flash photolysis-laser induced fluorescence experiment, on a millisecond timescale, heterogeneous chemistry is negligible and a better control over possible contaminants is obtained. However, OH radicals are lost via reaction with the precursor and small leaks combined with O_2 generation from H_2O_2 decomposition can potentially introduce sufficient O_2 to consume a significant amount of the HO-C_2H_4 specie. In the previous section it was demonstrated that chemistry represented by reactions R1a and R-1a is not sufficient for a

direct comparison between simulated profiles and raw experimental OH traces. Therefore, accounting for the hydrogen abstraction and the additional loss processes of OH and the C_2H_4-OH species (R1b, Rloss, R3) need to be incorporated in the ME simulated traces:

$$C_2H_4 + OH \xrightarrow{k_{1b}} H_2O + \cdot C_2H_3 \quad \text{(R1b)}$$

$$OH \xrightarrow{k_{loss}} \text{Loss} \quad (R_{loss})$$

$$C_2H_4\text{-}OH \xrightarrow{k_3} \text{Loss} \quad \text{(R3)}$$

The existence of the process represented by R3 was identified by Diau *et al.* [38], who have studied the OH + C_2H_4 reaction in the 544-673 K temperature range and 278-616 Torr of He using PLP-LIF. They report significant C_2H_4-OH losses which increased with temperature, $k_3 = \left(8.8^{+25}_{-1.5}\right) \times 10^9 \exp\left(\frac{-10400^{+1600}_{-400}}{T}\right)$ s^{-1}, but were unable to define the mechanistic pathway responsible. The authors have also measured the rate coefficients for the formation (k_{1a}) and decomposition (k_{-1a}) of the C_2H_4-OH adduct at elevated temperatures via a bi-exponential analysis. Their estimates for the enthalpy of formation of the adduct (126.78 ± 3.35 kJ mol^{-1}) and entropy change ((12.93 ± 0.41) $\times 10^{-2}$ kJ K^{-1} mol^{-1}) were extracted from a van't Hoff plot using the equilibrium constants measured at various temperatures.

In the current thesis, reactions R1b, R_{loss} and R3 were introduced in the set of equations E8, E9 and E10 as simple consumption terms for the involved species, and at least one additional ODE is necessary to describe the evolution of the products of the abstraction: H_2O and C_2H_3. The chemical path behind the loss of the C_2H_4-OH specie is unknown at first, but the importance of this consumption term in our measurements was explored by defining it as a fitted parameter. The abstraction rate coefficient is defined as an Arrhenius equation to account for its temperature dependence since a significant temperature range was covered. To elucidate the necessary alterations, the modified set of equations due to the inclusion of reactions R1b, R_{loss} and R3 is presented in the following:

$$\frac{d[OH]}{dt} = -(k_{1a,BW}[C_2H_4] + k_{1b}[C_2H_4] + k_{loss})[OH] + k_{-1a,BW}[HOC_2H_4] \quad \text{E11}$$

$$\frac{d[C_2H_4]}{dt} = -(k_{1a,BW} + k_{1b})[OH][C_2H_4] + k_{-1a,BW}[HOC_2H_4] \quad \text{E12}$$

$$\frac{d[HOC_2H_4]}{dt} = k_{1a,BW}[OH][C_2H_4] - (k_{-1a,BW} + k_3)[HOC_2H_4] \quad \text{E13}$$

$$\frac{d[H_2O]}{dt} = \frac{d[\cdot C_2H_3]}{dt} = k_{1b}[OH][C_2H_4] \quad \text{E14, E15}$$

The terms related to the new pieces of chemistry included are highlighted in red. An explicit description of the rate of the excess reagent, C_2H_4, is included. In equation E12 the right hand side of this equation is approximately equal to zero given that the current experiments were done under pseudo-first order conditions with a large excess of C_2H_4. In the current work, this set of ODEs was primarily solved via a numerical integration procedure using the ODE suite available in MATLAB, capable of dealing with stiff problems.[47] The list of adjustable parameters include (I) the ME energy transfer parameter for N_2, $A_{<\Delta E>d,N2}$, and (II) its temperature dependence m ($<\Delta E>_{d,N2} = A_{<\Delta E>d,N2} \times (T/298)^m$, (III) the enthalpy of formation of the C_2H_4-OH adduct, (IV) the temperature dependence of the OH addition, n, as described by equation E1, (V) the pre-exponential factor, $A_{1b,}$ and (VI) the activation energy, Ea_{1b}, of the abstraction reaction ($k_{1b}=A_{1b}\times\exp(-Ea_{1b}/RT)$) and finally, (VII) the aforementioned adduct loss, k_3. Tests in which one or more of these parameters were fixed were also undertaken for an evaluation of their importance. For example, the abstraction was allowed to float with bounds set around values reported in the previous literature ($k_{1b}=3.4\times10^{-11}$ exp(-24.86 kJ mol^{-1}/RT)), as supported by the investigations of Tully[16] and Baulch *et al.*[31] in the 650-1500 K temperature range.

Before the results are presented, it is important to define how the adjustable parameters were set in MATLAB and how important it is to pre-weight the experimental data so that the analysis does not favour particular traces with very high absolute signals. Section 5.2.6 explains the terminology and applications of the various types of adjustable parameters used in the global analysis. Section 5.2.6 also presents how the goodness of fit is evaluated.

Section 5.2.7 explains why it is primarily important to pre-weight the experimental traces in order to avoid undesirable biases in the analysis.

5.2.6 - A more programmatic view of the model parameters

As indicated previously global analysis is a very robust, consistent and versatile analysis technique, suitable for the exploitation of large amounts of data. In a global procedure, fitting operations of multiple traces are brought together in order to provide the best overall agreement of the model to the complete data set. During the procedure, a limited number of parameters, which may be fixed or floated, are shared by all the individual fits. These parameters, referred to as *global parameters*, will directly influence the model prediction of every single trace, and therefore tend to have a greater impact on the overall goodness of fit. For example, the pre-exponential factor and energy of activation of the abstraction reaction are shared by all traces being analysed. The bimolecular abstraction rate coefficient, used to construct a model prediction, is always obtained based on these two parameters and the corresponding temperature. Moreover, if a trace i has a temperature T_1 and a trace j was collected at temperature T_2, then $k_{1b}(T_1) = A_{1b} \times \exp(-Ea_{1b}/RT_1)$ and $k_{1b}(T_2)=A_{1b}\times\exp(-Ea_{1b}/RT_2)$. Note that both are calculated based on the aforementioned *global variables*. This aspect imposes a constraint that reinforces the kinetic consistency of the results obtained in the global fitting procedure. For example, for a well-defined energy barrier, if $T_1>T_2$, then not only is $k_{1b}(T_1)$ greater than $k_{1b}(T_2)$ but both are linked via a kinetically consistent Arrhenius formulation.

On the other hand, there are model parameters that can cause interferences exclusively in individual model predictions and hence, tend to have a smaller impact on the overall goodness of fit. These are referred to as *local variables* or *local parameters*. In each trace, the initial fluorescence signal from the OH radicals (t=0) collected by a photomultiplier is very uncertain, and for this reason it is common practice to have it as an adjustable parameter. This parameter, however, is not linked or related in any way to the initial OH concentration of the other traces or the other listed parameters, and represents

therefore an example of a *local parameter*. Despite the less significant direct impact on the quality of the global adjustment, *local variables* can eventually cause slight variations on the returned optimized parameters, especially when inappropriate guesses and bounds are set. In this case, the optimization algorithm might try to compensate the effect of this bad guess with significant changes in the other parameters. This issue can be minimized if a large number of traces are considered, making the identification of outliers a simpler task.

A third and final category of parameters is often useful and need to be addressed here: these are the *local-global parameters*. Similarly to the case of *global parameters*, these ones are shared by two or more traces, but not by the totality of the data set as it is the case for the *global* ones. Examples of local *global parameters* are k_{loss} and k_3. This is justified for $k_{loss,}$ for example, because this loss is typically kept constant throughout an experiment performed at a given temperature and pressure. Once the temperature and pressure are set, OH traces are collected in the course of a few hours depending on the quality of the signal being acquired. Given that the H_2O_2 flow was stable, all traces collected during this course of experiments will therefore share the same k_{loss}. However, if new experiments are performed with a different OH precursor or at different temperatures and pressures, it is likely that the value of k_{loss} will change as well. Moreover, if new traces at significantly higher temperatures are to be collected, it might be necessary to increase the H_2O_2 flow because this high temperature can potentially enhance a thermal decomposition of H_2O_2, changing k_{loss} for the next set of traces. As a general rule, each trace collected in the same day, under the same experimental conditions is assumed to have the same k_{loss}.

Analogously, if one postulates that the adduct loss occurs unimolecularly, it is also reasonable to assume this loss should be the same for the traces generated under the same experimental conditions. On the other hand, if a reaction with O_2 is invoked, this assumption would remain appropriate (a shared k_3 per experimental condition) since O_2 is likely to be produced primarily via the decomposition of the OH precursor, whose concentration is maintained

constant via the use of calibrated mass-flow controllers. With these aspects presented, the implementation of both k_{loss} and k_3 as *local-global parameters* is justified. The main difference between these two relies on the fact that, while a list of k_{loss} values, related to each set of experiments, can be easily measured and fed into the fitting procedure as fixed values, the list of k_3 (one for each T, p and day) is floated by the optimization algorithm in order to provide a good fit to the whole set of experimental data. The need to define *local-global parameters* and their complex linking is an example of an advantage of the use of the BW analysis supported by an external piece of software such as MATLAB. Figure 5.7 presents a flow chart of the procedure based on the BW analysis supported by MATLAB.

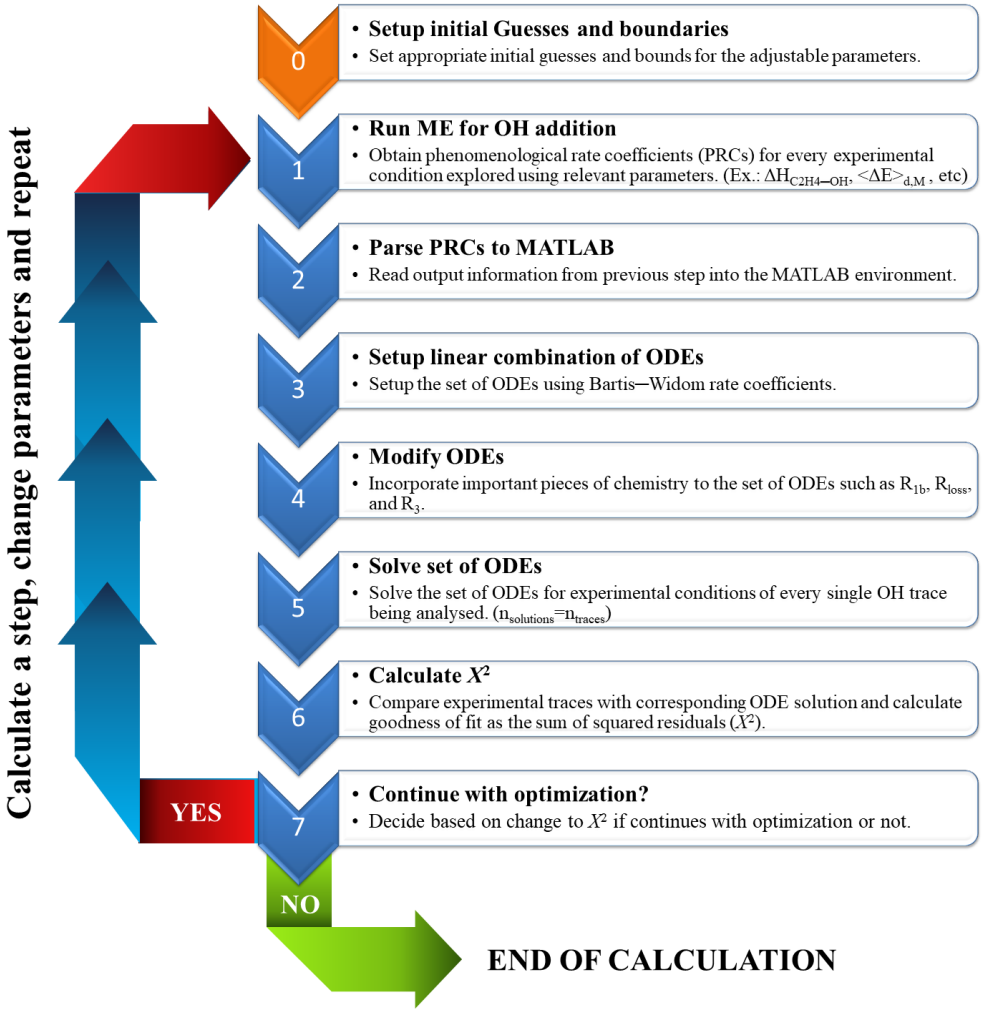

Figure 5.7 - Flow chart of the fitting based on BW rate coefficients followed by ODE modification.

As observed, the objective function to be minimized is the overall sum of squared residuals χ^2, as a measure of the goodness of fit. For *n* experimental traces, χ^2 is calculated as defined by equations E16 and E17:

$$\chi_i^2 = \sum_{j=1}^{k_i} (y_{j,\text{calc}} - y_{j,\text{exp}})^2 \qquad \text{E16}$$

$$\chi^2 = \sum_{i=1}^{n} \chi_i^2 \qquad \text{E17}$$

where χ_i^2 is the sum of squared residuals associated to the *i*th experimental trace, k_i is the number of points of the *i*th trace, $y_{j,\text{exp}}$ is the *j*th point within experimental trace *i* and $y_{j,\text{calc}}$ is the corresponding model prediction. The overall χ^2 is then calculated as a summation of all χ_i^2. The unweighted linear combination presented in equation E17 raises a slight concern regarding the importance attributed to each individual trace during the minimization procedure. This aspect that will be covered in the subsequent section where it is explained how the data are weighted to prevent this issue.

5.2.7 - Pre-weighting of experimental data

In LPF-LIF experiments, the OH induced fluorescence is typically collected by a photomultiplier whose voltage control enables the enhancement of the total signal being collected. However, this increase also leads to an increase of background counts, so that a voltage increase does not necessarily translate into an improvement of the signal/noise ratio. Increasing the voltage can be useful, for example, for tuning the wavelength of the probe if this has shifted away from the peak of the ~282 nm excitation line, a common effect observed when the temperature of the room varies during the course of an experiment.

Varying the photomultiplier voltage also alters the absolute scale of the OH signal being collected, and this difference needs to be addressed to avoid unfairly favouring the high signal traces when minimizing χ^2. Traces with larger absolute OH signals will tend to have a greater impact on the sum of squared residuals, causing the optimization algorithm to “focus” on getting these traces right, while traces with lower absolute signals will tend to be

ignored. The main assumption taken here is that every experimental trace is, at least at a first glance, equally important. Given that experiments are performed under pseudo-first order conditions, the absolute scale of the traces should not represent a crucial parameter.

To address this issue, all the experimental traces have been pre-weighted with the use of a flexible bi-exponential equation (see Chapter 4, equation E5), an analytical formulation commonly used for studying radical recycling in simple systems. Every experimental trace has been fitted individually with the bi-exponential equation, and at this stage, no significant importance was given to the obtained parameters. The qualities of the bi-exponential fits are very good in general, as exemplified in Figure 5.8. Additionally Figure 5.9 presents the residual plot of that fit, where the points are evenly distributed around the reference line placed at y=0.

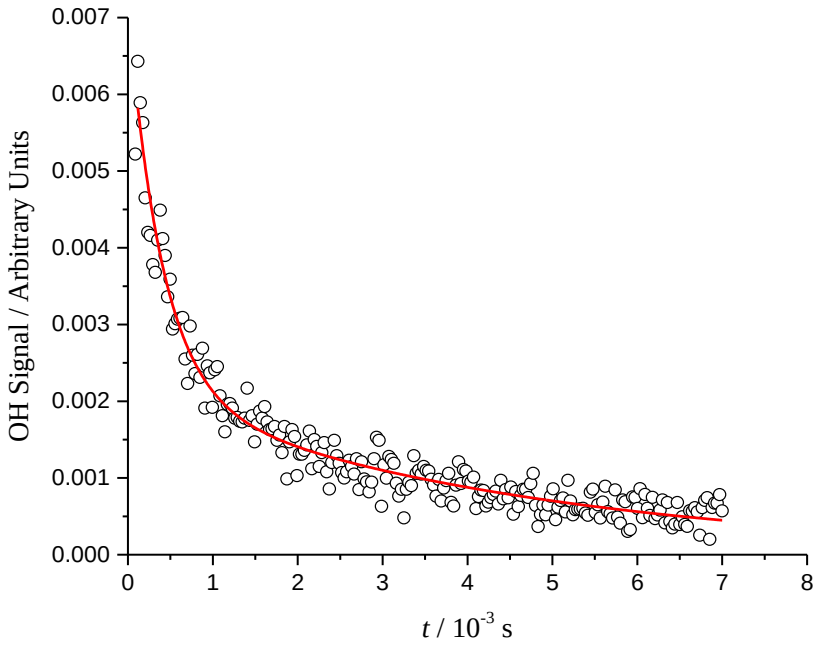

Figure 5.8 - Example of a bi-exponential fit to an OH trace related to the OH + C_2H_4 reaction. T = 610 K p = 110 Torr and [C_2H_4] = 9.5 × 10^{14} molecule cm^3. Points averaged after 4 scans.

From this fit, it is clear that the bi-exponential equation is capable of describing the observed chemistry. To weight the data appropriately, a second assumption is taken: the flexible bi-exponential fit is a good approximation to

the best possible fit of a suitable model to the data. This assumption means that the χ_i^2 value obtained for this bi-exponential fit is a good approximation to the lowest possible sum of squared residuals, and will be referred to as $\chi_{i,\min}^2$. If one then divides the points of the experimental trace by the squared root of this number, i.e., $\chi_{i,\min}$, and attempts another fit, then the new sum of squared residuals ($\chi_{i,\text{new}}^2$) can be calculated in an analogous manner to that previously presented:

$$\chi_{i,\text{new}}^2 = \sum_{j=1}^{k_i} \left(\frac{y_{j,\text{calc}} - y_{j,\text{exp}}}{\chi_{i,\min}}\right)^2 = \frac{1}{\chi_{i,\min}^2} \sum_{j=1}^{k_i} (y_{j,\text{calc}} - y_{j,\text{exp}})^2 \qquad \text{E18}$$

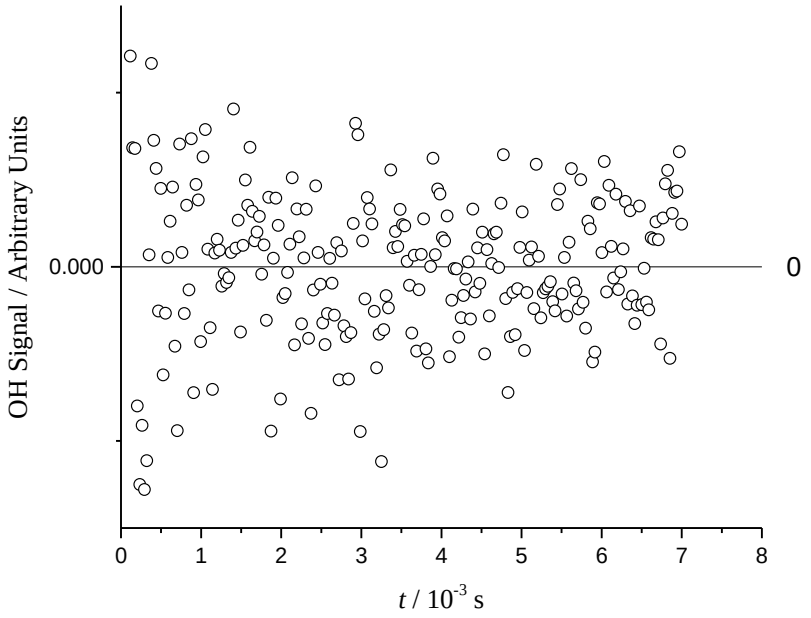

Figure 5.9 - Residual plot of the bi-exponential fit presented in Figure 5.8. T = 610 K p = 105 Torr and $[C_2H_4]$ = 9.5 × 10^{14} molecule cm^3. Points averaged after 4 scans.

From equation E18, it is clear that at the limit where $\sum_{j=1}^{k_i} (y_{j,\text{calc}} - y_{j,\text{exp}})^2$ approximates $\chi_{i,\min}^2$, $\chi_{i,\text{new}}^2$ is unity. This eliminates the issue associated to the existence of traces with significantly different signal heights. Note that independent of the height, a trace has a *chance* to add a total of one to the overall χ_i^2 if its fit resembles the corresponding bi-exponential one. If the new

fit is not as good as the corresponding bi-exponential, then $\sum_{j=1}^{k_i}(y_{j,\text{calc}} - y_{j,\text{exp}})^2 > \chi^2_{i,\text{min}}$ and therefore $\chi^2_{i,\text{new}} > 1$. The bi-exponential equation was used in this chapter, but for other systems, other appropriate equations (tri-exponentials, tetra-exponentials, etc) can also be used to fit experimental data in order to determine the weight associated with each individual trace. If no appropriate analytical equation is available, the traces can also be fitted with a numerical solution of a reaction scheme, allowing the estimation of $\chi_{i,\text{min}}$. It is important to inspect the resulting fits that generate the individual $\chi_{i,\text{min}}$ to make sure the model function (analytical or numeric) is capable of successfully describing all the traces under analysis and no bias towards a certain group of traces is inadvertently introduced. For example, new chemical processes can be turned on at elevated temperatures, and the lack of description of these processes in the model function can lead to elevated $\chi_{i,\text{min}}$ (poor fit) to the traces where this new piece of chemistry is important. As a result, the elevated $\chi_{i,\text{min}}$ would imply undesirable lower weights for these traces. For this reason, the inspection of the resulting fits of the weighting procedure described in this section is crucial.

In summary, as indicated by the left-hand side of equation E19, a weighted sum of squared residuals ($\chi^2_{i,\text{new}}$) can be obtained calculated as a moderate average of χ^2_i, where the weight corresponds to $1/\chi^2_{i,\text{min}}$. A good fit is obtained when $\chi^2_{i,\text{new}}$ associated with a trace is close to unity, and the new global sum of squared residuals χ^2_{new} is therefore close to the total number of traces (one per trace). This weighting procedure was applied to all traces prior to the execution of the ME global described in detail in sections 5.2.3-5.2.6.

5.3 RESULTS AND DISCUSSION

5.3.1 - Interpretation of the ethylene + OH ⇄ HO-C_2H_4 data.

A list of the experimental conditions at which the 96 experimental traces were collected is presented in Table 5.1. The table also includes a list of the chemically significant eigenvalues and the lowest internal energy redistribution eigenvalues obtained with the best-fit parameters, included in Table 5.2. The table shows a very clear separation between CSEs and IEREs of several orders of magnitude for all experimental conditions.

Table 5.1 - List of experimental conditions, the chemically significant eigenvalue and the lowest internal energy redistribution eigenvalue. Eigenvalues were obtained with the ME parameters presented in Table 5.2.

T / K	p / Torr	Number of Traces	$[C_2H_4]$ / 1×10^{15} molecule cm^{-3}	k_{loss} / s^{-1}	|CSE| / 10^3 s^{-1}	|Lowest IERE| / 10^7 s^{-1}
563	116	8	1.1 – 8.9	107	2.68	2.09
563	210	8	1.1 – 8.2	244	3.16	3.79
580	58	8	1.1 – 8.5	122	2.04	0.98
610	106	12	0.9 – 7.3	96	2.78	1.60
614	219	9	1.0 – 6.8	143	3.66	3.22
634	58	8	1.0 – 7.8	171	2.65	0.81
647	116	7	1.0 – 7.8	83	4.25	1.55
672	58	8	0.9 – 7.0	185	4.52	0.73
676	250	6	2.9 – 8.0	107	9.16	3.01
694	119	8	0.9 – 7.2	88	9.33	1.38
696	58	8	0.9 – 6.9	286	6.75	0.69
723	114	6	2.5 – 6.6	80	15.27	1.25

An excellent overall agreement was obtained when fitting the experimental data incorporating R_{loss}, R3 (loss of the adduct) and R1b (H abstraction). Figure 5.10 returns to the example trace that has been used to illustrate the improvement of the fits upon the addition of new pieces of chemistry, now including the fit with the complete modification of the set of ODEs. As expected, a superior fit is obtained for all the 96 traces explored in the current when the set of ODEs is augmented with the mentioned chemistry.

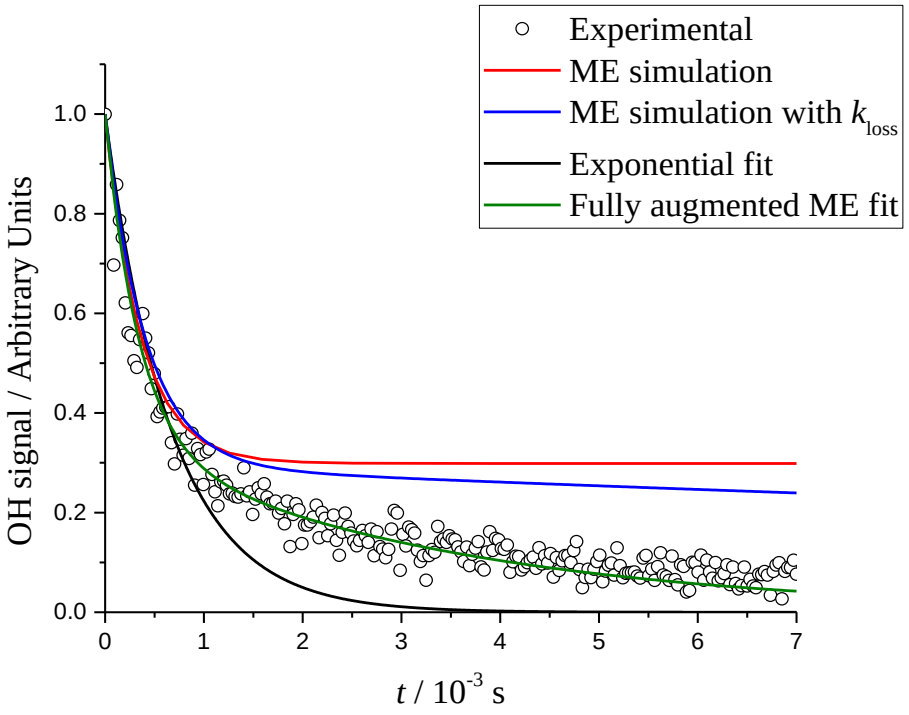

Figure 5.10 - Example of an OH trace recorded at ~610 K and ~110 Torr of N_2 using a conventional LFP-LIF instrument (black squares). $[C_2H_4] = 9.5 \times 10^{14}$ molecule cm^{-3}. The red line shows a Master Equation simulation under the same experimental conditions and the black line depicts a single exponential fit to the data. The blue line represents a ME fit in which the transition matrix was altered to incorporate k_{loss}, the sum of the pseudo-first order loss due to reaction of OH with its precursor and diffusion.

Table 5.2 includes all the fitted parameters along with goodness of fit. The errors reported in the table were extracted from the covariance matrix, and are quoted as 2σ. It is important to highlight the value of χ^2_{new} obtained in this case: 102.1. This is only ~6% greater than the total number of traces (96), which is an indicative measure of how much the model is skewed from the experimental measurements. Considering intrinsic experimental uncertainties related to manometric flow control, temperature and pressure measurements, this deviation is believed to be within experimental precision. Figure 5.11 shows examples of fits to a greater number of traces under various experimental conditions and provides a better overall picture of the fit.

Table 5.2 – List of optimized parameter for the augmented ME fit. Uncertainties quoted as 2

Parameter	Optimized value
$\Delta H_{C2H4\text{-}OH}$	111.8 ± 0.2 kJ mol^{-1}
A_{1a}	(8.13 ± 0.86)×10^{-12} cm^3 molecule^{-1} s^{-1}
n_{1a}	-0.99 ± 0.18
A_{1b}	(3.50 ± 0.75)×10^{-11} cm^3 molecule^{-1} s^{-1}
Ea_{1b}	26.2 ± 1.3 kJ mol^{-1}
$A_{<\Delta E>d,N2}$	234 ± 32 cm^{-1}
m (Energy transfer)**	0.11 ± 0.15
X^2/n_{traces}	1.06

$$k_{1a}^{\infty}=A_{1a}\left(\frac{T}{298\ \mathrm{K}}\right)^{n_{1a}};\ k_{1b}^{\infty}=A_{1b}\exp\left(\frac{-Ea_{1b}}{RT}\right);\ \langle\Delta E\rangle_{d,N2}=A_{\langle\Delta E\rangle_{d,N2}}\left(\frac{T}{298\ \mathrm{K}}\right)^{m}$$

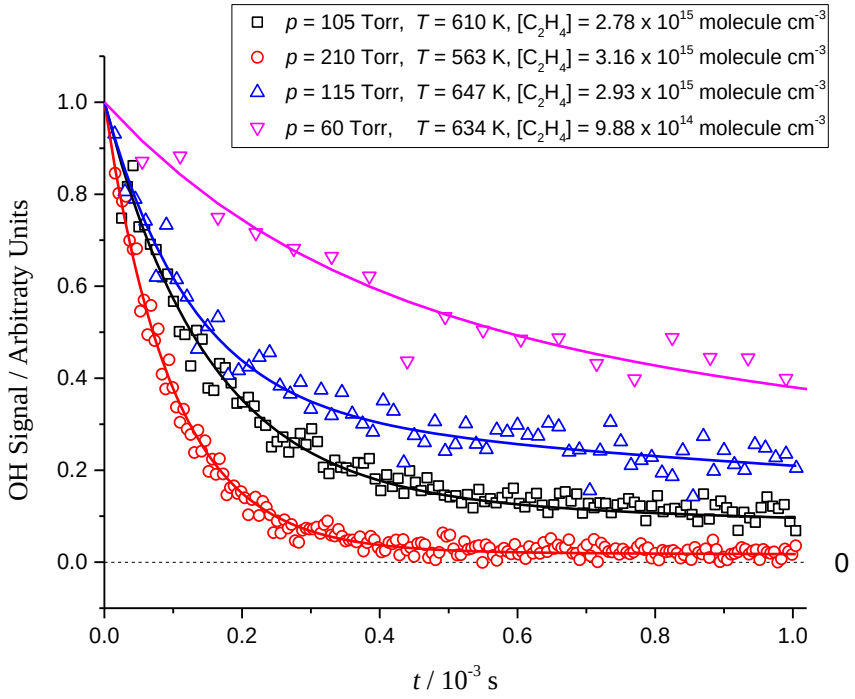

Figure 5.11 - Examples of augmented ME fits for multiple traces under significantly different experimental conditions. The dashed line represents y=0 for a better reference.

The enthalpy of formation determined for the C_2H_4-OH adduct ((111.8 ± 0.2) kJ mol^{-1}) is in excellent agreement with the theoretically determined value of $\Delta H_{0K,C2H4\text{-}OH}$ of 111.4 kJ mol^{-1}. This remarkably good agreement is accompanied with a relatively small uncertainty associated with the experimental determination. When compared to the uncertainty quoted in Chapter 4 for the isoprene-OH well depth for example (~5 kJ mol^{-1}), it is

postulated that the raw-trace global fitting procedure improves the precision of the parameters by imposing constraints to the fitted variables, such as the temperature dependence of bimolecular rate coefficients, reducing the degrees of freedom of the optimization. Furthermore, larger data sets employed covering wide ranges of experimental conditions (T and p) tend to be sensitive to a greater number of adjustable parameters. For example, while the activation energy of a process would be invisible in a single trace analysis, a trend comprised in a combination of them can provide information about this parameter.

Another advantage of the current method of analysis is the absence of the use of analytical equations to extract rate coefficients from the traces, as is the case in a classic ME fit. In the traditional procedure, experimental traces are *converted* into rate coefficients before being fed into the ME fitting. Recycling rate coefficients can be extracted from bi-exponential fits with some simplicity. If for example, however, a temperature dependence is imposed for this rate coefficient ($k_{-1a}(T) = A_{-1a} \times \exp(\frac{-Ea_{-1a}}{RT})$), the uncertainties of the obtained parameters A_{-1a} and Ea_{-1a} would require to be appropriately propagated for a calculation of $k_{-1a}(T)$. The complexity of multi-exponential equations can rapidly make the suitable computation of these uncertainties a difficult task. While the uncertainties obtained with the current method are largely controlled by the signal:noise ratio of the experimental OH traces, in a classic analysis the uncertainties are additionally dependent on the form by which a rate coefficient is extracted.

The bi-exponential formulation typically requires the incorporation of 3-5 parameters to describe recycling data. This includes the forward and backward rate coefficients and the various additional experimental losses from the system. This large number of parameters provide a great flexibility for fitting data, but represents a compromise to the fact that good fits may be obtained even when the chemistry being studied is not sufficiently understood. If an important piece of chemistry is missing, the remaining parameters are sometimes sufficient to compensate this effect and provide a good fit to the

data. The current method takes advantage of the global links to avoid this issue.

5.3.2 - Literature comparison of the OH addition and hydrogen abstraction

The parameters related to k_{1a}^{∞} and k_{1b}^{∞} were used for a comparison with literature investigations of the corresponding reactions. While the equation related to the OH addition was compared to the studies of Zellner and Lorenz[20], Fulle *et al.*[23], Vakhtin *et al.*[17], Diau *et al.*[38] and Liu *et al.*[48], the abstraction high pressure limiting coefficient was compared against a literature review by Baulch *et al.*[31] and the measurements of Tully [16], Liu *et al.*[30], Vasu *et al.*[35], Westbrook *et al.*[32], Srinivasan *et al.*[34] and Bhargava and Westmoreland.[33] The respective comparisons are presented in Figures 5.12 and 5.13.

In the context of the OH addition and except for the work of Fulle *et al.*[23], where the high pressure limiting rate coefficients for reaction R_{1a} were observed to be temperature independent, k_{1a}^{∞} falls monotonically with increasing temperatures in the depicted range. In the investigation of Fulle *et al.*, k_{1a}^{∞} was obtained from an extrapolation of measurements in the fall-off region between 300 and 800 K with the use of the Troe formalism (see Chapter 4 for an example of the use of such formulation). Even though pressures ranged from 1 to 150 bar, a very limited number of points was employed in each fit. The fact that the measurements were analysed separately, as per temperature, raises concerns with respect to the internal consistency of the measurements. It is not trivial to rationalize why their k_{1a}^{∞} values are independent of temperature for such a large temperature range

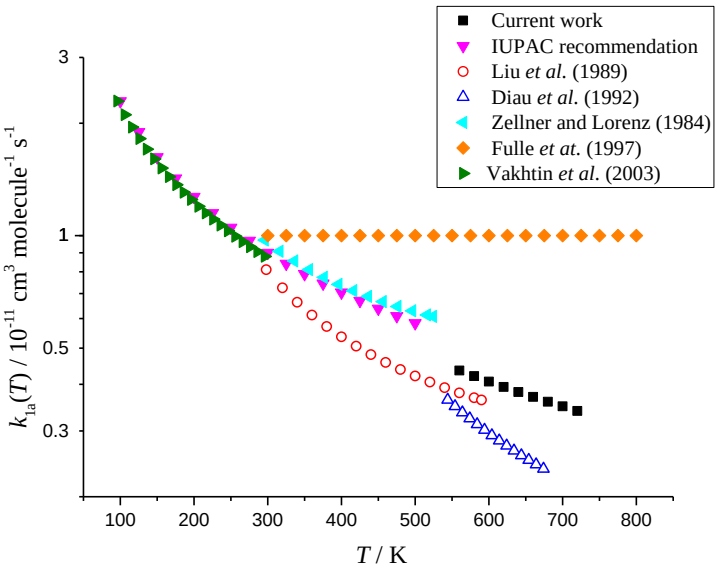

Figure 5.12 - Comparison of experimental recommendations for the ethylene + OH from different investigations. Pink triangles represent the IUPAC recommendation for the temperature dependence of the high-pressure limiting rate coefficient of the ethylene + OH reaction in the 100-500 K temperature range ($k_{1a}^{\infty}=9\times10^{-12}(\frac{T}{300\ K})^{-0.85}$ cm^3 molecule^{-1} s^{-1}). Black squares represent the recommendation of this work based on the best fit parameters reported in Table 5.2. Open markers represent pressure dependent rate coefficients and filled markers are estimates of k_{1a}^{∞}.

Zellner and Lorenz[20] have explored this reaction in the 296-524 K temperature range and pressures between 3 and ~100 Torr of argon, where a pressure dependence was identified. Their high pressure limiting rate coefficients were estimated via a simple Lindemann extrapolation (see Chapter 2 for a description of the Lindemann mechanism). As indicated previously, estimates based on such extrapolations will naturally enhance errors in the high pressure limiting rate coefficients. Their recommended equation for k_{1a}^{∞} tends to be greater than our recommendation.

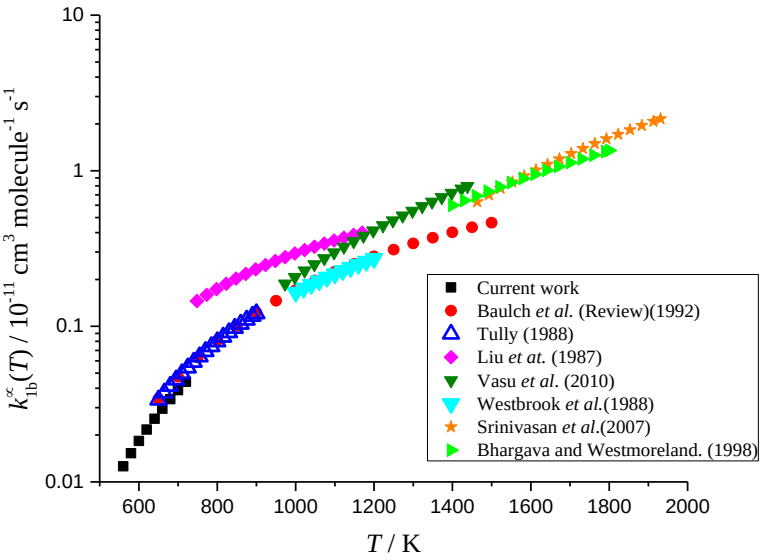

Figure 5.13 - Comparison of experimental recommendations for the ethylene + OH from different investigations. Red circles represent the recommendation from the review by Baulch *et al.*[31], blue open triangles refer to the work of Tully [16], pink diamonds refer to the work of Liu *et al.*[30], olive triangles correspond to the report of Vasu *et al.*[35], cyan triangles refer to the work of Westbrook *et al.*[32], orange stars correspond to the study of Srinivasan *et al.*[34], light green triangles refer the work of Bhargava and Westmoreland[33] and finally, black squares are the recommendation based on the best fit parameters reported in Table 5.2.

The measurements of Vakhtin *et al.*[17], used in in the development of the IUPAC recommendation, were also obtained from an extrapolation of pressure-dependent rate coefficients in the 96-296 K temperate range and pressures ranging from 0.2 to 100 Torr of N_2. Such extrapolations require a very large number of measurements for a more accurate determination of the parameters. While 12 pressures were evaluated at 296 K, only one pressure was employed at 96 K, 110 K and 165 K investigated, heavily limiting the accuracy of the extrapolated rate coefficients. If the current results are extrapolated to the conditions of their work, a very good agreement is observed, with deviations smaller than 10%.

Measurements by Diau *et al.*[38] were treated via a bi-exponential analysis of equilibrium traces collected at temperatures between 544 and 673 K and pressures between ~280 and 615 Torr of He. The authors do not provide a

pressure-dependent treatment to their data, but recognize that traces with $T <$ 590 K and pressures above 500 Torr are more likely to be closer to the high pressure limit. Considering only this subset of their data, they report an equation for $k_{1a}^{\infty} = (4 \pm 3)\times 10^{-13} \exp(\frac{9.98 \text{ kJ mol}^{-1}}{RT})$. Our best estimate for k_{1a} at 590 K and 615 Torr of He (3.5×10^{-12} cm^3 molecule^{-1} s^{-1}) is about 16% lower than our estimated high pressure limiting rate coefficient under the same temperature, 4.1×10^{-12} cm^3 molecule^{-1} s^{-1}, which suggests that even the selected subset of their data was within the fall-off region.

In the work of Liu *et al.*[48] measurements were undertaken at a relatively high pressure (760 Torr of Ar). Compared to helium, argon promotes energy transfer more efficiently[49], therefore reaching the high pressure limit faster than in helium. Even though the authors do not provide a proper pressure dependent treatment of their measurements, and our results indicate that their measurements at 590 K are not at the high pressure limit, being 13% lower than our estimate of k_{1a}^{∞}.

In terms of the abstraction channel, Figure 5.13 shows a good agreement between the current work and the recommendations reported by Tully[16] and Vasu *et al.*[35] Despite this fact, a ME simulation at the lowest pressure employed in the work of Tully (to disfavour the addition) (~100 Torr) and 650 K indicates that $k_{1a}(T,p) = 3.6 \times 10^{-12}$ cm^3 molecule^{-1} s^{-1} is still more than an order of magnitude faster than the abstraction channel $k_{1b} = 2.7 \times 10^{-13}$ cm^3 molecule^{-1} s^{-1}. Additional master equation simulations indicate that for 100 Torr of He, the H-abstraction just overcomes the OH addition at around 840 K, as depicted in Figure 5.14. The measurements of Liu *et al.*[30] for the abstraction coefficient are found to be systematically higher than our current measurements.

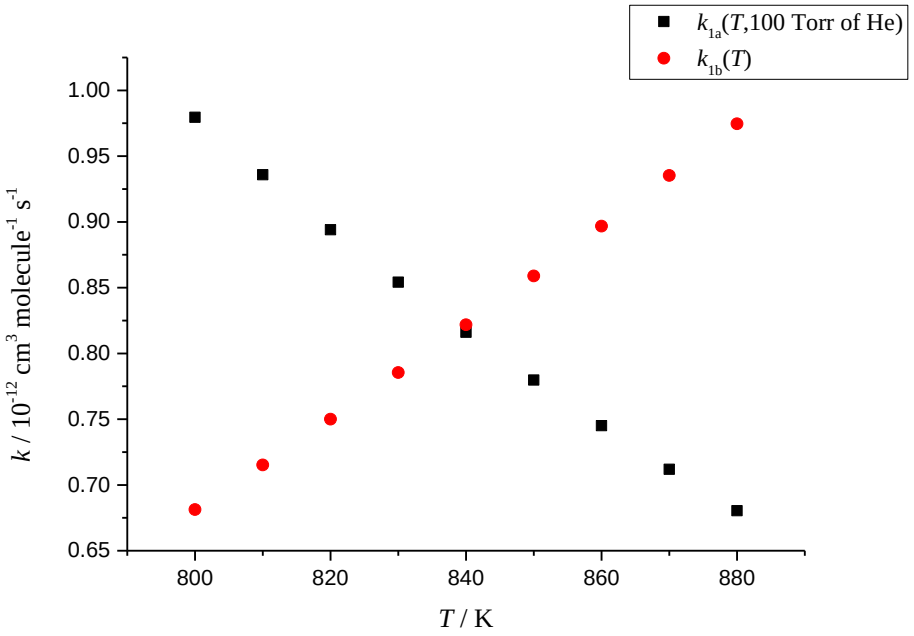

Figure 5.14 – The temperature dependence of H-abstraction and OH-addition rate coefficients at 100 Torr of He.

The energy transfer parameter related to the OH addition need to be addressed. The value of $A_{<\Delta E>d,N2}$ (234 ± 32 cm^{-1}) is in agreement with the one obtained for the work of isoprene + OH presented in Chapter 4 (150 ± 90). The temperature dependence of this parameter, *m*, is ill-defined as denoted by the large uncertainty reported. A test was performed by fixing the energy transfer parameter at the value of 0.25, but no significant variation on the returned parameters or χ^2_{new} was observed.

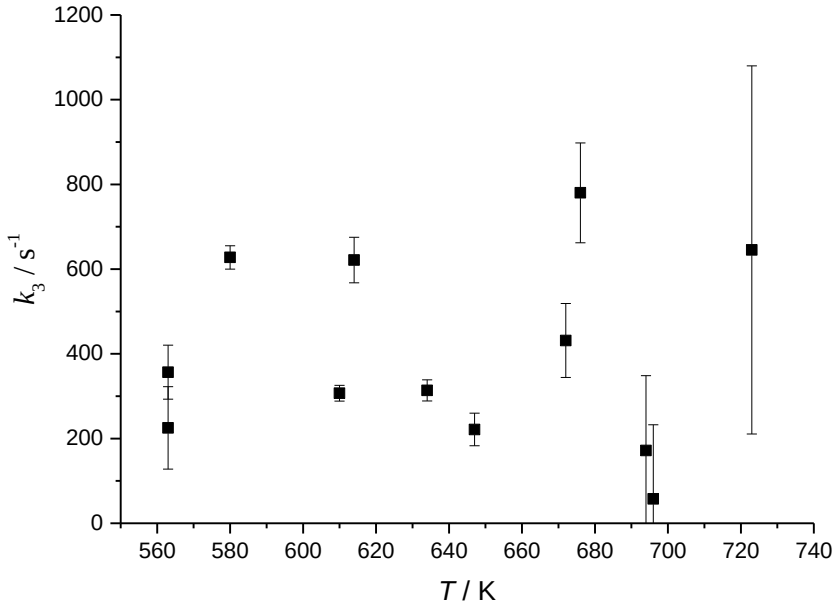

Figure 5.15 – List of k_3' values obtained from the augmented BW-ME fit as a function of temperature.

Omitted from Table 5.2, the list of the fitted k_3 values is presented in Figure 5.15 as a function of the temperature at which the corresponding OH traces were collected. This figure is an attempt to identify a potential relationship between the temperature in the reaction and the chemical process responsible for k_3. According to conventional oxidation pathways for β-hydroxyalkyl radicals, the O_2 addition to a radical is likely to be the main removal process involved.[50-51] Even though no experimental measurements of the C_2H_4-OH + O_2 reaction are available, the literature reports rate coefficients for β-hydroxyalkyl radicals + O_2 reactions in the 10^{-11} – 10^{-12} cm^3 molecule^{-1} s^{-1} range.[51] Considering the largest k_3' (the prime is used to denote a pseudo-first order rate coefficient) value obtained (780 s^{-1}) and a slow C_2H_4-OH + O_2 bimolecular rate coefficient of 1×10^{-12}, the largest concentration of O_2 introduced in the reaction cell is estimated to be ~7.8×10^{14} molecule cm^{-3}. Estimates undertaken by other personnel using the same instrumental setup, based on well-skipping reactions in the diethyl ether + OH reaction oxidation suggest an oxygen concentration around 2×10^{14} molecule cm^{-3} which does not seem to vary significantly with temperature.[52]

Addition reactions are typically barrierless processes and for this reason, generally present a negative temperature dependence, something that is not evident from Figure 5.15. This fact reinforces the importance of the definition of k_3' as a *local-global* parameter. For example, since the potential O_2 contamination is not being controlled, measurements generated at 723 K could have a larger k_3' simply because more O_2 was introduced in those experiments. As O_2 production is likely to come from H_2O_2 decomposition, the fact that H_2O_2 in the delivery vessel gets concentrated with time means that no relationship can be attributed to k_3' values determined in different days of experiment. The delivery vessel where the precursor is stored also can run out of liquid and needs to be topped up eventually, again, altering the concentration of the OH precursor being delivered and potentially, altering O_2 contamination. Nonetheless, the figure shows that, except for the highest temperature explored, parameters are reasonably well-defined, given the size of the error bars, quoted as 2σ.

A quick evaluation of the impact of the use of an alternative OH precursor is finally considered for shedding a little bit of light on the nature of k_3'. Urea-H_2O_2 ($(NH_2)_2CO$-H_2O_2, ALFA AESAR, 97%) is a commercially available solid, verified to successfully serve as a source of gas-phase H_2O_2,[53] as first demonstrated by Ludwig *et al.*[54] The authors have used time-resolved mass spectrometry to study the reaction of C_2H_5 radicals with HO_2 and urea-H_2O_2 was implemented as a precursor of gas-phase H_2O_2 and subsequently, HO_2 was produced via 193 nm photolysis. The precursor was introduced in a thermostated flask to control the H_2O_2 concentration via its vapour pressure, which depends on the temperature of the flask. The authors acknowledge that beyond 328 K small amounts of H_2O and O_2 were detected, and for this reason they have kept the thermostated flask below this temperature.

Figure 5.16 shows OH traces collected under the same experimental conditions (T~610 K and p= 110 Torr) but with the use of the two OH precursors: H_2O-H_2O_2 (blue triangles) and urea-H_2O_2 (red crosses).

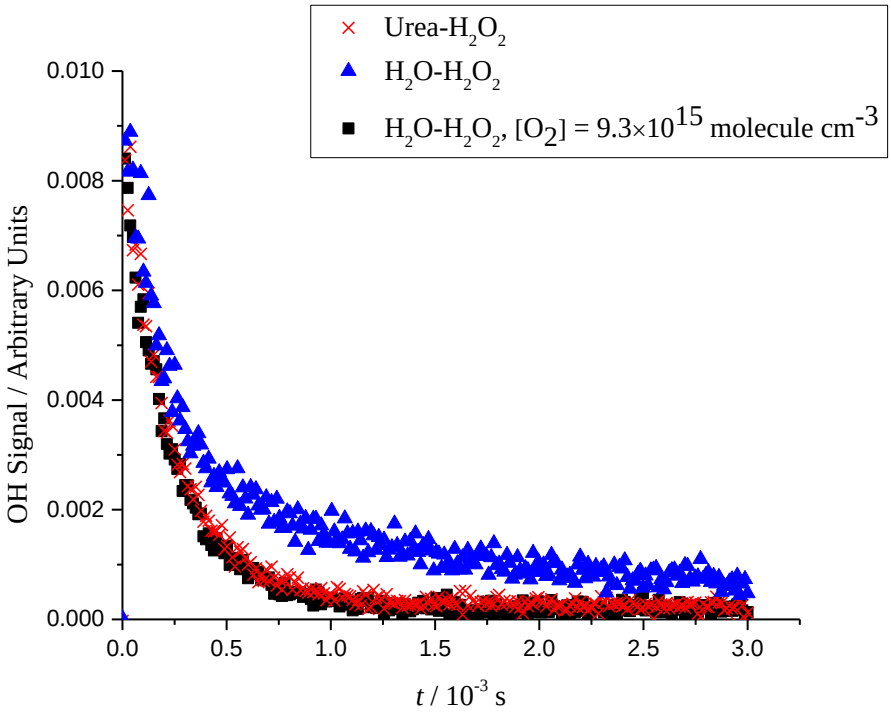

Figure 5.16 – Experimental traces collected at ~610 K and ~110 Torr with the use of different precursors. While blue triangles and red crosses were collected with the use of H_2O-H_2O_2, the black squares represent a trace collected with urea-H_2O_2.

A very clear difference is observed between the blue triangles and black squares, an indication that the concentration of O_2 when urea-H_2O_2 is used is much greater when compared to the alternative precursor. As a final test, a flow of O_2 was introduced in the H_2O-H_2O_2 experiment ($[O_2] = 9.3 \times 10^{15}$ molecule cm^{-3}), giving rise to the trace represented by red crosses. This new trace very similarly resembles the urea-H_2O_2 one, an effect that corroborates with the postulation of O_2 removal being the cause of k_3'.

5.4 SUMMARY AND CONCLUSIONS

In summary, a new method for analysing temperature and pressure dependent experimental data via a global raw-trace analysis has been presented and tested against a large number of complex OH traces associated with the ethylene + OH reaction. The structure, assumptions and implementation of the method were discussed in detail. The augmentation of the phenomenological ordinary differential equations, the heart of the method, have also allowed a systematic evaluation of the mechanism that governs the experimental observations, enhancing the reliability of the thermochemical parameters obtained from the fitting procedure. OH traces were collected under a wide range of pressures (~60 - 220 Torr) and temperatures (563 – 723 K) to ensure significant chemical differences are present in each trace. Remarkably, the fits are found be skewed only 6% from the corresponding experimental measurements in average.

Nonetheless, a comparison of the predicted high pressure limiting rate coefficients for the OH addition with previous literature investigations shows that due to the lack of appropriate pressure dependency treatments on the previous investigations a significant inconsistency of the literature with respect to the OH addition is observed. For the abstraction reaction on the other hand, good agreement with the work of Tully[16] is obtained. An excellent agreement is observed between a theoretical prediction of the C_2H_4-OH well-depth (111.4 kJ mol^{-1}) and the experimental determination (111.8 ± 0.20 kJ mol^{-1}).

The subsequent chapter of the current thesis deals with radical recycling from the OH + isoprene reaction will take advantage of the current method to exploit this atmospherically relevant chemical process. The chapter will inherit the basis of the method described here, as well as their assumptions and programmatic implementation.

5.5 REFERENCES

1. Benham, E.; McDaniel, M., Ethylene Polymers, HDPE. In *Encyclopedia of Polymer Science and Technology*, 4th ed.; John Wiley & Sons, Inc.: 2002.

2. Proceedings of the 3rd World Conference on Detergents Global Perspectives. Cahn, A., Ed. AOCS Press: Champaign, Ill. :, 1994.

3. Handbook of Detergents, Part F: Production. In *Surfactant Science Series*, Zoller, U.; Sosis, P., Eds. CRC Press 2008; Vol. 142.

4. Barry, C. S.; Giovannoni, J. J. Ethylene and Fruit Ripening. *Journal of Plant Growth Regulation* **2007,** *26*, 143.

5. Sabljic, A., *Environmental and Ecological Chemistry*. 1st ed.; EOLSS Publishers Co Ltd: 2009; Vol. 2.

6. Morgott, D. A. Anthropogenic and Biogenic Sources of Ethylene and the Potential for Human Exposure: A Literature Review. *Chemico-Biological Interactions* **2015,** *241*, 10-22.

7. Sawada, S.; Totsuka, T. Natural and Anthropogenic Sources and Fate of Atmospheric Ethylene. *Atmospheric Environment (1967)* **1986,** *20*, 821-832.

8. Reactive Hydrocarbons in the Atmosphere. 1st ed.; Hewitt, C. N., Ed. Academic Press: 1999.

9. Olivier, J.; Peters, J.; Granier, C.; OPetron, G.; Muller, J. F.; Wallens, S. *Present and Future Surface Emissions of Atmospheric Compounds*; 2003.

10. Hakola, H.; Hellén, H.; Laurila, T. Ten Years of Light Hydrocarbons (C_2–C_6) Concentration Measurements in Background Air in Finland. *Atmospheric Environment* **2006,** *40*, 3621-3630.

11. Cleary, P. A.; Romero, M. T. B.; Blitz, M. A.; Heard, D. E.; Pilling, M. J.; Seakins, P. W.; Wang, L. Determination of the Temperature and Pressure Dependence of the Reaction $OH+C_2H_4$ from 200-400 K Using Experimental and Master Equation Analyses. *Physical Chemistry Chemical Physics* **2006,** *8*, 5633-5642.

12. Sander, S. P. et al. *Chemical Kinetics and Photochemical Data for Use in Atmospheric Studies*; Jet Propulsion Laboratory: Pasadena, 2003.

13. Gas-Phase Combustion Chemistry. 2nd ed.; Gardiner, W. C., Jr., Ed. Springer: New York, 2000.

14. Greenwald, E. E.; North, S. W.; Georgievskii, Y.; Klippenstein, S. J. A Two Transition State Model for Radical-Molecule Reactions: A Case Study of the Addition of OH to C_2H_4. *Journal of Physical Chemistry A* **2005,** *109*, 6031-6044.

15. Liu, A.; Mulac, W. A.; Jonah, C. D. Kinetic Isotope Effects in the Gas-Phase Reaction of Hydroxyl Radicals with Ethylene in the Temperature Range 343-1173 K and 1-Atm Pressure. *The Journal of Physical Chemistry* **1988,** *92*, 3828-3833.

16. Tully, F. P. Hydrogen-Atom Abstraction from Alkenes by OH, Ethene and 1-butene. *Chemical Physics Letters* **1988,** *143*, 510-514.

17. Vakhtin, A. B.; Murphy, J. E.; Leone, S. R. Low-Temperature Kinetics of Reactions of OH Radical with Ethene, Propene, and 1-Butene. *The Journal of Physical Chemistry A* **2003,** *107*, 10055-10062.

18. Tully, F. P. Laser Photolysis/Laser-Induced Fluorescence Study of the Reaction of Hydroxyl Radical with Ethylene. *Chemical Physics Letters* **1983,** *96*, 148-153.

19. Atkinson, R.; Perry, R. A.; Pitts, J. N., Jr. Rate Constants for the Reaction of OH Radicals with Ethylene over the Temperature Range 299–425 °K. *The Journal of Chemical Physics* **1977,** *66*, 1197-1201.

20. Zellner, R.; Lorenz, K. Laser Photolysis/Resonance Fluorescence Study of the Rate Constants for the Reactions of Hydroxyl Radicals with Ethene and Propene. *The Journal of Physical Chemistry* **1984,** *88*, 984-989.

21. Klein, T.; Barnes, I.; Becker, K. H.; Fink, E. H.; Zabel, F. Pressure Dependence of the Rate Constants for the Reactions of Ethene and Propene with Hydroxyl Radicals at 295 K. *The Journal of Physical Chemistry* **1984,** *88*, 5020-5025.

22. Atkinson, R.; Aschmann, S. M.; Winer, A. M.; Pitts, J. N., Jr. Rate Constants for the Reaction of OH Radicals with a Series of Alkanes and Alkenes at 299 ± 2 K. *International Journal of Chemical Kinetics* **1982,** *14*, 507-516.

23. Fulle, D.; Hamann, H. F.; Hippler, H.; Jansch, C. P. The High Pressure Range of the Addition of OH to C_2H_2 and C_2H_4. *Berichte Der Bunsen-Gesellschaft-Physical Chemistry Chemical Physics* **1997,** *101*, 1433-1442.

24. Nielsen, O. J.; Jørgensen, O.; Donlon, M.; Sidebottom, H. W.; O'Farrell, D. J.; Treacy, J. Rate Constants for the Gas-Phase Reactions of OH Radicals with Nitroethene, 3-Nitropropene and 1-Nitrocyclohexene at 298 K and 1 Atm. *Chemical Physics Letters* **1990,** *168*, 319-323.

25. Lloyd, A. C.; Darnall, K. R.; Winer, A. M.; Pitts, J. N. Relative Rate Constants for Reaction of the Hydroxyl Radical with a Series of Alkanes, Alkenes, and Aromatic Hydrocarbons. *The Journal of Physical Chemistry* **1976,** *80*, 789-794.

26. Troe, J. Theory of Thermal Unimolecular Reactions at Low Pressures. I. Solutions of the Master Equation. *The Journal of Chemical Physics* **1977,** *66*, 4745-4757.

27. Glowacki, D. R.; Liang, C. H.; Morley, C.; Pilling, M. J.; Robertson, S. H. MESMER: An Open-Source Master Equation Solver for Multi-Energy Well Reactions. *Journal of Physical Chemistry A* **2012,** *116*, 9545-9560.

28. Pilling, M. J.; Robertson, S. H. Master Equation Models for Chemical Reactions of Importance in Combustion. *Annual Review of Physical Chemistry* **2003,** *54*, 245-275.

29. Johnson, M. S.; Feilberg, K. L.; Hessberg, P. v.; Nielsen, O. J. Isotopic Processes in Atmospheric Chemistry. *Chemical Society Reviews* **2002,** *31*, 313-323.

30. Liu, A.; Mulac, W. A.; Jonah, C. D. Pulse Radiolysis Study of the Reaction of OH Radicals with C_2H_4 over the Temperature Range 343–1173 K. *International Journal of Chemical Kinetics* **1987,** *19*, 25-34.

31. Baulch, D. L. et al. Evaluated Kinetic Data for Combustion Modelling. *Journal of Physical and Chemical Reference Data* **1992,** *21*, 411-734.

32. Westbrook, C. K.; Thornton, M. M.; Pitz, W. J.; Malte, P. C. A Kinetic Study of Ethylene Oxidation in a Well-Stirred Reactor. *Symposium (International) on Combustion* **1989,** *22*, 863-871.

33. Bhargava, A.; Westmoreland, P. R. Measured Flame Structure and Kinetics in a Fuel-Rich Ethylene Flame. *Combustion and Flame* **1998,** *113*, 333-347.

34. Srinivasan, N. K.; Su, M. C.; Michael, J. V. Reflected Shock Tube Studies of High-Temperature Rate Constants for OH + C_2H_2 and OH + C_2H_4. *Physical Chemistry Chemical Physics* **2007,** *9*, 4155-4163.

35. Vasu, S. S.; Hong, Z.; Davidson, D. F.; Hanson, R. K.; Golden, D. M. Shock Tube/Laser Absorption Measurements of the Reaction Rates of OH with Ethylene and Propene. *The Journal of Physical Chemistry A* **2010,** *114*, 11529-11537.

36. Greenwald, E. E.; North, S. W.; Georgievskii, Y.; Klippenstein, S. J. A Two Transition State Model for Radical−Molecule Reactions: Applications to Isomeric Branching in the OH−Isoprene Reaction. *The Journal of Physical Chemistry A* **2007,** *111*, 5582-5592.

37. Buczek, A.; Kupka, T.; Broda, M. A.; Żyła, A. Predicting the Structure and Vibrational Frequencies of Ethylene Using Harmonic and Anharmonic Approaches at the Kohn–Sham Complete Basis Set Limit. *Journal of Molecular Modeling* **2016,** *22*, 42.

38. Diau, E. W. G.; Lee, Y. P. Detailed Rate Coefficients and the Enthalpy Change of the Equilibrium Reaction OH + C_2H_4 ⇄ HOC_2H_4 over the Temperature-Range 544-673-K. *Journal of Chemical Physics* **1992,** *96*, 377-386.

39. Onel, L.; Blitz, M.; Seakins, P. W.; Bunkan, A. J. C.; Solimannejad, M.; Nielsen, C. J. Gas Phase Reactions of OH with Methyl Amines in the Presence or Absence of Molecular Oxygen. An Experimental and Theoretical Study. *The Journal of Physical Chemistry A* **2013,** *117*, 10736–10745.

40. Onel, L.; Blitz, M. A.; Seakins, P. W. Direct Determination of the Rate Coefficient for the Reaction of OH Radicals with Monoethanol Amine (MEA) from 296 to 510 K. *Journal of Physical Chemistry Letters* **2012,** *3*, 853-856.

41. Onel, L.; Blitz, M. A.; Breen, J.; Rickardcd, A. R.; Seakins, P. W. Branching Ratios for the Reactions of OH with Ethanol Amines Used in Carbon Capture and the Potential Impact on Carcinogen Formation in the Emission Plume from a Carbon Capture Plant. *Physical Chemistry Chemical Physics* **2015,** *17*, 25342-25353.

42. Atkinson, R.; Baulch, D. L.; Cox, R. A.; Crowley, J. N.; Hampson, R. F.; Hynes, R. G.; Jenkin, M. E.; Rossi, M. J.; Troe, J. Evaluated Kinetic and Photochemical Data for Atmospheric Chemistry: Volume I - Gas Phase Reactions of Ox, HOx, NOx and SOx Species. *Atmospheric Chemistry and Physics* **2004,** *4*, 1461-1738.

43. Seakins, P. W.; Pilling, M. J.; Niiranen, J. T.; Gutman, D.; Krasnoperov, L. N. Kinetics and Thermochemistry of R+HBr = RH+Br Reactions - Determinations of the Heat of Formation of C_2H_5, i-C_3H_7, sec-C_4H_9, and t-C_4H_9. *Journal of Physical Chemistry* **1992,** *96*, 9847-9855.

44. Peterson, K. A.; Woon, D. E.; Jr., T. H. D. Benchmark Calculations with Correlated Molecular Wave Functions. IV. The Classical Barrier Height of the $H+H_2 \rightarrow H_2+H$ Reaction. *The Journal of Chemical Physics* **1994,** *100*, 7410-7415.

45. Sharma, S.; Raman, S.; Green, W. H. Intramolecular Hydrogen Migration in Alkylperoxy and Hydroperoxyalkylperoxy Radicals: Accurate Treatment of Hindered Rotors. *The Journal of Physical Chemistry A* **2010,** *114*, 5689-5701.

46. MathWorks, I., *MATLAB and Optimization Toolbox Release R2016a*. Natwick : Math Works Inc.: 2016.

47. Shampine, L. F.; Reichelt, M. W. The MATLAB ODE Suite. *SIAM Journal on Scientific Computing* **1997,** *18*, 1-22.

48. Liu, A.; Jonah, C. D.; Mulac, W. A. The Gas-Phase Reactions of Hydroxyl Radicals with Several Unsaturated Hydrocarbons at Atmosphere Pressure. *International Journal of Radiation Applications and Instrumentation. Part C. Radiation Physics and Chemistry* **1989,** *34*, 687-691.

49. Blitz, M. A.; Salter, R. J.; Heard, D. E.; Seakins, P. W. An Experimental and Master Equation Study of the Kinetics of OH/OD + SO_2: The Limiting High-Pressure Rate Coefficients. *The Journal of Physical Chemistry A* **2017,** *121*, 3184-3191.

50. Orlando, J. J.; Tyndall, G. S.; Wallington, T. J. The Atmospheric Chemistry of Alkoxy Radicals. *Chemical Reviews* **2003,** *103*, 4657-4690.

51. Miyoshi, A.; Matsui, H.; Washida, N. Rates of Reaction of Hydroxyalkyl Radicals with Molecular Oxygen. *The Journal of Physical Chemistry* **1990,** *94*, 3016-3019.

52. Potter, D., Oxygen Concentration Generated in Conventional LFP-LIF Instrument Based on Well-Skipping Reactions in the Diethyl Ether + OH System. Private Communication.

53. Hong, Z.; Farooq, A.; Barbour, E. A.; Davidson, D. F.; Hanson, R. K. Hydrogen Peroxide Decomposition Rate: A Shock Tube Study Using Tunable Laser Absorption of H_2O near 2.5 μm. *The Journal of Physical Chemistry A* **2009,** *113*, 12919-12925.

54. Ludwig, W.; Brandt, B.; Friedrichs, G.; Temps, F. Kinetics of the Reaction C_2H_5 + HO_2 by Time-Resolved Mass Spectrometry. *The Journal of Physical Chemistry A* **2006,** *110*, 3330-3337.

Chapter 6. Investigation of the Isoprene + OH Reaction in the Presence of Oxygen to Confirm the Leuven Isoprene Mechanism 1.

Overview of the chapter

In this chapter the chemistry of the isoprene + OH reaction in the presence of O_2 is explored experimentally via laser flash photolysis-laser induce fluorescence experiments. Experiments were under taken at relatively high temperatures (T > 400 K) following predictions obtained via numerical simulations of the most promising atmospheric mechanism for oxidation of isoprene: the Leuven Isoprene Mechanism, version 1 (LIM1).

The background of this reaction is discussed in section 6.1, while details of supporting *ab initio* calculations are presented in section 6.2. The OH recycling is evidenced in section 6.3.1 via simple single and bi-exponential fits to the data and a brief residual analysis.

The collection of OH traces was initially explored via a global fitting procedure based on numerical simulations of the LIM1. Section 6.3.2 shows the results of this analysis, in which effects of pressure-dependence and well-skipping were neglected. The best-fit parameters were used for an assessment of the amospheric impact by simulating the atmospheric conditions of the OP3 Borneo campaign.

The assumptions of no well-skipping and pressure dependence are tested in the following section, 6.3.3, which employs an augmented-ME analysis, as described in Chapter 5 in the context of the ethylene + OH reaction.

6.1 INTRODUCTION

The introduction of Chapter 4 dealt with the atmospheric chemistry of isoprene and its importance to the Earth's atmosphere. Given that the current chapter is focused on the same reaction, but under different experimental conditions, the reader is referred to Chapter 4 for the context and background. A good understanding of the current chapter depends also on the analytical method presented in Chapter 5. The method will be used to exploit this complex chemical system to identify and quantify OH recycling which, as discussed, has been the focus a controversy in the literature in the last decades.[1-5]

As discussed in Chapter 4, the atmospheric chemistry of isoprene is complex and highly dependent on the subchemistry of peroxy radicals (HO-RO_2). In polluted environments, characterized by large concentrations of nitrogen oxides, these radicals will primarily react with nitric oxide to yield hydroxyl alkoxy radicals (HO-RO) and nitrogen dioxide (R1).[6] Moreover, NO_2 is also produced from the reaction between NO and HO_2 radicals (R2), an important process in the chemistry of polluted atmospheres, given that this reaction can reform large amounts of OH radicals.[6] In the presence of light, NO_2 is photolysed to give nitric oxide and a ground state oxygen atom, $O(^3P)$, (R3) which will react with molecular O_2 (R4) to produce tropospheric ozone. The list of negative implications of tropospheric O_3 formation includes damage to crops and natural vegetation.[7] When inhaled, O_3 can cause irritation of the respiratory tract, reducing lung function and worsening respiratory diseases such as asthma.[8] Ozone is also implicated as an important factor for the temperature rise in Northern Hemisphere extratropics.[9] Recently, the European Comission has sent a warning to the United Kingdom to comply with European environmental legislation on air quality. The UK has been in breach of the NO_2 limits since 2010 and it is estimated that around 50,000 people die every year in the country as a result of respiratory deseases caused by air pollution, such as particulate matter, ozone and NO_2.[10]

$HOCH_2C(O_2)(CH_3)CH=CH_2 + NO \rightarrow HOCH_2C(O)(CH_3)CH=CH_2 + NO_2$ R1

$HO_2 + NO \rightarrow OH + NO_2$ R2

$NO_2 + h\nu_{(\lambda<430\ nm)} \rightarrow NO + O(^3P)$ R3

$O(^3P) + O_2 \rightarrow O_3$ R4

In pristine environments, HO-RO_2 radicals were observed to react with HO_2 and form hydroperoxides (HO-ROOH) which can subsequently react with OH radicals to generate isoprene epoxides.[11] These epoxides are believed to serve as precursors of secondary organic aerosols.[11] Due to isoprene's high emission rates, and rapid reaction with OH radicals, it was expected that isoprene would consume considerable amounts of these radicals. Given the reduction of the importance of reaction R2 under clean atmospheres, this combination should in theory, translate into low concentrations of hydroxyl radicals in such environments. However, a large discrepancy has been noticed between current models estimates and the OH concentrations measured in several campaigns performed in known isoprene-abundant pristine regions. As discussed in Chapter 4, the ratio of approximately 0.1 is often observed between model estimates and actual measurements of OH.[5, 12] These comparisons evidence significant OH radical propagation from isoprene oxidation and reinforce the need of a reliable and validated model to describe the isoprene HO-RO_2 chemistry.

In order to elucidate these radical-recycling processes, Peeters *et al.* proposed a mechanism based on theoretical calculations. The mechanism named *The Leuven isoprene mechanism* (LIM), presented new pathways for regeneration of OH involving peroxy radicals.[13] Figure 6.1 shows a simplified scheme of the mechanism, with respect to the OH addition to carbon C_1 of the isoprene chain (Case 1). An analogous scheme regarding the OH addition to carbon C_4 (Case 2) is also available in the original publication. From this point, references to Case 1 relate to the mechanism involving the OH addition to carbon C_1 and Case 2 corresponds to the OH addition to carbon C_4.

As observed in Figure 6.1, the essential steps for the regeneration of hydroxyl radicals from isoprene oxidation include (1) rapid interconversion of δ-hydroxy and β-hydroxy-isoprenylperoxy radicals, (2) the direct propagation of OH by isomerization of *β*-OH-isoprenyl-peroxy radicals (1,5-H shift) followed by decomposition to the Prod I and subsequently OH, formaldehyde and methylvinyl ketone (MVK), (3) the formation of hydroperoxy-methylbutenals (HPALDs) by rapid isomerization of *Z*-δ-OH-isoprenyl-peroxy radicals (1,6-Hshift) and finally, (4) HPALD photolysis to give OH. It is worth mentioning that in the case of OH addition to carbon C_4, the co-product of OH and formaldehyde from the 1,5-H shift is methacrolein (MACR).

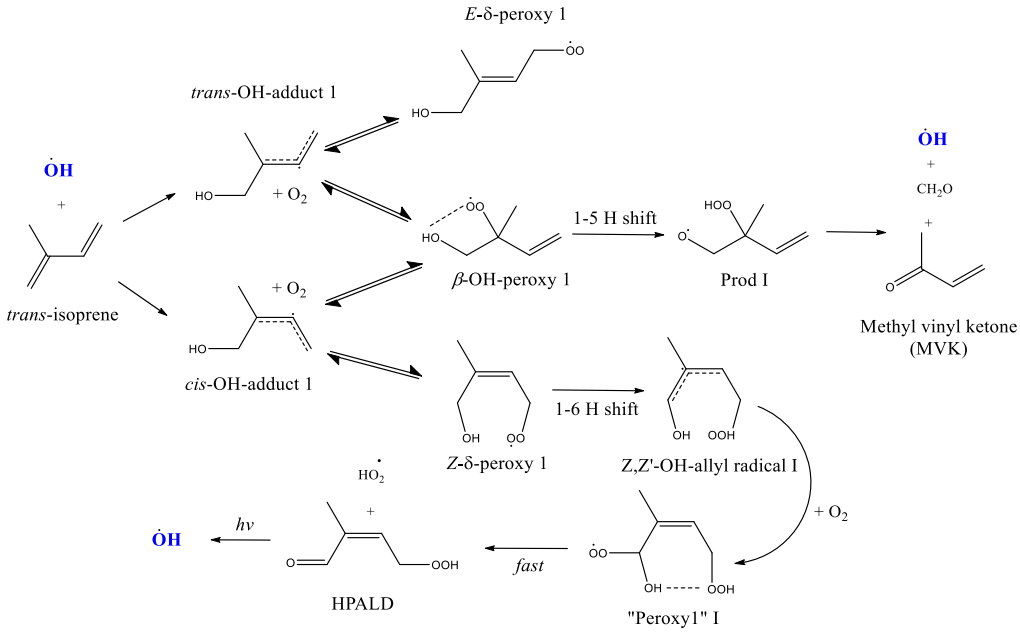

Figure 6.1 – The Leuven Isoprene Mechanism as proposed by Peeters *et al.*[13]

Despite its recognised importance when presented to the atmospheric community, the original LIM, often referred to as LIM0, significantly overestimated the production of hydroperoxy-methylbutenals (HPALDs), species which can photolytically generate OH, as indicated by the work of Crounse *et al.*[3, 14] Furthermore, isoprene chemistry has also been explored by Fuchs *et al.*[1] in an atmospheric simulation chamber study, in which the authors attempted to use LIM0 to describe experimental measurements of OH and HO_2 radicals. Their results show that the mechanism was too generous when

predicting these two species, with OH and HO_2 overestimated by factors of 4 and 2 respectively. Despite the fact that the rate of the isoprene oxidation was overestimated by the model, it ended up underestimating the formation of methyl vinyl ketone and methacrolein, products of the 1,5-H shifts. This is justified by the fact that the model was dominated by the 1,6-H shift chemistry, evidencing that the assigned rate coefficient for the 1,6-H shift ($k_{1\text{-}6H}$ ~0.64 s^{-1} at 298 K) was too fast when compared to the 1,5-H shifts ($k_{1\text{-}5H}$ ~0.002 s^{-1} at 298 K).

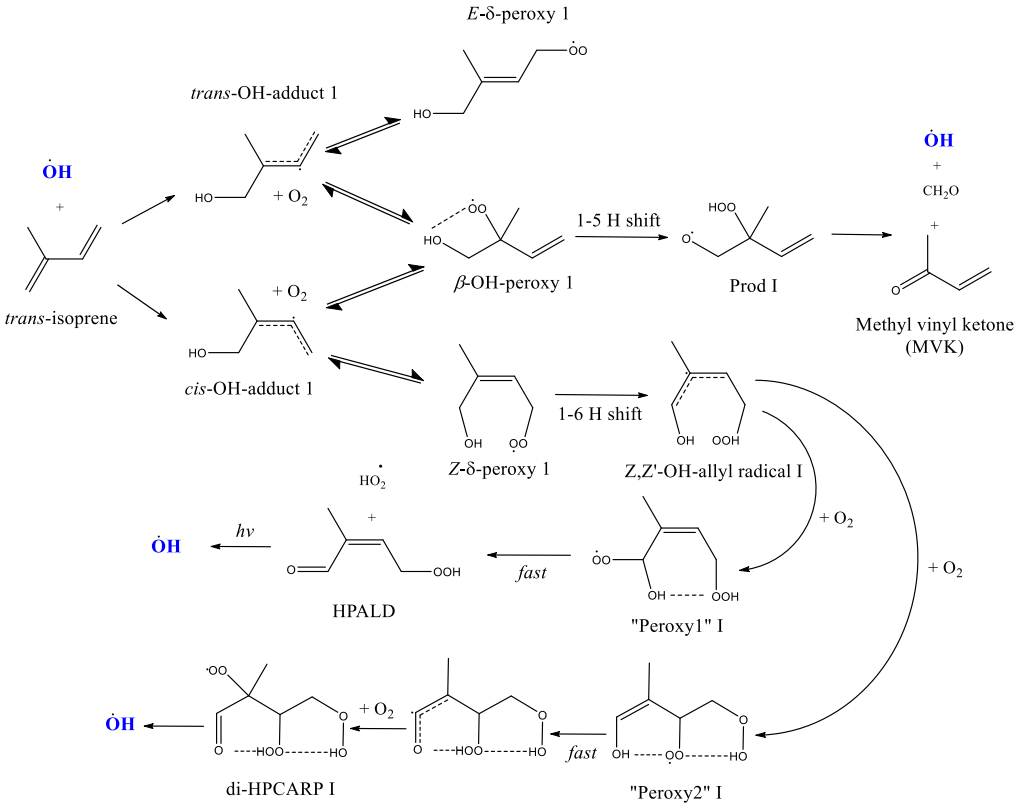

Figure 6.2 - The Leuven Isoprene Mechanism 1 as proposed by Peeters *et al.*[3]

The mechanism proposed by Peeters *et al.* was later upgraded and presented in a second publication[3] where the rate coefficients for the important processes have been re-evaluated at a higher theoretical level. The upgraded version, now named LIM1 and illustrated in Figure 6.2, takes into account the London dispersion effect, important for hydrogen-bonded structures such as those in the intermediate isomerization steps. To account for tunnelling effects, Peeters *et al.* have implemented the asymmetric Eckart-barrier approximation, which

matches well the small curvature tunnelling factors for similar H-shifts in n-propylperoxy radicals at 300 K.[15] The 1,6-H shifts of both Cases 1 and 4 are believed to occur predominantly via hydrogen tunnelling (>99 %) and according to the authors, the LIM1 mechanism is theoretically more reliable for describing the OH recycling. A new path following these 1,6-H shifts is now included, which leads to the formation of dihydroperoxy-carbonyl peroxy radicals (di-HPCARPs), species that can thermally decompose to regenerate OH. Figure 6.2 shows a simplified scheme of LIM1, corresponding again to the addition to carbon C_1. Quantitatively speaking, the rate coefficients for the 1,5-H shift in Case 1 as calculated by LIM1 are much slower $k_{1,5\text{-H}} \sim 6.5\times10^{-4}\ s^{-1}$ when compared to the prediction of LIM0, $k_{1,5\text{-H}} \sim 2.0\times10^{-3}\ s^{-1}$. The rate coefficients for the 1,6-H shift have not seen much change, $k_{1,\text{-6H}}$ being reduced from ~0.64 to ~0.52 s^{-1} at 298 K, which does not help improve the underestimation of MVK and MACR observed by Fuchs *et al.*[1]

In LIM1, the most stable peroxy radicals in both addition cases are the *β*-OH peroxys, which can proceed via the 1,5-H shifts to regenerate OH. These radicals are more stable than the also important *Z*-δ-OH peroxys by approximately 10 kJ mol^{-1}. Despite being less stable, *Z*-δ-OH peroxys can undergo multiple paths to regenerate OH, namely via HPALD and di-HPCARP dissociation. For this reason, if the chemistry of isoprene predominantly follows the 1,6-H shifts, the more significant potential to explain the discrepancy of current atmospheric models when predicting OH in pristine environments is compromised. On the other hand, if most of the chemistry follows the 1,5-H shift, this scenario diminishes the importance of isoprene chemistry in the OH cycle in pristine environments. For this reason, understanding the importance of each peroxy radical in the isoprene reaction chain is crucial for shedding light on the atmospheric chemistry of pristine environments.

In an investigation published in 2017, the research group headed by Paul Wennberg (Teng *et al.*[16]) attempted to assess the relative populations of $HO\text{-}RO_2$ radicals in the isoprene oxidation via measurements of

HO-RO_2-specific nitrate formation in the presence of NO. The mechanism behind the nitrate formation includes a couple of steps: the NO addition to the peroxy radicals forming a hot nitrite (HO-RO_2NO*) (R5), followed by a prompt isomerization to give a nitrate HO-$RONO_2$ (R6). The fate of hot nitrites also include collisional stabilization (R7) and prompt dissociation to give an activated alkoxy radical and NO_2 (R8).[17] Theoretical and master equation (ME) calculations by Zhang *et al.*[17] indicate that the dissociation is the most energetically favourable path and previous experimental studies suggest small ratios for the nitrate formation, between 4 and 12%.[18-19]

$$HO\text{-}RO_2 + NO \rightarrow HO\text{-}RO_2NO^* \quad \text{R5}$$

$$HO\text{-}RO_2NO^* \rightarrow HO\text{-}RONO_2 \quad \text{R6}$$

$$HO\text{-}RO_2NO^* \xrightarrow{M} HO\text{-}RO_2NO \quad \text{R7}$$

$$HO\text{-}RO_2NO^* \rightarrow HO\text{-}RO^* + NO_2 \quad \text{R8}$$

The experiments by Teng *et al.*[16] were performed in a Teflon chamber, where the isoprene oxidation was initiated via its reaction with OH, which was generated via the photolysis of methyl nitrite (CH_3ONO). By adding large enough concentrations of NO, it is expected that the nascent population of HO-RO_2 radicals will be rapidly intercepted by NO, forming, among other products, isomer-specific nitrates, whose distribution should be kinetically determined and correspond to the HO-RO_2 population distribution. On the other hand, if small amounts of NO are added, i.e., the lifetimes of the peroxy radicals are long enough; their relative populations intercepted by NO are defined by the thermodynamics of the system, favouring the formation of the nitrates corresponding to the most stable *β*-OH peroxy radicals. Moreover, the population of isomer-specific nitrates should therefore reflect this thermodynamically defined population. This assumption ignores the possibility of interconversion between nitrates, from their formation to detection, something that was, in fact, acknowledged by the authors of that work. The nitrates were separated by gas-chromatography and detected via chemical ionization mass spectrometry. They recognize that the *β*-OH nitrates appear to

be converted to the less important *E*-δ-OH ones within the chromatographic column. The authors claimed to have applied corrections to account for such interconversions, even though details about these corrections are not provided either in the publication or the supplementary information of that work. The *β*-OH nitrates were also verified to undergo hydrolysis in the column, and the authors have therefore tried as far as possible to prevent water from getting trapped in the column.

Furthermore, the extra energy of a possible hot nitrate formation could in theory, provoke a re-scrambling of the molecule structure, which would rule out the correspondence between the relative populations of nitrates and HO-RO_2 radicals. This possibility does not seem to have been considered by the authors. Additionally, the reactions between the different peroxy radicals with NO were all assumed to have identical rate coefficients (8.6×10^{-12} cm^3 $molecule^{-1}$ s^{-1}) and nitrate yields (13 ± 2%). This identical yield assumption is based on a test where isoprene is oxidized in competition to references such as 1-hexene and methylpropene.[16] The ratio between the concentrations of isoprene-nitrates and reference-nitrates were observed to be independent of the concentration of NO, which should, in theory, alter the isoprene HO-RO_2 populations. It is important to reinforce however, that if hot isoprene-nitrates isomerize upon formation, the assumption that the nitrate distribution depicts the peroxy distribution cannot be supported.

The presented aspects raise questions regarding the accuracy of their measurements, suggesting that the results of the study should be considered predominantly in a qualitative manner. The authors propose modifications to the rate coefficients of LIM1, including the HO-RO_2 decompositions back to reagents and H-shifts, to better suit their nitrate distributions. Their results suggest that for NO concentrations such that the lifetime of the peroxy radicals are greater than 10 s, the *β*-OH-peroxy radicals, the most thermodynamically favourable *β*-OH-peroxy radicals account for approximately 95% of the pool of HO-RO_2 radicals. Even though HO_2 concentrations were not reported in the work of Teng *et al*., the chamber work of Fuchs *et al*.,[1] in which very low

concentrations of NO were measured (~ 1×10^9 molecule cm^{-3}) can provide an idea of the HO_2 concentrations in the study of Teng *et al*. as HO_2 is largely consumed via its reaction with NO. As discussed earlier in the chapter, the HO-RO_2 radicals can also react with HO_2 radicals and for this reason, influencing the lifetime of the peroxy radicals. Considering an HO_2 concentration of 1×10^8 molecule cm^{-3} based on the work of Fuch *et al*.,[1] $k_{HO\text{-}RO2+NO} = 8.8 \times 10^{-12}$ cm^3 $molecule^{-1}$ s^{-1} following the IUPAC recommendation[20] and $k_{HO\text{-}RO2+HO2} = 1.7 \times 10^{-11}$ cm^3 $molecule^{-1}$ s^{-1} based on the estimate by Boyd *et al*.,[21] the lifetime of 10 s^{-1} is predominantly controlled by the HO-RO_2 + NO reactions and the corresponding NO concentration is estimated to be approximately 1×10^{10} molecule cm^{-3}. Even if an HO_2 concentration of 1×10^9 molecule cm^{-3} is considered ($k_{HO\text{-}RO2+HO2} \times [HO_2] \sim 0.02$ s^{-1}), the lifetime of 10 s would remain dominated by the HO-RO_2 + NO reactions and require an NO concentration of approximately 1×10^{10} molecule cm^{-3} ($k_{HO\text{-}RO2+NO} \times [NO] \sim 0.08$ s^{-1}).

In the kinetic limit, with HO-RO_2 lifetimes with respect to the reaction with NO shorter than 10^{-2} s ([NO] > 1×10^{13} molecule cm^{-3}), the *β*-OH-peroxy radicals comprise ~75% of the radical pool, the *Z*-δ-OH peroxys about 11% and the *E*-δ-OH ones approximately 14%. This last result contradicts the theoretical predictions of Peeters *et al*., which suggests a much greater abundance of *Z*-δ-OH peroxy radicals, accounting for 26% of the total radical pool, while the *E*-δ-OH and *β*-OH-peroxy radicals should account for ~6 and ~68% respectively in the kinetic limit. The measurements by Teng *et al*. diminish the importance of the subsequent chemistry of the 1,6-H shift in the kinetic limit, given the significant reduction of the relative abundance of the *Z*-δ-OH peroxy radicals.

As denoted by the H-shift rate coefficients, the OH recycling from the isoprene oxidation occurs on a timescale of hundreds of seconds, which can make its evaluation at room temperature a very challenging task. Given the importance of long-lived hydroperoxy species such as HPALDs and di-HPCARPs in the mechanism, it is very difficult to rule out the impact of heterogeneous

chemistry in chamber investigations such as the work by Fuchs *et al.*[1] As discussed in the previous chapters, laser flash photolysis-laser induced fluorescence experiments on a millisecond timescale represent a good alternative in terms of control over heterogeneous interference and contaminants. However, the timescale of the OH recycling at low temperatures (T~298 K) remains an issue. It is theoretically possible, however, to promote the chemistry of the OH recycling on the millisecond timescale, compatible with LFP-LIF experiments, if high enough temperatures are employed. Under such conditions, the crucial isomerization steps are promoted, greatly reducing the time span of the OH recycling.

On the other hand, the implementation of high temperatures also means an enhancement of the dissociation of the intermediate peroxy radicals back to reagents and the establishment of equilibrium between peroxy formation and unimolecular decomposition. Moreover, the results of such high temperature experiments have their immediate application under significantly different conditions. For this reason, their translation to more atmospherically relevant conditions requires a robust and reliable procedure, using a validated model.

To help promote the peroxy formation, one can consider implementing very large O_2 concentrations. This effect was explored in the current work, initially via simple numerical simulations of LIM1. Figure 6.3 shows the results of such simulations, where large O_2 concentrations were set ($[O_2] \sim 1 \times 10^{19}$ molecule cm^{-3}) and temperatures above 400 K were considered. The depicted simulations were undertaken with the aid of the *Kintecus* chemical modelling software.[22] Under the pseudo-first order conditions simulated, the deficient reactant (OH) should decay exponentially, as discussed on many occasions in the previous chapters.

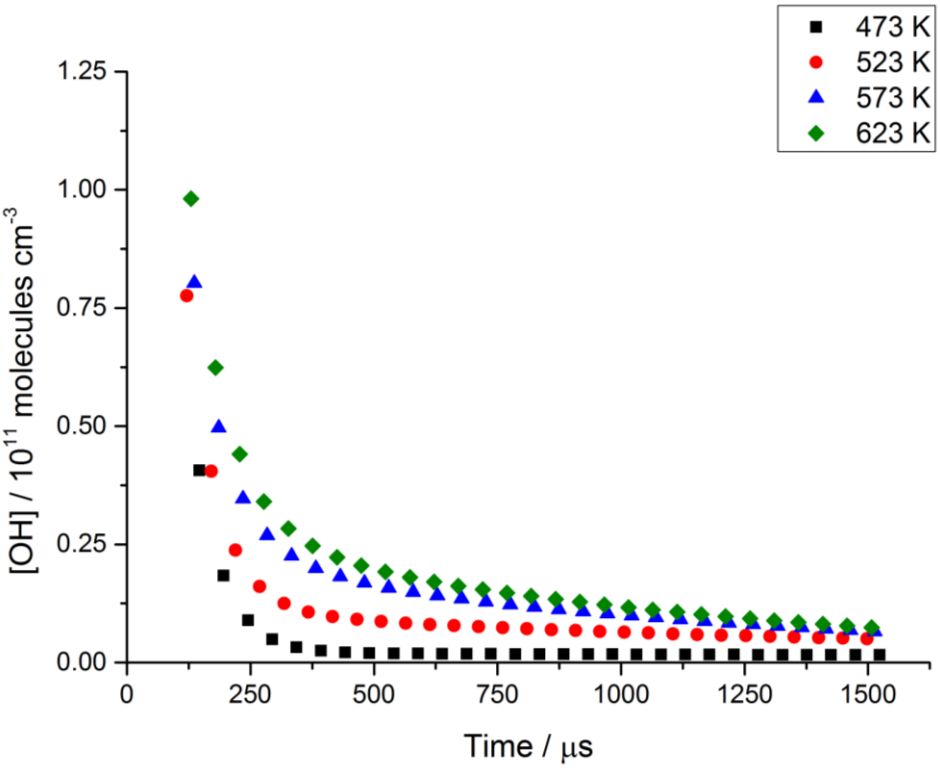

Figure 6.3 - Simulations of LIM1 under various temperatures. $[O_2]$ = 1 × 10^{18} molecule cm^{-3}. These simulations were all done with the aid of the computational package *Kintecus*.[22]

However, the simulations not only deviate from an exponential trend, but clearly indicate a promotion of the recycling somewhere between 473 K and 523 K, as denoted by the elevation of the *tails* of the simulated traces. This prediction was used to justify the execution of LFP-LIF experiments under such conditions (T>400 K, $[O_2]$ ~1 × 10^{18} molecule cm^{-3}) in order to verify and evaluate the OH recycling from the isoprene + OH chemistry. As will be discussed later, the corresponding experimental traces not only provided insight regarding the aforementioned recycling, but also allowed a validation of LIM1. The mechanism was tested in a number of ways, including a high-pressure limit assumption, an augmented ME fit where vibrational modes were treated using the harmonic oscillator approach and a final augmented ME fit where hindered rotors were used to describe a total of 40 vibrational modes. As indicated previously, these various fits are intended to allow a comprehensive extrapolation of high-temperature measurements to more relevant atmospheric conditions. The LIM1 modifications proposed by Wennberg's research group were also tested, and will be addressed in the results section.

As discussed in the previous chapters, ME calculations require a number of molecular parameters, and therefore, the details of *ab initio* calculations undertaken are outlined in the following, prior to the presentation of the results.

6.2 *AB INITIO* CALCULATIONS

The methodology implemented in the current chapter is basically the same as described in Chapter 3 and therefore, only a brief description is provided. Stationary structures of reagents, intermediates and products were computed with the DFT functional M06-2X[23] and a large basis set (6-311++G(3df,2p))[24], as implemented in the work of Peeters *et al*.[3] Optimizations were carried out with the aid of the Berny algorithm[25-26] available in the Gaussian 09 D.01 programme suite.[27] The minimization used redundant internal coordinates and analytical gradients. The potential energy surface used in section 6.3.3 (see Figure 6.12) have employed the calculations reported in the work of Peeters *et al*.,[3] which gave support to the implementation of LIM1 in the numerical and ME models.

6.3 RESULTS AND DISCUSSION

6.3.1 – Analysis of non-exponential traces

As discussed in Chapter 4, the addition of O_2 to LFP-LIF experiments of the isoprene + OH reaction did not provoke any significant observable changes up to 460 K. Above this temperature however, a deviation from the expected single exponential decays was observed. An example of such traces, generated at 540 K and 2 atm of N_2 is shown in Figure 6.4, where a single exponential (orange line) and a bi-exponential curve (red line) were fitted to the depicted trace. The green line represents the baseline, calculated as the average of the background signal, which was probed before the excimer beam crosses through the reaction cell (negative delay). The decay of the OH signal clearly shows a delay, not returning to the original background levels. The depicted curve, which resembles a bi-exponential decay, denotes the existence of one or more

channels by which OH radicals are regenerated. The residual plots for the fits are presented in Figure 6.5 and Figure 6.6.

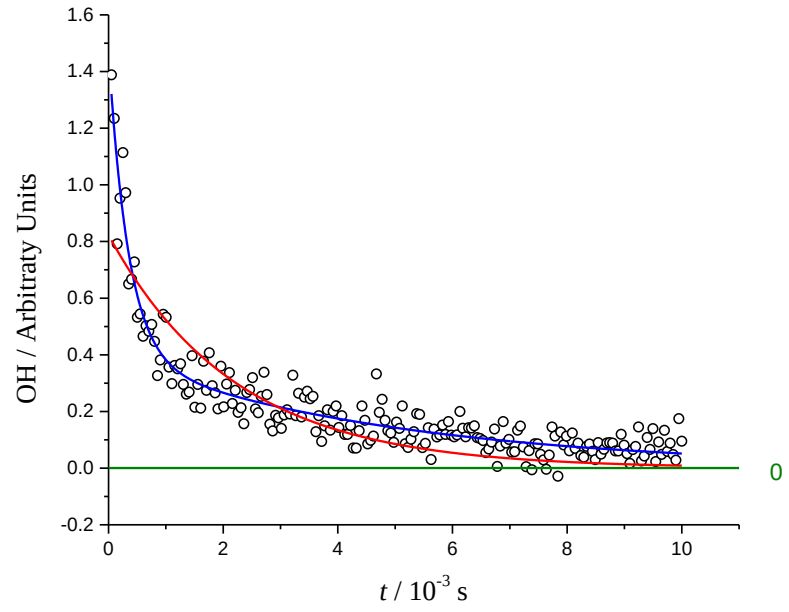

Figure 6.4 - An example of a non-exponential decay, generated for $[C_5H_8] \approx 1.00 \times 10^{14}$ molecule cm^{-3}, 10^{19} O_2 cm^{-3}, 540 K and 2 atm. The data were averaged after 10 scans. The blue line represents a bi-exponential curve fitted to the data while the red line represents a single exponential curve fit. The green line represents the average for the background OH signal.

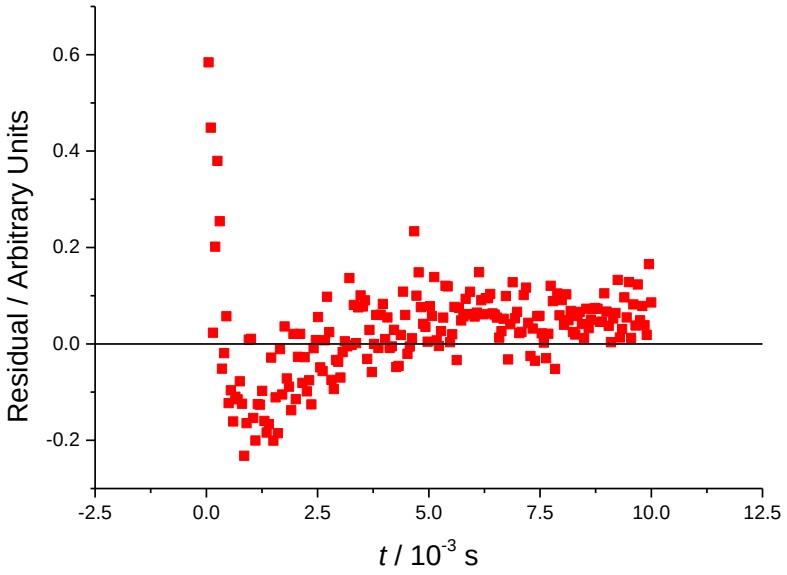

Figure 6.5 - The residuals plot for the single exponential fit presented in Figure 6.4.

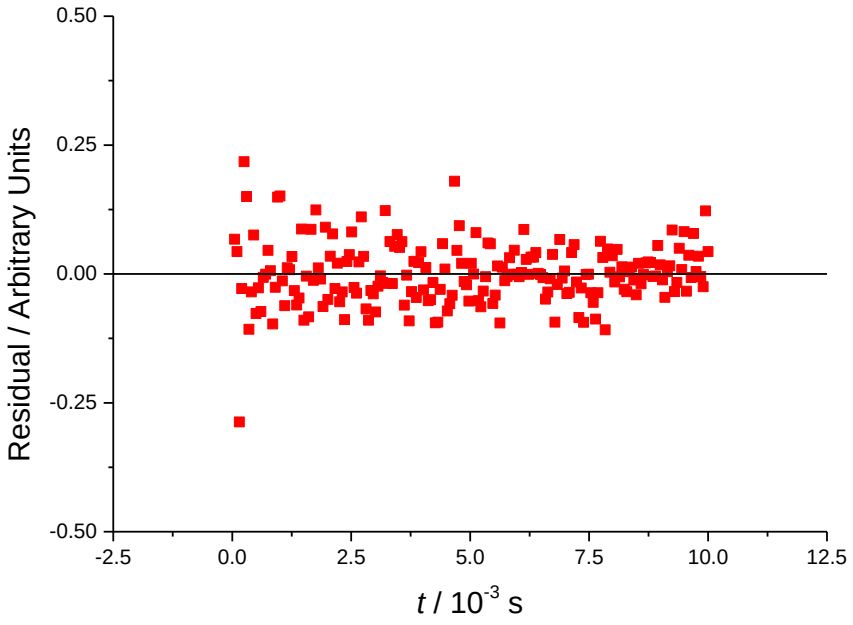

Figure 6.6 - The residuals plot for the bi-exponential fit presented in Figure 6.4.

Significant changes are observed on the residuals of the single exponential fit, where a transition from a model underestimation to a model overestimation is found at near t=0. The residuals indicate another shift back to an underestimation somewhere between 2.5 and 5.0 ms. These shifts between underprediction and overprediction indicate that the use of the single-exponential equation is not appropriate to describe the observed kinetics The more balanced distribution around zero observed for the residuals of the bi-exponential fit suggest a better suitability of this model, again, denoting the existence of significant OH recycling.

Such non-exponential traces were ultimately analysed with the novel method presented in detail in Chapter 5 where LIM1 was modelled via the ME approach and modified to incorporate the H-abstraction explored in Chapter 4. However, the high-pressure limit assumption was initially made and LIM1 was implemented in a simpler fitting exercise, where all the rate coefficients involved were assumed to be pressure independent. Moreover, these rate coefficients and their temperature dependencies were taken directly from the work of Peeters *et al*.[3] These results will be discussed in the following, prior to the presentation of the ME treatment. The extrapolation of the obtained results

to atmospheric conditions is of primary importance to enable an assessment of the impact of this recycling in current atmospheric models predictions. The use of various approaches to analyse the data will shed light into the extrapolation procedure, attributing more confidence to the obtained results.

Table 6.1 – List of experimental conditions at which OH traces were collected for the isoprene + OH reaction in the presence of O_2.

T / K	p / Torr	k_{loss} / s^{-1}	n_{traces}
420	1404	1362	4
477	1404	1480	8
478	134	396	5
480	125	234	21
498	1404	1458	8
513	162	31	8
543	140	334	10
543	140	335	12
550	1366	1693	8
584	124	89	10

A total of 94 traces were analysed, comprising temperatures between 420 and 585 K and pressures between ~125 and ~1400 Torr. Table 6.1 contains the complete list of conditions along with the number of traces collect under each one of them. In this table k_{loss} refers to the loss of OH due to diffusion and reaction with the precursor, measured in the absence of isoprene. Even though traces at 420 K do not present observable recycling, their inclusion in the analysis help constrain the optimized parameters. For example, if the recycling is unreasonably facilitated by the optimization algorithm, the simulations of traces generated 420 K could present recycling, something that would need to be addressed by the algorithm. These traces can help define for example, lower limits of recycling-related energy barriers.

As discussed in Chapter 4, temperatures above 700 K would be necessary for the decomposition of the isoprene-OH adducts to be comparable to the forward

addition reaction. Given that the highest temperature explored in the presence of O_2 is below 600 K, the assumption that the observed OH recycling in this case is directly related to the chemistry of the isoprene peroxy radicals is reinforced. These traces can therefore be used for an examination of the thermochemistry of these O_2-involving processes. Additionally, according to Chapter 4, only measurements collected above 700 K presented signs of pressure dependence. Considering that the isoprene-OH wells are very deep ($\Delta H_{C4H8\text{-}OH,\ 0\ K}$ ~150 kJ mol^{-1}) compared to the peroxy ones ($\Delta H_{\beta\text{-}OH\text{-}peroxy\ I,\ 0\ K}$ < 100 kJ mol^{-1}), one would not expect to detect a pressure dependence of the O_2 additions to the isoprene-OH adducts under these significantly lower temperatures ($|\Delta T|$ > 100 K). For this reason, the high-pressure assumption should be a reasonable approximation, and as will be verified in the next section, can yield reliable and consistent results.

6.3.2 - Numerical integration coupled with a global fit

The experimental traces generated in the presence of O_2 were analysed via a multi-temperature global fitting procedure using MATLAB R2016.[28] The Trust Region Reflective Algorithm[29] was implemented for the minimization of the objective function, defined as the sum of squared residuals, calculated from a comparison between experimental measurements and their corresponding numerical simulation. The chemical model consisted of LIM1, coupled with the OH additions and H-abstraction, from the recommended results of Chapter 4:

$$k_{1a}^{\infty} = (9.5 \pm 0.2) \times 10^{-11} \left(\frac{T}{298\ \mathrm{K}}\right)^{-1.33 \pm 0.07} \qquad \text{E1}$$

$$k_{1b} = (1.3 \pm 0.3) \times 10^{-11} \exp\left(\frac{-3.61\ \mathrm{kJ\ mol^{-1}}}{RT}\right) \qquad \text{E2}$$

The loss of OH due to diffusion and reaction with the precursor was simply set as an equivalent unimolecular loss of OH. The list of reactions was processed with the aid of a recently developed Excel interface (illustration available in Appendix 4), programmed to interpret chemical reactions and translate them into a set of ODEs describing the rate laws of the involved species. This

interface also allows the definition of adjustable parameters such as the pre-exponential factors or activation energies of the involved bimolecular rate coefficients. Every rate coefficient was described in the form of a modified Arrhenius equation, which also contains a term related to quantum mechanical tunnelling. Equation E3 generically shows this formulation with respect to a generic reaction *i*.

$$k_i = A_i \times (T/298\ \mathrm{K})^{n_i} \times \exp\left(\frac{Ea_i}{RT}\right) \times \exp\left(\frac{Q_i}{T^3}\right) \qquad \text{E3}$$

This equation is versatile enough to allow the incorporation of barrierless reactions such as the OH and O_2 additions and processes with well-defined activation energies as the previously studied hydrogen abstraction. The last factor in the equation was used by Peeters *et al*. to account for quantum mechanical tunnelling of the 1,6-H shift reactions. For example, in Case 1, their recommended equation for this process is presented in Equation E4.

$$k_{\text{1-6-H, Case 1}} = 3.556\times10^{10} \times \exp\left(\frac{-71.41\ \mathrm{kJ\ mol^{-1}}}{RT}\right) \times \exp\left(\frac{1.0265\times10^{8}\ \mathrm{K^3}}{T^3}\right) \qquad \text{E4}$$

This equation does not contain the $(T/298\ \mathrm{K})^{n_i}$ term, something that can be programmatically implemented by setting n_i to zero. Analogously, any other term in equation E3 can be turned off by simply setting the corresponding temperature dependence parameter to zero. The aforementioned interface also requires the temperature at which each trace was generated and the initial concentration of the involved species. Once everything is provided, a MATLAB script is generated, containing a code to numerically integrate the set of ODEs for each experimental condition, compare the results with experimental measurements and minimize the objective function. Appendix 4 contains an example of a MATLAB script used to fit 6 traces using LIM1. The list of adjustable parameters includes a scaling factor for the pre-exponential factor of all the isoprene-OH + O_2 reactions, so that their ratios are maintained unchanged. An attempt to include an adjustable temperature dependence for these reactions was made, but the returned parameters were ill-defined, i.e., the

uncertainty was significantly greater than the actual optimized parameter. For this reason, the C_2H_5-OH + O_2 reactions were only adjusted via their pre-exponential factors. The barriers of the crucial hydrogen shifts were adjusted in unison, *i.e.*, their relative difference was maintained constant throughout the fitting procedure. Figure 6.7 is an attempt to demonstrate a change in the energy barriers of 1,5 and 1,6-H shifts, where both of them are modified by the same quantity, indicated in red.

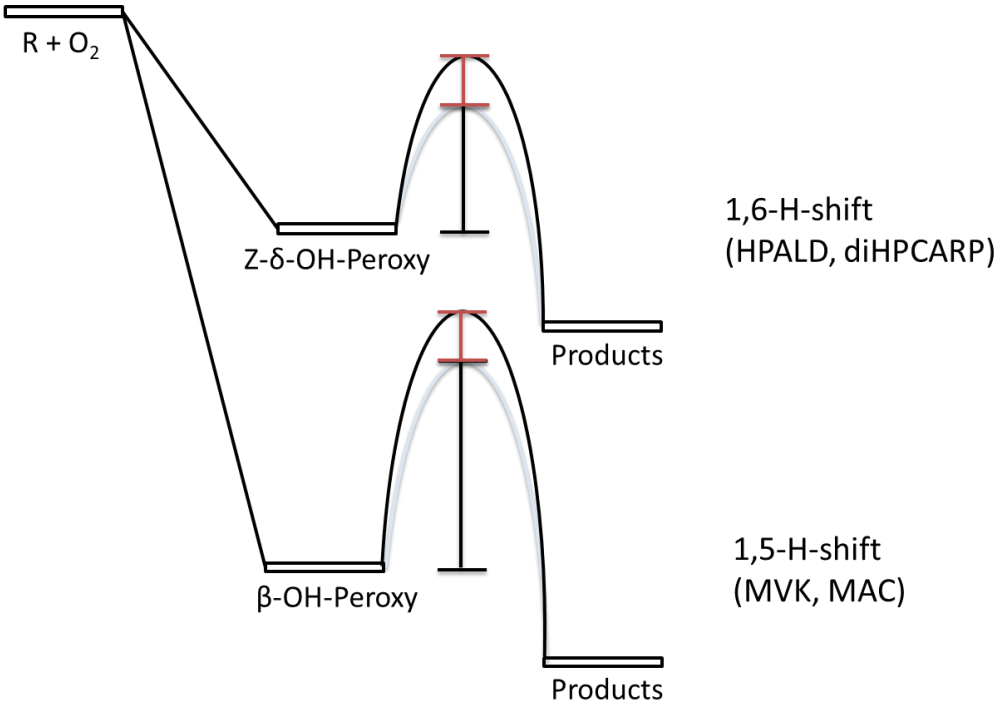

Figure 6.7 – Energy barriers of the hydrogen shifts being modified in unison, as implemented in the fitting procedures.

Changing the barriers of these processes ultimately means changing the product yield of HPALD and di-HPCARP. As discussed in the introduction section, the HPALD production rate has been measured in the work of Crounse *et al.*[14] and therefore needs to be taken into account in the current analysis. During the fitting procedures, the branching ratios of the subsequent chemistry of the Z,Z'-allyl-radicals, the intermediate specie formed from the 1,6-H shift (see Figure 6.2) were adjusted as to maintain the agreement with the production rates of HPALD reported by Crounse *et al*. The fit proceeds following this logic: if the barriers are reduced, HPALD yields at 298 K would

naturally increase and disagree with the measurements by Crounse *et al*. To avoid this consequence, the branching ratio of the HPALD channel is reduced proportionally as to re-establish the agreement, redirecting the chemistry to the di-HPCARP channel. The necessary branching ratios were mapped out as a function of the H-Shift barriers with the much appreciated collaboration of Dr Lisa Whalley, using an atmospheric model based on the Master Chemical Mechanism (MCM) version 3.2.[30] The MCM is a near-explicit chemical mechanism dedicated to describe the gas-phase tropospheric chemistry of volatile organic compounds and in this analysis has been modified to incorporate the chemistry of LIM1. The model has incorporated the NO_x conditions of the Borneo OP3 field campaign[2, 4], a work in which the discrepancy between measured and modelled OH was approximately a factor of 2. At room temperature, a branching ratio of approximately 25% for the HPALD channel and consequently, 75% for the di-HPCARP channel, is required if the barriers of the H shifts are assumed to be those as reported by Peeters *et al*., guaranteeing a good agreement with the HPALD measurements by Crounse *et al*. The branching ratios were mapped out for a maximum change of approximately 5 kJ mol^{-1}, a reasonable range for the adjustment of the barriers. The mapped branching ratio with respect to the HPALD channel, utilized in this work can be calculated from equation E5:

$$BR_{\mathrm{HPALD}} = 4.3160\times10^{-7} \times (Ea_{\text{1-5-H shift}} / \mathrm{R})^2 - 7.8937\times10^{-3} \times (Ea_{\text{1-5-H shift}} / \mathrm{R}) + 36.187 \qquad \text{E5}$$

where BR_{HPALD} is the branching ratio for the HPALD channel (in %), $Ea_{\text{1-5-H shift}}$ is the assigned activation energy for the 1-5-H shift of Case 1 and R is the gas constant with the appropriate units. It is important to reinforce that the activation energies of the remaining H shifts are linked to this one during the fitting procedures, as to maintain their relative energy differences intact, as illustrated in Figure 6.7. This fitting procedure is referred to as *BR-linked*, to denote the fact that the branching ratio is linked to the adjustable barriers via equation E5.

Finally, a fit where the aforementioned branching ratio was set as an independent adjustable parameter was also undertaken. In this case, Equation E5 is not considered and the branching ratio is freely allowed to assume any value between 0 and 100 %. This fitting procedure is referred to as *BR-free* to analogously indicate that the Z,Z'-allyl-radical + O_2 → HPALD branching ratio is a *global variable*, programmatically independent of the other parameters. Table 6.2 shows the resulting parameters of the two fits along with uncertainties quoted at 2σ. The table also includes the sum of squared residuals χ^2 divided by the total number of traces (94), as a measure of the goodness of each fit. Figure 6.8 exemplifies the fits of multiple traces, generated under various experimental conditions.

Table 6.2 – Best-fit parameters for both *BR-Linked* and *BR-free* fitting procedures. Errors quoted at 2σ

Parameter	*BR-Linked*	*BR-free*	Peeters *et al.* [3]
C_5H_8-OH + O_2 Scaling Factor	3.00 ± 1.46	3.00 ± 1.62	1.00
1-5-H shift barrier / kJ mol^{-1}	81.31 ± 0.17	80.48 ± 0.28	81.03
BR_{HPALD}	0.27*	0.37 ± 0.03	0.50
χ^2 / n_{traces}	1.17	1.16	-

*- Calculated with equation E5 during the fit.

Before the results are discussed, it is important to highlight an aspect of the recommended LIM1 H-shift rate coefficients. Peeters *et al.* have incorporated the tunnelling contribution to the 1,5-H shifts as effective reductions of the classic Arrhenius barriers. For example, their theoretical calculations indicate an activation energy of 89.08 kJ mol^{-1} for the 1,5-H shift in case1, but the corresponding recommended equation for this rate coefficient $k_{1\text{-}5H\text{-}shift} = 1.038 \times 10^{11} \times \exp(-9746.4\ K\ /\ T)$ employs an effective barrier of 81.03 kJ mol^{-1}. The fitting procedures are directly adjusting the equations of the rate coefficients, which mean that effective barriers are being adjusted.

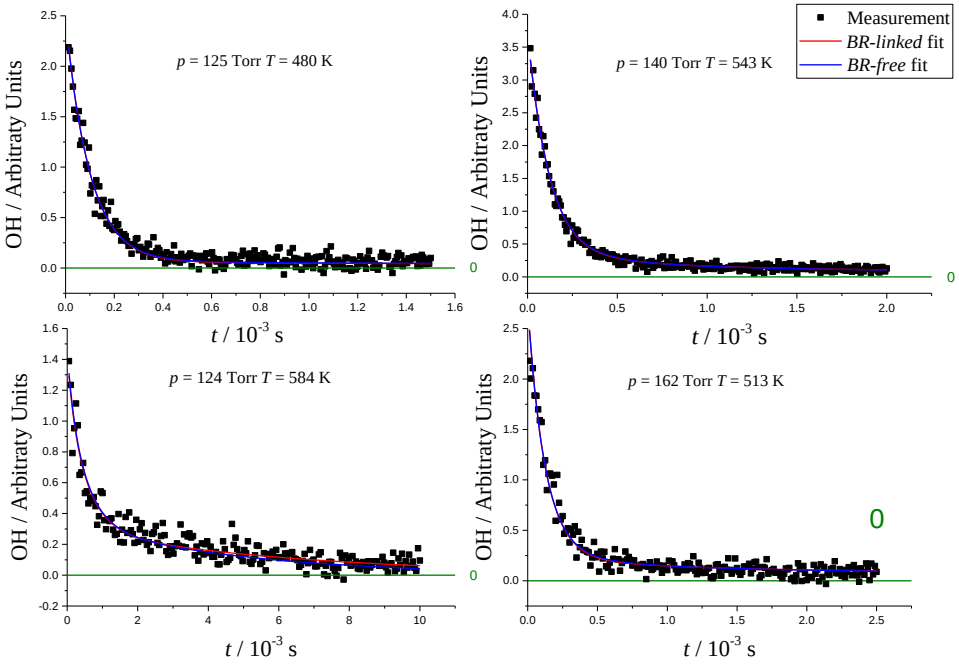

Figure 6.8 - Examples of LIM1 fits to the data for various experimental conditions.

As denoted by both the values of χ^2 /n_{traces} in Table 6.2 and the examples presented in Figure 6.8; constraining the fits to agree with the HPALD production rates of Crounse *et al*. did not provoke a worsening of the quality of the global fit. This is clear, not only from the very similar goodness of fits, but also from careful visual inspections of the traces. It is difficult to find a clear difference between the red (*BR-linked*) and blue (*BR-free*) fits in Figure 6.8. The C_5H_8-OH + O_2 rate constants of LIM1 were scaled by a factor of 3 in both flavours of fit, which is the upper limit set for this adjustable parameter. However, the significant errors reported (~50%) indicate that lower values are also acceptable. The barriers only required small modifications to the theoretically developed values ($|\Delta Ea| < 1$ kJ mol^{-1}) in order to provide a very good fit to the data. This excellent agreement is somewhat impressive given that LIM1 is a purely theoretically developed mechanism.

When fitted, the branching ratio of the HPALD channel appears as a very well-defined parameter, as evidenced by the small uncertainty obtained (0.37 ± 0.03). This value is slightly skewed from the one which guarantees a good agreement with the HPALD production rates of Crounse *et al*. for the

barrier of 80.48 kJ mol^{-1} (BR_{HPALD} ~0.23). However, this value is qualitatively aligned with the idea that most of the chemistry needs to be directed to the di-HPCARP channel if the barriers are to be reduced. The fact that the data contain a good sensitivity to this parameter is not a surprise, given that the two channels present an important and fundamental difference: while OH recycling from HPALD is photolytic, di-HPCARP is believed to thermally decompose to OH.[3]

To verify whether a product photolysis is significant or not for the observed kinetics, checks were undertaken by varying the excimer repetition rate (1- 10 Hz) with no evident changes in the OH traces being observed. Considering a total flow of 2 litres per minute flowing through the reaction cell, a diameter of 3 cm and cell length of 27 cm, the residence time of the gas in the reaction cell is of about 5.7 seconds. Considering a repetition rate of 1 Hz, the gas was flashed about 6 times before leaving the cell and the absence of an obvious effect when the repetition rate is varied indicates that a potential photolysis of HPALD at 248 nm does not generate significant amounts of OH. A YAG laser (Quantel, Q-smart laser) tuned at 355 nm was used for additional checks at this wavelength, being fired between the 248 nm excimer and 282 nm probe to check for an enhancement of the detected OH. Once again, no increase in the OH signal was observed. These checks indicate that HPALD does not photolyze to produce OH during our experiments, and therefore, this channel represents a loss of OH from the system. The di-HPCARP channel on the other hand is believed to thermally recycle OH, keeping it alive for longer periods. By adjusting the branching ratio between the two channels, the minimization algorithm is capable of finding the ratio that best describes the slope observed at longer times of the non-exponential traces. The graph on the bottom left corner of Figure 6.8 clearly shows a slope in the recycling section beyond 1 ms.

Two modifications were made to LIM1 in order to further explore features of the mechanism: the first one, to assume that the di-HPCARP species do not decompose to OH and the second, to apply the LIM1 modifications suggested

in the work of Teng *et al.*[16] Figure 6.9 depicts a representative trace, in which the various flavours of models implemented can be easily discriminated.

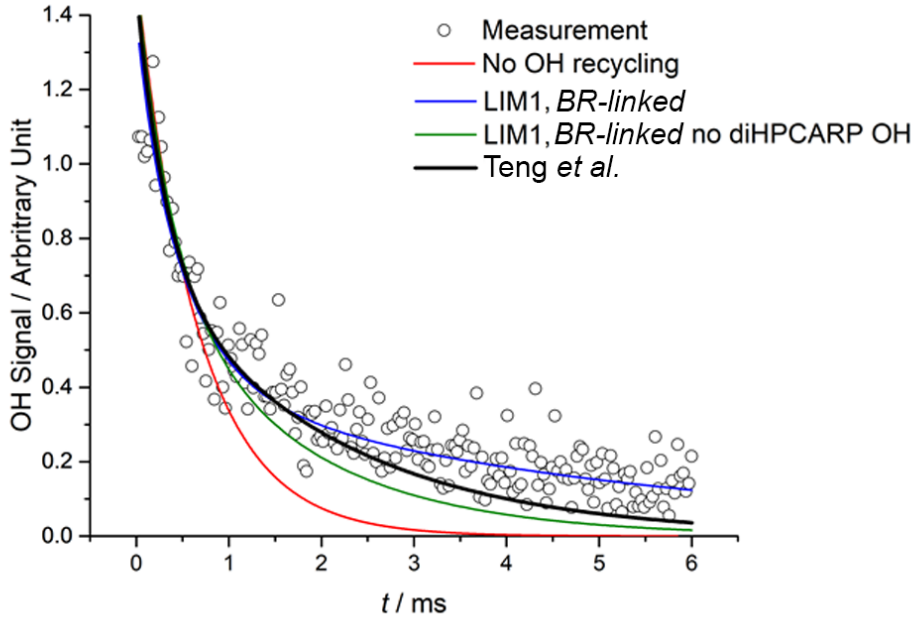

Figure 6.9 – Comparison of the various models implemented when fitting a trace generated at 584 K and 124 Torr of N_2. $[C_5H_8] \sim 4\times10^{13}$ molecule cm^{-3}, $[O_2] \sim 1\times10^{17}$ molecule cm^{-3}. The red line shows a single-exponential fit to the data.

It is not a surprise that the blue line (*BR-linked*) is a good fit, as discussed previously. The green line shows the best-fit result if the di-HPCARP specie is assumed not to decompose to OH. As a response to such a severe modification, the optimization algorithm attempts to reduce the barriers of the H-shifts, enhancing the OH recycling from the 1,5-H shifts. In fact, the green fit is obtained by reducing the effective barriers from 81.03 to 76.31 ± 0.27 kJ mol^{-1}. The poor fit shows that the 1,5-H shift is not capable of compensating the lack of the di-HPCARP chemistry. This is justified by the fact that the timescales of these recycling processes are considerably different. While the di-HPCARP formation requires two extra O_2 additions following the 1,6-H shift, the product of the 1,5-H transfer rapidly falls apart to OH (see Figure 6.2).

Following this idea, it is clear why the model produced from the modifications of Teng *et al.* is not capable of providing a good fit to the data (black line). As

discussed in the introduction section, the modifications greatly reduce the importance of the *Z*-δ-OH peroxy radicals and consequently, that of the di-HPCARP channel. The change is not as severe as completely turning off the OH recycling from this channel (green line), and this is why its fit is located between the blue (LIM1 *BR-linked*) and the green lines (No di-HPCARP OH). In the fit of the Teng *et al*. model, the barriers are increased by 1.71 ± 0.26 kJ mol^{-1}. By enhancing the abundance of the *β*-OH-peroxy radicals, a significant enhancement of the recycling at earlier times, compared to those of the di-HPCARP channel is caused, which is rapidly translated into an overestimation of the recycling at early times. This effect is diminished by the optimization algorithm by increasing the barriers of the H shifts. Because the 1,6-H shift barriers are also increased (they are all moved in unison), the recycling at longer times is affected, presenting a prolific slope in the numerically integrated traces.

Additionally to these fits, the resulting parameters of the LIM1-*BR-linked* and Teng *et al*. models were incorporated in MCM atmospheric simulations of the OP3 Borneo campaign in order to evaluate the impact of these results in an atmospheric model. Figure 6.10 shows the results of these simulations compared to the experimental OH measurements in one of the days of the OP3 campaign.

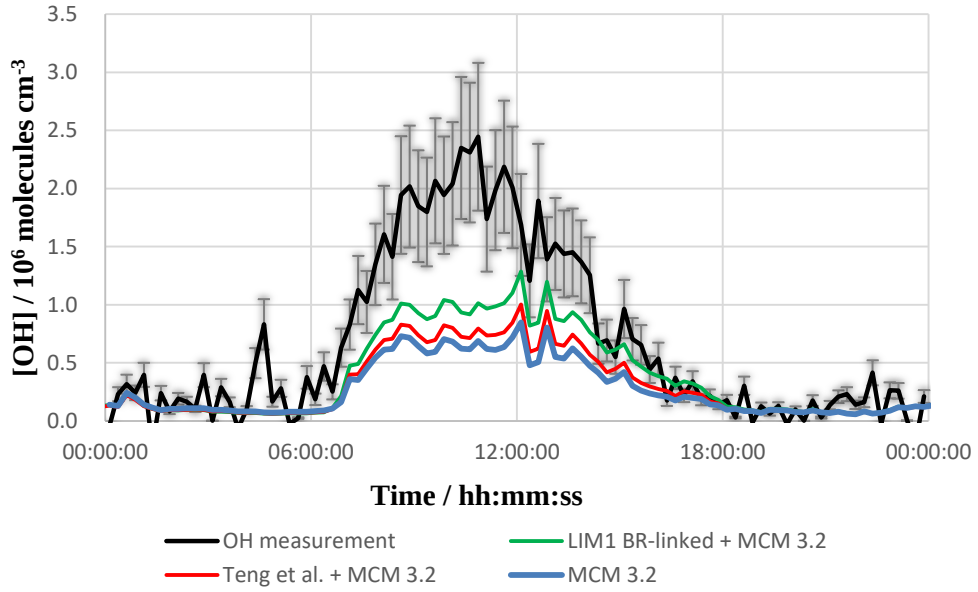

Figure 6.10 – MCM atmospheric simulations of the OP3 campaign against the actual OH measurements for various models. Error bars represent the 28% uncertainty associated with the OH measurements undertaken during the OP3 field campaign.[4]

The blue line represents a model that does not incorporate LIM1 and the figure clearly indicates an improvement of the OH prediction when the LIM1-*BR-linked* parameters are incorporated (green line). The reduced importance of the *Z*-δ-OH-peroxy radicals and enhancement of less important *E*-δ-OH peroxy radicals in the work of Teng *et al*. contributes to the observed reduction of the predicted OH when this model is used. As presented in Figure 6.2, the chemistry of the *E*-δ-OH isomers does not lead to OH regeneration. The area under the red line (Teng *et al*.) represents ~50% the area under the black line (measurements) and the area under the green line (LIM1-*BR-linked*) represents ~60% of the measurement area. The unmodified MCM 3.2 accounts for ~45% of the measurement area.

Finally, the OH data of the LIM1-*BR-linked* and Teng *et al*. models were further consolidated as to identify the sources from which the modelled OH is being generated. The pie charts presented in Figure 6.11 show that even for the pristine environment of Borneo ($[NO]_{average}$~ 1× 10^9 molecule cm^{-3}), the reaction of NO with HO_2 radicals is still the most important process for OH

generation, accounting for more than 40% in the case of the LIM1-*BR-linked* model and more than 50% if the Teng *et al*. MCM model is employed.

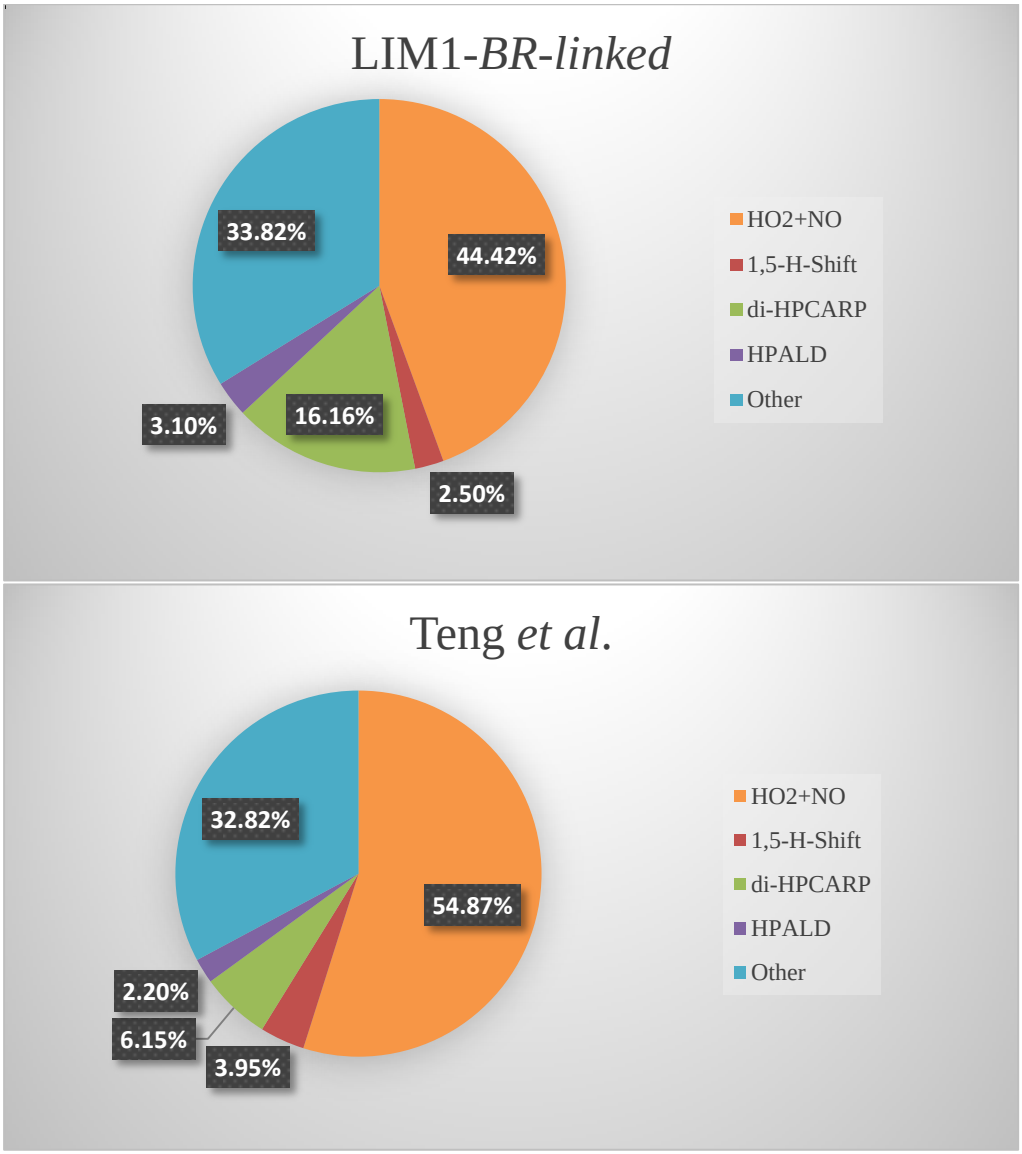

Figure 6.11 - Sources of OH in the atmospheric simulations of the LIM1-*BR-linked* and Teng *et al*. models included in Figure 6.10.

The chemistry of non-isoprene related species accounts for approximately 30% of the total OH in both models. Ozone photolysis and OH recycling from alternative available species such as monoterpenes are examples of processes accounted for as *Other* in these pie charts. The OH generated from the isoprene chemistry is split into three sources: (I)1,5-H shifts, where OH is a co-product of formaldehyde and methyl vinyl ketone (case 1) and methacrolein (case 2); (II) photolysis of HPALD and (III) thermal decomposition of di-HPCARP. While the isoprene chemistry is responsible for more than 20% of the total OH

when the LIM1-*BR-linked* model is considered, this value is reduced to 12.3% when the Teng *et al*. variant is assumed. The greater importance of the di-HPCARP specie in the LIM1-*BR-linked* model is an interesting feature, given that the di-HPCARP decomposition also gives rise to dihydroperoxy-carbonyl radicals, which according to Peeters *et al*., could photolyze to further reform OH.[3] However, the fact that these dihydroperoxy-carbonyl radicals can also react with OH means that the net budget in this case is controlled by the competition between this reaction and the photolytic process. Either way, the larger di-HPCARP chemistry contribution for the modelled OH in the case of LIM1-*BR-linked* represents a greater potential for further improving the correspondence between current atmospheric model predictions and measured OH, as exemplified in Figure 6.10.

This section demonstrated that, by making the high-pressure limit assumption, LIM1 successfully described the kinetics of the isoprene + OH reaction in the presence of O_2 at elevated temperatures (400 K<T<600 K). The model was capable of describing the experimental traces in a robust multi-temperature fit. Results also indicated that there is enough room in the fits to constrain the procedures as to force an agreement to the production rates of HPALDs reported by Crounse *et al.*[14] without compromising the overall goodness of fit. The fits were capable of identifying distinct OH recycling processes in the mechanism, based on their timescales. This is consistent with the formation and thermal decomposition of di-HPCARP species, as theoretically predicted in the work of Peeters *et al*.[3] The atmospheric impacts of the optimized parameters were evaluated by simulating the atmospheric conditions comprised at the OP3 Borneo campaign, being LIM1 capable of describing up to 60% of the total OH measured in that field work.

6.3.3 – Augmented-ME analysis

In order to enable the use of the ME-based fitting strategy presented in Chapter 5, the LIM1 was modelled via the Master Equation approach and augmented with a hydrogen abstraction, as described in Chapter 4 and the OH loss due to diffusion and reaction with the precursor. Figure 6.12 shows the potential energy diagram of LIM1 with respect to the OH addition to carbon C_1 as implemented in the Master Equation calculations. As indicated in that Figure, effective barriers from the work of Peeters *et al*. were used as first guesses, but were subsequently adjusted in unison, in the same fashion presented in the previous section.

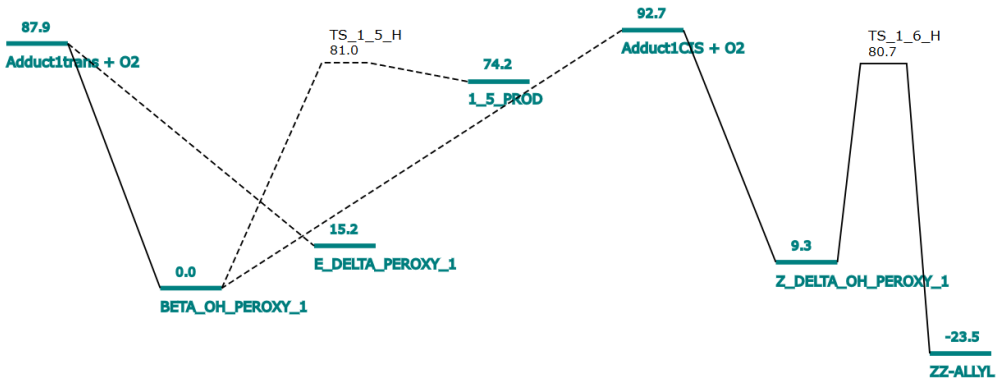

Figure 6.12 - Potential energy diagram for the Leuven Isoprene Mechanism 1 used in the current analysis. Depicted energetics represent effective barriers that account for tunnelling from the work of Peeters *et al*. Energies in kJ mol^{-1}.

For the 1,5-H shifts, the rate coefficients were obtained directly from the ME calculations. For the 1,6-H shifts however, the ME computations did not include any tunnelling corrections but these were posteriorly incorporated via the recommendations of Peeters *et al*. Equation E4 showed their recommendation for the 1,6-H shift in Case 1, and Equation E6 now shows the corresponding correction for Case 2. The parts highlighted in red are the tunnelling corrections recommended by Peeters *et al*. It is important to mention however, that the barriers incorporated in the exponential terms highlighted in blue were also modified by Peeters *et al*. in order to best describe their predictions of $k_{1\text{-}6\text{-H, Case 1}}$ and $k_{1\text{-}6\text{-H, Case 2}}$. In order to estimate the tunnelling factors of these processes and their temperature dependences, the authors have

implemented the asymmetric Eckart-barrier approximation,[15] which yielded strongly curved, negative temperature-dependences, as denoted by the T^{-3} terms of equations E4 and E6. These equations were directly taken from the work of Peeters *et al.*, and were derived from least-squares fits of their estimations of the tunnelling factors, estimated in the 280-320 K temperature range.

$$k_{\text{1-6-H, Case 1}} = 3.556\times10^{10}\times \exp\left(\frac{-71.41\ \text{kJ mol}^{-1}}{RT}\right)\times \exp\left(\frac{1.0265\times10^{8}\ \text{K}^{3}}{T^{3}}\right) \qquad \text{E5}$$

$$k_{\text{1-6-H, Case 2}} = 1.070\times10^{11}\times \exp\left(\frac{-67.96\ \text{kJ mol}^{-1}}{RT}\right)\times \exp\left(\frac{1.0000\times10^{8}\ \text{K}^{3}}{T^{3}}\right) \qquad \text{E6}$$

Effective barriers were implemented in the augmented-ME approach in order to allow the incorporation of the T^{3} tunnelling corrections as predicted by Peeters *et al*. However, it is possible that the rate coefficients calculated via this methodology will disagree with predictions by Peeters *et al*. This is justified by the fact that their recommendations were based on multi-conformer transition-state theory calculations[31], as opposed to the current ME-based predictions. As a consequence, the augmented-ME analysis does not guarantee an agreement to the production rate of HPALD as reported by Crounse *et al*. as the rate coefficients for the H shifts are now partially derived from the ME calculations undertaken in the current work. The current ME calculations are based on lowest energy conformers only.

Despite this fact, the results of the current augmented-ME computations are still relevant as to show the importance of potential well-skipping reactions under the covered experimental conditions. If the chemistry is dominated by well-skipping of the HO-RO_2 wells, the extrapolations of the results to atmospherically relevant conditions become a more challenging task. The fits were performed using both a vibration-only model, where all the vibrational modes of all involved species were described with the harmonic oscillator approach; and with a model in which a total of 40 small vibrational frequencies, related rotational torsions, were described with the hindered rotor approach. This last variant will be referred to as *Hindered Rotor model*. As

discussed in Chapter 4, the change in the density of states caused by the augmentation of the degrees of freedom of the species is better captured with the use of the latter approach. The best-fit parameters of the augmented-ME fits are presented in Table 6.3, and Table 6.4 shows the 298 K extrapolated rate coefficients for the 1,5 and 1,6-H shifts calculated from the best-fit parameters in Table 6.3. Figure 6.13 exemplifies fits of both the vibration-only and *Hindered Rotor* models to a representative OH trace generated at T=584 K and p=125 Torr.

Table 6.3 - Best-fit parameters for both *Vibration-only* and *Hindered Rotor* fitting procedures. Errors quoted at 2σ

Parameter	*Vibration-only*	*Hindered Rotors*	Peeters *et al.* [3]
C_5H_8-OH + O_2 Scaling Factor	0.20 ± 0.16	0.20 ± 0.11	1.00
1-5-H shift barrier / kJ mol^{-1}	86.33 ± 0.08	82.50 ± 0.17	81.03
BR_{HPALD}	0.76	0.36	0.50
χ^2 /n_{traces}	1.32	1.22	-

Table 6.4 - Calculated rate coefficients for the H shifts extrapolated to 298 K and 760 Torr.

		Vibration Only	*Hindered Rotors*	*High-Pressure Assumption*	Peeters *et al.*
Case 1	1-5 H shift	1.34×10^{-3}	2.13×10^{-3}	5.80×10^{-4}	6.50×10^{-4}
	1-6 H shift	3.33	1.44	0.46	0.52
Case 2	1-5 H shift	3.00×10^{-3}	5.41×10^{-3}	1.03×10^{-3}	1.20×10^{-3}
	1-6 H shift	51.93	7.28	5.11	5.70

Rate coefficients in s^{-1}.

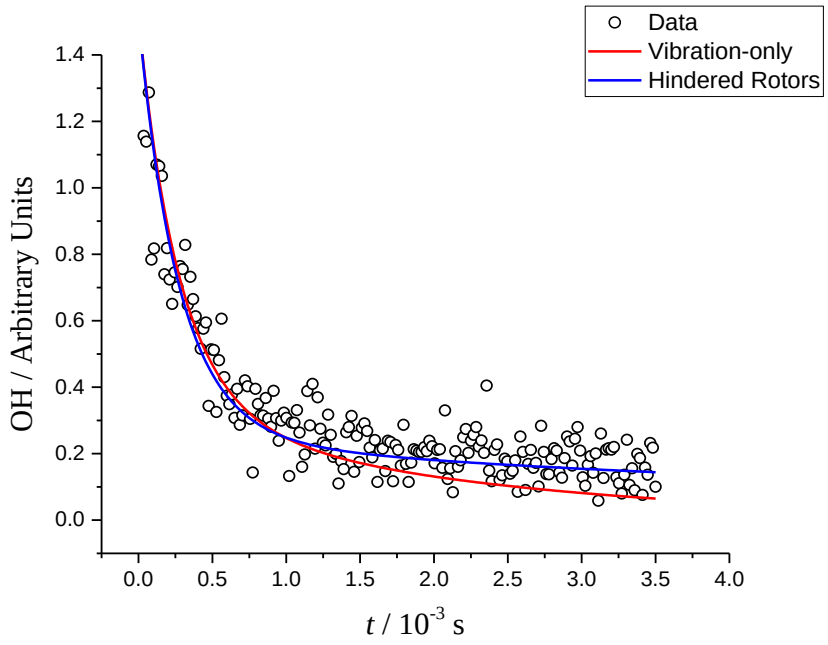

Figure 6.13 – Fits of the vibration-only model and a model which incorporate a total of 40 hindered-rotors to describe corresponding rotational torsions.

Table 6.4 also includes the 298 K rate coefficients extrapolated from the results presented in section 6.3.2 when making the high-pressure limit assumption (*High-Pressure Assumption*). The original recommended values by Peeters *et al*. are included in the final column of that table for reference. According to this table, the vibration-only model heavily overestimates the values recommended by Peeters *et al*., justifying the significantly larger barrier obtained when this model was incorporated (86.33 kJ mol^{-1}), as an attempt to compensate this effect. Analogously, in section 6.3.2 when LIM1 was modified to incorporate the recommendations from the work of Teng *et al*.[16], the chemistry of the 1,5-H shift was significantly enhanced. To compensate this effect, the optimization algorithm attempted to increase the barriers, affecting the capability of the model to describe the recycling at longer times (see Figure 6.9). Here, a similar effect is observed, as depicted in Figure 6.13, when the vibration-only model is adopted. The significant overestimation of the OH recycling leads to an increase of the barriers, which are all linked, provoking a poor fit over the sections of the traces where the di-HPCARP chemistry is important.

The model which incorporated the hindered rotors is more aligned with the predictions by Peeters *et al*. although the rate coefficients are systematically higher. As pointed out before, the estimations of Peeters *et al*. were computed via Transition-State Theory calculations which took into account a combination of multiple conformers of the involved intermediate species, while the current Master Equation calculations are purely based on the lowest energy conformers. This fact certainly goes some way into explaining the observed discrepancy. The hindered-rotor model is expected to overestimate the HPALD production by approximately a factor of 3, based on a comparison of the simulated production rates of HPALD between this model and the *High-pressure assumption* variant, presented in section 6.3.2.

At the most extreme experimental conditions covered in this work, 584 K and ~125 Torr, the *Hindered Rotor* model predicts that the largest possibility of well-skipping occurs over the 15-H shift in Case 2. In this case, the products of the 1-5 H shifts can be formed directly from the reactions of the *cis* and *trans* conformations of the C_5H_8-OH adducts with O_2 (see Figure 6.2), as indicated by reactions R9 and R10.

cis-OH-adduct 2 + O_2 → Prod II R9

trans-OH-adduct 2 + O_2 → Prod II R10

However, even for the mentioned experimental conditions, the ME calculations indicate that the well-skipping contribution is small, representing less than 4% of the reactions of the aforementioned C_5H_8-OH adducts with O_2. The vast majority of these O_2 reactions proceed via the formation of the *β*-OH-peroxy radical, followed by the corresponding 1,5-H shift. For the other possibilities of well-skipping, including skipping over the *Z*-δ-OH peroxy radicals, these account for approximately 1% of the total C_5H_8-OH reactions with O_2. No signs of pressure dependence under the covered experimental conditions were predicted in the ME calculations.

As indicated by the *Hindered Rotor* results, very small adjustments to the effective energy barriers and C_5H_8-OH + O_2 reactions are sufficient to provide a good fit of a ME-based model to the collection of OH traces. This is aligned with the results of section 6.3.2, where a small change of approximately 2 kJ mol^{-1} in the H-transfer barriers was necessary. Well-skipping over the peroxy radicals was found to be of minor importance even at the experimental conditions where these reactions are most likely to potentially influence the kinetics (T ~584 K, p ~125 Torr). Therefore, this section reinforces the suitability of the analysis presented in section 6.3.2, in which the well-skipping possibility was ignored and the chemistry was assumed to be pressure-independent. The current work was capable of demonstrating OH recycling from isoprene-peroxy chemistry, and proved the suitability of LIM1 to describe the mentioned recycling. Given the variety of tests and experimental compatibility, the current work represents an appropriate validation of the Leuven Isoprene Mechanism 1. Further explorations of the LIM1 can provide valuable insight regarding the remaining missing OH.

6.4 SUMMARY AND CONCLUSIONS

In Chapter 6, the OH recycling observed for the reaction of isoprene with OH radicals in the presence of O_2 for temperatures between 460 K and 584 K was elucidated with the aid of the Leuven Isoprene Mechanism 1.[3] A variety of fits were undertaken in order to extract as much information as possible from the experimental measurements.

Initially, the high-pressure limit assumption was made and LIM1 was explored via numerical simulations of the reaction scheme. The mechanism was not only capable of qualitatively predicting OH recycling at the aforementioned temperatures, but also provided a very accurate description of the experimental observations, requiring small changes to the activation energies employed in the model (|ΔEa| ~2 kJ mol^{-1}). The analysis also showed that there is sufficient flexibility in the data in order to constrain the fits so that the production rate of HPALDs, important products of the isoprene oxidation, agrees with the previous measurements of Crounse *et al.*[14] The modifications to LIM1

recommended in the work of Teng *et al.*[16] based on RO_2-specific nitrate measurements were also adopted, but in this case the fits to the data became significantly poorer. A discussion of potential sources of error in the measurements of Teng *et al*. is provided, which helps rationalize the disagreement.

The impact of these findings were assessed in an atmospheric model that simulated the atmospheric conditions of the OP3 Borneo campaign[2, 4], showing that via the incorporation of the optimized LIM1 model, it is possible to describe up to ~60% of the measured OH in a day of that field work. The results of this modelling shows that a model based on the recommendations of Teng *et al*. is also capable of explaining the majority of the OH. However the chemistry of the dihydroperoxy-carbonyl peroxy radicals (di-HPCARPs) is significantly diminished, reducing the possibility of further improvements of the OH agreement via subsequent isoprene chemistry.

The novel method presented in Chapter 5 was incorporated for the analysis of LIM1, being the algorithm augmented with the H-abstraction explored in Chapter 4 and the OH loss due to diffusion and reaction with the precursor. The results show that the use of a vibration-only model heavily overestimated the rate coefficients for the crucial H-shifts taking place in the mechanism, when compared to the original predictions by Peeters *et al*. Even though a model that incorporates 40 hindered rotors among the various intermediate species provides a better agreement to the original LIM1 values, the rate coefficients are overestimated by factors varying from ~1.25 to ~4.5. Finally, the possibility of well-skipping for the reactions of the isoprene-OH adducts with O_2 over the various peroxy radicals was explored. These reactions appear to be unimportant even at the highest temperature comprised in this work (584 K), reinforcing the validity of the best-fit parameters obtained with the pressure-independent analysis.

6.5 REFERENCES

1. Fuchs, H. et al. Experimental Evidence for Efficient Hydroxyl Radical Regeneration in Isoprene Oxidation. *Nature Geoscience* **2013,** *6*, 1023.

2. Edwards, P. M. et al. OH Reactivity in a South East Asian Tropical Rainforest During the Oxidant and Particle Photochemical Processes (OP3) Project. *Atmospheric Chemistry and Physics Discussions* **2013,** *13*, 5233-5278.

3. Peeters, J.; Muller, J. F.; Stavrakou, T.; Nguyen, V. S. Hydroxyl Radical Recycling in Isoprene Oxidation Driven by Hydrogen Bonding and Hydrogen Tunneling: The Upgraded LIM1 Mechanism. *Journal of Physical Chemistry A* **2014,** *118*, 8625-8643.

4. Stone, D. et al. Isoprene Oxidation Mechanisms: Measurements and Modelling of OH and HO_2 over a South-East Asian Tropical Rainforest During the OP3 Field Campaign. *Atmospheric Chemistry and Physics* **2011,** *11*, 6749-6771.

5. Whalley, L. K. et al. Quantifying the Magnitude of a Missing Hydroxyl Radical Source in a Tropical Rainforest. *Atmospheric Chemistry and Physics* **2011,** *11*, 7223-7233.

6. Finlayson-Pitts, B. J.; Pitts, J. N., *Chemistry of the Upper and Lower Atmosphere : Theory, Experiments, and Applications*. Academic Press: San Diego, California, USA. London, UK., 2000.

7. Benjamin S. Felzer, T. C., John M. Reilly, Jerry M. Melillo, Xiaodong Wang Impacts of Ozone on Trees and Crops. *Comptes Rendus Geoscience* **2007,** *339*, 784–798.

8. Weschler, C. J. Ozone's Impact on Public Health: Contributions from Indoor Exposures to Ozone and Products of Ozone-Initiated Chemistry. *Environmental health perspectives* **2006,** *114*, 1489-1496.

9. Shindell, D.; Faluvegi, G.; Lacis, A.; Hansen, J.; Ruedy, R.; Aguilar, E. Role of Tropospheric Ozone Increases in 20th-Century Climate Change. *Journal of Geophysical Research-Atmospheres* **2006,** *111*.

10. Neslen, A. Europe Escalates Action against Uk for Breaching Air Pollution Limits 06/02/2017. https://www.theguardian.com/environment/2017/feb/06/european-commission-escalates-action-uk-breaching-air-pollution-limits (accessed 23/02/2017).

11. Paulot, F.; Crounse, J. D.; Kjaergaard, H. G.; Kurten, A.; St. Clair, J. M.; Seinfeld, J. H.; Wennberg, P. O. Unexpected Epoxide Formation in the Gas-Phase Photooxidation of Isoprene. *Science* **2009,** *325*, 730-733.

12. Bela, M. M. et al. Ozone Production and Transport over the Amazon Basin During the Dry-to-Wet and Wet-to-Dry Transition Seasons. *Atmospheric Chemistry and Physics* **2015,** *15*, 757-782.

13. Peeters, J.; Nguyen, T. L.; Vereecken, L. HOx Radical Regeneration in the Oxidation of Isoprene. *Physical Chemistry Chemical Physics* **2009,** *11*, 5935-5939.

14. Crounse, J. D.; Paulot, F.; Kjaergaard, H. G.; Wennberg, P. O. Peroxy Radical Isomerization in the Oxidation of Isoprene. *Physical Chemistry Chemical Physics* **2011,** *13*, 13607-13613.

15. Zhang, F.; Dibble, T. S. Impact of Tunneling on Hydrogen-Migration of the n-propyperoxy Radical. *Physical Chemistry Chemical Physics* **2011,** *13*, 17969-17977.

16. Teng, A. P.; Crounse, J. D.; Wennberg, P. O. Isoprene Peroxy Radical Dynamics. *Journal of the American Chemical Society* **2017,** *139*, 5367-5377.

17. Zhang, D.; Zhang, R.; Park, J.; North, S. W. Hydroxy Peroxy Nitrites and Nitrates from OH Initiated Reactions of Isoprene. *Journal of the American Chemical Society* **2002,** *124*, 9600-9605.

18. Tuazon, E. C.; Atkinson, R. A Product Study of the Gas-Phase Reaction of Isoprene with the OH Radical in the Presence of NOx. *Int. J. Chem. Kinet.* **1990,** *22*, 1221-1236.

19. O'Brien, J. M.; Czuba, E.; Hastie, D. R.; Francisco, J. S.; Shepson, P. B. Determination of the Hydroxy Nitrate Yields from the Reaction of C_2−C_6 Alkenes with OH in the Presence of NO. *The Journal of Physical Chemistry A* **1998,** *102*, 8903-8908.

20. Iupac Task Group on Atmospheric Chemical Kinetic Data Evaluation. Data Sheet Roo_50. *http://iupac.poleether.fr* **2010**.

21. Boyd, A. A.; Flaud, P.-M.; Daugey, N.; Lesclaux, R. Rate Constants for RO_2 + HO_2 Reactions Measured under a Large Excess of HO_2. *The Journal of Physical Chemistry A* **2003,** *107*, 818-821.

22. Ianni, J. C. Kintecus, Windows Version 6.80. www.kintecus.com.

23. Zhao, Y.; Truhlar, D. G. The M06 Suite of Density Functionals for Main Group Thermochemistry, Thermochemical Kinetics, Noncovalent Interactions, Excited States, and Transition Elements: Two New Functionals and Systematic Testing of Four M06-Class Functionals and 12 Other Functionals. *Theoretical Chemistry Accounts* **2008,** *120*, 215-241.

24. Frisch, M. J.; Pople, J. A.; Binkley, J. S. Self-Consistent Molecular-Orbital Methods .25. Supplementary Functions for Gaussian-Basis Sets. *Journal of Chemical Physics* **1984,** *80*, 3265-3269.

25. Peng, C. Y.; Ayala, P. Y.; Schlegel, H. B.; Frisch, M. J. Using Redundant Internal Coordinates to Optimize Equilibrium Geometries and Transition States. *Journal of Computational Chemistry* **1996,** *17*, 49-56.

26. Li, X. S.; Frisch, M. J. Energy-Represented Direct Inversion in the Iterative Subspace within a Hybrid Geometry Optimization Method. *Journal of Chemical Theory and Computation* **2006,** *2*, 835-839.

27. Frisch, M. J. et al., Gaussian 09, Revision D.01. Wallingford CT, 2009.

28. MathWorks, I., *MATLAB and Optimization Toolbox Release R2016a*. Natwick : Math Works Inc.: 2016.

29. Moré, J. J.; Sorensen, D. C. Computing a Trust Region Step. *SIAM Journal on Scientific and Statistical Computing* **1983,** *4*, 553-572.

30. The Master Chemical Mechanism (MCM) Version 3.2. http://mcm.leeds.ac.uk/MCM.

31. Vereecken, L.; Peeters, J. The 1,5-H-Shift in 1-Butoxy: A Case Study in the Rigorous Implementation of Transition State Theory for a Multirotamer System. *The Journal of Chemical Physics* **2003,** *119*, 5159-5170.

Chapter 7. Conclusions and Further Work

Overview of the chapter

The hydroxyl radical (OH), is the most important oxidizing agent in the atmosphere.[1] The reaction with OH initiates the oxidation of the vast majority of volatile organic compounds (VOC) in the atmosphere,[1] and for this reason, understanding the chemistry of this radical is crucial for the development of more reliable and accurate atmospheric models. The focus of the thesis was the development of reliable methods of analysis, capable of evaluating the kinetics and thermodynamics of atmospherically important processes, and providing accurate parameters which can be incorporated for the improvement of atmospheric models.

Direct experimental measurements collected for the reactions of OH with SO_2, ethylene and isoprene were treated in a number of ways, which included (I) a classic Master Equation analysis, in which experimental measurements correspond to an eigenvalue of the Master Equation and (II) a bi-exponential analysis of ME-simulated traces to derive overall recycling coefficients from the contributions of multiple recycling species, which was used to determine the well-depth of the isoprene-OH adducts. (III) A global multi-temperature multi-pressure analysis of raw traces was derived, in which the Master Equation is modified to incorporate the necessary pieces of chemistry to enable a direct comparison to experimental traces. (IV) An alternative approach which takes advantage of the use of phenomenological rate coefficients to enable a heavy simplification of the problem was also derived. The use of a small number of phenomenological rate coefficients attributes sufficient flexibility to the method, so that the communication with alternative software becomes facile. This approach was used for the study of the reaction of OH with ethylene, and has yielded an enthalpy of formation for the C_2H_4-OH adduct whose agreement to a theoretical prediction is of the order of 1 kJ mol^{-1}. Furthermore, the chemistry of the OH addition was successfully discriminated from the hydrogen abstraction, yielding well-defined kinetic parameters for both processes.

CHAPTER 3 - The Role of the Pre-reaction Complex in the OH + SO2 Reaction

The chemistry of the atmospherically important OH + SO_2 reaction has been investigated in Chapter 3. This reaction is directly linked to the occurrence of acid rain, a phenomena with significant environmental, economic and health implications.[2]

A controversy with respect to the high-pressure limiting rate coefficients for this reaction has been observed among literature studies. Recent high-level theoretical calculations indicate a small activation energy (~1.1 kJ mol^{-1}) for the reaction.[3] On the other hand, experimental measurements by Bltiz *et al.*[4-6] contrarily indicate very small high-pressure limiting rate coefficients for a reaction believed to be nearly barrierless.

In Chapter 3, experimental measurements of the OH + SO_2 reaction from previous studies by Blitz *et al.*[4, 6] and Wine *et al.*[7] were submitted to a Master Equation (ME) procedure, to verify if their data were compatible. With this, the chapter provided an example of a classic ME procedure, in which the experimental measurements were fitted to an eigenvalue of the Master Equation. A recently discovered weakly-bound pre-reaction complex was incorporated in the model to have its importance evaluated. The results indicated that it is not possible to reconcile all the experimental measurements by Blitz *et al*. and Wine *et al*. Furthermore, the experimental data by Wine *et al*. appears to be internally inconsistent, since the measurements with the various bath gases employed in their work (He, N_2, Ar, SF_6) could not be reproduced via ME modelling. If, on the other hand, the data by Blitz *et al*. is assumed to be correct, a reasonable internal agreement is observed, suggesting that this set of data is more reliable. The argon data from Wine *et al*. is the only dataset which agrees with the measurements of Blitz *et al*., and for this reason, were incorporated for an analysis of the potential energy surface of the reaction. The pre-reaction complex was observed to be unimportant as the chemistry is dominated by the transition state. A good fit to the measurements of Blitz *et al*. however, could only be obtained with a slightly submerged

transition state with respect to reagents (~-1.0 kJ mol^{-1}). For this reason, theoretical predictions by Long *et al.*[3] which indicated a slightly positive barrier for the process, deviate from the ME predictions. This positive barrier implies a positive temperature dependence, something not supported by experimental evidence. However, an excellent agreement is observed for the experimentally derived enthalpy of reaction (110.5 ± 6.6 kJ mol^{-1}) when compared to the theoretically derived prediction by Long *et al.* (111.5 kJ mol^{-1}).

Future work – OH + SO_2

The results presented in the chapter clearly indicate the need of additional experiments for the OH + SO_2 reaction. This is evident from the fact that the measurements by Wine *et al.* which were verified to be internally inconsistent were incorporated in the IUPAC recommendation for low-pressure rate coefficients of the OH + SO_2 reaction.[8] Blitz *et al.*[6] highlight the fact that SO_2 photolysis is highly significant at 248 nm, and gives rise to very reactive species ($O(^1D)$ and SO), which can significantly influence the observed kinetics. While the SO_2 + OH high pressure limiting rate coefficient is around 2×10^{-12} cm^3 $molecule^{-1}$ s^{-1}, [4] the reaction of SO with OH is much faster $k^{\infty}_{OH+SO} = (8.17 \pm 0.36) \times 10^{-11}$ cm^3 $molecule^{-1}$ s^{-1}.[9] For this reason, additional experiments must appropriately account for this interference. Additional measurements for this reaction at elevated temperatures (T > 300 K) to promote pressure dependence are desirable in order to indicate a preferable. These measurements can also help further elucidate the role of the transition state in this reaction and its energetic position with respect to the reagents.

CHAPTER 4 - Kinetics of the Reaction of OH with Isoprene over a Wide Range of Temperature and Pressures

In Chapter 4, direct measurements of the rate coefficient for the reaction of OH with isoprene, $k_{1,}$ were made for wide temperature (298 - 794 K) and pressure ranges (50-1670 Torr). The work presented in this chapter includes the definition of the temperature dependence for the OH + isoprene reaction, a discrimination between the mechanisms by which this reaction occurs, the determination of the enthalpy of formation of the isoprene-OH adduct, a pressure dependent treatment via ME calculations necessary for measurements above 700 K, and an assessment of the available literature covering this reaction. The measurements of this chapter significantly expanded the temperature by which the rate coefficients for this reaction is known, since prior to the execution of this work, no data above 420 K were available.

Above 700 K the OH temporal profiles exhibit non-exponential behaviour, consistent with the establishment of the OH + C_5H_8 ⇌ adduct equilibrium. The rate coefficients for the dissociation were extracted from such traces via a bi-exponential analysis. This data however are a product of the combination of the dissociation of multiple isoprene-OH adducts, and inputting this information in a ME fitting is difficult. In Chapter 3, dissociation rate coefficients associated with one simple reaction were directly compared an eigenvalue of the ME. In this case however, an equivalent overall dissociation rate coefficient calculated theoretically was obtained via a bi-exponential analysis of ME simulated traces. These traces were influence by the two most important OH additions in the isoprene system (C1 and C4), being therefore compatible with the experimentally determined value. This analysis determined an enthalpy of formation of (153.5 ± 6.2) kJ mol^{-1} for adduct 1, C1, and (143.4 ± 6.2) kJ mol^{-1} for adduct 4, C4, which are in excellent agreement with undertaken *ab initio*-based predictions (well depth for C1 adduct = 154.1 kJ mol^{-1}). These parameters however, were verified to vary depending on the level of treatment of the internal modes of reagents and products. To obtain these values, low vibrational frequencies related to rotational torsions were described via the Hindered Rotor approach. If harmonic oscillators are

assumed however, the returned well-depths become significantly deeper, (166.5 ± 7.0 kJ mol^{-1} for C1 and 156.9 ± 7.0 kJ mol^{-1} for C4).

The equilibrium data required the incorporation of a minor abstraction channel to describe the measurements and the product of this reaction was tentatively identified via proton transfer reaction mass spectrometry, where an observed response in m/z = 83 Da is consistent with the formation of 2-methylene-3-butenal. This specie is expected to be the stable product of the abstraction. Our experiments suggested an abstraction coefficient of $k_{\text{abstraction}} = (1.3 \pm 0.3) \times 10^{-11} \exp\left(\frac{-3.61 \text{ kJ mol}^{-1}}{RT}\right)$.

Finally, rate coefficients measured from this work were coupled with previous measurements for a literature assessment. The procedure was the same as implemented for the literature assessment undertaken in Chapter 3, and the results showed that only our measurements at T > 700 K were in the fall-off region, contradicting some previous studies. A recommendation for the temperature dependence of the high pressure limiting rate constant based on the results of the literature assessment and the determinations of the abstraction channel is:

$$k^{\infty}_{\text{isoprene+OH}} = (9.5 \pm 0.2) \times 10^{-11} \left(\frac{T}{298 \text{ K}}\right)^{-1.33 \pm 0.07} + (1.3 \pm 0.3) \times 10^{-11} \exp\left(\frac{-3.61 \text{ kJ mol}^{-1}}{RT}\right)$$

.

Future Work

The lack of measurements of this reaction on temperatures above 400 K suggests that more measurements in this temperature range are needed. This study was part of a more complete investigation of oxidation of isoprene, with a focus on the chemistry of the isoprene peroxy radicals. As verified in Chapter 6, high temperature measurements are a good alternative for evaluating the chemistry of isoprene and potentially other similar OH recycling species. For it to be possible however, the rate coefficients for the starting reactions need to be known to a good accuracy at these temperatures in order to enable a proper analysis of the data. For this reason, more isoprene + OH measurements above 420 K are desirable. In the 420 – 700 K temperature range, experiments performed at 100 Tor of N_2 are independent of pressure.

Measurements at even higher temperatures (T > 800 K) would enable a more accurate determination of the importance of abstraction channel. Also, the lack of theoretical studies on the isoprene + OH abstraction reaction in the literature represents a good opportunity for further work. The product with mass m/z = 83 Da needs to be identified with more confidence. Spectroscopic techniques could be of great help in this case, and a study of the kinetic isotope effect can provide valuable insights in the matter. The study of other similar and symmetric VOCs such as dimethyl butadiene would reduce the number of possible adducts and simplify the analysis.

Finally, the technique of analysing ME simulated traces for the study of equilibration data needs to be thoroughly tested. An obvious candidate would be the reaction of OH with butadiene, given its structural similarity to isoprene, but the absence of allylic hydrogens. In this case, longer non-exponential traces would be expected as an effect of the diminishment of the importance of the competing abstraction. This means that, in theory, the enthalpy of formation of the butadiene-OH adducts could be determined more accurately. A very good comparison to theoretical determinations of this value could be undertaken, and enabling an assessment of the quality of theoretical calculations.

CHAPTER 5 - Kinetics of the reaction of ethylene with OH radicals: developing a global Master Equation-based, raw-trace fitting technique

In Chapter five, a new method for analysing temperature and pressure dependent experimental data via a global raw-trace analysis has been presented. In contrast to the techniques presented in Chapters 3 and 4, in this case, the ME transition matrix is altered to incorporate important experimental processes, in order to enable a direct comparison of the simulated traces to the experimental time profiles. The Master Equation transition matrix represents a set of coupled ordinary differential equations (ODEs), and the method basically introduces new formation and consumption terms inside them. While the potentially pressure-dependent processes are dealt with at an energy-grained level, the additional processes such as a hydrogen abstraction are accounted for by these simple consumption or formation terms, which may be set as constants or adjustable parameters. An alternative and interesting approach is presented, in which the phenomenological rate coefficients, obtained from the chemically significant eigenvalues are used to model the problem, granting a great simplification of it. The heavily simplified set of ODEs can incorporate the necessary consumption and formation terms in a similar manner to their incorporation to the full-ME. Their simplicity however, provides enough flexibility in other to establish data processing with alternative software.

In Chapter 5, MATLAB was used to control the global non-linear optimizations undertaken for the analysis of a large number of complex OH traces associated with the ethylene + OH reaction. A global procedure represents a good option to guarantee the consistency of the results, by imposing reasonable relationships between the measurements from kinetic point of view. For example, for traces generated at the same temperature and pressure, the pseudo-first order rate coefficients employed in each trace are calculated from the same bimolecular rate coefficient. The concentrations of the excess reagents were manometrically controlled during the experiments and therefore, a clear kinetic relationship between the fits of multiple traces was imposed. The ethylene + OH reaction was chosen due to its simplicity and

wide previous literature coverage. The augmented ME analysis was capable of describing a total of 96 experimental traces simultaneously, to an excellent accuracy, being the fits skewed approximately 6% of the best possible flexible bi-exponential fits to the data. OH traces were collected under a wide range of pressures (~60 - 220 Torr) and temperatures (563 – 723 K) to promote the direct of equilibration between the reagents and the ethylene-OH adduct and the hydrogen abstraction, enhancing the complexity of the data being analysed. While the addition chemistry was treated at ME level, the abstraction was introduced to the set of ODEs that represented the simplified Master Equation.

Following the results of Chapter 4, a couple of low frequency vibrations of the ethylene-OH adduct were described with the hindered rotor description. Again, an excellent agreement is observed between a theoretical prediction of the C_2H_4-OH well-depth (111.4 kJ mol^{-1}) and an experimental determination (111.8 ± 0.20 kJ mol^{-1}).

Future Work

The promising results of this chapter suggest that the technique needs to be tested for increasing levels of complexity. Again, butadiene + OH would a good test, representing a complexity between the isoprene case, explored in Chapter 6, and the ethylene case, explored in Chapter 5. Alkenes such as propene and butane can be used for a test of the consistency of the results when more favourable abstraction channels are studied. The technique has an obvious application for the discrimination of competing processes, and for this reason, the study of the atmospheric chemistry of alkenes and dienes in general can make use of it. Nonetheless, the method can be used for the study of radical recycling for evaluations of enthalpies of formation and energy barriers.

As discussed in the chapter, the high temperature kinetics of the reactions of hydrocarbons with OH are important parameters in the construction of complex combustion models. In this context, the high temperature oxidation of oxygenated species used as fuel additives such as dimethyl, diethyl and diisopropyl ethers, initiated by the reaction with OH are relevant processes.[10-11]

In these systems, internal hydrogen shifts to form hydroperoxy species tend to be ignored by the atmospheric community due to their large barriers (>70 kJ mol^{-1}). At high temperatures however (T~650 K), these hydrogen shifts become more important.[10] The developed method of analysis can be employed for the study of such processes, in which the chemistry of the O_2 addition and hydrogen shifts are treated with a ME approach and competing processes are incorporated as consumption and loss terms to the set of ODEs. Furthermore, with an effective dataset, it is probably possible to assess the barriers of the hydrogen shifts, providing important information to combustion models.

The technique can also be adapted for the application in chamber studies, which could potentially enable a more reliable treatment of such experiments.

CHAPTER 6 - Investigation of the Isoprene + OH Reaction in the Presence of Oxygen to Confirm the Leuven Isoprene Mechanism 1

Chapter 6 is focused on shedding light on the discrepancy of the concentrations of OH between those estimated with atmospheric current models and field measurements undertaken in pristine environments dominated by biogenic emissions. In a number of environments, including from rainforests to Mediterranean pine forests[12] the model predictions significantly underestimated the measured OH concentrations.[13-15] At the same time, a very good understanding of the chemistry of remote environments, where the atmospheric chemistry of OH is dominated by the reactions with methane and carbon monoxide suggests a poor understanding of the oxidation processes of biogenic VOCs. The oxidation of the most abundant VOC is believed to regenerate OH radicals, so as to explain the *missing* OH. In this context, the Leuven Isoprene Mechanism 1 (LIM1)[16] appears as the most promising mechanism which attempts to describe the OH recycling from the chemistry of isoprene peroxy radicals.

Direct high O_2 (>10^{17} molecule cm^{-3}), high temperature (400 K < T < 600 K) monitoring of OH were undertaken in order to promote the OH recycling to a timescale suitable for the execution of laser flash photolysis-laser induced fluorescence experiments. At high temperatures, crucial hydrogen shifts involved in the OH regeneration are promoted and high oxygen concentrations are employed as to promote the peroxy formation, which will equilibrate with it unimolecular decomposition. Under pseudo-first-order conditions, non-exponential OH time profiles indicated OH recycling from isoprene peroxy chemistry. As discussed in Chapter 4, in the absence of O_2 and at temperatures below 650 K, OH decayed exponentially.

A total of 96 traces were initially fitted with LIM1, where a remarkably good agreement was observed, and the necessary changes of the barriers of the hydrogen shifts reported in the LIM1 publication in the order of 2 kJ mol^{-1}. The fits were constrained as to respect the product yield of hydroperoxy

aldehydes (HPALDs) measured by Crounse *et al.*[17] without compromising the quality of the fits.

An attempt to use the model modifications suggested by Teng *et al.* [18] based on measurements of peroxy-specific nitrates cased the fits to become significantly poorer. The modifications suggested by Teng *et al*. diminish the importance of a channel by which OH is regenerated at longer timescales, via the formation of dihydroperoxy-carbonyl peroxy radicals (di-HPCARPs), and the experimental data appears to be sensitive to this recycling.

The best-fit parameters were incorporated in an atmospheric model based on the Master Chemical Mechanism,[19] to evaluate the impact of these findings in the experimental measurements of OH undertaken during the Borneo OP3 field campaign.[20] Upon incorporation of the new barriers, a significant improvement was obtained for the description of the temporal concentration of OH during a day of the campaign which was analysed. In this case, more than 50% of the OH peak concentration was successfully described by the model. If the modifications by Teng *et al*. are incorporated, similar total OH predictions are obtained. However, a closer look at the modelled data shows that while the isoprene chemistry is responsible for more than 20% of the total OH when the LIM1 is incorporated with the obtained best-fit parameters, this value is reduced to 12.3% when the Teng *et al*. modifications are assumed, diminishing the importance of the isoprene chemistry for the OH chemistry in pristine environments.

Finally, the novel ME-based method of analysis developed in Chapter 5 was used for a further elucidation of the results. The LIM1 mechanism was modelled via the ME, and the system was augmented with the inclusion of the hydrogen abstraction reaction studied in Chapter 5, and experimental losses such as the reaction of OH with its precursor. Both a vibration-only model and an alternative model with the incorporation of 40 hindered rotor descriptions were employed. The hindered rotor model overpredicts the rate coefficients for the hydrogen shifts calculated by Peeters *et al*. in the LIM1 publication by

factors between 1.25 and 4.5. This discrepancy is partially derived from the fact that Peeters *et al*. employed a multi-conformer transition state theory calculation for the determinations of their rate coefficients In contrast, the undertaken ME model incorporated only the lowest energy conformers. Finally, the method was used to evaluate the possibility of the occurrence of significantly interfering well-skipping reactions under the experimental conditions of the study, but these were found to be unimportant even at the highest temperature comprised in the work (584 K).

Future work

Given the success of the LIM1 mechanism to describe the observed kinetics at high temperatures for the isoprene + OH reaction in the presence of O_2, further theoretical evaluations of the potential energy surface of these processes are highly desirable and encouraged. For example, a theoretical estimate of the branching ratios of the HPALD and di-HPCARP channels would provide further information about the mechanism, and reinforce the results of atmospheric models. The work of Peeters *et at*. suggests a value of 50% for each channel, but recognizes that the di-HPCARP channel might be favoured over the HPALD alternative.

Additional chamber studies with a focus on the detection and quantification of the products of the di-HPCARP channel are also necessary for a good understanding and further elucidation of the isoprene oxidation. However, these experiments require a very good control over NOx presence and heterogeneous interference. Quartz chambers are probably more appropriate for the execution of such experiments, as these tend to suffer less from heterogeneous processes on the walls when compared to metal and Teflon chambers.

The exploration of such experiments with a real-time detection of OH via the FAGE technique for example can provide valuable OH temporal information which can be analysed with the LIM1 to elucidate the mechanism. A quick simulation of the LIM1 mechanism indicates that at elevated temperatures as

high as 323 K, the thermal decomposition of di-HPCARPs may be enhanced in a detectable level in a chamber, from which the yield of di-HPCARPs may be derived. The good limit of detection of the FAGE technique (10^6-10^7 molecules cm^{-3}) seems appropriate for this task.

REFERENCES

1. Finlayson-Pitts, B. J.; Pitts, J. N., *Chemistry of the Upper and Lower Atmosphere : Theory, Experiments, and Applications*. Academic Press: San Diego, California, USA. London, UK., 2000.

2. Singh, A.; Agrawal, M. Acid Rain and Its Ecological Consequences. *J Environ Biol* **2008,** *29*, 15-24.

3. Long, B.; Bao, J. L.; Truhlar, D. G. Reaction of SO_2 with OH in the Atmosphere. *Physical Chemistry Chemical Physics* **2017,** *19*, 8091-8100.

4. Blitz, M. A.; Hughes, K. J.; Pilling, M. J. Determination of the High-Pressure Limiting Rate Coefficient and the Enthalpy of Reaction for OH + SO_2. *The Journal of Physical Chemistry A* **2003,** *107*, 1971-1978.

5. Blitz, M. A.; Salter, R. J.; Heard, D. E.; Seakins, P. W. An Experimental Study of the Kinetics of OH/OD(ν = 1,2,3) + SO_2: The Limiting High-Pressure Rate Coefficients as a Function of Temperature. *The Journal of Physical Chemistry A* **2017,** *121*, 3175-3183.

6. Blitz, M. A.; Salter, R. J.; Heard, D. E.; Seakins, P. W. An Experimental and Master Equation Study of the Kinetics of OH/OD + SO_2: The Limiting High-Pressure Rate Coefficients. *The Journal of Physical Chemistry A* **2017,** *121*, 3184-3191.

7. Wine, P. H.; Thompson, R. J.; Ravishankara, A. R.; Semmes, D. H.; Gump, C. A.; Torabi, A.; Nicovich, J. M. Kinetics of the Reaction OH + SO_2 + M → $HOSO_2$ + M. Temperature and Pressure Dependence in the Fall-Off Region. *The Journal of Physical Chemistry* **1984,** *88*, 2095-2104.

8. Atkinson, R.; Baulch, D. L.; Cox, R. A.; Crowley, J. N.; Hampson, R. F.; Hynes, R. G.; Jenkin, M. E.; Rossi, M. J.; Troe, J. Iupac Task Group on Atmospheric Chemical Kinetic Data Evaluation – Data Sheet I.A4.86 Sox15. *Atmospheric Chmistry and Physics* **2004,** *4*, 1461.

9. Blitz, M. A.; McKee, K. W.; Pilling, M. J. Temperature Dependence of the Reaction of OH with SO. *Proceedings of the Combustion Institute* **2000,** *28*, 2491-2497.

10. Wang, S.; Wang, L. The Atmospheric Oxidation of Dimethyl, Diethyl, and Diisopropyl Ethers. The Role of the Intramolecular Hydrogen Shift in Peroxy Radicals. *Physical Chemistry Chemical Physics* **2016,** *18*, 7707-7714.

11. Orlando, J. J. The Atmospheric Oxidation of Diethyl Ether: Chemistry of the C2H5–O–Ch(O˙)CH3 Radical between 218 and 335 K. *Physical Chemistry Chemical Physics* **2007,** *9*, 4189-4199.

12. Carslaw, N. et al. OH and HO_2 Radical Chemistry in a Forested Region of North-Western Greece. *Atmospheric Environment* **2001,** *35*, 4725-4737.

13. Martinez, M. et al. Hydroxyl Radicals in the Tropical Troposphere over the Suriname Rainforest: Airborne Measurements. *Atmospheric Chemistry and Physics* **2010,** *10*, 3759-3773.

14. Whalley, L. K. et al. Quantifying the Magnitude of a Missing Hydroxyl Radical Source in a Tropical Rainforest. *Atmospheric Chemistry and Physics* **2011,** *11*, 7223-7233.

15. Lelieveld, J. et al. Atmospheric Oxidation Capacity Sustained by a Tropical Forest. *Nature* **2008,** *452*, 737-740.

16. Peeters, J.; Muller, J. F.; Stavrakou, T.; Nguyen, V. S. Hydroxyl Radical Recycling in Isoprene Oxidation Driven by Hydrogen Bonding and Hydrogen Tunneling: The Upgraded LIM1 Mechanism. *Journal of Physical Chemistry A* **2014,** *118*, 8625-8643.

17. Crounse, J. D.; Paulot, F.; Kjaergaard, H. G.; Wennberg, P. O. Peroxy Radical Isomerization in the Oxidation of Isoprene. *Physical Chemistry Chemical Physics* **2011,** *13*, 13607-13613.

18. Teng, A. P.; Crounse, J. D.; Wennberg, P. O. Isoprene Peroxy Radical Dynamics. *Journal of the American Chemical Society* **2017,** *139*, 5367-5377.

19. The Master Chemical Mechanism (MCM) Version 3.2. http://mcm.leeds.ac.uk/MCM.

20. Stone, D. et al. Isoprene Oxidation Mechanisms: Measurements and Modelling of OH and HO_2 over a South-East Asian Tropical Rainforest During the OP3 Field Campaign. *Atmospheric Chemistry and Physics* **2011,** *11*, 6749-6771.

APPENDIX 1

A set of pictures of the high pressure and high temperature instrument is presented in this section for a better comprehension of the experimental setup.

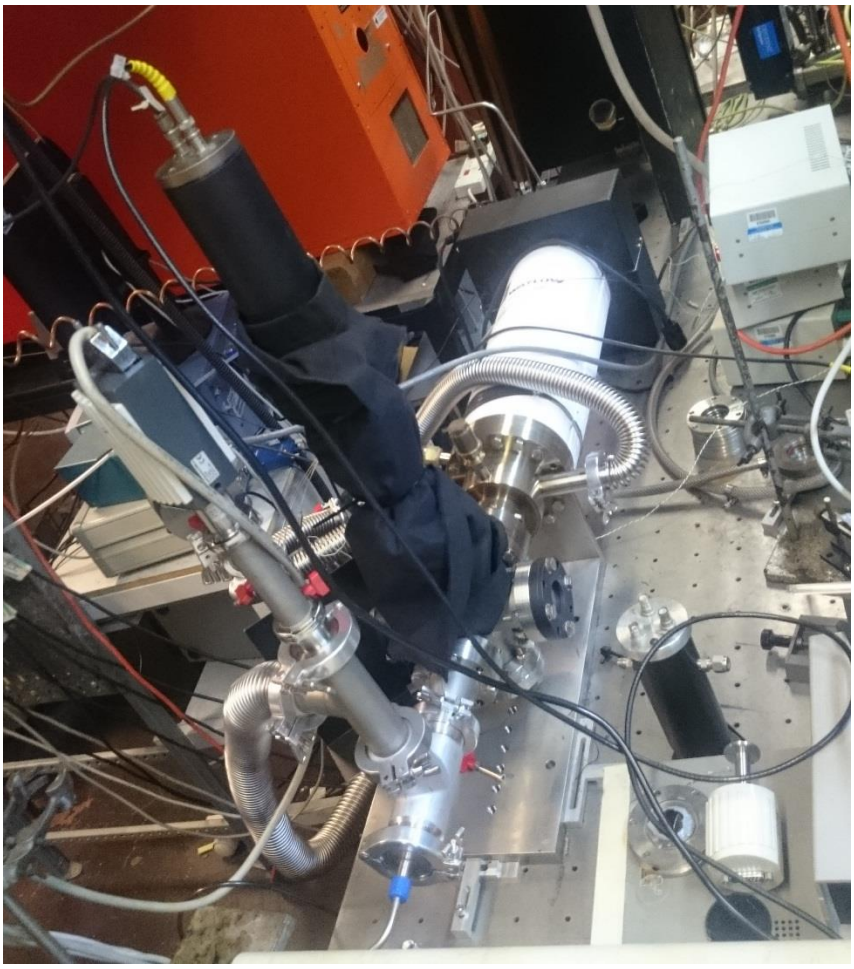

Figure A1.1 - Overview of the high pressure and high temperature LPF-LIF instrument.

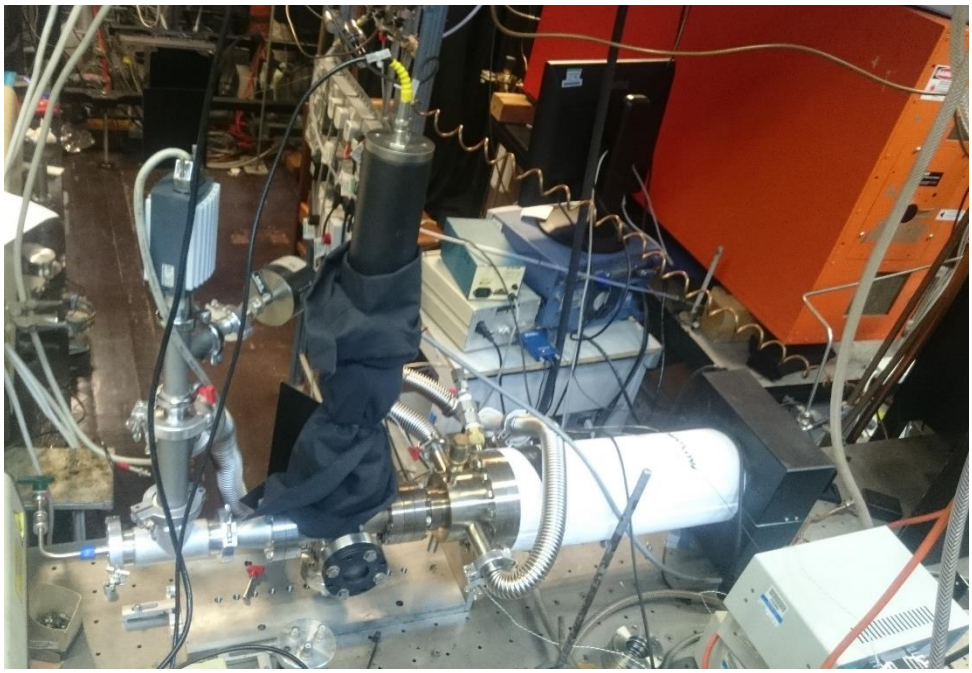

Figure A1.2 - The high pressure LPF -LIF instrument. View of the window from which the probe beam enters the reaction cell.

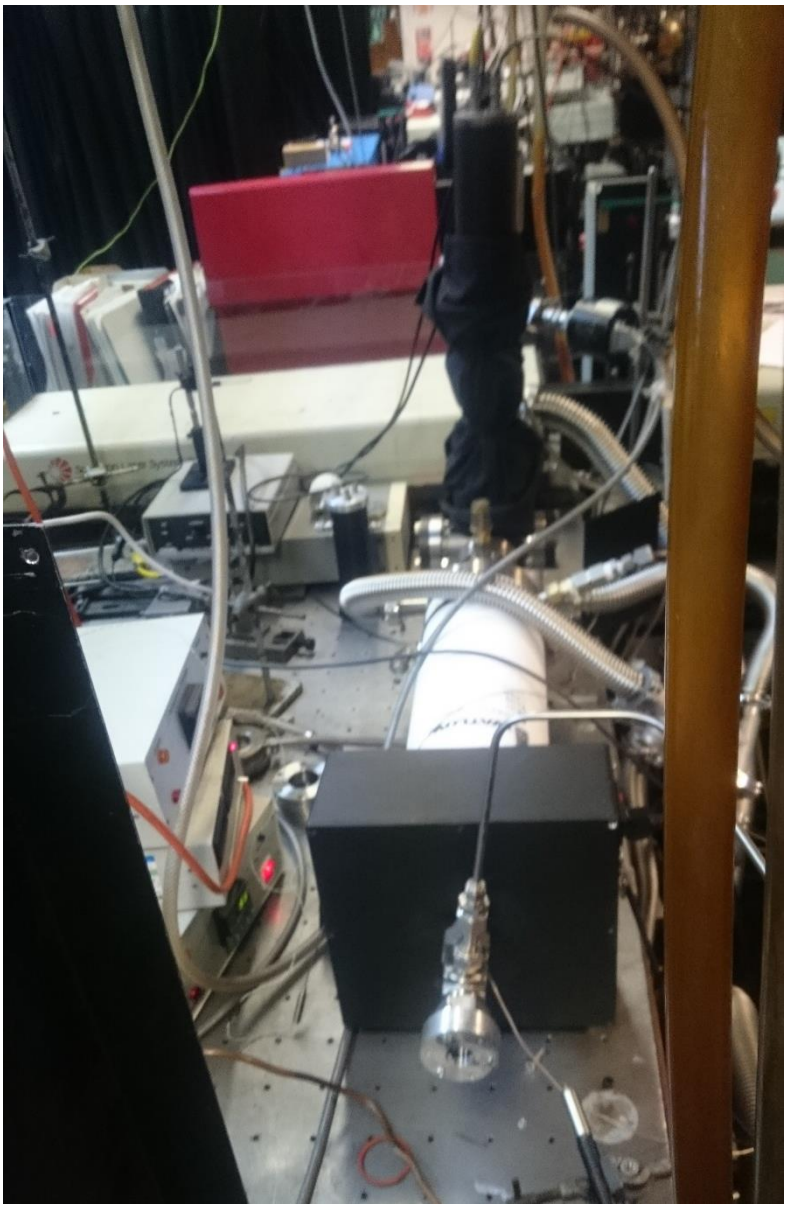

Figure A1.3 - The high pressure LPF -LIF instrument. View of the window from which the excimer beam enters the reaction cell.

APPENDIX 2

Table A2.1 - Measurements by Blitz *et al.*[1-2] incorporated in the OH + SO_2 fits. Errors assigned as 10% of the rate coefficients.

p / Torr (He)	T / K	k_1 / 10^{13} cm^3 $molecule^{-1}$ s^{-1}
100	295	1.68
210	295	3.13
53	295	1.28
25	295	0.825
52	295	1.71
301	295	3.22
104	295	2.11
154	295	2.31
202	295	2.77
509	563	0.498

Table A2.2 - Measurements by Blitz *et al.*[2] incorporated in the OH + SO_2 fits.

p / Torr (He)	T / K	k_{-1} / s^{-1}
506	523	316 ± 64
508	543	371 ± 74
509	563	672 ± 135
504	583	852 ± 170

Table A2.3 - Measurements by Wine *et al*.[3] incorporated in the OH + SO_2 fits. Errors assigned as 10% of the rate coefficients. Helium used as the bath gas.

p / Torr (He)	T / K	k_1 / 10^{13} cm^3 $molecule^{-1}$ s^{-1}
16	300	0.467
31	300	0.69
62	300	1.03
124	300	1.44
249	300	2.11
497	300	3.4

Table A2.4 - Measurements by Wine *et al*. incorporated in the OH + SO_2 fits. Errors assigned as 10% of the rate coefficients. Argon used as the bath gas.

p / Torr (Ar)	T / K	k_1 / 10^{13} cm^3 $molecule^{-1}$ s^{-1}
16	300	0.491
31	300	0.775
62	300	1.21
124	300	1.58
249	300	2.34
497	300	3.39
13	260	0.821
19	360	0.279
22	420	0.226
27	260	1.18
37	360	0.435
44	420	0.353
54	260	1.67
75	360	0.622
87	420	0.49
108	260	2.36
149	360	0.959
174	420	0.722
215	260	3.65
298	360	1.34
348	420	1.09
431	260	5.46
597	360	1.85
696	420	1.58

Table A2.5 - Measurements by Wine *et al*. incorporated in the OH + SO_2 fits. Errors assigned as 10% of the rate coefficients. N_2 used as the bath gas.

p / Torr (Ar)	T / K	k_1 / 10^{13} cm^3 $molecule^{-1}$ s^{-1}
16	300	1.13
31	300	1.81
62	300	2.89
124	300	4.17

Table A2.6 - Measurements by Wine *et al*. incorporated in the OH + SO_2 fits. Errors assigned as 10% of the rate coefficients. SF_6 used as the bath gas.

p / Torr (Ar)	T / K	k_1 / 10^{13} cm^3 $molecule^{-1}$ s^{-1}
16	300	1.92
31	300	2.9
62	300	4.38
124	300	5.22
249	300	7.17
497	300	10
13	260	2.96
19	360	1.29
22	420	1.07
27	260	3.7
37	360	2.18
44	420	1.51
54	260	6.04
75	360	2.86
87	420	2.19
108	260	7.52
149	360	4.38
174	420	3.9
215	260	9.5
298	360	5.83
348	420	4.91
431	260	12.4
597	360	7.45
696	420	7.16

1. Blitz, M. A.; Salter, R. J.; Heard, D. E.; Seakins, P. W. An Experimental Study of the Kinetics of OH/OD(v = 1,2,3) + SO_2: The Limiting High-Pressure Rate Coefficients as a Function of Temperature. *The Journal of Physical Chemistry A* **2017,** *121*, 3175-3183.

2. Blitz, M. A.; Hughes, K. J.; Pilling, M. J. Determination of the High-Pressure Limiting Rate Coefficient and the Enthalpy of Reaction for OH + SO_2. *The Journal of Physical Chemistry A* **2003,** *107*, 1971-1978.

3. Wine, P. H.; Thompson, R. J.; Ravishankara, A. R.; Semmes, D. H.; Gump, C. A.; Torabi, A.; Nicovich, J. M. Kinetics of the Reaction OH + SO_2 + M → $HOSO_2$ + M. Temperature and Pressure Dependence in the Fall-Off Region. *The Journal of Physical Chemistry* **1984,** *88*, 2095-2104.

APPENDIX 3

Table A3.1 Experimental Determinations of k_1 at high pressure.

T / K	p / Torr	$k_1 \times 10^{11}$ / cm^3 molecule^{-1} s^{-1}	$k_{1a} \times 10^{11}$ / cm^3 molecule^{-1} s^{-1}	$k_{1b} \times 10^{11}$ / cm^3 molecule^{-1} s^{-1}
300	1290	9.90 ± 0.07	9.59	0.31
300	1365	10.01 ± 0.06	9.70	0.31
406	1367	6.68 ± 0.27	6.23	0.45
417	1497	7.24 ± 0.80	6.78	0.46
418	1418	6.24 ± 0.17	5.78	0.46
433	1546	5.99 ± 0.77	5.51	0.48
475	1394	5.61 ± 0.25	5.09	0.52
508	1673	5.67 ± 0.63	5.12	0.55
564	1350	4.74 ± 0.22	4.14	0.60
618	1536	3.99 ± 0.23	3.35	0.64
630	1373	4.71 ± 0.28	4.06	0.65

Table A3.2 Experimental Determinations of k_1 at low pressure.

T / K	p / Torr	$k_1 \times 10^{11}$ / cm^3 molecule^{-1} s^{-1}	$k_{1a} \times 10^{11}$ / cm^3 molecule^{-1} s^{-1}	$k_{1b} \times 10^{11}$ / cm^3 molecule^{-1} s^{-1}
300	96	10.60 ± 0.18	10.29	0.31
300	56	10.40 ± 0.16	10.09	0.31
337	57	8.28 ± 0.11	7.92	0.36
426	103	5.56 ± 0.13	5.09	0.47
472	99	5.81 ± 0.43	5.29	0.52
473	99	4.98 ± 0.18	4.46	0.52
477	128	5.30 ± 0.5	4.78	0.52
478	114	6.12 ± 0.18	5.60	0.52
533	132	4.91 ± 0.12	4.33	0.58
540	141	5.27 ± 0.18	4.69	0.58
573	51	4.40 ± 0.53	3.79	0.61
729	115	2.46 ± 0.79	1.74	0.72
766	122	2.32 ± 0.73	1.58	0.74
794	100	2.23 ± 0.69	1.48	0.75

Table A3.3 Wavenumbers of isoprene calculated at the M06-2X/6-311++G(3df,2p) level of theory.

Mode #	Wavenumber cm^{-1}
1	160.16
2	239.94
3	291.65
4	407.99
5	434.42
6	532.67
7	650.83
8	795.58
9	806.46
10	953.58
11	964.35
12	971.95
13	1012.56
14	1041.92
15	1069.27
16	1088.48
17	1323.80
18	1342.80
19	1412.71
20	1439.66
21	1460.97
22	1489.90
23	1506.10
24	1687.26
25	1737.33
26	3039.57
27	3097.70
28	3139.52
29	3142.24
30	3144.79
31	3153.72
32	3229.56
33	3232.20

Table A3.4 Cartesian coordinates for the isoprene structure optimized at the M06-2X/6-311++G(3df,2p) level of theory.

Atom	x	y	z
C	0.517499	-0.099008	-0.000001
C	0.636141	1.397503	-0.000001
C	-0.826523	-0.688292	0.000001
C	1.588187	-0.892823	-0.000002
C	-1.964262	-0.000256	0.000002
H	0.149241	1.824206	-0.878950
H	1.679931	1.704179	-0.000002
H	0.149243	1.824207	0.878949
H	-0.862185	-1.773179	0.000001
H	2.592606	-0.490543	-0.000003
H	1.485503	-1.970615	-0.000002
H	-2.921377	-0.502828	0.000003
H	-1.979219	1.081832	0.000002

Table A3.5 Wavenumbers of the isoprene-OH adduct 1 calculated at the M06-2X/6-311++G(3df,2p) level of theory.

Mode #	Wavenumber cm^{-1}
1	68.78
2	91.30
3	188.89
4	276.06
5	290.80
6	343.65
7	385.51
8	460.99
9	557.03
10	619.60
11	792.37
12	829.25
13	948.82
14	983.66
15	988.01
16	1023.19
17	1058.70
18	1081.34
19	1184.42
20	1224.96
21	1261.47
22	1346.22
23	1384.97
24	1413.03
25	1424.71
26	1448.68
27	1482.59
28	1500.93
29	1509.01
30	1531.50
31	3018.81
32	3047.80
33	3074.58
34	3090.76
35	3129.20
36	3139.99
37	3158.06
38	3253.24
39	3899.92

Table A3.6 Cartesian coordinates for the isoprene-OH adduct 1 structure optimized at the M06-2X/6-311++G(3df,2p) level of theory.

Atom	x	y	z
C	-0.061504	0.054587	0.186191
C	-0.134746	1.545617	0.087286
C	-1.183972	-0.750765	0.030269
C	1.274368	-0.549102	0.484202
C	-2.456837	-0.298647	-0.210810
H	-0.603420	1.863619	-0.846627
H	0.860221	1.984055	0.132720
H	-0.736071	1.960634	0.901837
H	-1.034215	-1.823355	0.114307
H	1.659247	-0.169221	1.434847
H	1.189995	-1.636968	0.568826
H	-3.281214	-0.987056	-0.319880
H	-2.676562	0.756401	-0.297081
O	2.257516	-0.188746	-0.476030
H	1.938040	-0.448276	-1.343532

Table A3.7 Wavenumbers of the isoprene-OH adduct 2 calculated at the M06-2X/6-311++G(3df,2p) level of theory.

Mode #	Wavenumber cm^{-1}
1	106.32
2	174.05
3	259.21
4	294.04
5	307.28
6	331.62
7	370.98
8	424.52
9	440.53
10	531.94
11	585.8
12	709.11
13	759.09
14	906.37
15	971.95
16	981.09
17	997.35
18	1035.68
19	1046.41
20	1059.46
21	1219.74
22	1276.72
23	1320.46
24	1332.8
25	1390.31
26	1440.77
27	1449.42
28	1484.68
29	1498.46
30	1725.07
31	3045.16
32	3131.01
33	3134.61
34	3141.25
35	3153.24
36	3157.31
37	3235.13
38	3271.41
39	3871.44

Table A3.8 Cartesian coordinates for the isoprene-OH adduct 2 structure optimized at the M06-2X/6-311++G(3df,2p) level of theory.

Atom	x	y	z
C	-0.37849	-0.04503	0.01455
C	-1.08250	1.31214	0.13623
C	0.98250	0.03261	0.67001
C	-1.19259	-1.11985	0.66009
C	2.13367	0.02912	0.01922
H	-0.50463	2.06361	-0.40171
H	-2.07902	1.24430	-0.29887
H	-1.16851	1.60633	1.18155
H	0.96553	0.10686	1.75377
H	-2.09707	-1.44568	0.16572
H	-0.99690	-1.44237	1.67179
H	3.07562	0.09504	0.54607
H	2.16526	-0.02640	-1.06122
O	-0.27700	-0.28568	-1.38160
H	0.08010	-1.17026	-1.50490

Table A3.9 Wavenumbers of the isoprene-OH adduct 3 calculated at the M06-2X/6-311++G(3df,2p) level of theory.

Mode #	Wavenumber cm^{-1}
1	68.31
2	171.05
3	218.73
4	239.44
5	275.55
6	344.76
7	369.92
8	428.95
9	460.95
10	570.59
11	602.91
12	756.89
13	820.00
14	915.54
15	961.48
16	972.18
17	1029.97
18	1070.82
19	1074.20
20	1155.86
21	1228.48
22	1313.40
23	1321.43
24	1387.17
25	1408.70
26	1453.88
27	1456.57
28	1480.00
29	1500.30
30	1741.98
31	2972.11
32	3045.69
33	3105.81
34	3138.02
35	3140.62
36	3179.40
37	3223.41
38	3300.20
39	3898.05

Table A3.10 Cartesian coordinates for the isoprene-OH adduct 3 structure optimized at the M06-2X/6-311++G(3df,2p) level of theory.

Atom	x	y	z
C	-0.764805	-0.084526	0.045702
C	-1.045669	1.368470	-0.200780
C	0.703322	-0.479331	0.092302
C	-1.712048	-0.999393	0.208361
C	1.443262	0.242961	1.157483
H	-0.711673	1.967984	0.648689
H	-2.108039	1.544957	-0.356725
H	-0.492461	1.718749	-1.073222
H	0.747495	-1.561908	0.287138
H	-2.762667	-0.739031	0.175051
H	-1.466430	-2.038922	0.388651
H	1.127320	0.151627	2.185037
H	2.315934	0.824013	0.904193
O	1.342519	-0.189224	-1.141984
H	0.866005	-0.642771	-1.841343

Table A3.11 Wavenumbers of the isoprene-OH adduct 4 calculated at the M06-2X/6-311++G(3df,2p) level of theory.

Mode #	Wavenumber cm^{-1}
1	46.46
2	148.66
3	186.58
4	260.18
5	351.77
6	381.15
7	469.59
8	495.20
9	517.78
10	578.86
11	753.26
12	831.45
13	854.32
14	929.34
15	1001.30
16	1021.12
17	1056.95
18	1084.09
19	1155.95
20	1204.68
21	1248.34
22	1349.80
23	1388.02
24	1402.90
25	1432.16
26	1465.11
27	1494.39
28	1503.41
29	1515.92
30	1535.67
31	3044.01
32	3048.26
33	3084.24
34	3109.27
35	3140.15
36	3146.66
37	3160.03
38	3244.43
39	3906.75

Table A3.12 Cartesian coordinates for the isoprene-OH adduct 4 structure optimized at the M06-2X/6-311++G(3df,2p) level of theory.

Atom	x	y	z
C	1.054407	-0.121719	0.020786
C	1.335098	1.357966	-0.109674
C	-0.239831	-0.575430	0.261110
C	2.093406	-1.016361	-0.093371
C	-1.453661	0.274514	0.415823
H	0.756064	1.800155	-0.921557
H	2.389288	1.531036	-0.315008
H	1.076387	1.892490	0.804794
H	-0.403063	-1.644302	0.352990
H	3.104796	-0.685199	-0.280082
H	1.922319	-2.080036	0.000876
H	-1.235458	1.321352	0.186586
H	-1.817361	0.238126	1.446681
O	-2.537437	-0.198153	-0.371105
H	-2.230000	-0.302219	-1.274480

Table A3.13 Wavenumbers of the transition state of the abstraction, calculated at the M06-2X/6-311++G(3df,2p) level of theory.

Mode #	Wavenumber cm^{-1}
1	968.22*i*
2	82.86
3	112.79
4	160.63
5	260.62
6	299.77
7	365.28
8	406.36
9	426.57
10	534.62
11	624.6
12	751.97
13	793.76
14	822.77
15	948.19
16	966.99
17	982.52
18	988.81
19	1017.1
20	1045.71
21	1086.37
22	1229.27
23	1324.86
24	1332.55
25	1372.84
26	1427.46
27	1445.01
28	1460.35
29	1491.7
30	1679.48
31	1724.59
32	3077.27
33	3144.03
34	3151.09
35	3152.95
36	3159.93
37	3234.54
38	3242.34
39	3777.41

Table A3.14 Cartesian coordinates for the transition state of the abstraction, optimized at the M06-2X/6-311++G(3df,2p) level of theory.

Atom	x	y	z
C	-0.866548	-0.209943	0.082766
C	0.113942	-1.009598	0.861568
C	-0.583557	1.212196	-0.151368
C	-1.974055	-0.760098	-0.422726
C	0.503126	1.856023	0.267683
H	0.387106	-0.550582	1.811174
H	1.118250	-1.064873	0.271301
H	-0.197227	-2.041572	1.001644
H	-1.335491	1.750901	-0.719147
H	-2.202219	-1.807362	-0.276288
H	-2.681628	-0.17146	-0.992614
H	0.644842	2.906421	0.054388
H	1.282236	1.360846	0.833916
O	2.244360	-0.852557	-0.592818
H	1.871807	-0.093342	-1.069373

Table A3.15 Wavenumbers of the allylic radical formed upon H abstraction, calculated at the M06-2X/6-311++G(3df,2p) level of theory.

Mode #	Wavenumber cm^{-1}
1	26.59
2	313.48
3	417.26
4	437.70
5	511.67
6	537.26
7	580.73
8	739.69
9	787.11
10	832.56
11	848.72
12	966.48
13	982.53
14	1035.91
15	1041.11
16	1071.63
17	1262.22
18	1342.17
19	1381.70
20	1466.64
21	1493.33
22	1545.39
23	1721.95
24	3147.70
25	3157.69
26	3159.96
27	3171.39
28	3233.69
29	3257.81
30	3266.77

Table A3.16 Cartesian coordinates for the allylic radical formed upon H abstraction, optimized at the M06-2X/6-311++G(3df,2p) level of theory.

Atom	x	y	z
C	0.524231	0.001767	0.023430
C	0.685619	1.383070	0.047998
C	-0.820341	-0.613859	0.101872
C	1.611649	-0.839419	-0.069065
C	-1.977200	0.006993	-0.08632
H	-0.147842	2.056097	0.176064
H	1.671314	1.816678	-0.038775
H	-0.825268	-1.677722	0.316266
H	2.615522	-0.445312	-0.140599
H	1.490254	-1.913112	-0.077862
H	-2.913560	-0.528430	-0.014608
H	-2.034165	1.060487	-0.327975

Calculation of the collision broadening factor (*F*) for the TROE formalism

$$F(x) = (1 + \frac{x}{x_0}) / [1 + (\frac{x}{x_0})^{n_1}]^{1/n_1} \quad \text{A3.1}$$

$$x = k_0[\mathrm{M}] / k_{1a}^{\infty}(T) \quad \text{A3.2}$$

$$n_1 = \left[\frac{\ln 2}{\ln(\frac{2}{F_{cent}})}\right] [1 - b + b\,(\frac{x}{x_0})^{q}] \quad \text{A3.3}$$

$$q = (F_{cent} - 1) / \ln(\frac{F_{cent}}{10}) \quad \text{A3.4}$$

$$F_{cent}(T) = F_{cent}\mathrm{A} \times \exp(-F_{cent}\mathrm{B} \times T) + F_{cent}\mathrm{C} \quad \text{A3.5}$$

APPENDIX 4

Figure A4.1 The excel interface used to generate a MATLAB script which solves the chemical problem defined. The figure shows a simplified version of the Leuven Isoprene Mechanism 1 which supresses the di-HPCARP channels.

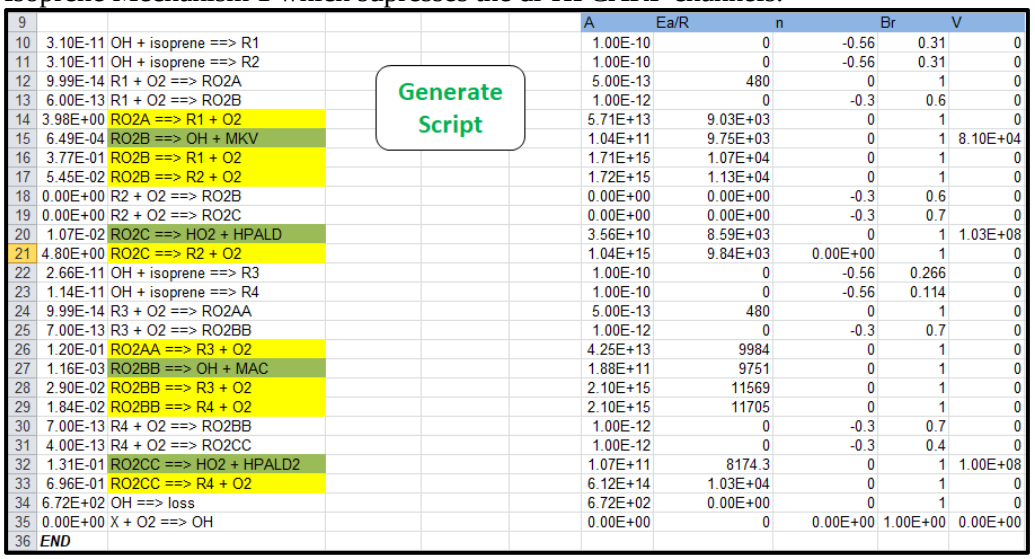

Generate Script

			A	Ea/R	n	Br	V
10	3.10E-11	OH + isoprene ==> R1	1.00E-10	0	-0.56	0.31	0
11	3.10E-11	OH + isoprene ==> R2	1.00E-10	0	-0.56	0.31	0
12	9.99E-14	R1 + O2 ==> RO2A	5.00E-13	480	0	1	0
13	6.00E-13	R1 + O2 ==> RO2B	1.00E-12	0	-0.3	0.6	0
14	3.98E+00	RO2A ==> R1 + O2	5.71E+13	9.03E+03	0	1	0
15	6.49E-04	RO2B ==> OH + MKV	1.04E+11	9.75E+03	0	1	8.10E+04
16	3.77E-01	RO2B ==> R1 + O2	1.71E+15	1.07E+04	0	1	0
17	5.45E-02	RO2B ==> R2 + O2	1.72E+15	1.13E+04	0	1	0
18	0.00E+00	R2 + O2 ==> RO2B	0.00E+00	0.00E+00	-0.3	0.6	0
19	0.00E+00	R2 + O2 ==> RO2C	0.00E+00	0.00E+00	-0.3	0.7	0
20	1.07E-02	RO2C ==> HO2 + HPALD	3.56E+10	8.59E+03	0	1	1.03E+08
21	4.80E+00	RO2C ==> R2 + O2	1.04E+15	9.84E+03	0.00E+00	1	0
22	2.66E-11	OH + isoprene ==> R3	1.00E-10	0	-0.56	0.266	0
23	1.14E-11	OH + isoprene ==> R4	1.00E-10	0	-0.56	0.114	0
24	9.99E-14	R3 + O2 ==> RO2AA	5.00E-13	480	0	1	0
25	7.00E-13	R3 + O2 ==> RO2BB	1.00E-12	0	-0.3	0.7	0
26	1.20E-01	RO2AA ==> R3 + O2	4.25E+13	9984	0	1	0
27	1.16E-03	RO2BB ==> OH + MAC	1.88E+11	9751	0	1	0
28	2.90E-02	RO2BB ==> R3 + O2	2.10E+15	11569	0	1	0
29	1.84E-02	RO2BB ==> R4 + O2	2.10E+15	11705	0	1	0
30	7.00E-13	R4 + O2 ==> RO2BB	1.00E-12	0	-0.3	0.7	0
31	4.00E-13	R4 + O2 ==> RO2CC	1.00E-12	0	-0.3	0.4	0
32	1.31E-01	RO2CC ==> HO2 + HPALD2	1.07E+11	8174.3	0	1	1.00E+08
33	6.96E-01	RO2CC ==> R4 + O2	6.12E+14	1.03E+04	0	1	0
34	6.72E+02	OH ==> loss	6.72E+02	0.00E+00	0	1	0
35	0.00E+00	X + O2 ==> OH	0.00E+00	0	0.00E+00	1.00E+00	0.00E+00
36	***END***						

```
function [ b, fval, exitflag, output, solutions ] = pfo()

clc;
clear all;
close all;
data=importdata('/home/home02/cmddjm/MESMER/Mesmer4.1-
source/examples/matlab_ethylene_12112018/Exp_data.txt');

data2=importdata('/home/home02/cmddjm/MESMER/Mesmer4.1-
source/examples/matlab_ethylene_12112018/Weights.txt');

data3=importdata('/home/home02/cmddjm/MESMER/Mesmer4.1-
source/examples/matlab_ethylene_12112018/Loss_rate.txt');

tspan1=data(:,1);
Ca_data1=data(:,2);
tspan1(~any(~isnan(tspan1), 2),:)=[];
Ca_data1(~any(~isnan(Ca_data1), 2),:)=[];
s1=size(tspan1);
tspan1=tspan1/1e3;

tspan2=data(:,3);
Ca_data2=data(:,4);
tspan2(~any(~isnan(tspan2), 2),:)=[];
Ca_data2(~any(~isnan(Ca_data2), 2),:)=[];
s2=size(tspan2);
tspan2=tspan2/1e3;

tspan3=data(:,5);
Ca_data3=data(:,6);
tspan3(~any(~isnan(tspan3), 2),:)=[];
Ca_data3(~any(~isnan(Ca_data3), 2),:)=[];
s3=size(tspan3);
tspan3=tspan3/1e3;

tspan4=data(:,7);
Ca_data4=data(:,8);
tspan4(~any(~isnan(tspan4), 2),:)=[];
Ca_data4(~any(~isnan(Ca_data4), 2),:)=[];
s4=size(tspan4);
tspan4=tspan4/1e3;

tspan5=data(:,9);
Ca_data5=data(:,10);
tspan5(~any(~isnan(tspan5), 2),:)=[];
Ca_data5(~any(~isnan(Ca_data5), 2),:)=[];
s5=size(tspan5);
tspan5=tspan5/1e3;

tspan6=data(:,11);
Ca_data6=data(:,12);
tspan6(~any(~isnan(tspan6), 2),:)=[];
Ca_data6(~any(~isnan(Ca_data6), 2),:)=[];
s6=size(tspan6);
```

```
tspan6=tspan6/1e3;


Ca_data1=Ca_data1/data2(1);
Ca_data2=Ca_data2/data2(2);
Ca_data3=Ca_data3/data2(3);
Ca_data4=Ca_data4/data2(4);
Ca_data5=Ca_data5/data2(5);
Ca_data6=Ca_data6/data2(6);



s0=0;
tspan=[tspan1;tspan2;tspan3;tspan4;tspan5;tspan6;];
Ca_data=[Ca_data1;Ca_data2;Ca_data3;Ca_data4;Ca_data5;Ca_data6];
parguess=[1.98466996809536,1.64722346293468,1.07981103615226,1.24810314998
381,1.16948206026735,1.56841012973971,-110,0.822,-0.35,1,1,221,0.26,400];
ub=[3.77087293938119,3.1297245795759,2.05164096868929,2.37139598496924,2.2
2201591450796,2.97997924650545,-100,0.86,1.35,1.1,1.1,400,0.95,2000];
lb=[0.198466996809536,0.164722346293468,0.107981103615226,0.1248103149983
81,0.116948206026735,0.156841012973971,-135,0.78,-1.35,0.9,0.9,100,0.05,0];




global contador_global;
global last_call;
global save_print;

   global arquivo_aberto;
   global contcoeff;
   global ratecoeffs;

contador_global=0;

last_call=[-999999999999 -999999999999 -999999999999 -999999999999];


function [output] = myfunc2(paras,tspan)

%Primeiro resolve o Mesmer
% persistent arquivo_aberto;
% persistent contcoeff;
% persistent ratecoeffs;
arquivo_aberto=false;

if(last_call(1,1) ~= paras(7) || last_call(1,2) ~= paras(8) || last_call(1,3) ~= paras(9) ||
last_call(1,4) ~= paras(12) || last_call(1,5) ~= paras(13))

%Editar o arquivo com os novos parametros e rodar
% Read txt into cell A
tmpName=tempname;
```

```
        tmpName=tmpName(5:end);
        FulltmpName = ['/home/home02/cmddjm/MESMER/Mesmer4.1-
source/examples/matlab_ethylene_12112018/',tmpName,'.xml'];

        copyfile('/home/home02/cmddjm/MESMER/Mesmer4.1-
source/examples/matlab_ethylene_12112018/Ethylene_MATLAB_updated_96_traces
_12112018.xml',[FulltmpName]);
   fid = fopen(FulltmpName,'r');


i = 1;
tline = fgetl(fid);
A{i} = tline;
while ischar(tline)
   i = i+1;
   tline = fgetl(fid);
   A{i} = tline;
end
fclose(fid);


patternyy='<molecule id="ethylene_OH"';
for i = 1:numel(A)
   control=~isempty(strfind(A{i},patternyy));
   if control==true
      break;
   end
end







patternyy='dictRef="me:ZPE"';
for i = i:numel(A)
   control=~isempty(strfind(A{i},patternyy));
   if control==true
      break;
   end
end

%paras(1)=3.25e-12;

variavel_definida=['       <scalar units="kJ/mol">' num2str(paras(7)) '</scalar>'];
A{i+1} = sprintf('%s',variavel_definida);
%A{i+1} = sprintf('       <scalar units="kJ/mol">-150.690685 dIOGO</scalar>');




patternyy='me:ExponentialDown';
for i = i:numel(A)
   control=~isempty(strfind(A{i},patternyy));
```

```
   if control==true
      break;
   end
end

%paras(1)=3.25e-12;

variavel_definida=['                <me:deltaEDown bathGas="N2" units="cm-1">'
num2str(paras(12)) '</me:deltaEDown>'];
A{i+1} = sprintf('%s',variavel_definida);
variavel_definida=['                <me:deltaEDownTExponent bathGas="N2"
referenceTemperature="298">' num2str(paras(13)) '</me:deltaEDownTExponent>'];
A{i+2} = sprintf('%s',variavel_definida);
%A{i+1} = sprintf('       <scalar units="kJ/mol">-150.690685 dIOGO</scalar>');



patternyy='reactionList';
for i = i:numel(A)
   control=~isempty(strfind(A{i},patternyy));
   if control==true
      break;
   end
end

%reaction 1

patternyy='<reaction id="R1">';
for i = i:numel(A)
   control=~isempty(strfind(A{i},patternyy));
   if control==true
      break;
   end
end


patternyy='<me:preExponential';
for i = i:numel(A)
   control=~isempty(strfind(A{i},patternyy));
   if control==true
      break;
   end
end

variavel_definida=['   <me:preExponential units="cm3molecule-1s-1">' num2str(1E-
11*paras(8)) '</me:preExponential>'];
A{i} = sprintf('%s',variavel_definida);


patternyy='<me:nInfinity>';
for i = i:numel(A)
   control=~isempty(strfind(A{i},patternyy));
   if control==true
      break;
```

```
   end
end



variavel_definida=['  <me:nInfinity>' num2str(paras(9)) '</me:nInfinity>'];
A{i} = sprintf('%s',variavel_definida);

fid = fopen(FulltmpName, 'w');
for i = 1:numel(A)
   if A{i+1} == -1
      fprintf(fid,'%s', A{i});
      break
   else
      fprintf(fid,'%s\n', A{i});
   end
end

fclose(fid);


 temporario='Mesmer is running';
%            temporario=[num2str(contador_global),'       param(1)=',num2str(paras(1)),'
param(2)=',num2str(paras(2)),' param(3)=',num2str(paras(3))];

 disp(temporario);
  %contador_global=contador_global+1;

%uma vez o arquivo editado, roda-lo e extrair informacoes pertinentes
command=['mesmer -N ',tmpName(2:end),'.xml',' -o ',tmpName(2:end),'.out'];
[status, cmdout]=system(command);

temporario='Mesmer has finished a calculation';
%            temporario=[num2str(contador_global),'       param(1)=',num2str(paras(1)),'
param(2)=',num2str(paras(2)),' param(3)=',num2str(paras(3))];
 disp(temporario);

%copyfile                                  /home/home02/cmddjm/MESMER/Mesmer4.1-
source/examples/matlab_ethylene_12112018//mesmer_out.xml;

%se o arquivo for ser aberto pela primeira vez, contar o numero de
%coeficientes de reacao.
if arquivo_aberto==false

      fileID          =          fopen(['/home/home02/cmddjm/MESMER/Mesmer4.1-
source/examples/matlab_ethylene_12112018/',tmpName,'.out']);
   line=fgetl(fileID);

   %indicar que o arquivo foi aberto e buscar o numero de coeficientes
   arquivo_aberto=true;

   patternyy='me:rateList';

   control=~isempty(strfind(line,patternyy));
```

```
   while control==false
   line=fgetl(fileID);
   control=~isempty(strfind(line,patternyy));
   end

   patternyy='fromRef';
   control=false;
   while control==false
   line=fgetl(fileID);
   control=~isempty(strfind(line,patternyy));
   end

   %essa linha ja contem o primeiro rate coefficient
   contcoeff=1;
   patternyy='me:rateList';
   control=false;
   while control==false
   contcoeff=contcoeff+1;
   line=fgetl(fileID);
   control=~isempty(strfind(line,patternyy));
   end
   contcoeff=contcoeff-1;
   fclose(fileID);

end
  %aqui ja se sabe o numero de constantes, guardado em contcoeff

   fileID = fopen(['/home/home02/cmddjm/MESMER/Mesmer4.1-
source/examples/matlab_ethylene_12112018/',tmpName,'.out']);
   line=fgetl(fileID);

   %indicar que o arquivo foi aberto e buscar o numero de coeficientes
   arquivo_aberto=true;

   patternyy='me:rateList';

   control=~isempty(strfind(line,patternyy));

   while control==false
   line=fgetl(fileID);
   control=~isempty(strfind(line,patternyy));
   end

   patternyy='fromRef';
   control=false;
   while control==false
   line=fgetl(fileID);
   control=~isempty(strfind(line,patternyy));
   end

   %essa linha ja contem o primeiro rate coefficient
   patternyy='analysis';
   control=false;
```

```
control2=false;
control3=false;
ratecoeffs=[];
ratecoeffscomplete=[];
counter=1;
while control==false

   patternyy='<me:rateList ';
   control2=~isempty(strfind(line,patternyy));
   if control2==true
      ratecoeffscomplete=[ratecoeffscomplete ratecoeffs];
      ratecoeffs=[];

      patternyy='fromRef';
      control3=false;
      while control3==false
      line=fgetl(fileID);
      control3=~isempty(strfind(line,patternyy));
      end

      counter=counter+1;
      control2=false;
   end

      key1=strfind(line,'>');
      key2=strfind(line,'<');

         [m,n] =size(key1);
         [m2,n2] =size(key2);

         if(n<2 || n2<2)
         line=fgetl(fileID);
         patternyy='analysis';
         control=~isempty(strfind(line,patternyy));
         continue
         end

      key1=key1(1)+1;
      key2=key2(2)-1;




      line=str2double(line(key1:key2));
      ratecoeffs=[ratecoeffs;line];

      line=fgetl(fileID);
      patternyy='analysis';
      control=~isempty(strfind(line,patternyy));
end
ratecoeffs=[ratecoeffscomplete ratecoeffs];
fclose(fileID);

                delete([tmpName(2:end),'.out']);
```

```
                delete([tmpName(2:end),'.log']);
                delete([tmpName(2:end),'.test']);
                delete([tmpName(2:end),'.xml']);
%removendo valores muito pequenos do array
    indices_neg=find(ratecoeffs<1e-10);
    ratecoeffs(indices_neg)=0;

end

A1_=ratecoeffs(1,:)/1e15;
Ea1_=0;
n1_=0;
V1_=0;
A2_=ratecoeffs(2,:);
Ea2_=0;
n2_=0;
V2_=0;
A3_=data3;
Ea3_=0;
n3_=0;
V3_=0;
A4_=0;
Ea4_=0;
n4_=0;
V4_=0;
A5_=0;
Ea5_=0;
n5_=0;
V5_=0;

A6_=3.4e-11*paras(10);
Ea6_=2990*paras(11);
n6_=0;
V6_=0;

OH1=paras(1);
OH2=paras(2);
OH3=paras(3);
OH4=paras(4);
OH5=paras(5);
OH6=paras(6);


function f=ode(t,y)

f(1,1)=-(A1_(int64(y(6)))*exp(-
Ea1_/y(5))*((y(5)/298)^n1_)*(exp(V1_/(y(5))^3)))*y(2)*y(1)+(A2_(int64(y(6)))*exp
(-Ea2_/y(5))*((y(5)/298)^n2_)*(exp(V2_/(y(5))^3)))*y(3)-(A3_(int64(y(6)))*exp(-
Ea3_/y(5))*((y(5)/298)^n3_)*(exp(V3_/(y(5))^3)))*y(1)+(A4_*exp(-
Ea4_/y(5))*((y(5)/298)^n4_)*(exp(V4_/(y(5))^3)))*y(3)*y(2)-(A6_*exp(-
Ea6_/y(5))*((y(5)/298)^n6_)*(exp(V6_/(y(5))^3)))*y(2)*y(1);
f(2,1)=-(A1_(int64(y(6)))*exp(-
Ea1_/y(5))*((y(5)/298)^n1_)*(exp(V1_/(y(5))^3)))*y(2)*y(1)+(A2_(int64(y(6)))*exp
(-Ea2_/y(5))*((y(5)/298)^n2_)*(exp(V2_/(y(5))^3)))*y(3)-(A4_*exp(-
```

```
Ea4_/y(5))*((y(5)/298)^n4_)*(exp(V4_/(y(5))^3)))*y(3)*y(2)-(A6_*exp(-
Ea6_/y(5))*((y(5)/298)^n6_)*(exp(V6_/(y(5))^3)))*y(2)*y(1);
f(3,1)=(A1_(int64(y(6)))*exp(-
Ea1_/y(5))*((y(5)/298)^n1_)*(exp(V1_/(y(5))^3)))*y(2)*y(1)-
(A2_(int64(y(6)))*exp(-Ea2_/y(5))*((y(5)/298)^n2_)*(exp(V2_/(y(5))^3)))*y(3)-
(A4_*exp(-Ea4_/y(5))*((y(5)/298)^n4_)*(exp(V4_/(y(5))^3)))*y(3)*y(2)-(y(7)*exp(-
Ea5_/y(5))*((y(5)/298)^n5_)*(exp(V5_/(y(5))^3)))*y(3);
f(4,1)=(A3_(int64(y(6)))*exp(-
Ea3_/y(5))*((y(5)/298)^n3_)*(exp(V3_/(y(5))^3)))*y(1)+(y(7)*exp(-
Ea5_/y(5))*((y(5)/298)^n5_)*(exp(V5_/(y(5))^3)))*y(3)+(A6_*exp(-
Ea6_/y(5))*((y(5)/298)^n6_)*(exp(V6_/(y(5))^3)))*y(2)*y(1);
f(5,1)=0;
f(6,1)=0;
f(7,1)=0;

end
Cao1=[OH1,6.64E+15,0,0,723,1,paras(14)];
tspani1=[0.0;tspan(s0+1:s1,1)];
[t1,Ca1]=ode15s(@ode,tspani1,Cao1);
Ca1plot=Ca1;
Ca1(1,:)=[];
output1=Ca1(:,1);

Cao2=[OH2,5.81E+15,0,0,723,1,paras(14)];
tspani2=[0.0;tspan(s0+s1+1:s1+s2,1)];
[t2,Ca2]=ode15s(@ode,tspani2,Cao2);
Ca2plot=Ca2;
Ca2(1,:)=[];
output2=Ca2(:,1);

Cao3=[OH3,5.01E+15,0,0,723,1,paras(14)];
tspani3=[0.0;tspan(s0+s1+s2+1:s1+s2+s3,1)];
[t3,Ca3]=ode15s(@ode,tspani3,Cao3);
Ca3plot=Ca3;
Ca3(1,:)=[];
output3=Ca3(:,1);

Cao4=[OH4,4.17E+15,0,0,723,1,paras(14)];
tspani4=[0.0;tspan(s0+s1+s2+s3+1:s1+s2+s3+s4,1)];
[t4,Ca4]=ode15s(@ode,tspani4,Cao4);
Ca4plot=Ca4;
Ca4(1,:)=[];
output4=Ca4(:,1);

Cao5=[OH5,3.34E+15,0,0,723,1,paras(14)];
tspani5=[0.0;tspan(s0+s1+s2+s3+s4+1:s1+s2+s3+s4+s5,1)];
[t5,Ca5]=ode15s(@ode,tspani5,Cao5);
Ca5plot=Ca5;
Ca5(1,:)=[];
output5=Ca5(:,1);

Cao6=[OH6,2.51E+15,0,0,723,1,paras(14)];
tspani6=[0.0;tspan(s0+s1+s2+s3+s4+s5+1:s1+s2+s3+s4+s5+s6,1)];
[t6,Ca6]=ode15s(@ode,tspani6,Cao6);
```

```
Ca6plot=Ca6;
Ca6(1,:)=[];
output6=Ca6(:,1);



output=[output1;output2;output3;output4;output5;output6];

last_call=[paras(7) paras(8) paras(9) paras(12) paras(13)];


 temporario=[num2str(contador_global),'                param(97)=',num2str(paras(7)),'
param(98)=',num2str(paras(8)),'                       param(99)=',num2str(paras(9)),'
param(100)=',num2str(paras(10)),'                   param(101)=',num2str(paras(11)),'
param(102)=',num2str(paras(12)),'                   param(103)=',num2str(paras(13)),'
param(104)=',num2str(paras(14))];
 disp(temporario);
 contador_global=contador_global+1;

 save('matlab2.mat');

end

scaling=[];
for i=1:104
scaling=[scaling 0.025];
end

options=optimoptions('lsqcurvefit','MaxIterations',10,'Display','iter','TolFun',1e-
6,'TolX',1e-6,'FinDiffRelStep',scaling,'UseParallel',true);
[x,resnorm,residual,exitflag,output,lambda,jacobian]=lsqcurvefit(@myfunc2,parguess
,tspan, Ca_data, lb, ub, options);
fit=myfunc2(x,tspan);
ci=nlparci(x,residual,'jacobian',jacobian);

save('matlab.mat');


end
```